

DEVELOPMENT OF THE JUNGFRAUJOCH MULTI-WAVELENGTH LIDAR SYSTEM FOR CONTINUOUS OBSERVATIONS OF THE AEROSOL OPTICAL PROPERTIES IN THE FREE TROPOSPHERE

THÈSE N° 2539 (2002)

PRÉSENTÉE À LA FACULTÉ ENAC SECTION DES SCIENCES ET INGÉNIERIE DE L'ENVIRONNEMENT

ÉCOLE POLYTECHNIQUE FÉDÉRALE DE LAUSANNE

POUR L'OBTENTION DU GRADE DE DOCTEUR ÈS SCIENCES

PAR

Gilles LARCHEVÊQUE

ingénieur du génie rural diplômé EPF
de nationalité suisse et originaire de Collex-Bossy (GE)

acceptée sur proposition du jury:

Prof. B. Calpini, directeur de thèse
Dr U. Baltensperger, rapporteur
Prof. J.-P. Borel, rapporteur
Dr C. Böckmann, rapporteur
Prof. R. Monot, rapporteur
Dr V. Simeonov, rapporteur
Prof. H. van den Bergh, rapporteur

Lausanne, EPFL
2002

Extrait d'un discours tenu par un chef de tribu en 1855 devant le président des Etats-Unis d'Amérique

«Tout ce qui arrive à la terre arrive aussi aux enfant de la terre. Quand les hommes crachent sur la terre, ils crachent sur eux-mêmes. Car nous savons ceci: la terre n'appartient pas aux hommes, mais les hommes appartiennent à la terre. Toutes les choses sont liées entre elles [...] l'être humain n'a pas tissé le fil de la vie, il est seulement un élément de ce fil. Tout ce qu'il fait à ce fil, il le fait à lui-même».

Table of Contents

| | |
|---|------------|
| Remerciements | vii |
| Jungfrauoch Picture Gallery | ix |
| Résumé | 1 |
| Summary | 3 |
| | |
| Chapter 1 Introduction | 5 |
| 1.1. The Earth-atmosphere system | 6 |
| 1.2. Radiative forcing | 10 |
| 1.3. Aerosol direct effects on climate | 13 |
| 1.4. Aerosol measurements | 15 |
| 1.5. Conclusion | 17 |
| 1.6. References | 17 |
| | |
| Chapter 2 Theory | 21 |
| 2.1. Lidar principle | 22 |
| 2.2. Basic scattering lidar equation | 23 |
| 2.3. Atmospheric interactions | 23 |
| 2.4. Rayleigh scattering | 25 |
| 2.4.1. Angular scattering cross section | 25 |
| 2.4.2. Total volume scattering cross section | 26 |
| 2.4.3. Phase function | 27 |
| 2.4.4. Mean molecular concentration | 27 |
| 2.4.5. Refractive index of the dry air | 28 |
| 2.4.6. King factor | 29 |
| 2.4.7. Volume scattering coefficient | 30 |
| 2.4.8. US-Standard-Atmosphere 1976 | 31 |
| 2.5. Mie scattering | 32 |
| 2.5.1. Intensity distribution functions | 32 |
| 2.5.2. Angular scattering cross section | 34 |
| 2.5.3. Volume angular scattering coefficient (monodispersion) | 35 |
| 2.5.4. Total scattering cross section and efficiency factor | 36 |
| 2.5.5. Volume extinction coefficients | 37 |

| | |
|--|-----------|
| 2.5.6. Angstrom exponent. | 40 |
| 2.6. Geometric scattering. | 41 |
| 2.7. Raman scattering | 41 |
| 2.7.1. Raman scattering cross section. | 42 |
| 2.7.2. Raman shifted wavelengths calculation | 42 |
| 2.8. Molecular absorption | 43 |
| 2.9. Elastic Lidar equation. | 46 |
| 2.10. Raman lidar equation | 48 |
| 2.11. Water vapor mixing ratio | 50 |
| 2.12. Depolarization ratio | 50 |
| 2.13. Retrieval of microphysical aerosol parameters | 51 |
| 2.14. Conclusion | 53 |
| 2.15. References | 53 |
| Chapter 3 Experimental Setup | 59 |
| 3.1. System description | 60 |
| 3.2. Ray tracing analysis | 62 |
| 3.2.1. Overlap function | 62 |
| 3.2.2. Simulation of the detection part | 65 |
| 3.3. Filter polychromators | 71 |
| 3.3.1. Newtonian filter polychromator | 71 |
| 3.3.2. Cassegrain filter polychromator | 72 |
| 3.4. Detectors. | 73 |
| 3.5. The Hamamatsu photosensor modules | 74 |
| 3.5.1. Anode spatial uniformity | 74 |
| 3.5.2. Linearity of the photosensor | 76 |
| 3.5.3. After pulse effect | 78 |
| 3.5.4. Conclusion | 80 |
| 3.6. Conclusion | 80 |
| 3.7. References | 81 |
| Chapter 4 Data Treatment & Error Analysis | 83 |
| 4.1. Data treatment | 84 |
| 4.1.1. Fernald inversion | 84 |
| 4.1.2. Raman inversion | 89 |
| 4.2. Error analysis | 90 |
| 4.2.1. Error propagation | 90 |
| 4.2.2. Errors of the Fernald inversion | 90 |
| 4.2.3. Errors of the Raman inversion | 97 |
| 4.2.4. Error of the backscatter profile | 102 |
| 4.2.5. Error on the lidar ratio | 104 |
| 4.2.6. Error on the depolarization ratio. | 105 |

| | |
|--|------------|
| 4.3. Angstrom exponent | 107 |
| 4.4. Conclusion | 107 |
| 4.5. References | 108 |
| Chapter 5 Hardware & Software intercomparisons | 111 |
| 5.1. Elastic algorithm. | 112 |
| 5.1.1. Data simulation. | 112 |
| 5.1.2. Intercomparison results. | 114 |
| 5.2. Raman algorithm | 119 |
| 5.2.1. Data simulation. | 119 |
| 5.2.2. Intercomparison results. | 119 |
| 5.3. System intercomparison | 123 |
| 5.4. Conclusion | 127 |
| 5.5. References | 127 |
| Chapter 6 Applied Optics Article. | 129 |
| Chapter 7 Advances in global change research Article | 151 |
| Chapter 8 Case studies | 169 |
| 8.1. Sunphotometer comparison | 170 |
| 8.2. Cirrus study. | 172 |
| 8.2.1. Meteorological conditions | 172 |
| 8.2.2. Lidar setup | 173 |
| 8.2.3. Aerosol backscatter, extinction and lidar ratio profiles | 175 |
| 8.2.4. Depolarization ratio | 180 |
| 8.2.5. Size retrieval | 181 |
| 8.3. Conclusion | 186 |
| 8.4. References | 186 |
| Chapter 9 Conclusion and perspectives. | 189 |
| Chapter 10 Annex | 191 |
| 10.1. Mie extinction and backscattering coefficients | 192 |
| 10.2. Lidar specification table | 194 |
| 10.2.1. Transmitter | 194 |
| 10.2.2. Receiver | 195 |
| 10.3. Overlap function. | 201 |
| 10.4. Laser beam radius depending on the altitude above the Station. | 202 |
| 10.5. Error on the backscatter coefficient determined by Raman lidar | 203 |
| 10.6. Elastic intercomparisons. | 205 |

| | |
|---|------------|
| 10.6.1. Case 1 | 205 |
| 10.6.2. Case 2 | 208 |
| 10.6.3. Case 3 | 211 |
| Curriculum Vitae & Personal publications | 215 |

Remerciements

Une thèse est aussi un travail personnel, mais elle n'est pas réalisable sans aide. Je tiens donc à remercier tout particulièrement les personnes suivantes

Le professeur Hubert van den Bergh, chef du laboratoire de pollution de l'air et du sol, pour m'avoir accueilli et supporté durant toutes ces années. Mais surtout pour avoir su éveiller mon intérêt pour la pollution atmosphérique.

Le professeur Bertrand Calpini, mon directeur de thèse, pour son esprit d'ouverture et pour la grande marge de manœuvre dont j'ai pu profiter durant toute la durée de ma thèse.

Philippe Quaglia, pour son aide durant le développement du système lidar et surtout pour sa dextérité en monocycle.

Valentin Simeonov, pour ses conseils avisés tout au long de mon travail et ses choix judicieux en matière de biscuits.

Benoît Lazzarotto, pour qu'il n'oublie pas ma bouteille de Macallan 50 ans d'âge!! et François Jeanneret qui ne va pas se gêner de la boire.

Ioan Balin, le futur président de Crossair, Rodrigo Jimenez, Remo Nessler et Pablo Ristori. Mais aussi Alfonso, Fernando et Manuel, les trois mousquetaires colombiens.

Flavio Comino, pour avoir minutieusement usiné les parties mécaniques.

Les lopettes du groupe modélisation qui n'ont jamais vu un vrai nuage de leur vie, soit Alain «Hamster Jovial» Clappier, Olivier Couach, Martin Junier, Frank Kirchner, Jérôme Kübler, Alberto Martilli et Yves-Alain Roulet.

Les Brono et Clono du groupe hétéro, soit Carine Jornod, Arnaud Aguzzi, Christophe Delval, Benjamin Demirdjian, Benoît Fluckiger et Christian Santschi, sans oublier leur chef adoré, le Dr. Michel Rossi pour qui tout n'est que chimie...

Albert Einstein qui a su remettre les chimistes à leur juste place, c'est à dire à la cafétéria, n'est ce pas Michel Carrara???? Un jour tu comprendras que le côté obscur du fluide n'a pas d'égal.

Sandra Reinhard et Adonella Sterzi pour les agréables soirées passées en leur compagnie.

Les criquets du WBL qui ont attendu avec patience la fin de ma thèse mais surtout l'apéro de la soutenance publique.

Les joueuses du BBC Rosay qui n'ont pas besoin d'attendre une fin de thèse pour fêter une victoire...

Liliane Künzi pour sa gentillesse et plus encore!!!

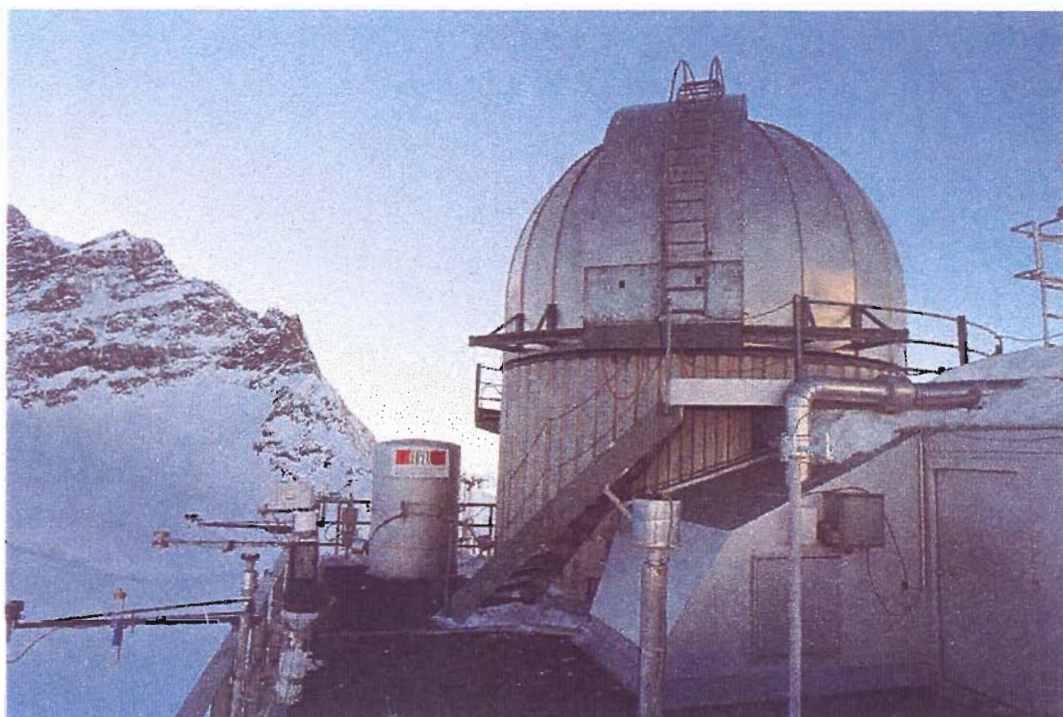
Et enfin mes parents pour m'avoir donné l'opportunité de poursuivre mes études contre vents et marées...

Jungfrauoch Picture Gallery



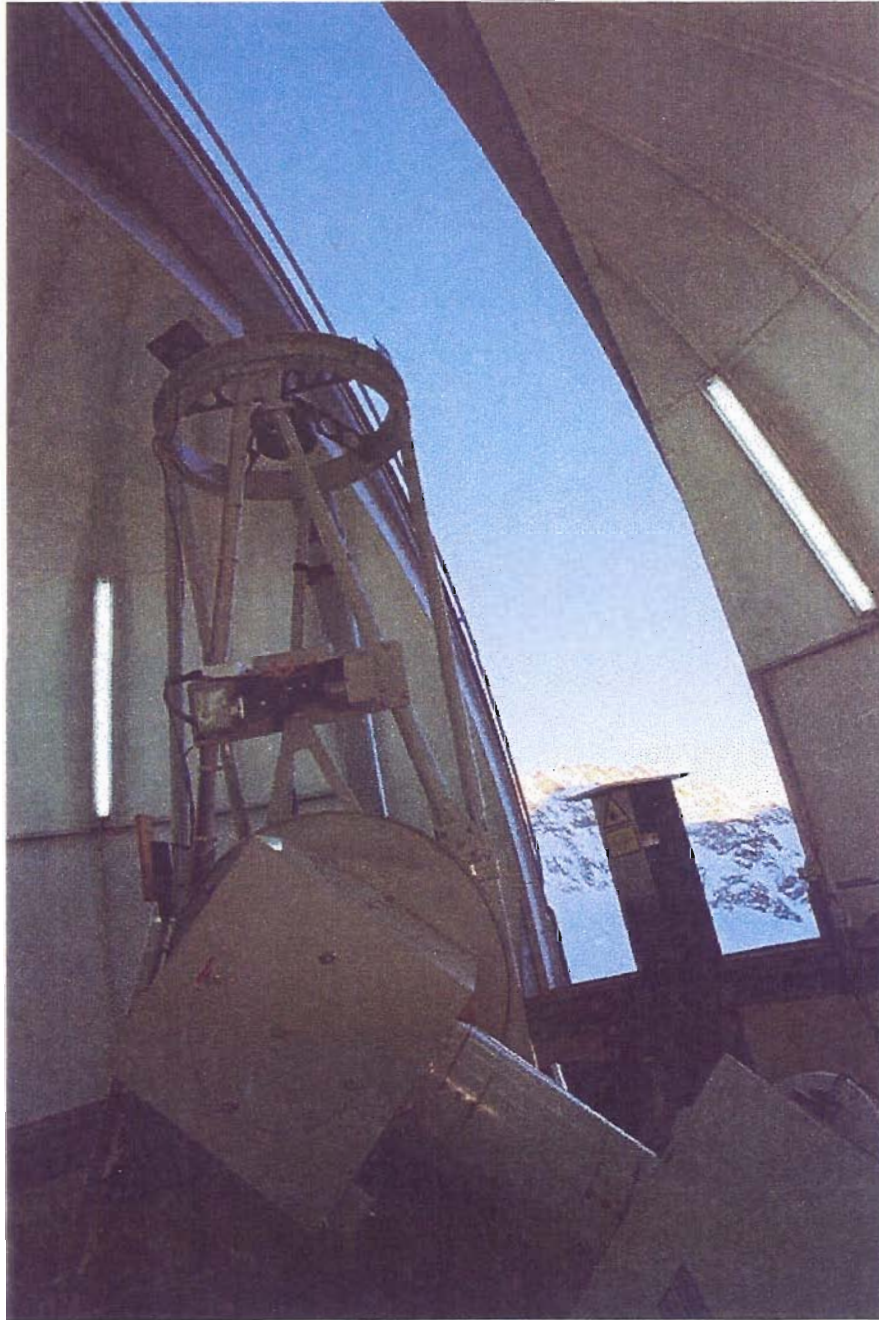
Picture from <http://www.jungfrauoch.ch>

FIGURE 1. General view of the Jungfrauoch observatory and the Aletsch Glacier. The lidar system is installed inside the astronomical dome whereas the small cupola contains the sunphotometer of the Swiss Meteorological Institute.



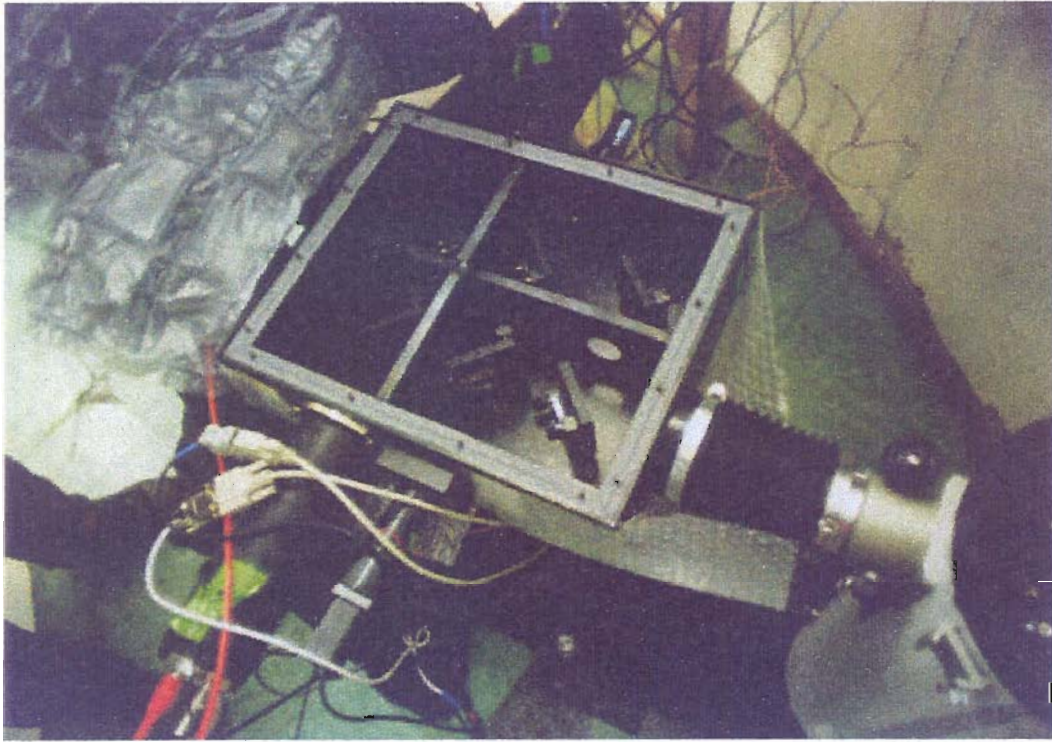
Picture from Alain Herzog

FIGURE 2. Close shot of the astronomical dome. The two tubes in the foreground distance are the two inlets for the Paul Scherrer Institute aerosol studies. The big can in the background is the sun tracker of the FTIR system whereas the small box on the gate is the SAOZ system.



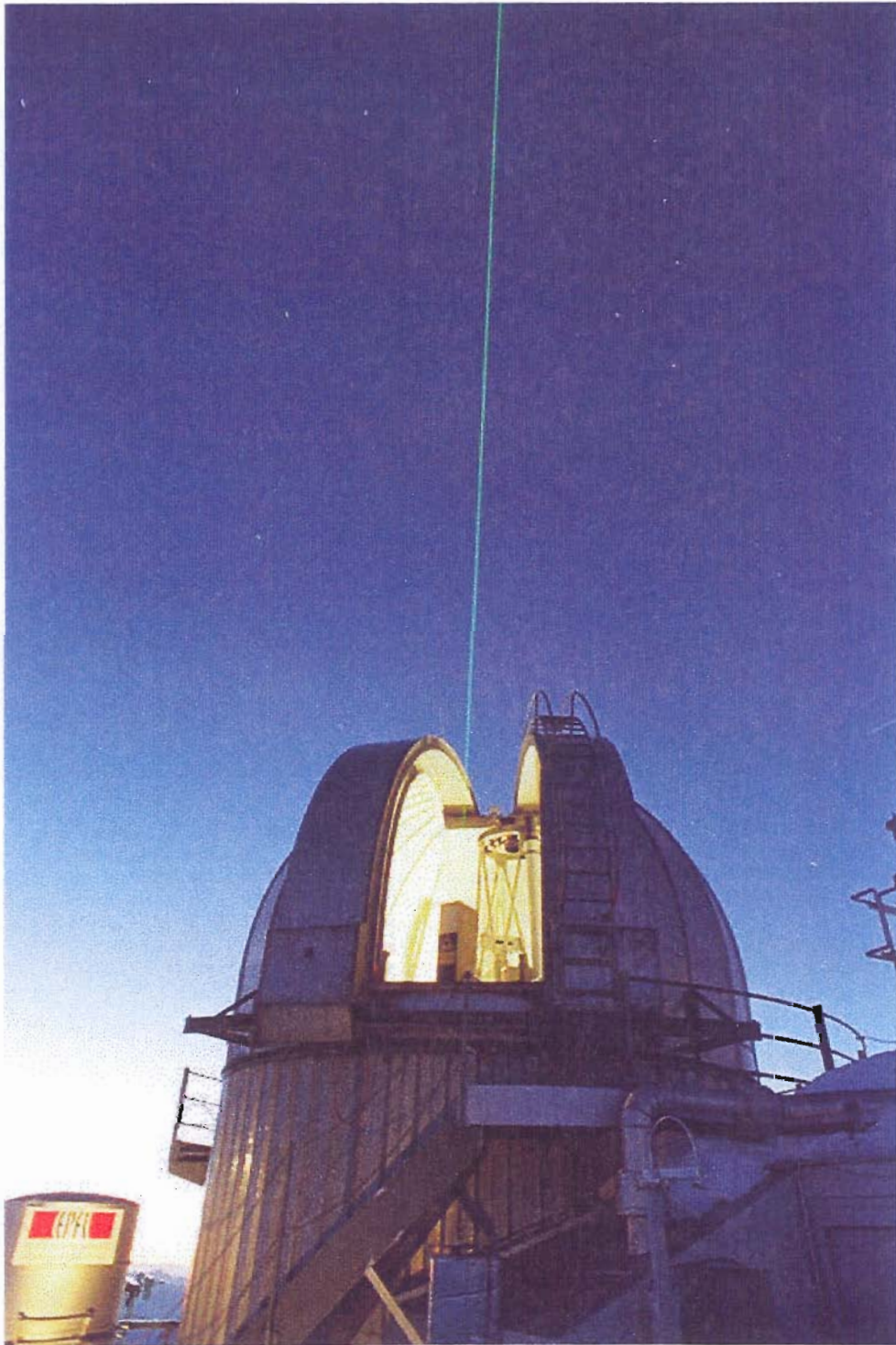
Picture from Alain Herzog

FIGURE 3. Close shot of the Cassegrain telescope. The tube in the background is the eye-safe chimney for the three laser beams.



Picture from Philippe Quaglia

FIGURE 4. Close shot of the Newtonian filter polychromator. The light coming from the Newtonian telescope, enters from the right and is collimated by one lens inside the sleeve. The six beamsplitters are visible as well as the two webs against the scattering. On each side the two large tubes are the housing of the Thorn-Emi PMTs. The small box on the upper side is one Hamamatsu photosensor module whereas the thin tube on the other side contains the Wollaston prism and two other photosensor modules. The last housing and the APD are hidden by the plastic cover.



Picture from Alain Herzog

FIGURE 5. Lidar at work...



Picture from Alain Herzog

FIGURE 6. Sunset in heaven...

Résumé

Le réchauffement planétaire et les changements climatiques sont généralement associés à la variation de l'effet de serre induit par les activités humaines. Ce changement peut être régionalement masqué par l'effet inverse induit par les aérosols qui ont tendance à refroidir l'atmosphère. Mais leurs fortes variations spatio-temporelles et l'impossibilité de les caractériser globalement induisent de larges incertitudes dans les prédictions des modèles numériques. De plus, ces incertitudes sont du même ordre de grandeur que la variation de l'effet de serre, ce qui n'est pas tolérable. Pour minimiser ces erreurs, il est nécessaire d'améliorer le panel des instruments (in situ et télédétection) capables de détecter les changements de la quantité troposphériques et stratosphériques d'aérosols et de leurs propriétés radiatives, les changements de la quantité d'eau dans l'atmosphère ainsi que les profils de températures et les changements de la couverture nuageuse et des propriétés radiatives de ces nuages. Le forçage radiatif est un indicateur de la contribution d'un agent (gaz à effet de serre, aérosols) au changement du bilan radiatif de la planète Terre. Un de ces forçages est le forçage direct dû aux aérosols qui dépend de la profondeur optique et de la fraction de diffusion vers le haut des aérosols. Ces deux paramètres dépendent de la composition chimique et de la distribution en fonction de la taille des aérosols. Donc les principales caractéristiques de ces aérosols sont la composition chimique au travers de l'indice de réfraction et la distribution en fonction de la taille.

Ce présent travail traite du développement et de la mise en opération d'un système lidar multi-longueur d'ondes à la station scientifique de la Jungfraujoch (Alt. 3560m au dessus du niveau de la mer). Ce système est une combinaison d'un lidar élastique avec un lidar à effet Raman dont la partie réceptrice a été conçue par un logiciel de *ray tracing*. La source laser est un laser solide Nd:YAG triplé et la lumière rétrodiffusée est collectée par deux télescopes, le premier est en configuration de Newton pour les mesures troposphérique, alors que le second est du type Cassegrain pour les futures mesures stratosphériques. Les longueurs d'ondes détectées sont les trois longueurs d'ondes du laser (355, 532 et 1064nm) rétrodiffusées élastiquement par les molécules et aérosols atmosphériques. De plus, les rétrodiffusions induites par l'effet Raman spontané sur les molécules d'azote (387 et 607nm) et sur les molécules d'eau (408nm) sont aussi utilisées. La séparation spectrale de ces signaux optiques est faite par deux polychromateurs à filtres. Ils sont construits autour de séparateurs de faisceaux et de filtres étroits avec un haut taux de réjection en dehors des bandes passantes. Sur les signaux à 532nm, un prisme de Wollaston est ajouté afin de séparer sa composante polarisée parallèlement (532(p)nm) de sa composante polarisée perpendiculairement (532(c)nm). Des photomultiplicateurs assurent la détection des signaux dans l'UV et le visible alors qu'une photodiode à effet avalanche est

choisie pour les signaux dans le proche infrarouge. Le système d'acquisition des données fonctionne simultanément en mode analogique et en mode de comptage de photons.

Dans le cadre du projet EARLINET (European Aerosol Research Lidar Network) une inter-comparaison des algorithmes et du système en lui-même a été faite. La partie dédiée aux algorithmes a aussi bien porté sur l'inversion des signaux élastiques que sur l'inversion des signaux ramans. Le micro-lidar mobile de l'Observatoire Cantonal de Neuchâtel a été utilisé lors de l'intercomparaison au niveau du système lidar.

Le système actuel permet la mesure troposphérique de profils de rétrodiffusion et d'extinction des aérosols de manière indépendantes, du rapport de dépolarisation et du rapport de mélange de la vapeur d'eau. Les incertitudes associées peuvent être plus petites que 20% et rendre possible l'extraction de la microphysique des aérosols comme la distribution volumique et des valeurs moyennes et intégrées de la distribution des aérosols en fonction de leur taille (rayon effectif, surface totale, volume total et nombre total d'aérosols). Cette extraction est faite par un logiciel de l'institut de mathématique de l'université de Postdam. Il est basé sur une méthode hybride de régularisation. Les premiers résultats obtenus avec trois valeurs de rétrodiffusion (355, 532 et 1064nm) et une valeur d'extinction (355nm) sont prometteurs. Des mesures de concentrations d'ozone et des profils de températures sont prévus dans un proche avenir.

Summary

Climate changes and global warming are generally associated with the enhanced greenhouse effect, but aerosols can induce a cooling effect and thus regionally mask this warming effect. Unfortunately, the strong variability both in space and in time of the aerosols and thus the difficulty to characterize their global basic properties induce large uncertainties in the predictions of the numerical models. Those uncertainties are as high as the absolute level of the enhanced greenhouse forcing. To solve this problem it is necessary to improve the set of well-calibrated instruments (both *in situ* and remote sensing) with the ability to measure the changes in stratospheric and tropospheric aerosols amounts and their radiative properties, changes in atmospheric water vapor and temperature distributions, and changes in clouds cover and cloud radiative properties. The quantity used to assess the importance of one compound (greenhouse gases, aerosols) to the variation of the radiative budget of the Earth is the radiative forcing. One of those forcings is the direct aerosol radiative forcing and it depends on the optical depths and the upscatter fraction of the aerosols. Those two parameters depend on the chemical composition and size distribution of the aerosols. Thus the key parameters of this radiative forcing are the chemical composition through its refractive index and the size distribution of the aerosols.

This thesis deals with the design and the implementation of one multi-wavelength lidar system at the Jungfraujoch Alpine Research Station (Alt. 3580m asl). This lidar system is a combination of one standard backscatter lidar and one Raman lidar. Its design have been supported by a ray tracing analysis of the receiver part. The laser transmitter is based on a tripled Nd:YAG laser and the backscattered light is collected by one Newtonian telescope for the tropospheric measurements and by one Cassegrain telescope for the future stratospheric measurements. The received wavelengths for each telescope include three elastically scattered wavelengths (355, 532 and 1064nm), two spontaneous Raman signals from nitrogen (387 and 607nm) and one spontaneous Raman signal from the water vapor (408nm). The optical signals received by each of the telescopes are separated spectrally by two filter polychromators. They are build up around a set of beamsplitters and custom design thin band pass filters with high out-of-band rejection. On the visible channel, the adds of a Wollaston prism separates the parallel polarized backscattered signal (532(p)nm) of the perpendicular polarized one (532(c)nm). Photomultiplier tubes perform the detection of the signals for the UV and visible wavelengths and by Si-avalanche photodiodes for the near-infrared signal. The acquisition of the signals is performed by seven transient recorders in analog and in photon counting modes.

Within the frame of the EARLINET (European Aerosol Research Lidar Network), hardware

and software intercomparisons have been done. The software intercomparison has been divided into the validation of the elastic algorithm and the Raman algorithm. Those intercomparisons of the inversions of the lidar signals have been performed using synthetic data for a number of situations of different complexity. The hardware intercomparison have been achieved with the mobile micro-lidar of the Observatoire Cantonal de Neuchâtel.

The present lidar system provides independent aerosol extinction and backscatter profiles, depolarization ratio and water vapor mixing ratio up to the tropopause. Their uncertainties could be smaller than 20% and thus make possible the retrieval of the microphysical aerosol parameters like the volume concentration distribution and the mean and integral parameters of the particle size distribution, (effective radius, total surface-area concentration, total volume concentration and number concentration of particles). This retrieval is performed by one algorithm of the Institute of Mathematic of the University of Postdam based on the hybrid regularization method. The first results of the retrieval of the volume concentration distribution with three backscatter (355, 532 and 1064nm) and one extinction (355nm) profiles has demonstrated promising results. Future upgrades of the system will add ozone concentration and temperature profile up to the stratopause.

During the last century the number of natural disasters has increased: floods, tropical cyclones, drought, storms, etc (Houghton 1997). There is not any more a doubt that the climate is changing. A vast majority of the world's scientific community estimates that a significant climatic change of anthropogenic source is now evident (Santer 1995; Houghton 1997; Shine 1999; IPCC 2001; Ramanathan 2001). However for some, this evidence is contestable, even equivocal (Lenoir 2001; Lomborg 2001). As it is impossible to make full-scale experiments in the atmosphere and as an experiment on a regional scale would hardly make sense because of the complexity of the involved phenomena, numerical models are the only provider of detailed estimates of climate responses and of regional features (de Félice 2001). Such model cannot yet simulate all aspects of the climate and there are particular uncertainties associated with clouds and their interactions with radiation and aerosols (Jennings 1993; Charlson 1995; Houghton 1997; Seinfeld and Pandis 1998; Kondratyev 1999; Finlayson-Pitts 2000; de Félice 2001; IPCC 2001).

A key aspect of this problem is the difficulty to characterize the global basic aerosol properties of the principal types of aerosol like the number concentration, size distribution and optical parameters. This difficulty arises from the fact that the most important typical feature of the aerosols is their strong variability both in space and in time (Charlson 1995; Kondratyev 1999; Ramanathan 2001). To solve this problem it is necessary to improve the set of well-calibrated instruments (both *in situ* and remote sensing) with the ability to measure the changes in stratospheric and tropospheric aerosols amounts and their radiative properties, changes in atmospheric water vapor and temperature distributions, and changes in clouds cover and cloud radiative properties (Charlson 1995; Ramanathan 2001).

This chapter describes the principle of the radiative budget of the Earth and highlights the main agents of the radiative forcing, in particular the direct aerosol radiative forcing. Afterwards the advantages and drawbacks of the *in situ* and remote sensing aerosol measurements are presented briefly.

1.1. The Earth-atmosphere system

Some simple consideration of the fate of the incoming solar radiation and the emitted infrared and reflected visible radiation shows which factors are important for the average temperature of the Earth. In the case of long-term global average, the radiation balance has to be zero, i.e. the incoming and outgoing radiation have to be equal. With no sources for energy within the planet the same amount than the solar radiation \bar{S} has to be emitted or reflected by the body. Schematics of the fluxes considered in the following cases are shown in Figure 1-1.

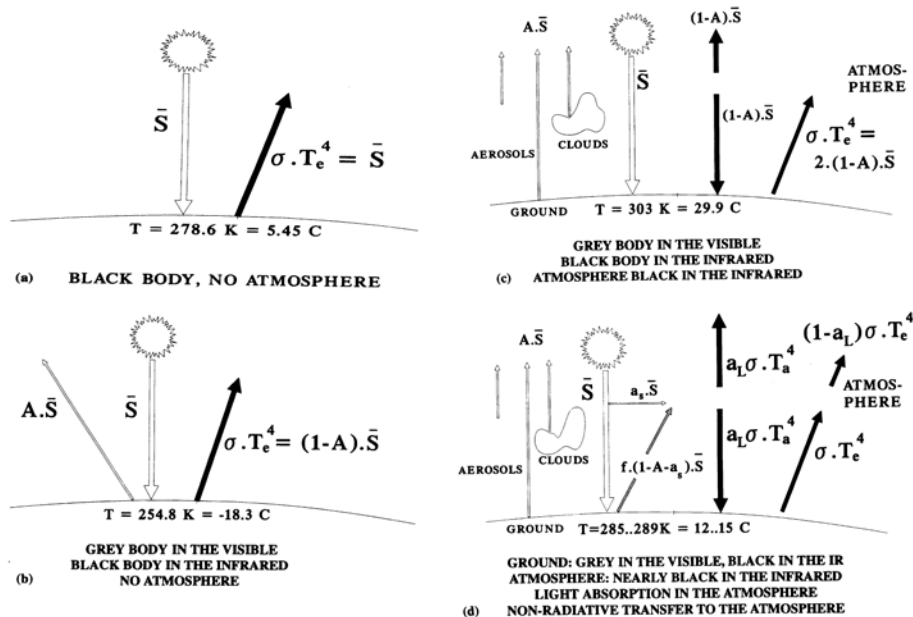


FIGURE 1-1. Radiative fluxes of a body receiving solar radiation and emitting infrared radiation: (a) black body; (b) grey body in the visible and black body in the infrared; (c) same as (b) but with a greenhouse atmosphere; (d) model of realistic atmosphere with light absorption in the visible, a non-radiative energy transfer from the ground to the atmosphere, and some transmission in the infrared. From (Harrison 1998).

The simplest case is the Earth as a black body without atmosphere (Figure 1-1(a)). In this case the solar flux is totally absorbed by the planet and emitted as infrared radiation to space. Equating the solar radiation to the temperature of a black body given by the Stefan Boltzmann law (the energy emitted is proportional to the fourth power of the absolute temperature of the body), one obtains a mean temperature of $T_e=278.6\text{K}$ (5.5°C). But the Earth is not a black body in the visible and has an global mean albedo $A=0.3$, i.e. a fraction of 30% of the incoming radiation is reflected and thus only $(1-A)$ or 70% of the solar radiation can be emitted as infrared. This is only possible if the surface temperature decreases with regard to the previous case as it is shown in Figure 1-1(b). This correspond to a surface temperature of 254.8K (-18.3°C) which is cold. One can immediately see that a change in the albedo drastically alters the surface temperature. An increase of this parameter will reduce this temperature and conversely. Now an atmosphere around the body is taken into account and it contains some compounds which

absorb the infrared radiation emitted by the planet. By this absorption the atmosphere heats itself and emits radiation in all directions according to its temperature (see Figure 1-1(c)). As a first approximation the atmosphere is a black body in the infrared. Radiation budget out of the atmosphere makes it clear that the average absorbed solar flux density has to be emitted by the atmosphere. But the atmosphere emits in both directions (upwards and downwards) and therefore the radiation received at the Earth's surface is twice the absorbed solar radiation. This amount has to be emitted by temperature radiation, which is only possible if the surface temperature is higher (303K or 29.9°C). The dramatic increase in the surface temperature due to an absorbing atmosphere, whose temperature is -18.3°C, is evident.

The atmosphere of the Earth is not completely absorbing and some other transfers not yet discussed take place as well. Now some sunlight passing through the atmosphere is absorbed and transferred as heat to the atmosphere, obtained from the absorbance of short-wave (solar) radiation a_s (see Figure 1-1(d)). A certain fraction f of the absorbed energy is transported from the ground to the atmosphere by non-radiative processes (latent and sensible heats). The other energy is radiated in the infrared from the surface of temperature T_e to the atmosphere which has an absorbance a_l for the infrared (long-wave) radiation and thus absorbs this fraction of the radiation from the Earth and transmits $(1-a_l)$ upwards. Finally the atmosphere, having a temperature T_a , emits its grey body infrared radiation both upwards and downwards.

The balance of the fluxes for the surface is given by

$$\bar{S}(1 - A - a_s) + a_l \sigma T_a^4 = \sigma T_e^4 + f \cdot \bar{S}(1 - A - a_s) \quad (\text{EQ 1.1})$$

where σ is the Stefan-Boltzmann constant. For the atmosphere the balance of the fluxes is

$$\sigma T_e^4 + f \cdot \bar{S}(1 - A - a_s) + a_s \bar{S} = (1 - a_l) \sigma T_e^4 + 2a_l \sigma T_a^4 \quad (\text{EQ 1.2})$$

Resolving (EQ 1.1) and (EQ 1.2) for the atmospheric temperature T_a and rearranging gives

$$\bar{S} \frac{(2 - f)(1 - A - a_s) + a_s}{2 - a_l} = \sigma T_e^4 \quad (\text{EQ 1.3})$$

With a fraction of $f=30\%$ non-radiative transfer, $a_s=1\%$ light absorption of the atmosphere and $a_l=92-97\%$ infrared absorbance of the atmosphere a global mean temperature between 285.0 and 288.4K (11.9 - 15.3°C) is obtained. The corresponding temperatures of the atmosphere are -21.5 and -19.6°C (Harrison 1998).

(EQ 1.3) shows the effects of the different variables on the global mean surface temperature:

- Increasing short-wave absorption (visible) a_s reduces the surface temperature but increases the atmospheric temperature.
- Increasing long-wave absorption (infrared) a_l increases both the surface and atmospheric temperatures.
- Increasing non-radiative heat transfer f reduces the surface temperature.

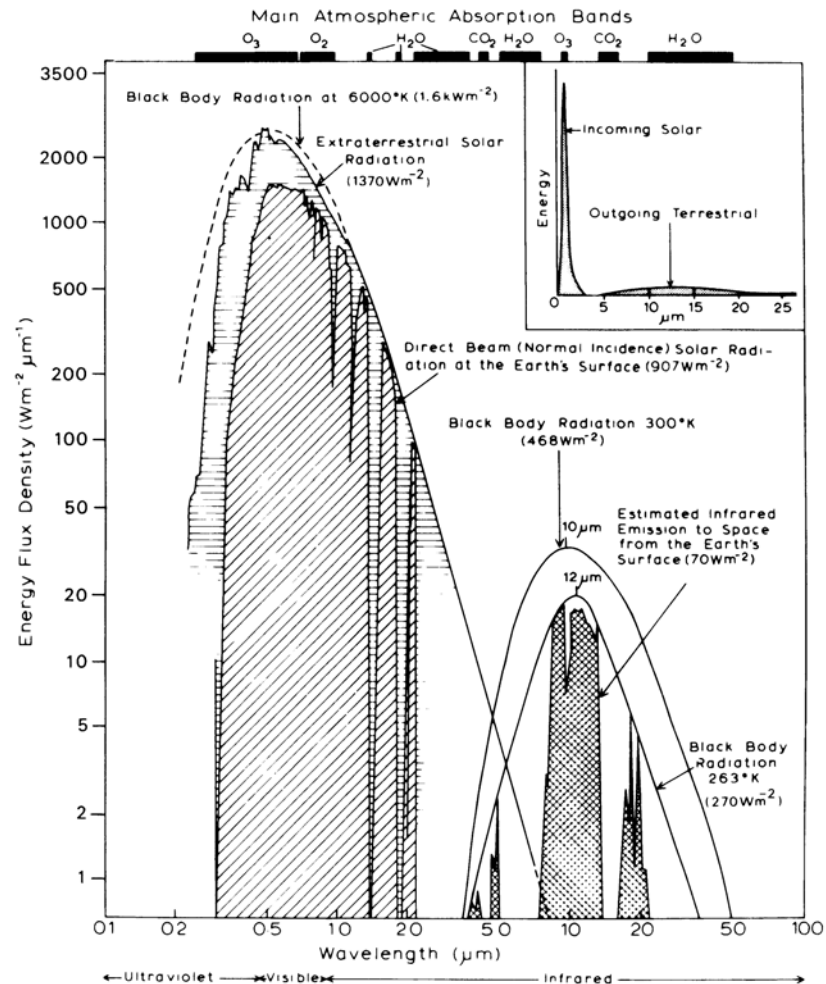


FIGURE 1-2. Spectral distribution of solar and terrestrial radiation, plotted logarithmically, together with the main atmospheric absorption bands. The cross-hatched areas in the infrared spectrum indicate the «atmospheric windows» where radiation escape to space. The black body radiation at 6000k is that proportion of flux which would be incident on the top of the atmosphere. The inset shows the same curves for incoming and outgoing radiation with the wavelength plotted arithmetically on an arbitrary vertical scale. From (Barry 1998).

More infrared absorption by the atmosphere causes an increase in the temperature since the radiation is reradiated to the ground by the atmosphere, this is the so-called greenhouse effect. The main greenhouse gases (GHG) are: water vapor (H_2O), carbon dioxide (CO_2), ozone (O_3),

methane (CH₄), nitrous oxide (N₂O), and halocarbons (CFC). Those gases, except CFC, have both natural and anthropogenic sources and an increase of the anthropogenic sources induces an enhanced greenhouse effect. More reflectivity in the visible causes a decrease in temperature, this is the so-called whitehouse effect (Schwartz 1996). This effect is mainly due to scattering by atmospheric particles (aerosols) and air molecules, clouds, and reflection by the Earth's surface itself.

The spectral distribution of the incoming (short-wave) and outgoing (long-wave) radiations is shown in Figure 1-2. The dot-line gives the black body radiation at 6000K which correspond to the solar surfacic temperature, the horizontal-hatched area is the extraterrestrial solar radiation whereas the slant-hatched areas are the direct solar radiation at the surface. The cross-hatched areas indicate the «atmospheric windows» where radiations escape to space. The black body curves for 300 and 263K are also presented and represent the long-wave spectral distributions. Gases do not behave as black bodies and the top of the Figure 1-2 shows the absorption bands in the atmosphere, which cause its emission to be much less than that from a black body (Barry 1998).

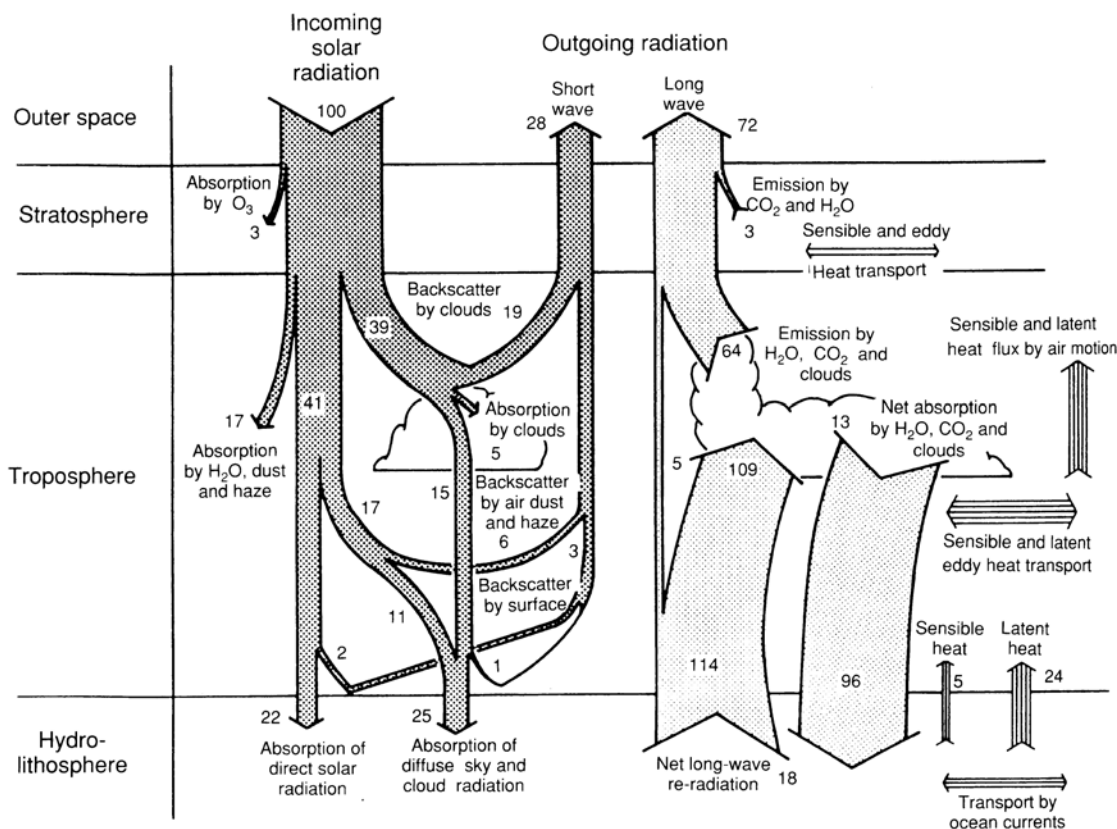


FIGURE 1-3. The annual mean global energy balance for the Earth-atmosphere system. Sensible heat is that transferred to the atmosphere from the heated surface by turbulent eddies; latent heat is that supplied to the atmosphere upon condensation of water vapor. The numbers are percentages of the energy of the incoming solar radiation. From (Graedel 1993).

The solar radiation is very intense and is mainly between 0.2 and 4.0 μm , with a maximum per unit wavelength at 0.5 μm , whereas the much weaker long-wave radiation has a peak intensity at 10 μm and a range of about 4 to 100 μm .

Figure 1-3 illustrates the efficiency of reflection, absorption and radiation with regard to the incoming solar radiation. An average of 28% of the incoming radiation is returned into space by backscattering from clouds (19%), air molecules and particles (6%), and by the surface (3%). Almost 25% is absorbed within the atmosphere, mostly by stratospheric ozone (3%), clouds (5%) and tropospheric water vapor (17%). The remaining 47% is absorbed by the Earth (Graedel 1993).

A little bit more than half of the solar radiation absorbed at the surface is transformed into latent heat (24%), and sensible heat (5%) whereas only 5% are lost by radiation, because the remainder is captured in the atmosphere by the greenhouse gases. But have those components the same impact on the energy balance and thus on the climate change? The quantity used to assess the importance of one compound to the climate system is the *radiative forcing*.

1.2. Radiative forcing

The definition given by (IPCC 2001) of the radiative forcing of the climate system is: «The radiative forcing of the surface-troposphere system due to perturbation in or the introduction of an agent (say, a change in greenhouse gas concentrations) is the change in net (down minus up) irradiance (solar plus long-wave; in Wm^{-2}) at the tropopause after allowing for stratospheric temperatures to readjust to radiative equilibrium, but with surface and tropospheric temperatures and states held fixed at the unperturbed values.». Thus this definition is applied to perturbation in the radiation balance of the surface-troposphere system without any feedbacks. To reestablish equilibrium, a temperature change ΔT_e results, which is related to the radiative forcing ΔF_{net} by the climate sensitivity factor λ_0 [$\text{K} (\text{Wm}^{-2})^{-1}$]. The radiative forcing is not the climate response. The former is a change imposed on the planetary energy balance whereas the latter is the meteorological results of those forcings, such as global temperature change, rainfall changes, or sea level changes.

Figure 1-4 gives the global mean radiative forcing of the climate system for the year 2000, relative to 1750 (IPCC 2001). The height of the rectangular bar denotes a central or best estimate value, while its absence denotes no best estimate is possible. The vertical line about the rectangular bar with «X» delimiters indicates an estimate of the uncertainty range, whereas a vertical line without a vertical bar and with «O» delimiters denotes a forcing for which non central estimate can be given owing to large uncertainties. Also shown in this figure is the level of the scientific understanding, which represents subjective judgement about the reliability of the forcing estimate, involving factors such as the assumptions necessary to evaluate the forcing, the degree of knowledge of the physical and chemical mechanisms determining the forcing, and the uncertainties surrounding the quantitative estimate of the forcing. A positive radiative forcing, such as that produced by increasing concentration of greenhouse gases, tends to warm the surface whereas a negative radiative forcing, which can arise from an increase in some types of aerosols tends to cool the surface (whitehouse effect).

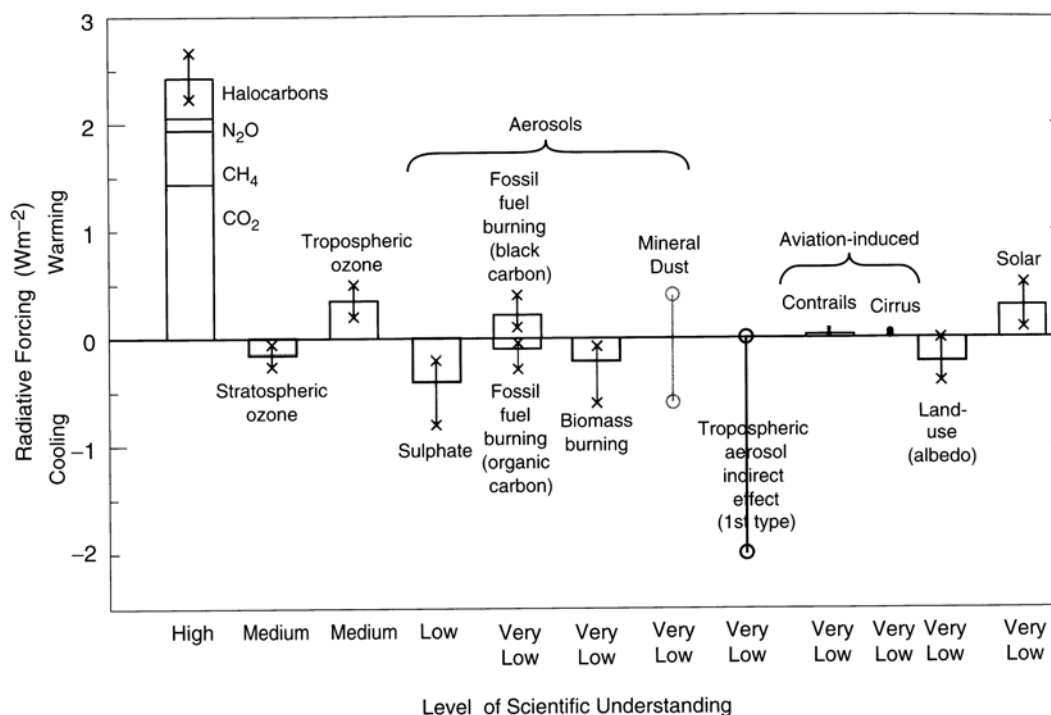


FIGURE 1-4. Global, annual mean radiative forcings [Wm⁻²] due to a number of agents for the period from pre-industrial (1750) to present. For detailed explanations see the text. From (IPCC 2001).

As the water vapor is the most important greenhouse gas, it would be logical to start with its radiative forcing. However, its distribution is strongly variable in space and in time. This distribution is mainly driven by the air motions and the changes of physical states of the water, but is only slightly affected by human activities (e.g., deforestation on a large scale, which can matter regionally) (Brasseur 1999). This assumption is disputed and the sign of the greenhouse effect could be inverted if the atmospheric motions of the water vapor are taken into account (de Félice 2001).

The radiative forcing due to increases of well-mixed greenhouse gases is estimated to be $+2.43\text{Wm}^{-2}$: $+1.46\text{Wm}^{-2}$ from the CO_2 , $+0.48\text{Wm}^{-2}$ from the CH_4 , $+0.34\text{Wm}^{-2}$ from the halocarbons, $+0.15\text{Wm}^{-2}$ from the N_2O . The depletion of the stratospheric ozone is estimated to have cause a negative radiative forcing of -0.15Wm^{-2} , whereas the radiative forcing of the tropospheric is $+0.35\text{Wm}^{-2}$. Ozone forcing varies considerably by region and responds much more quickly to changes in emission than the long-lived greenhouse gases (CO_2 , CH_4 , N_2O and CFCs). Those radiative forcing have a high or medium level of scientific understanding. Concerning the well-mixed greenhouse gases, the infrared absorption and radiative transfer are well quantified, while concerning the short-lived greenhouse gases, their infrared absorption is reasonably well quantified, radiative aspect is well posed, but they are highly variable in space and time (Seinfeld and Pandis 1998).

Aerosol particles affect the radiative balance of the Earth both directly, by scattering and absorbing solar and terrestrial radiation, and indirectly through their action as cloud condensation nuclei (CCN) with subsequent effects on the microphysical and optical properties of clouds. Concerning the direct radiative forcing, the aerosols are divided into four categories: sulfate, fossil fuel burning (black carbon and organic carbon), biomass burning and mineral dust. Their values are -0.4Wm^{-2} for sulfate, -0.2Wm^{-2} for biomass burning aerosols, -0.1Wm^{-2} for fossil fuel organic carbon and $+0.2\text{Wm}^{-2}$ for fossil fuel black carbon. The sign of the effects due to mineral dust is itself an uncertainty. Aerosol radiative forcings also vary considerably by region and respond quickly to changes in emissions. The level of scientific understanding is low for the sulfate and very low for the other aerosols. The determination of forcing is relatively a well-posed problem, but is dependent on empirical values for several key aerosol properties and is also dependent on models for geographical and temporal variations of forcing. A more detailed description of the direct aerosol radiative forcing is given in the next section. The indirect aerosol radiative forcing is divided into the first indirect effect (increase in droplet number associated with increases in aerosols) and the second indirect effect (decrease in precipitation efficiency with increases in aerosols). The former has strong observational support (Charlson 1995) whereas the latter has only limited support (IPCC 2001). Only the first type of indirect radiative forcing is considered here and is poorly understood. The same is true for the forcing due to aviation via its effect on contrails and cirrus. The indirect radiative forcing depends on aerosol number distribution, but the inadequacy of descriptions of aerosols and clouds seriously restricts abilities to predict this forcing. The radiative forcing associated with the stratospheric aerosols from volcanic actions is highly variable and is not presented here. Generally, volcanic eruptions lead to a negative radiative forcing, which lasts a few year after the eruptions.

Changes in the physical character of the land surface can affect land-atmosphere exchanges of radiation, momentum, heat and water. Only the radiative forcing due to change in surface albedo is presented here and leads to a negative radiative forcing. The radiative forcing due to a change in solar irradiance, which is a natural forcing, is estimated to be about $+0.3\text{Wm}^{-2}$.

Unfortunately, the resulting radiative forcing cannot be a simple sum of the positive and negative bars due to the strong regional signatures of certain radiative forcing agents, such as aerosols. Nevertheless the simulations indicates that the estimated net effect of those perturbations is to have warmed the global climate since 1750 (IPCC 2001). But the uncertainties, in particular on the aerosols, are unacceptably large and present serious limitations to modeling of climate (Charlson 1995). This uncertainty is as high as the absolute level of the additional greenhouse forcing. The radiative forcing attributable to aerosol changes is still available only as semiquantitative estimate. Part of the reason for this is the greater radiative complexity of aerosols, their large variabilities in space and in time, and their relatively short atmospheric lifetime. However, in addition, to these modeling related problems, the persistent uncertainty in aerosol forcing is due to the continued absence of monitoring system that is capable of measuring and monitoring changes in aerosol amounts and their radiative properties with sufficient accuracy (Charlson 1995).

The next sections are dedicated to the direct effect of aerosols on climate and to observations of aerosol properties.

1.3. Aerosol direct effects on climate

An aerosol is defined as: «a suspension of fine solid or liquid particles in a gas» (Seinfeld and Pandis 1998). They can be both emit directly as particles (primary aerosol) or due to gas-to-particle conversion processes (secondary aerosol). Their natural sources are soil and rock debris (terrestrial dust), volcanic action, sea spray, biomass burning, and reaction between natural gaseous emissions. Emissions of particulate matter attributable to the human activities arise primarily from four sources categories: fuel combustion, industrial processes, non-fugitive sources (roadway dust, wind erosion of cropland, construction,...) and transportation sources (automobiles,...) (Seinfeld and Pandis 1998). Aerosols range in size from a few nanometers to tens of micrometers as it is illustrated in Figure 1-5. This figure shows the surface area distribution of an idealized atmospheric aerosol. Fines aerosols have a diameter smaller than 2.5µm whereas coarse particles have a diameter greater than 2.5µm. Those coarse particles are formed by mechanical processes and consists of man-made and natural dust particles. The fine particles are divided into two modes: the transient nuclei or Aitken nuclei range (from about 0.005 to 0.1µm) and the accumulation range (from 0.1 to 2.5µm). The former are formed from condensation of hot vapors during combustion processes and from nucleation of atmospheric species to form fresh particles. They are lost principally by coagulation with larger particles. The latter are formed from the coagulation of particles in the nuclei mode and from condensation of vapors onto existing aerosols, causing them to growth into this size range. The removal mechanisms are least efficiency causing particles to accumulate there.

Greenhouse gases such as CO₂, CH₄, N₂O and CFCs are virtually uniform globally in the troposphere due to their high atmospheric lifetimes of decades to centuries, whereas aerosol concentrations are highly variable in space and time as water vapor and ozone concentrations. With lifetimes of about a week, sulfate aerosols are most abundant close to their sources in the industrialized areas of the Northern Hemisphere. Biomass aerosols are emitted predominantly during dry season in tropical areas. Mineral dust appears downwind of large arid regions. Moreover, greenhouse gas forcing operates day and night; aerosol forcing operates only during day.

The aerosols influence directly the radiative budget by the scattering and the absorption of the solar radiation. This effect depends on the amount of light scattered back to space. This amount is the fraction of light that is scattered into the upwards hemisphere relative to the horizon. This so-called upscatter fraction **b** depends on the size distribution and optical properties of the particles, and on the solar angle. Note that this upscatter fraction is not the backscatter fraction of light with regard to the direction of propagation of the light.

The direct radiative forcing of an aerosol layer, with the assumptions of the Sun at its zenith and cloud free atmosphere, is given by (Finlayson-Pitts 2000)

$$\Delta F_R = -\left(\frac{1}{4}F_T\right)(1 - A_c)T^2 \left[(1 - R_s)2bt_{scat} - 4R_s t_{abs} \right]$$

(EQ 1.4)

where ΔF_R [Wm⁻²] is the net global average short-wave radiative forcing due to aerosols, F_T

$[Wm^{-2}]$ is the incoming solar radiation, $A_c [-]$ is the fraction covered by clouds, $T [-]$ is the fraction of light transmitted above the aerosol layer, $R_s [-]$ is the surface albedo, $\beta [-]$ is the upscatter fraction, $\tau_{scat} [-]$ is the effective aerosol optical scattering depth and $\tau_{abs} [-]$ is the optical depth due to aerosol absorption.

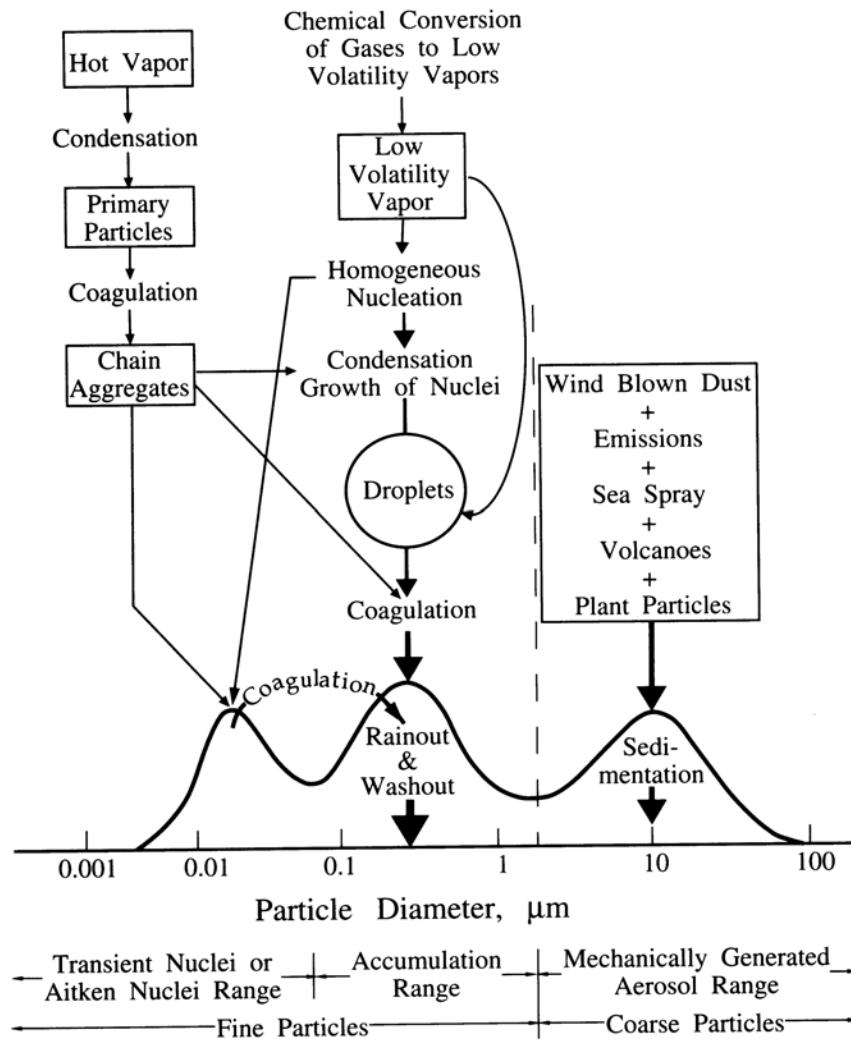


FIGURE 1-5. Idealized schematic of the distribution of particle surface area of an atmospheric aerosol. Principal modes, sources, and particles formation and removal mechanisms are indicated. From (Seinfeld and Pandis 1998).

The radiative forcing depends on the optical depths and the upscatter fraction of the aerosols. Those parameters depend on the chemical composition and size distribution of the aerosols. Thus the key parameters of the radiative forcing are the chemical composition through its refractive index and the size distribution of the aerosols. And the largest uncertainties of this radiative forcing is associated with the radiative properties of the aerosols, in particular the influence of the relative humidity.

As it was mentioned in the previous section, those semiquantitative estimates can seldom be compared to atmospheric data and thus limits the validation of the models. So the 3D global database on aerosol properties and effects needs to be enhanced drastically (Heintzenberg 2001).

1.4. Aerosol measurements

The type of aerosol measurements can be divided into *in situ* and remote sensing. The latter can also be divided in active and passive remote sensing. The former uses its own source of radiation (radar, lidar, etc) while the latter is dependent on an external source (spectral radiometers, sunphotometers, etc).

The *in situ* measurements have the advantage that optical, chemical and microphysical parameters can be determinate, but do not have any vertical resolution, except the airborne platforms. The data of *in situ* measurements of size distribution and chemical composition of aerosols, although reliable, cannot, however, be considered representative for large spatial and temporal scales. Therefore new complex results of ground, aircraft, balloon, and satellite observations should form the basis for climatological aerosol models (Kondratyev 1999). Figure 1-6 illustrates the diverse types of observation made on the stratospheric layer after the El Chichon eruption. Obviously those observations can be extended to the overall atmosphere. *In situ* measurements are performed by airborne platforms (U-2, WB57) and balloon (Stratostat). Spaceborne radiometric measurements (NOAA-7) can be inverted to yield optical depth and size distribution. Satellites are the only one to provide global coverage, but they have the drawback of being presently passive sensors. They can be only applied over Oceans under clear-sky conditions. Crude vertical resolution can be obtained by the occultation method (SME), but is restricted to the upper atmosphere. Another drawback is the possible drift of the platforms that cannot be directly corrected and thus satellite data are frequently validated by ground-level measurements. The present platforms take advantages of higher spectral resolution like AVHRR (Advanced Very High Resolution Radiometer), but the main drawbacks remain the same.

In order to gain a good vertical resolution, lidar measurements are now mature to provide aerosol measurements. Lidar systems are similar to a radar, but they use radiations in the UV, visible and near-infrared radiations. Lidar is an acronym which stands for Light Detection And Ranging. Lidar systems are active sensors and provide range-resolved data, but only the combination of several methods enables well-defined physical parameters. The standard backscatter lidar is appropriate in clean areas, the upper troposphere and the stratosphere. The limitation of this method is due to the ill-posed lidar equation: one signal is determined by two unknowns that are the backscatter and the extinction coefficients of the atmosphere. Three methods have been demonstrated to overcome this problem: high-spectral-resolution lidar (HSRL) (Grund 1991), multi-zenith-angle measurements (Gutkowitz-Krusin 1993) and Raman lidar (Ansmann, Wandinger et al. 1992).

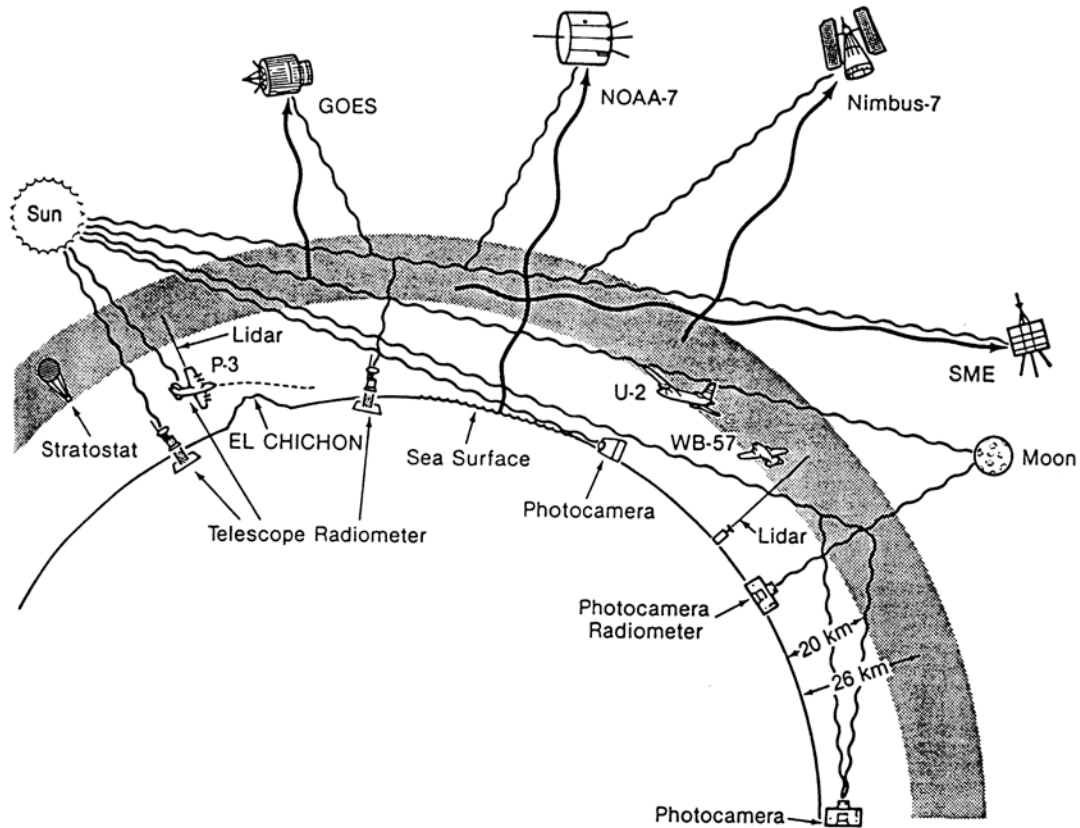


FIGURE 1-6. A schematic diagram illustrating the diverse type of observations made on the stratospheric aerosol layer after the 1982 El Chichon eruption. This illustrates the needs to combine different methods. From (Jennings 1993).

The lidar system of this present work is a multispectral backscatter lidar combined with a Raman lidar. Aerosol optical properties in the UV, visible and near-infrared regions can be retrieved from such system, as well as water vapor mixing ratio. Table 1-1 summarizes the present and future performances and planned upgrading of the Jungfraujoch lidar system and gives the characteristics of two similar systems: the Alomar Rayleigh/Mie/Raman lidar (von Zahn 2000) and the scanning 6-Wavelength 11-Channel Aerosol Lidar (Althausen 2000).

This system is implemented at the Jungfraujoch Alpine Station (3580m asl). This Station is a unique site for atmospheric observations, most of the time located in the free troposphere. It is equipped with instruments that have since decades performed essential Global Observation, and in particular column measurements by FTIR of some of the most important trace gases in the earth atmosphere (Delbouille 1995), a 16-channels precision filter radiometer (Heimo 1998), a detailed local characterization of the aerosol formation (particle size and chemical composition) (Baltensperger 1997) and a passive microwave remote sensing in the stratosphere (Maier 1998). The Jungfraujoch Station is also part of the Network for Detection of Stratospheric Change (NDSC). Thus this station provides all the complementary data that the

lidar needs to perform reliable measurements. Indeed ground base remote sensing combined with in situ chemical characterizations are required to reduce the uncertainties of aerosol radiative forcing.

TABLE 1-1 Comparisons between different lidar systems

| Lidar System | Wavelength [nm] | Measurement |
|--------------|---|-------------------------------------|
| Alomar | 355, 387, 532, 607, 1064 | Aerosol properties |
| | 532 | Doppler wind (with 2 telescopes) |
| | 355, 532 | Temperature (without aerosols) |
| | 387, 607 and 530.4, 529.1 | Temperature (with aerosols) |
| ITR | 355, 387, 400, 532, 607, 710, 790, 1064 | Aerosol properties |
| | 607, 660 | Water vapor |
| | 710 | Depolarization ratio |
| This work | 355, 387, 532, 607, 1064 | Aerosol properties |
| | 387, 408 | Water vapor |
| | 532 | Depolarization ratio |
| | 355, 532 | Temperature (without aerosols)* |
| | 387, 607 and 530.4, 529.1 | Temperature (with aerosols)* |
| | 308, 355 | Ozone* |

* Future upgrade

In order to establish a quantitative database of both horizontal and vertical distribution of aerosols on a continental scale, a network of lidar stations is implemented: EARLINET (European Aerosol Research Lidar Network). This network will contribute to the characterization of the aerosol concentrations, radiative properties and prediction of future trends. It will also provide input for the aerosol retrievals by all planned spaceborne lidar mission (Bösenberg 1998; Bösenberg 2001). The lidar of the Jungfraujoch Station is one of the participants.

1.5. Conclusion

This chapter highlights the important agents that drive the radiative budget of the Earth. The greenhouse effect allows the life on the planet in keeping the surface temperature around +15°C. This effect is natural and do not alter the climate, whereas the enhanced greenhouse effect whose origin is anthropogenic, is certainly the prime environmental problem of this new millennium. The climatic response to this effect is a global warming of the surface, but up to now the aerosol contribution was generally not taken into account. This gap, both in the modeling and monitoring parts, induces large uncertainties. Therefore new complex results of ground, aircraft, balloon, and satellite observations should form the basis for climatological aerosol models. As a part of these efforts a new multispectral backscatter lidar combined with a Raman lidar is implemented at the Jungfraujoch Alpine Station.

1.6. References

- Althausen, D., Müller, D., Ansmann, A., Wandinger, U., Hube, H., Clauer, E., and Zörner, S. (2000). "Scanning 6-Wavelength 11-Channel Aerosol Lidar." Am. Meteorol. Soc.: 1469-1482.
- Ansmann, A., U. Wandinger, et al. (1992). "Independent Measurement of Extinction and Backscatter Profiles in Cirrus Clouds by Using a Combined Raman Elastic-Backscatter Lidar." Applied Optics **31**(33): 7113-7131.
- Baltensperger, U., Gäggeler, H. W., Jost, D. T., Lugauer, M., Schwikowski, M., Weingartner, E., and Seibert, P. (1997). "Aerosol climatology at high-alpine site Jungfraujoch, Switzerland." Journal of Geophysical Research-Atmospheres **D102**: 19707-19715.
- Barry, R. G., Chorley, R. J. (1998). Atmosphere, Weather & Climate. New-York, Routledge.
- Bösenberg, J., and al. (1998). "A lidar network for the establishment of an aerosol climatology." in the proceedings of the 19th ILRC, Annapolis MA, USA NASA/CP-1998-207671/PT1: 23-24.
- Bösenberg, J., and al. (2001). EARLINET: A European Aerosol Research Lidar Network. Palaiseau, Editions de l'Ecole polytechnique.
- Brasseur, G. P., Orlando, J. J., and Tyndall G. S. (1999). Atmospheric Chemistry and Global Change, Oxford University Press.
- Charlson, R. J., and Heintzenberg, J. (Eds.) (1995). Aerosol forcing of climate. New-York, John Wiley & Sons, Ltd.
- de Félice, P. (2001). L'effet de serre: un changement climatique annoncé. Paris, L'Harmattan.
- Delbouille, L., and Roland, G. (1995). "High resolution solar and atmospheric spectroscopy from the Jungfraujoch high altitude station." Optical Engineering **34**: 2736-2739.
- Finlayson-Pitts, B. J., and Pitts, J.N. (2000). Upper and lower atmosphere: theory, experiments, and applications. San Diego, Academic Press.
- Graedel, T. E., and Crutzen, P.J. (1993). Atmospheric Change: an Earth system perspective. New-York, W. H. Freeman and Compagny.
- Grund, C. J., and Eloranta, E.W. (1991). "University of Wisconsin high spectral resolution lidar." Optical Engineering **30**: 6-12.
- Gutkowitz-Krusin, D. (1993). "Multiangle lidar performance in the presence of horizontal inhomogeneities in atmospheric extinction and scattering." Applied Optics **32**: 3266-3272.
- Harrison, R. M., and van Grieken, R. E. (1998). Atmospheric particles. New-York, John Wiley & Sons. Ltd.
- Heimo, A., and al. (1998). "The Swiss atmospheric radiation monitoring network CHARM." paper presented at the WMO technical conference on meteorological and environmental instruments and methods of observation (TECO-98), Casablanca, Morocco.

- Heintzenberg, J. (2001). Aerosol influence on the radiation budget: Where do we stand? Palaiseau, Editions de l'Ecole polytechnique.
- Houghton, J. (1997). Global Warming: the complete briefing, Cambridge University Press.
- IPCC (2001). Climate Change 2001: The Scientific Basis, Cambridge University Press.
- Jennings, S. G. (1993). Aerosol Effects on Climate, The University of Arizona Press.
- Kondratyev, K. Y. (1999). Climatic effects of aerosols and clouds. Berlin, Springer-Verlag.
- Lenoir, Y. (2001). Climat de panique, Edition Favre.
- Lomborg, B. (2001). The sceptical environmentalist, Cambridge University.
- Maier, D., and al. (1998). "EMCOR radiometer: calibration and first tests." Proceedings of SPIE SPIE's First International Asia-Pacific Symposium on remote sensing of the atmosphere, environment and space: 362-373.
- Ramanathan, V., Crutzen, P.J., Kiehl, J.T., Rosenfeld, D. (2001). "Aerosols, Climate, and the Hydrological Cycle." Science **294**: 2119-2124.
- Santer, B., and al. (1995). "Towards the detection and attribution of an anthropogenic effect on climate." Climate Dynamics **12**: 77-100.
- Schwartz, S. E. (1996). "The whitehouse effect: Shortwave radiative forcing of climate by anthropogenic aerosols." Journal of Aerosol Science **27**: 359-382.
- Seinfeld, J. H. and S. N. Pandis (1998). Atmospheric Chemistry and Physics, Wiley Interscience.
- Shine, K. P., de Forster, P.M. (1999). "The effect of human activity on radiative forcing of climate change: a review of recent developments." Global and Planetary Change **20**: 205-225.
- von Zahn, U., von Cossart, G., Fiedler, J., Fricke, K. H., Nelke, G., Baumgarten, G., Rees, D., Hauchecorne, A., Adolfsen, K. (2000). "The ALOMAR Rayleigh/Mie/Raman lidar: objectives, configuration, and performance." Ann. Geophys. **18**: 815-833.

This chapter deals with the basic principle of the lidar and the different interactions between the laser beam and the atmospheric components. Those interactions can be divided into two classes, the elastic interaction whose wavelength of the scattered light is the same as that of the incident beam and inelastic interaction whose scattered radiation has a wavelength different from that of the incident radiation. The former gives the elastic lidar equation whereas the latter gives the Raman lidar equation.

The elastic interaction is described by the Rayleigh and the Mie scattering theories. Elements of those theories are briefly presented in this chapter, just like the Raman scattering theory. The retrieval of the water vapor mixing ratio is explained in more details in the chapter “Advances in global change research Article”, p 151.

More information is available in the received signal because of the additional parameters defining its polarization characteristics. The depolarization ratio is a good indicator of the shape of the aerosols.

The Angstrom exponent is an indicator of the scattering regime, but do not provide reliable information on the aerosol size distribution. Taking the advantage of the multiple-wavelength configuration of the lidar, it is possible to determine independent extinction and backscatter coefficients and thus to retrieve some aerosol microphysical parameters.

2.1. Lidar principle

A lidar is similar to the more familiar radar, and can be thought of as a laser radar. In a radar, radio waves are transmitted into the atmosphere, which scatters some of the power back to the radar's receiver. A lidar also transmits and receives electromagnetic radiation, but at a higher frequency. Lidars operate in the ultraviolet, visible and infrared region of the electromagnetic spectrum. Lidar is an acronym which stands for **L**ight **D**etection **A**nd **R**anging.

The lidar system of the Jungfrauoch is based on the same model, composed of a transmitting and a receiving section as shown in the Figure 2-1.

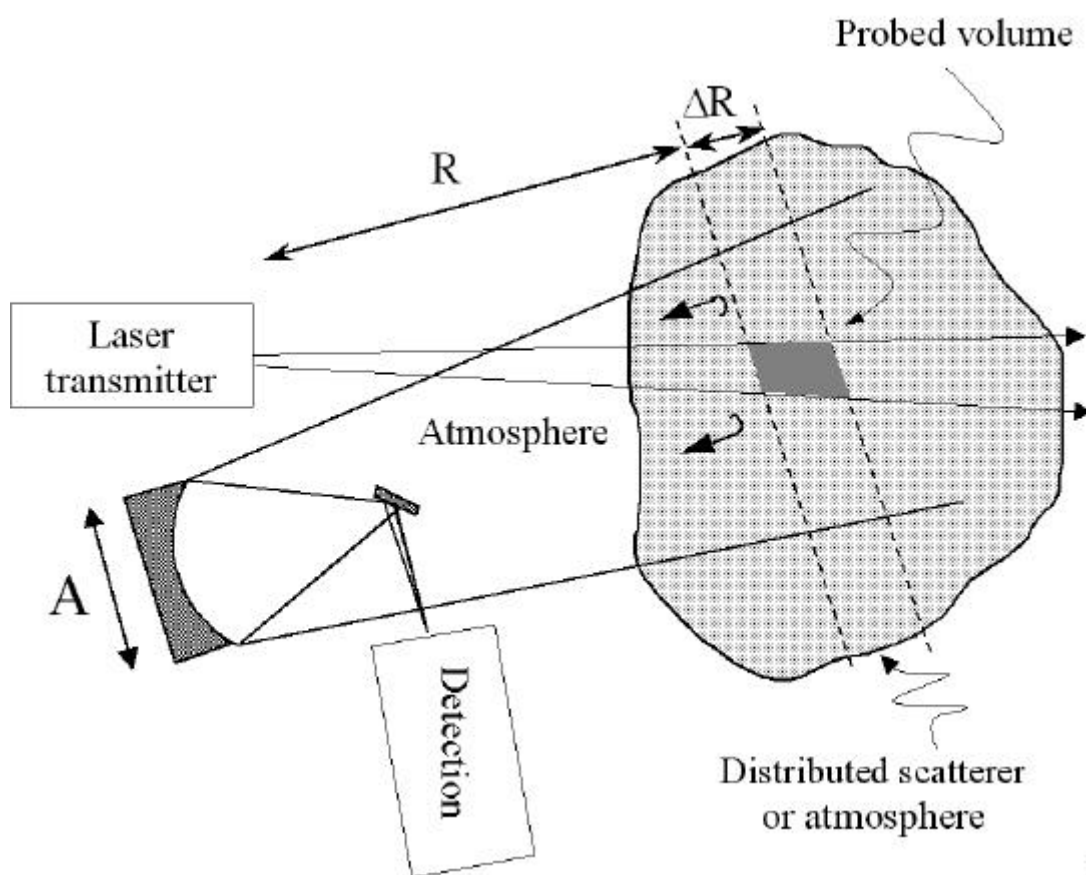


FIGURE 2-1. Lidar principle (biaxial type). From (Lazzarotto 2000).

As the transmitted laser energy passes through the atmosphere, the gas molecules and aerosols encountered cause scattering (Rayleigh, Mie, Raman,...) and absorption. A small fraction of this energy is backscattered in the direction of the lidar system and is available for detection. This produces an electrical signal, the intensity of which at any instant is proportional to the optical power received. Since the light travels at known velocity, the range of the scattering volume producing the signal can be uniquely determined from the time interval since the transmission of the pulse. The magnitude of this signal is determined by the backscattering properties of the atmosphere and by the two-way atmospheric attenuation. Those properties depend upon the wavelength of the laser energy used and the number, size distribution, shape and

refractive index properties of the molecules or particles intercepted by the incident laser energy (Hinkley 1976; Measures 1992).

2.2. Basic scattering lidar equation

For a single-wavelength pulsed lidar, the single-scattering lidar equation may be expressed as (Measures 1992)

$$P(\mathbf{l}, R) = P_L \frac{A_0}{R^2} \mathbf{x}(\mathbf{l}) \mathbf{x}(R) \frac{c\tau}{2} \mathbf{b}(\mathbf{l}_L, \mathbf{l}, R) \exp \left\{ - \int_0^R [\mathbf{a}(\mathbf{l}_L, r) + \mathbf{a}(\mathbf{l}, r)] dr \right\} \quad (\text{EQ 2.1})$$

where $P(\lambda, R)$ [W] is the total signal power received by the detector at wavelength λ and time t , corresponding to the range R ($t=2R/c$), P_L [W] is the laser emitted power at wavelength λ_L , A_0 [m²] is the receiver area, R [m] is the range between the receiver and the atmospheric target, $\xi(\lambda)$ [-] is the receiver's spectral transmission factor at wavelength λ , $\xi(R)$ [-] is the overlap function of the lidar system, c [m s⁻¹] is the velocity of light, τ [s] is the integration period of the detector, $\beta(\lambda_L, \lambda, R)$ [m⁻¹sr⁻¹] is the volume backscatter coefficient at wavelength λ for incident radiation of wavelength λ_L and $\alpha(\lambda, R)$, $\alpha(\lambda_L, R)$ [m⁻¹] are the volume extinction coefficients at wavelength λ and λ_L respectively.

2.3. Atmospheric interactions

The volume extinction and backscatter coefficients are a sum of contributions from both the gaseous and particulate components of the atmosphere

$$\begin{aligned} \mathbf{a}(\mathbf{l}, r) &= \mathbf{a}_m(\mathbf{l}, r) + \mathbf{a}_p(\mathbf{l}, r) + \mathbf{a}_a(\mathbf{l}, r) \\ \mathbf{b}(\mathbf{l}, r) &= \mathbf{b}_m(\mathbf{l}, r) + \mathbf{b}_p(\mathbf{l}, r) \end{aligned} \quad (\text{EQ 2.2})$$

where the subscript m stands for molecules, p for particles and a for the molecular absorption. These contributions are discussed in more details later.

The final form of the lidar equation to be used in any given situation depends upon the kind of interaction invoked by laser radiation (Seinfeld and Pandis 1998). When a beam of light impinges on a molecule or particle, electric charges are excited into oscillatory motion. The excited electric charges reradiate energy in all directions (scattering) and may convert a part of the incident radiation into thermal energy (absorption). Light scattering mechanisms can be divided into three categories

- Elastic scattering, the wavelength of the scattered light is the same as that of the incident beam

- Quasi-elastic scattering, the wavelength shifts due to Doppler effects and diffusion broadening
- Inelastic scattering, the emitted radiation has a wavelength different from that of the incident radiation

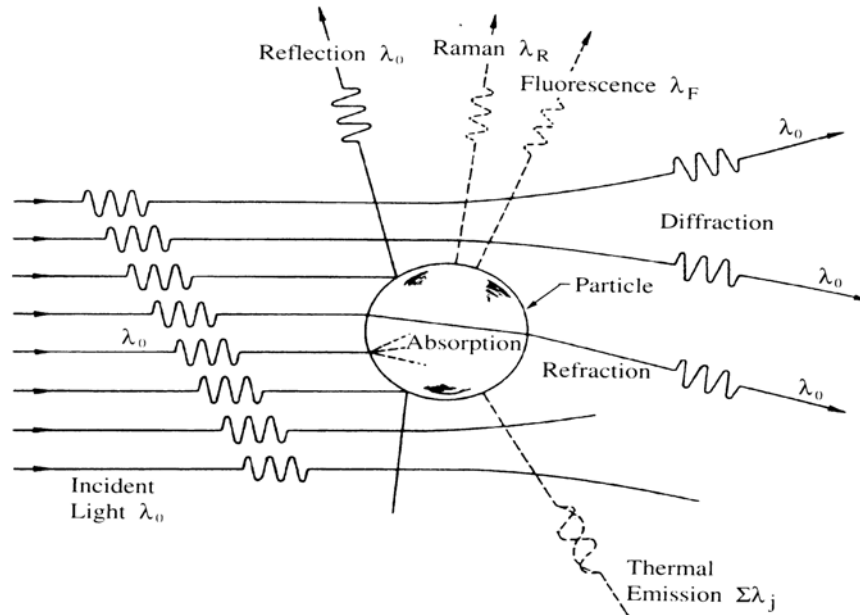


FIGURE 2-2. Mechanisms of interaction between incident radiation and a particle. From (Seinfeld and Pandis 1998).

Figure 2-2 illustrates the various processes that occur when radiation of wavelength λ interacts with a diffuser. Inelastic scattering processes include Raman and fluorescence. The key parameters that govern the scattering of light by a diffuser (molecule or particle) are:

- The wavelength λ of the incident radiation.
- The size of the diffuser, usually expressed as a dimensionless size parameter χ which is the ratio of the circumference of the diffuser to the wavelength of the light

$$c = \frac{2pr}{l} \quad (\text{EQ 2.3})$$

- The complex refractive index whose both the real part, n , and the imaginary part, k , are function of the wavelength. The real and imaginary parts represent the nonabsorbing and absorbing components, respectively.

$$m = n + ik \quad (\text{EQ 2.4})$$

Mie theory can serve as a basis of a computational procedure to calculate the scattering and absorption of light by any sphere as a function of wavelength (Bohren 1983). There are, in addition, approximate expressions, valid in certain limiting cases, that provide insight into physics of the problem. Based on the value of χ , light scattering can be divided into three domains

- $\chi \ll 1$, Rayleigh scattering,
- $\chi \sim 1$, Mie scattering,
- $\chi \gg 1$, Geometric scattering.

The next sections present the theory of the elastic scattering by molecules (Rayleigh) and particles (Mie), and of the inelastic scattering by molecules (Raman). Finally, the concept of molecular absorption is also treated.

2.4. Rayleigh scattering

When the particle or molecule is much smaller than the wavelength of the incident light, this is called the Rayleigh scattering regime, in which a closed form solution of the scattering problem is possible.

The concept of a scattering cross section is widely employed in dealing with the interactions of matter and radiant energy. In the domain of light scattering, the concepts of angular and volume scattering cross sections are basic concepts which leads to several coefficients and expressions having great practical utility (Mc Cartney 1976).

2.4.1. Angular scattering cross section

The angular scattering cross section of a molecule is defined as that cross section of an incident wave, acted on by the molecule, having an area such that the power flowing across it is equal to the power scattered by the molecule per steradian at an angle θ . Figure 2-3 shows some of the parameters used in the formula for calculating the angular scattering cross section. ϕ is the polarization angle of the linearly polarized incident wave propagating on the z-axis. The scattered radiation makes an angle θ with the z-axis (in the yz plane) and emits in a solid angle $d\Omega$.

The angular scattering cross section per molecule [$\text{cm}^2 \text{ molecule}^{-1} \text{sr}^{-1}$] is given by (Penndorf 1957)

$$\frac{dS_m(\mathbf{f}, \mathbf{q}, I)}{d\Omega} = \frac{9\rho^2(n_s^2 - 1)^2}{I^4 N_s^2 (n_s^2 + 2)^2} \left(\frac{6 + 3\mathbf{r}}{6 - 7\mathbf{r}} \right) \{ \cos^2 \mathbf{f} \cos^2 \mathbf{q} + \sin^2 \mathbf{f} \} \quad (\text{EQ 2.5})$$

where λ [cm] is the selected wavelength, N_s [molecule cm^3] is the molecular concentration, n_s [-] is the refractive index of the air, ρ [-] is the depolarization ratio, ϕ [rad] is the polarization angle and θ [rad] is the scattering angle.

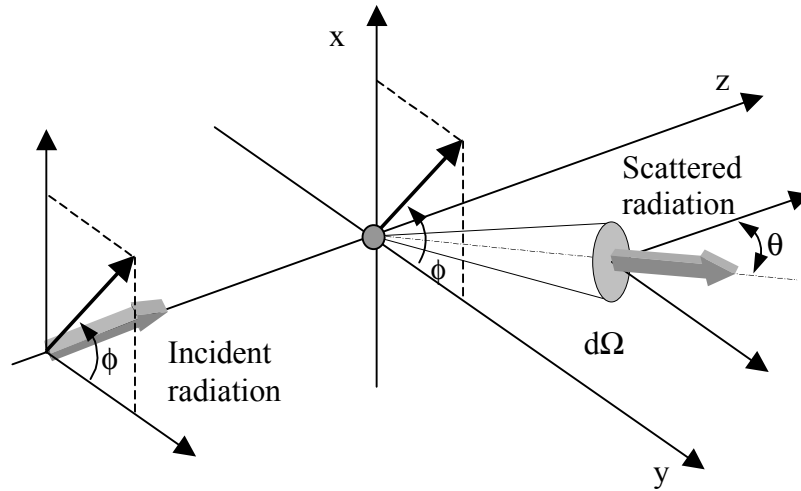


FIGURE 2-3. Schematic diagram for the incident and scattered beam. From (Lazzarotto 2000).

The King factor, $F(\text{air})$ or depolarization term [-] is defined as

$$F(\text{air}) = \frac{6 + 3r}{6 - 7r}$$

(EQ 2.6)

This factor describes the effect of molecular anisotropy. The $F(\text{air})$ term is the least known for purposes of Rayleigh scattering calculation and is responsible for the most uncertainty. The depolarization term does not depend on temperature and pressure, but does depend on the gas mixture. On contrary, N_S depends on temperature and pressure, but does not depend on the gas mixture. The resulting value of σ_m , the scattering cross section per molecule of gas is independent of temperature and pressure, but does depend on the composition of the gas. Note that N_S depends on Avogadro's number and the molar volume constant, and is expressed as molecule per cubic centimeter, and that values for N_S and n_S must be taken at the same temperature and pressure. However, since $(n_S^2 - 1)/(n_S^2 + 2)$ is proportional to N_S , the resulting expression for σ is independent of temperature and pressure (Bodhaine 1999).

2.4.2. Total volume scattering cross section

The volume scattering cross section per molecule σ_m [$\text{cm}^2 \text{ molecule}^{-1}$] is defined as that cross section of an incident wave, acted on by the molecule, having an area such that the power flowing across it is equal to the total power scattered by the molecule in all direction. A comparison of this definition with the one for the angular cross section indicates that σ_m is equal to the integral of the (EQ 2.5) over 4π sr.

The total volume scattering cross section per molecule, is given by (Bodhaine 1999)

$$s_m(I) = \frac{24p^3(n_s^2 - 1)^2}{I^4 N_s^2 (n_s^2 + 2)^2} \left(\frac{6 + 3r}{6 - 7r} \right)$$

(EQ 2.7)

2.4.3. Phase function

The concept of phase expresses in a formal manner the angular dependence of scattering. This use of the word phase has no relevance to the phase of an electromagnetic wave but is akin to the concept of lunar phase (angular aspect) as employed in astronomy. The phase function, denoted here by $P(\theta)$ is defined as «the ratio of the energy scattered per unit solid angle in this [given] direction to the average energy scattered per unit solid angle in all directions.» This definition requires that the integral of the phase function be normalized to unity (Mc Cartney 1976). The scattered light intensity pattern is symmetric in the forward and backward directions, totally polarized at 90° , and independent of the shape (Figure 2-4). Incident beam enters from right, 11 indicates the circular component independent of θ ; 12 is the θ -dependent term.

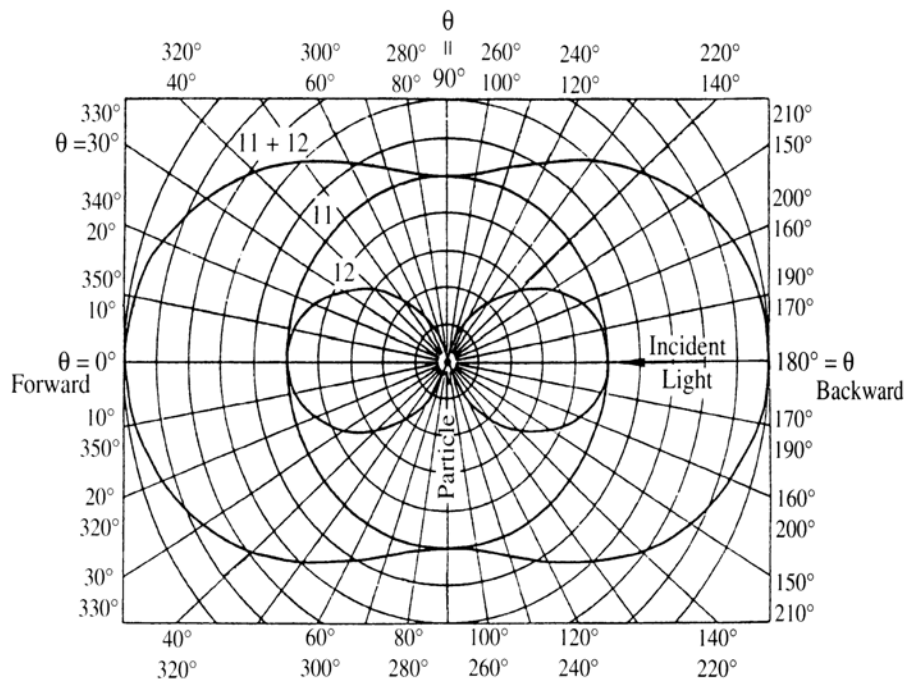


FIGURE 2-4. Rayleigh scattering phase function of an incident beam enters from the right ($\theta=180^\circ$). 11 indicates the circular θ -independent component and 12 the θ -dependent. From (Seinfeld and Pandis 1998).

A method of calculation of the Rayleigh scattering cross section is presented in the following paragraphs (Bodhaine 1999). The next sections will discuss how to determinate two key parameters: the refractive index of the air and the King factor. Then the volume scattering coefficient and the volume backscatter coefficient can be calculated using either balloon measurements or a model for the air concentration at an altitude R. One section is dedicated to the US-Standard-Atmosphere 1976.

2.4.4. Mean molecular concentration

In order to calculate the mean molecular weight of dry air with various concentrations of CO₂, the volume concentration of the constituent gases in air are taken from (Seinfeld and Pandis 1998) and the molecular weights of those gases are taken from (CRC 1997). Those values are shown in Table 2-1.

TABLE 2-1 Constituents and mean molecular weight of dry air

| Gas | Volume [%] | Molecular weight [gm mol ⁻¹] |
|---|-----------------------|--|
| N ₂ | 78.084 | 28.013 |
| O ₂ | 20.946 | 31.999 |
| Ar | 0.934 | 39.948 |
| Ne | 1.80 10 ⁻³ | 20.18 |
| He | 5.20 10 ⁻⁴ | 4.003 |
| Kr | 1.10 10 ⁻⁴ | 83.8 |
| H ₂ | 5.80 10 ⁻⁵ | 2.016 |
| Xe | 9.00 10 ⁻⁶ | 131.29 |
| CO ₂ | 0.036 | 44.01 |
| Mean molecular weight with zero CO ₂ | | 28.95949 gm mol ⁻¹ |
| Mean molecular weight with 360ppm CO ₂ | | 28.96491 gm mol ⁻¹ |

Assuming a simple linear relationship between the mean molecular weight (m_a) and CO₂ concentration, m_a may be estimated from the equation $m_a = 15.00556(\text{CO}_2) + 28.9595 \text{ gm mol}^{-1}$, where CO₂ concentration is expressed as part per volume. The molecular concentration is given by

$$N_s = \frac{N_A \cdot P}{T \cdot R \cdot m_a} \quad (\text{EQ 2.8})$$

where N_s [molecule cm³] is the molecular concentration at pressure P and temperature T, P [hPa] is the pressure, T [K] is the temperature, R is the universal gas constant, N_A [-] is the

Avogadro's number and m_a [gm mol⁻¹] is the mean molecular weight.

2.4.5. Refractive index of the dry air

The refractive index at wavelength λ of dry air with 300ppm CO₂ concentration (n_{300}) is calculated using (Peck and Reeder 1972)

$$(n_{300} - 1) \cdot 10^8 = 8060.51 + \frac{2480990}{132.274 - I^{-2}} + \frac{17455.7}{39.32957 - I^{-2}} \quad (\text{EQ 2.9})$$

and for any CO₂ concentration as

$$\frac{(n_{CO_2} - 1)}{(n_{300} - 1)} = 1 + 0.54(CO_2 - 0.0003) \quad (\text{EQ 2.10})$$

where the CO₂ concentration is expressed as part per volume (Edlén 1966). Thus the refractive index for dry air with zero ppm CO₂ and the refractive index for dry air with 360ppm CO₂ are

$$\begin{aligned} (n_0 - 1) \cdot 10^8 &= 8059.20 + \frac{2480588}{132.274 - I^{-2}} + \frac{17452.9}{39.32957 - I^{-2}} \\ (n_{360} - 1) \cdot 10^8 &= 8060.77 + \frac{2481070}{132.274 - I^{-2}} + \frac{17456.3}{39.32957 - I^{-2}} \end{aligned} \quad (\text{EQ 2.11})$$

where it must be emphasized that (EQ 2.9)-(EQ 2.11) are given for 288.15K and 1013.25mb, and λ is in micrometers.

Futhermore, corrections on temperature and pressure was proposed by (Edlén 1966) as an improvement of previous measurements (Barrell and Sears 1939) and is the following

$$(n_{TP} - 1) = (n - 1)_{288.15; 1013.25} \cdot \frac{P}{960.9279} \frac{1 + P(0.6128 - 0.0099758T)10^{-6}}{1 + 0.0036610T} \quad (\text{EQ 2.12})$$

For a temperature range of +5°C to +30°C, and with the temperature T in °C and the pressure P in mb. Edlèn (Edlén 1953; Edlén 1966) pointed out that the effect induced by high concentration of water vapor on the refractive index of the air may be of the same order as CO₂. Nevertheless, in most common atmospheric conditions, the total water vapor concentration in the vertical column is small and does not affect significantly the previous calculation. A more complex formula which is useful over a wide pressure (0 - 4atm), temperature (250 - 320K)

and relative humidity (0 - 100%) range was calculated by Owens (Owens 1967). No significantly difference between the two formulas were found, excepted an error of 0.25% at high temperature and high relative humidity. Therefore, (EQ 2.12) is used because of its simplicity.

2.4.6. King factor

As the King factor is wavelength and air composition dependent, the calculation of this term is a weighting of the depolarization terms for N₂, O₂, Ar and CO₂, ignoring the other gases (Bates 1984)

$$F(air) = \frac{78.084F(N_2) + 20.946F(O_2) + 0.934F(Ar) + x_{CO_2}F(CO_2)}{78.084 + 20.946 + 0.934 + x_{CO_2}} \quad (\text{EQ 2.13})$$

where ξ is expressed as part per volume by percent. The individual depolarization terms for N₂, O₂, Ar and CO₂ are described by the following equations, with λ in millimeters

$$\begin{aligned} F(N_2) &= 1.034 + 3.17 \cdot 10^{-4} \cdot I^{-2} \\ F(O_2) &= 1.096 + 1.385 \cdot 10^{-3} \cdot I^{-2} + 1.448 \cdot 10^{-4} \cdot I^{-4} \\ F(Ar) &= 1.00 \quad \text{and} \quad F(Ar) = 1.15 \end{aligned} \quad (\text{EQ 2.14})$$

The resulting value for the King factor is

$$F(air) = \frac{104.6297 + 1.15x_{CO_2} + 5.37628 \cdot 10^{-2} \cdot I^{-2} + 3.033 \cdot 10^{-3} \cdot I^{-4}}{99.964 + x_{CO_2}} \quad (\text{EQ 2.15})$$

2.4.7. Volume scattering coefficient

The volume scattering coefficient $\alpha_m(\lambda)$ is the ratio of the flux totally scattered in all direction, by unit of volume of a gas, to the irradiance of the incident flux. It describes the scattering efficacy of all molecules and is the real-world, measurable counterpart of the total scattering cross section of a single molecule. The volume scattering coefficient for a volume containing N molecules at an altitude r is (Mc Cartney 1976)

$$\mathbf{a}_m(\mathbf{I}, r) = N(r) \mathbf{s}_m(\mathbf{I}) \quad (\text{EQ 2.16})$$

where $\alpha_m(\lambda, r)$ [m⁻¹] is the volume scattering coefficient at altitude r and wavelength λ , $\sigma_m(\lambda)$

$[\text{cm}^2 \text{ molecule}^{-1}]$ is the scattering cross section per molecule at wavelength λ see (EQ 2.7) and $N(r)$ $[\text{molecules cm}^{-3}]$ is the air concentration at altitude r .

The volume backscatter coefficient $\beta_m(\lambda, r)$ $[\text{m}^{-1} \text{sr}^{-1}]$ is the second key parameter in (EQ 2.1). It can be calculated from (EQ 2.5) with $\theta=\pi$. Or by using the phase function S_m . In the case of Rayleigh scattering, the phase function is constant and equal to $3\pi/8$

$$\mathbf{b}_m(\mathbf{l}, r) = N(r) \frac{d\mathbf{s}(\mathbf{f}, \mathbf{p}, \mathbf{l})}{d\Omega}$$

$$\mathbf{b}_m(\mathbf{l}, r) = S_m \cdot \mathbf{a}_m(\mathbf{l}, r) = \frac{3\pi}{8} \mathbf{a}_m(\mathbf{l}, r)$$

(EQ 2.17)

The Rayleigh contribution $\alpha_m(\lambda, r)$ and $\beta_m(\lambda, r)$ to the volume extinction coefficient $\alpha(\lambda, r)$ and volume backscatter coefficient $\beta(\lambda, r)$, respectively, are given by (EQ 2.16) and (EQ 2.17).

Explicit values of the mentioned parameters calculated at standard conditions ($T=288.15\text{K}$, $P=1013.25\text{hPa}$ and $\text{CO}_2=360\text{ppm}$) for three wavelengths 355, 532 and 1064nm are presented in Table 2-2.

TABLE 2-2 Values calculated at standard conditions

| Wavelength [nm] | 355 | 532 | 1064 |
|---|------------------------|------------------------|-----------------------|
| $\alpha_m(\lambda)$ $[\text{m}^{-1}]$ | 6.89×10^{-5} | 1.313×10^{-5} | 7.96×10^{-7} |
| $\beta_m(\lambda)$ $[\text{m}^{-1} \text{sr}^{-1}]$ | 8.338×10^{-6} | 1.58×10^{-6} | 9.50×10^{-8} |
| n_S [-] | 1.0002857 | 1.0002782 | 1.0002734 |
| F(air) [-] | 1.0521 | 1.0489 | 1.0467 |
| ρ [-] | 0.2345 | 0.2201 | 0.2106 |

2.4.8. US-Standard-Atmosphere 1976

Various «standard atmospheres» have been established from time to time as reference for general scientific purposes and for designing and testing aerospace vehicles. Each of these references incorporated the best data available from the real atmosphere at the time. This real atmosphere at a given time and location necessarily differs from an annual model constructed for a single latitude belt. Weather, on both local and synoptic scales, produces large fluctuations in the properties in the troposphere, and the fluctuations frequently extend into the stratosphere. In addition, there are systematic variations due to latitude and season, and solar factors become important at high altitudes (Mc Cartney 1976). For this project, the US-Standard-Atmosphere 1976 is used. It is an idealized, steady-state representation of the earth's atmosphere from the surface to 1000km, as it is assumed to exist in a period of moderate solar activity. The air is assumed to be dry, and heights sufficiently below 86km, the atmosphere is assumed to be homogeneously mixed with a relative-volume composition leading to a mean molecular weight.

The standard atmosphere is divided in five layers: from 0 to the altitude of the tropopause, from this altitude to 20km, from 20 to 35km and from 35 to 50km with gradients of temperature of -0.65K/100m, +0.0K/100m, +0.1K/100m and +0.24K/100m, respectively.

The temperature and the pressure at a given altitude r are calculated by the following equations

$$T(r) = T(r_0) \left(\frac{1 - \frac{dT}{dr}}{T(r_0)(r - r_0)} \right)$$

$$P(r) = P(r_0) \left(\frac{1 - \frac{dT}{dr}}{T(r_0)(r - r_0)} \right)^{\frac{g}{R \frac{dT}{dr}}}$$

(EQ 2.18)

If the gradient of temperature is zero, (EQ 2.18) becomes

$$T(r) = T(r_0)$$

$$P(r) = P(r_0) \exp\left(-\frac{(r - r_0)g}{RT(r_0)}\right)$$

(EQ 2.19)

where r [m] is the altitude in a layer, r_0 [m] is the altitude of the bottom of the layer, g [m s^{-2}] is the acceleration due to gravity and R is the gas constant.

Figure 2-5 shows molecular density, temperature and pressure profiles above the Jungfraujoch calculated with (EQ 2.18) and (EQ 2.19). The ground-level temperature and pressure are 260K and 660mbar, respectively.

2.5. Mie scattering

In the presence of particles with a size comparable to the exciting wavelength, the Mie scattering becomes predominant. Its efficiency is generally much bigger than the Rayleigh's one, as it is shown in Figure 10-1, p 192 and Figure 10-2, p 193. Those figures show the extinction and backscatter coefficients as a function of the wavelength for the Rayleigh regime, hazes and clouds (Wright 1975; Rothmel J. 1989).

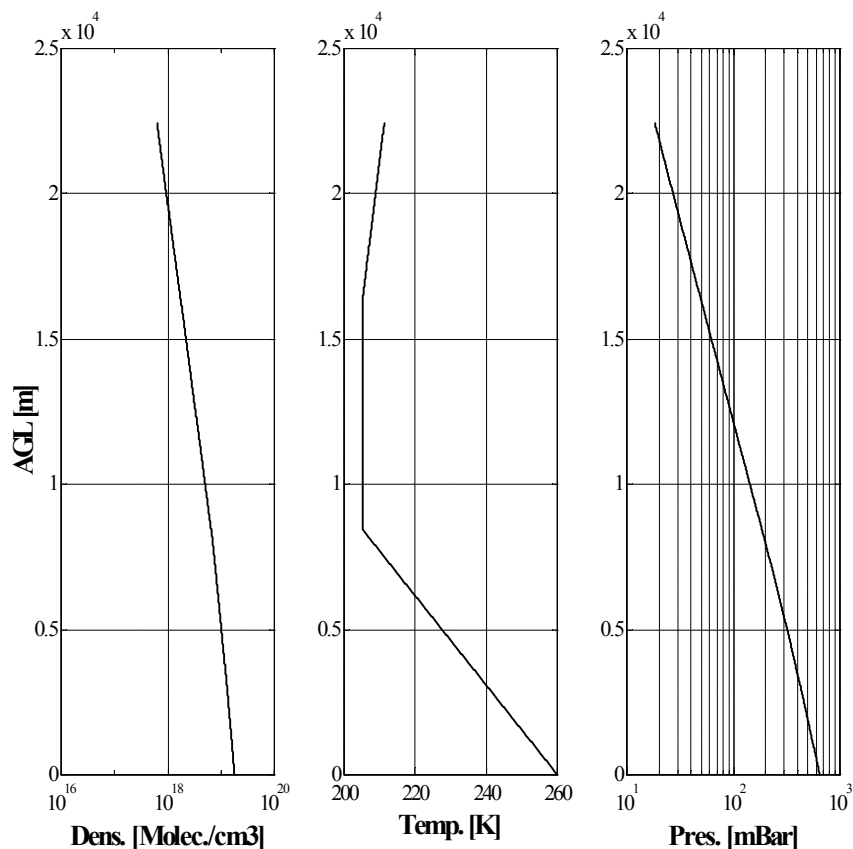


FIGURE 2-5. Molecular concentration, temperature and pressure above the Jungfraujoch station (3580m asl) from US-Standard-Atmosphere 1976. The ground-level temperature and pressure are 260K and 660mbar, respectively.

2.5.1. Intensity distribution functions

The angular characteristics of the Mie scattering for all particle sizes and wavelengths are expressed by two intensity distribution functions. These functions are basic for all subsequent definition of scattering cross sections and volume coefficients (Mc Cartney 1976).

The light scattered at observation angle θ by a particle may be treated as consisting of two components having intensities $I_c(\theta)$ and $I_p(\theta)$, polarized perpendicular and parallel to the plane of observation, respectively. The components are proportional to to intensity distribution function i_c and i_p , respectively.

$$\begin{aligned}
i_c(\mathbf{c}, m, \mathbf{q}) &= \left| \sum_{n=1}^{\infty} \frac{2n+1}{n(n+1)} (a_n \mathbf{p}_n + b_n \mathbf{t}_n) \right|^2 \\
i_p(\mathbf{c}, m, \mathbf{q}) &= \left| \sum_{n=1}^{\infty} \frac{2n+1}{n(n+1)} (a_n \mathbf{t}_n + b_n \mathbf{p}_n) \right|^2
\end{aligned}
\tag{EQ 2.20}$$

where the n 's are positive integers. The values of a_n and b_n are found from the Ricatti-Bessel functions, whose arguments are formed from the particle characteristics χ (EQ 2.3) and m (EQ 2.4). The functions π_n and τ_n depend only on the angle θ and involve the first and second derivatives of the Legendre polynomials having order n and argument $\cos\theta$. Henceforth the dependence on χ and m is not indicated, but it is understood. When the particle is illuminated by plane-polarized light whose electric vector is neither perpendicular nor parallel to the plane of observation, see Figure 2-3, the intensity of the scattered light in this plane is given by

$$I(\mathbf{q}, \mathbf{f}) = E_f \frac{I^2}{4p^2} (i_c \sin^2 \mathbf{f} + i_p \cos^2 \mathbf{f})
\tag{EQ 2.21}$$

where E_ϕ is the irradiance of the incident light.

2.5.2. Angular scattering cross section

The angular scattering cross section σ_p of a particle [$\text{cm}^2 \text{sr}^{-1} \text{molecule}^{-1}$] is analogous to that of a molecule and then is defined by

$$\begin{aligned}
\mathbf{s}_p(\mathbf{q}, \mathbf{f}) E_f &= I(\mathbf{q}, \mathbf{f}) \\
\mathbf{s}_p(\mathbf{q}) &= \mathbf{s}_p(\mathbf{q}, \mathbf{f}) = \frac{I(\mathbf{q}, \mathbf{f})}{E_f} = \frac{I^2}{4p^2} (i_c \sin^2 \mathbf{f} + i_p \cos^2 \mathbf{f})
\end{aligned}
\tag{EQ 2.22}$$

Figure 2-6 shows the scattering phase function (see 2.4.3. p 27 for the definition of the phase function) for several diameter D_p at $\lambda=0.550\mu\text{m}$. When the diameter is small compared with λ , the phase function is symmetric in the forward and backward directions, see Figure 2-4 (the incident beam enters from the left). Note that, for all but the very smallest particles, the scattering is highly peaked in the forward direction. The directional asymmetry becomes more and more pronounced as the particles size increases.

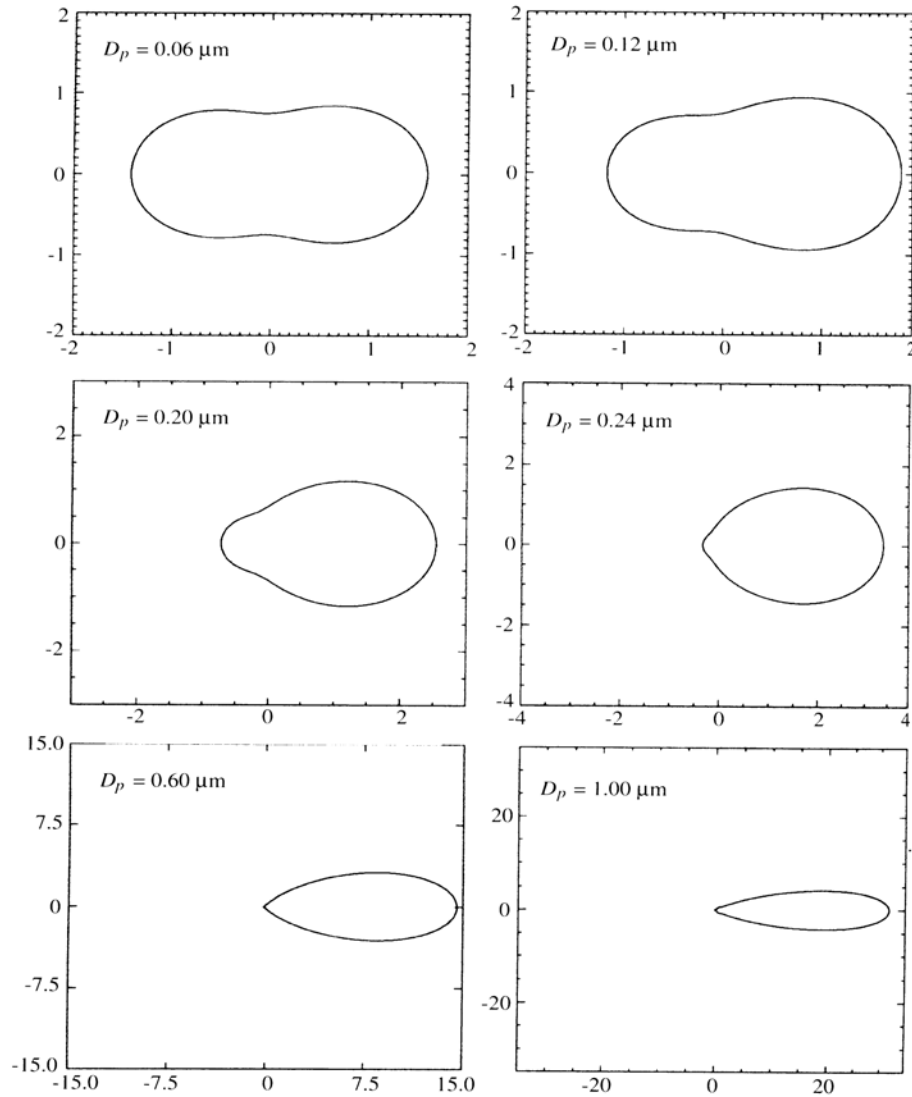


FIGURE 2-6. Mie scattering phase function at $\lambda=550\text{nm}$ versus diameter of the particle. The incident light enters from the left. From (Seinfeld and Pandis 1998).

The asymmetry parameter g , is defined as

$$g = \frac{\int_0^p \mathbf{s}_p(\mathbf{q}) \cos(\mathbf{q}) \sin(\mathbf{q}) d\mathbf{q}}{\int_0^p \mathbf{s}_p(\mathbf{q}) \sin(\mathbf{q}) d\mathbf{q}}$$

(EQ 2.23)

For isotropic or symmetric scattering (e.g. Rayleigh scattering) the asymmetry parameter is zero, for a purely forward scattering particle it is 1. The asymmetry parameter of the cloudless atmosphere ranges from 0.1 (very clean) to 0.75 (polluted); for a cloudy atmosphere the values are between 0.8 and 0.9 (Harrison 1998).

2.5.3. Volume angular scattering coefficient (monodispersion)

The volume angular scattering coefficient α_p [$\text{m}^{-1}\text{sr}^{-1}$] expresses the angular characteristic of a unit volume of aerosol and is found directly from the angular cross sections of the particles. When the particles are spherical and of the same size and refractive index, all the scattering patterns or cross sections are identical (monodispersion). If there are N particles in the unit volume, the scattered intensity in any direction is just N times that from one particle. The volume backscattering coefficient β_p [$\text{m}^{-1}\text{sr}^{-1}$] is obtained with $\theta=\pi$.

$$\begin{aligned} \mathbf{a}_p(\mathbf{q}) &= N\mathbf{s}_p(\mathbf{q}) \\ \mathbf{b}_p &= N\mathbf{s}_p(\mathbf{q}=\mathbf{p}) \end{aligned}$$

(EQ 2.24)

As in molecular scattering, the concept of total scattering by particles refers to the total amount of flux scattered in all direction from the incident flux.

2.5.4. Total scattering cross section and efficiency factor

The total scattering cross section σ_p [$\text{cm}^2\text{molec}^{-1}$] is defined as that cross section of an incident wave, acted on by the particle, having an area such that the power flowing across it is equal to the total power scattered in all directions.

$$\mathbf{s}_p = \int_0^{4\pi} \mathbf{s}_p(\mathbf{q}) d\omega = 2\mathbf{p} \int_0^{\pi} \mathbf{s}_p(\mathbf{q}) \sin q dq$$

(EQ 2.25)

Values of the total scattering cross section cover a wide range greater than the corresponding range of geometric cross section. The two are related by the efficiency factor Q_{sc} , often called the Mie coefficient K , which is the ratio of the scattering to the geometric cross section. The backscatter efficiency factor Q_{π} is obtained in a similar manner, using (EQ 2.24) with $\theta=\pi$.

$$\begin{aligned} Q_{sc} &= \frac{\mathbf{s}_p}{\mathbf{p}r^2} = \frac{2}{r^2} \int_0^{\pi} \mathbf{s}_p(\mathbf{q}) dq \\ Q_p &= \frac{\mathbf{s}_p(\mathbf{q}=\mathbf{p})}{\mathbf{p}r^2} \end{aligned}$$

(EQ 2.26)

where r is the radius of the particle.

The integration indicated in the preceding equations is more illustrative than practical. For purposes of computation, σ_p and Q_{sc} can be defined in terms of the complex functions a_n and b_n employed in (EQ 2.20) to define the functions i_c and i_p . In such terms the total scattering cross section is expressed by

$$s_p = \frac{I^2}{2p} \sum_{n=1}^{\infty} (2n+1) (|a_n|^2 + |b_n|^2) \quad (\text{EQ 2.27})$$

Division of this expression by πr^2 gives the scattering efficiency factor

$$Q_{sc} = \frac{I^2}{2p^2 r^2} \sum_{n=1}^{\infty} (2n+1) (|a_n|^2 + |b_n|^2)$$

$$Q_p = \frac{I^2}{4p^2 r^2} \left| \sum_{n=1}^{\infty} (2n+1) (-1)^n (a_n - b_n) \right|^2 \quad (\text{EQ 2.28})$$

The difference between the flux removed from the incident beam and the totally scattered flux must be attributed to absorption by particles. Absorption occurs when the refractive index is complex and the absorbed energy goes into heating the particles. The extinction efficiency factor Q_{ex} is the sum of the scattering and absorption efficiency factors.

$$Q_{ex} = Q_{sc} + Q_{ab}$$

$$Q_{ex} = \frac{I^2}{4p^2 r^2} \sum_{n=1}^{\infty} (2n+1) [\text{Re}(a_n + b_n)] \quad (\text{EQ 2.29})$$

Figure 2-7 shows the extinction efficiency factor Q_{ex} for a water droplet; (a) $\lambda=500\text{nm}$ and diameter is varied and (b) diameter= $2\mu\text{m}$ and λ is varied.

The ratio of the scattering efficiency factor to the extinction efficiency factor is called the single scattering albedo.

$$w = \frac{Q_{sc}}{Q_{ex}} = 1 - \frac{Q_{ab}}{Q_{ex}} \quad (\text{EQ 2.30})$$

It is the fraction of scattered light with respect to the total light which interacts with the particles. For a particle having no light absorption the single scattering albedo is 1.

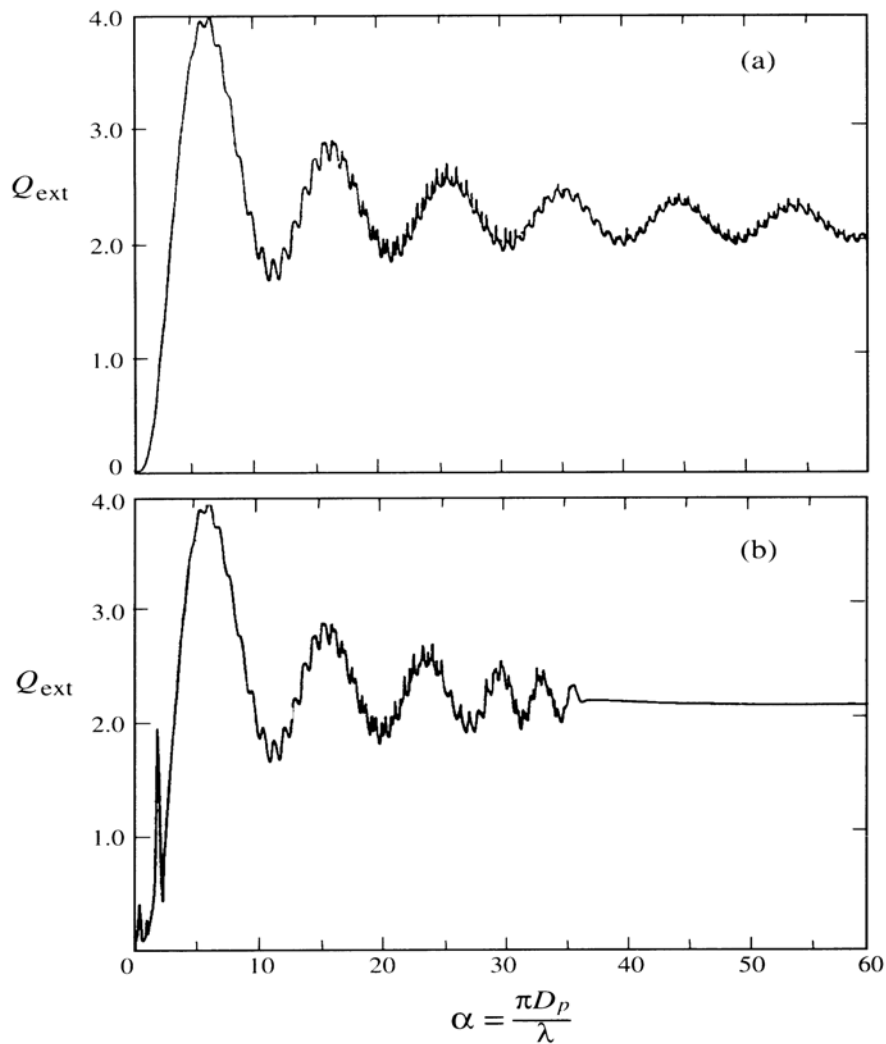


FIGURE 2-7. Extinction efficiency factor Q_{ext} for (a) a varying diameter and a constant wavelength at $\lambda=550\text{nm}$ and (b) a varying wavelength and a diameter of $2\mu\text{m}$. From (Seinfeld and Pandis 1998).

2.5.5. Volume extinction coefficients

The volume extinction coefficient expresses the total amount of flux removed from a beam per unit volume of particle suspension per unit irradiance of the volume. Assuming that the particles are spherical, and isotropic in other respects as well, this coefficient is independent of the polarization state of the incident light. Flux removal may be accomplished by pure scattering as indicated by Q_{sc} , or by any combination of scattering and absorption by particles as indicated by Q_{ex} . Since the processes are incoherent, the amount of flux removed by N particles is N times that removed by one particle. The volume total scattering coefficient for a monodispersion of particles thus is given by

$$\mathbf{a}_p^{sc} = N\mathbf{s}_p \quad (\text{EQ 2.31})$$

where N is the particle concentration and σ_p is the scattering cross section defined by (EQ 2.27). Because Q_{sc} , Q_{ab} and Q_{ex} are the ratio of the scattering, absorption and extinction, respectively, to the geometric cross section.

$$\begin{aligned} \mathbf{a}_p^{sc} &= N\mathbf{p}r^2Q_{sc} \\ \mathbf{a}_p^{ab} &= N\mathbf{p}r^2Q_{ab} \\ \mathbf{a}_p^{ex} &= N\mathbf{p}r^2Q_{ex} \end{aligned} \quad (\text{EQ 2.32})$$

where α_p^{sc} , α_p^{ab} , α_p^{ex} [m^{-1}] are the volume scattering, the volume absorption and volume extinction coefficients for a monodispersion of particles. The volume backscatter coefficient β_p [$\text{m}^{-1}\text{sr}^{-1}$] is given by

$$\mathbf{b}_p = N\mathbf{p}r^2Q_p \quad (\text{EQ 2.33})$$

In extending the scattering functions to polydispersion, the size distribution function is substituted for the monodispersion concentration N . The volume extinction coefficient α_p^{ex} [m^{-1}] and the volume backscatter coefficient β_p [$\text{m}^{-1}\text{sr}^{-1}$] are given by

$$\begin{aligned} \mathbf{a}_p^{ex} &= \mathbf{p} \int_0^{\infty} r^2 Q_{ex} n(r) dr \\ \mathbf{b}_p &= \mathbf{p} \int_0^{\infty} r^2 Q_p n(r) dr \end{aligned} \quad (\text{EQ 2.34})$$

The Mie contribution $\alpha_p(\lambda, r)$ to the volume extinction coefficient $\alpha(\lambda, r)$ and the contribution $\beta_p(\lambda, r)$ to the volume backscatter coefficient $\beta(\lambda, r)$ are given by (EQ 2.34).

Figure 2-8 shows the calculated spectral dependence on particle shape of the aerosol radiative parameters (Q_{ex} , g and ω) for a concentrated sulfuric acid composition (lefthand panel) and for different compositions for particles having the same gamma size distribution (righthand panel), excepted for the dust $2\mu\text{m}$. The extinction efficiency is normalized to unity at $\lambda=550\mu\text{m}$.

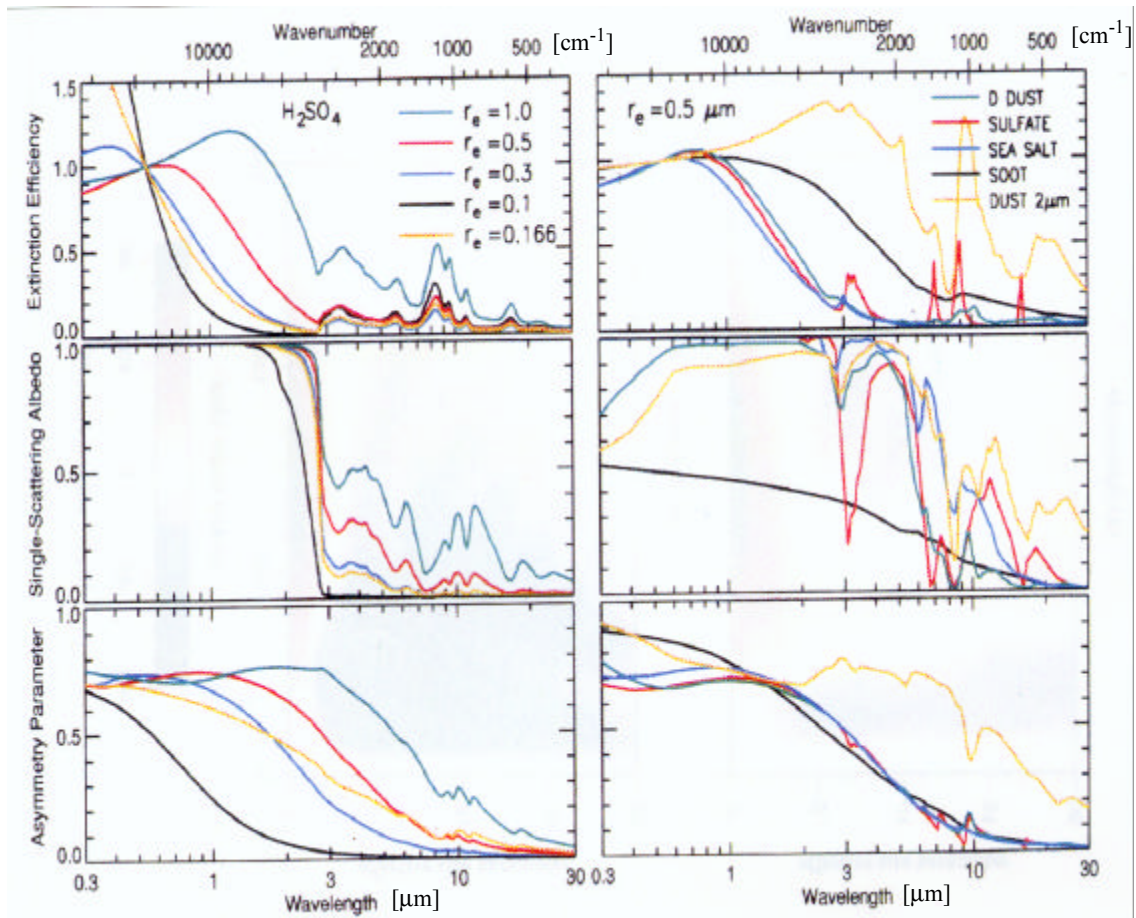


FIGURE 2-8. Mie extinction efficiency, single-scattering albedo and asymmetric parameter for different H_2SO_4 size distributions (left column) and for different chemical compositions (right column). From (Charlson 1995).

Basically, the results show that, except for soot, the radiative parameter dependence on composition, though significant, is not nearly as great as the parameter dependence on particle size. This strong dependence on particles size carries over both solar and thermal wavelength regimes, and underscores the need for accurate determination of not only the effective radius, but also the effective variance of the aerosol size distribution. This nonlinear dependence of the radiative parameters on particle size serves to demonstrate the complex behavior of those parameters (Charlson 1995).

2.5.6. Angstrom exponent

It is useful in some case to represent the wavelength dependence of the aerosol coefficient by $\alpha_p(\lambda, r) \sim \lambda^{-a}$. The exponent a is called the Angstrom exponent. It is calculated from measured values of the extinction coefficient as a function of wavelength by

$$a = -\frac{d \log(\mathbf{a})}{d \log(\mathbf{I})} \cong -\frac{\log\left(\frac{\mathbf{a}(I_1)}{\mathbf{a}(I_2)}\right)}{\log\left(\frac{I_1}{I_2}\right)} \quad (\text{EQ 2.35})$$

In the Rayleigh regime, the extinction coefficient varies with wavelength to a power between -3 and -4, whereas in the large-particle regime, this exponent ranges between 1 and 0 (Mc Cartney 1976; Seinfeld and Pandis 1998).

2.6. Geometric scattering

Particles for which $\chi \gg 1$ fall into the so-called geometric scattering regime. In this case the scattering can be determined on the basis of geometrical optics of reflection, refraction and diffraction. Scattering is strongly dependent on particle shape and orientation relative to the incoming beam. The extinction efficiency factor Q_{ex} approaches the limiting value 2 as the size parameter increases see Figure 2-7.

$$\lim_{c \rightarrow \infty} Q_{\text{ex}}(m, c) = 2 \quad (\text{EQ 2.36})$$

This is twice as large as predicted by geometrical optics, which is the so-called extinction paradox. In qualitative terms, the incident wave is influenced beyond the physical boundaries of the particle. Also, all the geometrically incident light that is not externally reflected enters the particles and is absorbed, as long as the absorptive part of the refractive index is not identically zero.

2.7. Raman scattering

When the laser radiation is inelastically scattered from molecules and is observed with a frequency shift characteristic of the molecule (and with a known backscattering cross-section), the Raman scattering is involved. In Figure 2-9 two types of Raman scattering that occurred simultaneously are shown: the Stokes process which shifts the wavelength to upper ones, and the anti Stokes one which shifts the wavelengths to lower values. In this scheme one photon is re-emitted with less (Stokes) or more (anti Stokes) energy than the incoming one. This scattering results from the interaction between the exciting radiation and the electric dipole moment of the molecule. It induces a change in the rotational or / and vibrational states of the molecule. The interaction life time is very small, quasi instantaneous, and smaller than 10^{-14} s. It is produced whatever the exciting wavelength is and gives a shifted lines spectrum with respect to this wavelength, whose shifting depends on the studied molecule.

The study of such a spectrum allows the simultaneous measure of a wide variety of components and the absolute measurement of their mixing ratio. This process has a very low efficiency (cross-sections about $10^{-32} - 10^{-28} \text{cm}^2 \text{molecule}^{-1}$), and can be improved by working in the UV, at shorter wavelengths, because the Raman differential cross-section is proportional to λ^{-4} .

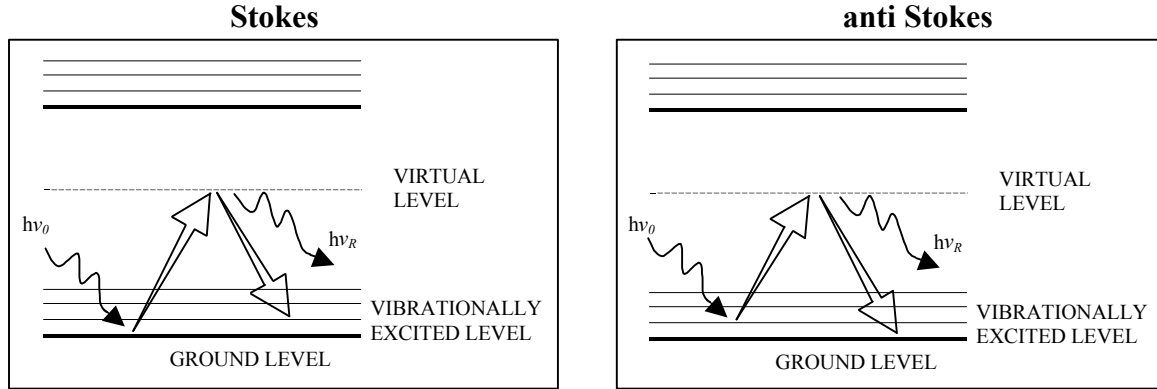


FIGURE 2-9. Raman interaction. From (Lazzarotto 2000).

2.7.1. Raman scattering cross section

Here is just presented the formula of the Raman scattering cross section. For more information, the reader is referred to (Inaba and Kobayashi 1972).

The intensity of a Raman line is determined by the scattering cross-section σ of the transition between the energy levels E_l and E_m . The expression for the total vibrational Raman backscattering cross-section of a Stokes shifted vibrational-rotational Raman band ν_j (sum of the Q-branch vibrational Raman backscattering cross-section and the O- and S- branches ones) is given by (Inaba and Kobayashi 1972)

$$\frac{dS}{d\Omega}(\mathbf{u}_0) = \frac{(2p)^4}{45} \frac{(\mathbf{u}_0 - \mathbf{u}_j)^4 b_j^2}{1 - \exp\left(-\frac{hc\mathbf{u}_j}{kT}\right)} g_j (45a_j^2 + 7g_j^2)$$

(EQ 2.37)

Where ν_j [cm^{-1}] is the frequency of the j^{th} vibrational mode of the molecule, b_j is the zero amplitude of this j^{th} vibrational mode, T [K] is the temperature, g_j is the degeneracy of the j^{th} vibrational mode, a_j and γ_j are the isotropic and anisotropic parts of the polarizability tensor derived with respect to the normal coordinates and k is the Boltzmann constant.

At atmospheric temperature most molecules are in their vibrational ground state $\nu=0$ (and also the electronic one). The Stokes bands will then be much more important than the anti-Stokes ones. In addition each vibrational line, gives rise to a closely spaced band of lines corresponding to different transitions in the rotational quantum number. Thus, the laser excitation of the O_2 , N_2 and H_2O atmospheric molecules due to the laser beam will give essentially the Stokes type transition $\nu 0 \rightarrow 1$.

2.7.2. Raman shifted wavelengths calculation

For a given excitation wavelength the Raman scattering will provide a shifted spectra characteristic to the excited molecule. Here was just computed the resulting shifted wavelength of the first vibrational Stokes, i. e. the most important one, and the one used in this work.

The wavenumber k [cm^{-1}] is defined as

$$l = \frac{c}{n} = \frac{1}{k} \quad (\text{EQ 2.38})$$

and the Raman shift Δk is given by

$$\Delta k = k_L - k_R \quad (\text{EQ 2.39})$$

where k_L [cm^{-1}] is the laser pump wavenumber and k_R [cm^{-1}] is the Raman shifted wavenumber. The Raman shift from the exciting wavelength are the following: 2331cm^{-1} for N_2 and 3652cm^{-1} for H_2O . The related Raman shifted wavelength λ_R [cm] is

$$l_R = \frac{l_L}{1 - \Delta k \cdot l_L} \quad (\text{EQ 2.40})$$

where Δk [cm^{-1}] is the raman shift, λ_L [cm] is the laser pump wavelength. Table 2-3 gives the corresponding values of the Raman shifted wavelengths at the wavelengths of a Nd:YAG laser (355 and 532nm)

TABLE 2-3 Raman shifted wavelengths for nitrogen and water vapor

| Gas | Nitrogen | Water vapor |
|----------------------------------|----------|-------------|
| Raman shift [cm^{-1}] | 2331 | 3652 |
| Wavelength [nm] | | |
| 355 | 386.68 | 407.51 |
| 532 | 607.41 | 660.40 |

2.8. Molecular absorption

In both Rayleigh and Mie cases, neither the linewidth nor its position is critical. It is important, obviously, to avoid coincidences with the absorption wavelengths of the atmosphere components. The molecular absorption coefficient $\alpha_a(\lambda, r)$ [cm^{-1}] for a group of molecules is given

by

$$a_a(I, r) = \sum n_i(r) s_i^{abs}(I, r)$$

(EQ 2.41)

where $n_i(r)$ [molecule cm^{-3}] is the concentration of the component i and $\sigma_i^{abs}(\lambda)$ [$\text{cm}^2 \text{molecule}^{-1}$] is the absorption cross section of the component i .

Figure 2-10 shows some molecular absorption coefficients between 250 and 1100nm, for a temperature of 243K which is representative of an altitude of 8km above the sea level and is taken as average value of the free troposphere. The absorption cross sections are calculated from Hitran and UV/Vis spectra of atmospheric constituents (HITRAN 1996; DLR 1998). Also presented in this figure is the Rayleigh extinction coefficient, which is here as a reference.

TABLE 2-4 Molecule concentrations at an altitude of 8km asl.

| Molecule | Concentration [ppb] |
|-------------------------------|---------------------|
| O ₃ | 50 |
| NO ₂ | 0.1 |
| NO ₃ | 0.01 |
| N ₂ O ₄ | 1 |

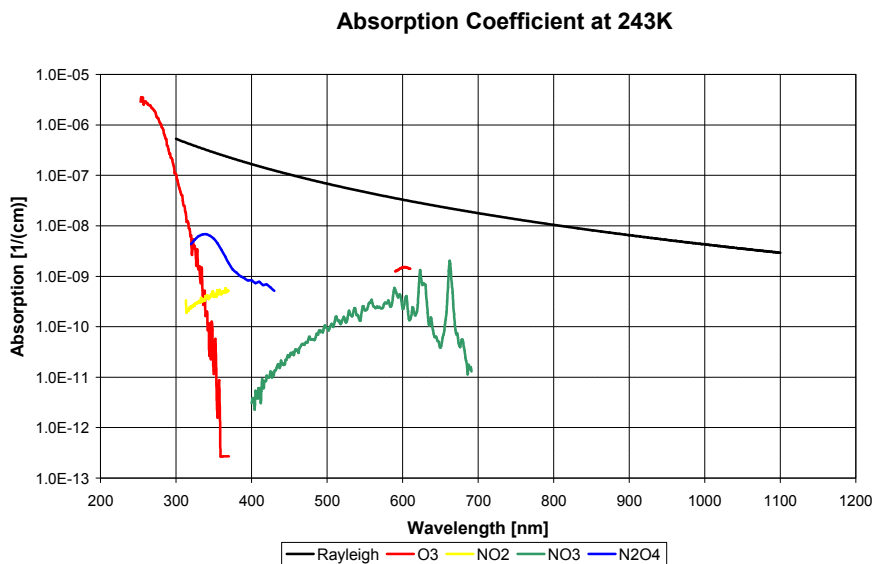


FIGURE 2-10. Molecular absorption coefficients at 243K versus the wavelength.

The species and their respective concentration are presented in Table 2-4 and come from the literature (Warneck 1988; Seinfeld and Pandis 1998) and from the GEOS-CHEM model, a three-dimensional (3-D) global model of transport-chemistry in the troposphere, implemented at EPFL. This model has been designed especially for the modeling of tropospheric ozone and related species (such as nitrogen oxides, carbon monoxide, hydrocarbons) as described in (Bey 2001), but additional applications include simulations of other species released in the atmosphere through various processes such as lead-210 and beryllium-7 (which provides a test of convective transport, large-scale subsidence, and precipitation scavenging in the model) (Liu 2001), methyl iodide (which provides a test for marine convection) and hydrogen cyanide (used as a tracer for biomass burning emissions) (Liu 2001).

At the wavelengths of interest (355, 387, 408, 532, 607 and 1064nm), the absorption is minimal and can be ignored in the free troposphere. But, the ozone absorption will increase in the stratosphere, due to the ozone layer, and can not be longer neglected as well in the UV as in the Chappuis band (Esposito 1998).

Knowing the main atmospheric interactions of interest, it is now possible to rewrite (EQ 2.1) p 23 in two different forms, elastic lidar equation involving only elastic scattering (Rayleigh and Mie) and Raman lidar equation. The next sections will develop those two formalisms used to determine the aerosol properties. How to retrieve water vapor will be also discussed. Polarized measurements provide more informations, as the particle shape, is useful for retrieving microphysical aerosol parameters.

2.9. Elastic Lidar equation

In the event that elastic (Rayleigh or Mie) scattering is used, then the wavelength detected is invariably the same as that of the laser, (EQ 2.1) can be written as (Hinkley 1976)

$$P(I_L, R) = P_L \frac{A_0}{R^2} \mathbf{x}(I_L) \mathbf{x}(R) \frac{\mathbf{a}}{2} \mathbf{b}(I_L, R) \exp \left[-2 \int_0^R \mathbf{a}(I_L, r) dr \right] \quad (\text{EQ 2.42})$$

A variety of methods (Fenner, Haytt et al. 1973; Klett 1981; Klett 1985; Sasano 1985; Krichbaumer and Werner 1994) have been proposed to obtain quantitative profiles of extinction and backscattering coefficients from an elastic lidar signal including both molecules and aerosols properties. The molecular atmosphere scattering properties, $\alpha_m(r)$ and $\beta_m(r)$, can be determined from appropriate standard atmosphere; therefore only the aerosol scattering properties, $\alpha_p(r)$ and $\beta_p(r)$, remain to be calculated. But in any case, (EQ 2.42) is an ill-posed problem because two unknowns are related to only one equation. A useful definition is the lidar ratio, defined as the ratio of the aerosol scattering coefficient to the aerosol backscatter coefficient

$$S_p(r) = \frac{\mathbf{a}_p(r)}{\mathbf{b}_p(r)} \quad (\text{EQ 2.43})$$

where $S_p(r)$ [sr] is the lidar ratio, $\alpha_p(r)$ [m^{-1}] is the aerosol extinction and $\beta_p(r)$ [$\text{m}^{-1} \text{sr}^{-1}$] is the aerosol backscatter coefficient. The relationship between those two coefficients is usually poorly or not at all known. However, it has been shown (Klett 1985) if such information is known, even approximately, it can and should be incorporated into the inversion. To date it has been very difficult to know, based on backscattered data alone, the accuracy of the calculated extinction obtained by lidar inversion.

The lidar ratio is constant in term of range, i.e. that β_p is proportional to α_p if either of the following is true

- The scattering medium does not change in index of refraction, size or orientation distribution
- Q_π is proportional to Q_{ex} , which is true for Rayleigh nonabsorbing particles and for strongly absorbing particles.

The backscatter coefficient profile for a longer wavelength has less sensitivity to the lidar ratio than those for a shorter wavelength (Sasano 1989). The proposed value of the lidar ratio from (Deepak 1983) for the visible and near infrared are presented in Table 2-5.

TABLE 2-5 Indicative values of the lidar ratio

| Altitude ranges | Aerosols type | Lidar ratio [sr] |
|---------------------------------|------------------------|------------------|
| 0 to 2km (PBL) | Urban | 43 |
| | Continental background | 43 |
| | Maritime | 23 |
| 2 to 11km (Free Troposphere) | Continental background | 43 |
| | Cirrus clouds | 13.5 |
| 11 to 30km | Fresh volcanic | 39 |
| | Aged volcanic | 59 |
| | Background | 59 |

A priori information must be used to specify the value of the aerosol and molecular scattering properties at a reference altitude R_f . Then the solution to (EQ 2.42) for the total backscattering coefficient can be written as (Sasano 1985)

$$\mathbf{b}_p(R) + \mathbf{b}_m(R) = \frac{P(R)R^2 \exp\left[-2 \int_{R_f}^R (S_p(r) - S_m) \mathbf{b}_m(r) dr\right]}{\frac{P(R_f)R_f^2}{\mathbf{b}_p(R_f) + \mathbf{b}_m(R_f)} - 2 \int_{R_f}^R S_p(r)P(r)r^2 \exp\left\{-2 \int_{R_f}^R (S_p(r') - S_m) \mathbf{b}_m(r') dr'\right\} dr} \quad (\text{EQ 2.44})$$

where S_m [sr] is the molecular phase function. The total backscattering coefficient is now expressed as a function of the scattering properties at a given altitude and those of the intervening atmosphere between the altitude R and R_f .

The aerosol backscatter cross section is uniquely determined according to the physical and chemical properties of the aerosols (size, shape and index of refraction). The wavelength dependence of the backscatter coefficient is mainly dependent on the aerosol size distribution and index of refraction. A multiwavelength lidar can, in principle, be used to measure the wavelength dependence of this coefficient. Different aerosol types are expected to have different size distribution and index of refraction, which implies that it may be possible to discriminate aerosol type according to the wavelength dependence (Sasano 1989).

2.10. Raman lidar equation

A first step towards a solution of the ill-posed problem of the elastic lidar equation is the additional use of Raman scattering. Indeed, the Raman backscattered signal is affected by aerosol extinction but the backscatter coefficient is well known. Therefore analysis of this signal alone permits the determination of the aerosol extinction (Leonard 1967; Cooney 1968; Inaba and Kobayashi 1969; Melfi, Lawrence et al. 1969; Ansmann, Riebesell et al. 1990). While the Raman lidar approach has the advantage of the simplicity in that one laser line can be used for a number of molecular species, it suffers in general from the reduced sensitivity and difficulty in daytime operation due to low Raman cross section. Let the Raman lidar equation be written as (Measures 1992)

$$P(R, \mathbf{I}_L, \mathbf{I}_R) = P_L \frac{A_0}{R^2} \mathbf{x}(\mathbf{I}_R) \mathbf{x}(R) \frac{ct}{2} \mathbf{b}(\mathbf{I}_L, \mathbf{I}_R, R) \exp \left[- \int_0^R \mathbf{a}(\mathbf{I}_L, r) + \mathbf{a}(\mathbf{I}_R, r) dr \right] \quad (\text{EQ 2.45})$$

Where the backscatter coefficient $\beta(\lambda_L, \lambda_R, R)$ at the elastic wavelength λ_L and Raman wavelength λ_R is linked to the differential Raman backscatter cross section $d\sigma/d\Omega$ of a gas with a molecule number density $N(R)$ by the relation

$$\mathbf{b}(\mathbf{I}_L, \mathbf{I}_R, R) = N(R) \frac{d\mathbf{s}(\mathbf{I}_L, \mathbf{I}_R, \mathbf{p})}{d\Omega} \quad (\text{EQ 2.46})$$

The profiles of both nitrogen and oxygen can be used since their number densities are usually well known. The particle extinction coefficient can be determinate from (EQ 2.45) and (EQ 2.46) using the following methodology.

$$\exp \left[\int_0^R \mathbf{a}_p(\mathbf{I}_L, r) + \mathbf{a}_p(\mathbf{I}_R, r) dr \right] = K(\mathbf{I}_R) \left\{ \frac{\mathbf{x}(R) N(R)}{P(R) R^2} \right\} \exp \left[- \int_0^R \mathbf{a}_m(\mathbf{I}_L, r) + \mathbf{a}_m(\mathbf{I}_R, r) dr \right] \quad (\text{EQ 2.47})$$

where $K(\lambda_R)$ is the all range-independ system parameters at wavelength λ_R . Taking the logarithm and then the derivative of (EQ 2.47), the extinction coefficients are given by

$$\mathbf{a}_p(\mathbf{I}_L, R) + \mathbf{a}_p(\mathbf{I}_R, R) = \frac{d}{dR} \ln \left\{ \frac{\mathbf{x}(R) N(R)}{P(R) R^2} \right\} - \mathbf{a}_m(\mathbf{I}_L, R) - \mathbf{a}_m(\mathbf{I}_R, R) \quad (\text{EQ 2.48})$$

Particle scattering is assumed to have an Angstrom coefficient equal to k (see (EQ 2.35)) and since $\Delta\lambda/\lambda_L$ is small, (EQ 2.48) can be presented approximately as

$$\mathbf{a}_p(\mathbf{I}_L, R) = \frac{\frac{d}{dR} \ln \left\{ \frac{\mathbf{x}(R) N(R)}{P(R) R^2} \right\} - \mathbf{a}_m(\mathbf{I}_L, R) - \mathbf{a}_m(\mathbf{I}_R, R)}{1 + \left(\frac{\mathbf{I}_L}{\mathbf{I}_R} \right)^k} \quad (\text{EQ 2.49})$$

For particles and water droplets with diameters comparable with the measurement wavelength, $k=1$ is an appropriate value, while in the case of large particles and ice particles, which are usually large compared with the laser wavelength, $k=0$ is justified.

The particle backscatter coefficient $\beta_p(\lambda_L, R)$ can be determined by using both elastically and Raman backscattered signals (Cooney 1969; Melfi 1972). Two measured signal pairs $P(R, \lambda_L)$ and $P(R, \lambda_L, \lambda_R)$ at altitude R and a reference altitude R_f are needed. A solution for the particle backscatter coefficient is obtained by forming the scattering ratio

$$\mathfrak{R}(\mathbf{I}_0, r) = \frac{\mathbf{b}_p(\mathbf{I}_0, r) + \mathbf{b}_m(\mathbf{I}_0, r)}{\mathbf{b}_m(\mathbf{I}_0, r)} \quad (\text{EQ 2.50})$$

The scattering ratio can be expressed in terms of the lidar signals by using elastic lidar equation (EQ 2.42) and Raman lidar equation (EQ 2.45). It is equal to unity in a region of atmosphere that is free of aerosols and exceeds unity where aerosols are present. The value of (EQ 2.50) at the aerosol-free height R_f is used to normalize the scattering ratio to unity and thus can be rewritten as

$$\mathfrak{R}(\mathbf{I}_0, R) = \frac{P(R, \mathbf{I}_L) \cdot P(R_f, \mathbf{I}_L, \mathbf{I}_R)}{P(R_f, \mathbf{I}_L) \cdot P(R, \mathbf{I}_L, \mathbf{I}_R)} \times \frac{\exp \left\{ \int_{R_f}^R [\mathbf{a}_p(\mathbf{I}_R, r) + \mathbf{a}_m(\mathbf{I}_R, r)] dr \right\}}{\exp \left\{ \int_{R_f}^R [\mathbf{a}_p(\mathbf{I}_L, r) + \mathbf{a}_m(\mathbf{I}_L, r)] dr \right\}} \quad (\text{EQ 2.51})$$

In the case of a high particle load throughout the whole range of measurement, a value of $\beta_p(\lambda_L, R_f)$ is needed with sufficient accuracy. In this special case a determination of the backscatter profile from (EQ 2.51) is not possible. Finally, the lidar ratio can be obtained from the

profiles of $\alpha_p(\lambda_L, R)$ and $\beta_p(\lambda_L, R)$ as determined with (EQ 2.49) and (EQ 2.51).

2.11. Water vapor mixing ratio

The water vapor mixing ratio is defined as the mass of water vapor per unit mass of dry air. It can be obtained from the measurement of the water vapor to reference signal ratio, where the reference gas is either oxygen or nitrogen (Melfi, Lawrence et al. 1969; Melfi and Whiteman 1985; Ansmann, Riebesell et al. 1992; Whiteman, Melfi et al. 1992; Sherlock 1998). Using two Raman lidar equations for the wavelengths λ_{H_2O} and λ_R , forming the signal ratio, and rearranging the terms, the resulting equation, the mixing ratio $m(R)$ is obtained as

$$m(R) = K_m \frac{P(R_f, \mathbf{I}_L, \mathbf{I}_{H_2O}) \exp\left\{-\int_0^R [\mathbf{a}(\mathbf{I}_{H_2O}, r)] dr\right\}}{P(R_f, \mathbf{I}_L, \mathbf{I}_R) \exp\left\{-\int_0^R [\mathbf{a}(\mathbf{I}_R, r)] dr\right\}} \quad (\text{EQ 2.52})$$

where $m(R)$ [$\text{gH}_2\text{O g}^{-1}$ dry air] is the water vapor mixing ratio, K_m [g/kg] is the overall system constant and can in principle be deduced from the known Raman cross sections and the measured properties of the receiver's spectral transmission, but in practice determined from comparison of the lidar measurement with evaluated data from radiosonde ascent. A more detailed theory is given in "Advances in global change research Article", p 151.

2.12. Depolarization ratio

It is well known that lidar measurements of the atmosphere are somewhat limited in the information they can provide because of the fact that most systems measure only the intensity of the backscattered signal. Considerably more information is available in the received signal because of the additional parameters defining its polarization characteristics. The complete information available in the lidar scattering process is contained in the scattering matrix describing the atmosphere. Using the conventional formalism of Stockes vectors this matrix would be a 4x4 matrix and would contain all available information about the atmosphere accessible in a scattering measurement. However it is difficult to obtain measurements of the atmospheric scattering matrix because it involves a measurement of the complete Stockes vector of the backscattered signal for a variety of transmitted signals with different Stockes parameters. These measurements are even more difficult because of the space and time dependence of the atmospheric properties (McNeil 1975). A useful quantity is the depolarization ratio δ , which is defined as

$$\mathbf{d}(R) = \frac{P_{\perp}(R)}{P_{\parallel}(R)} \quad (\text{EQ 2.53})$$

where P_{\parallel} and P_{\perp} are the backscattered signals measured with the receiver polarized parallel and perpendicular, respectively, to the direction of polarization of the linearly polarized transmitted pulse. Using (EQ 2.42), (EQ 2.53) becomes

$$\mathbf{d}(R) = \frac{\mathbf{x}_{\perp}(\mathbf{I}) \mathbf{b}_{\perp}(R)}{\mathbf{x}_{\parallel}(\mathbf{I}) \mathbf{b}_{\parallel}(R)} \frac{\exp\left\{-\int_0^R [\mathbf{a}_{\parallel}(r) + \mathbf{a}_{\perp}(r)] dr\right\}}{\exp\left\{-2\int_0^R \mathbf{a}_{\parallel}(r) dr\right\}} \quad (\text{EQ 2.54})$$

The two-way atmospheric transmissions are expected to be equal for randomly oriented scattering centers contributing to the crossed polarization. Thus the depolarization is given by

$$\mathbf{d}(R) = K_{\perp}^{\parallel}(\mathbf{I}) \frac{\mathbf{b}_{\perp}(R)}{\mathbf{b}_{\parallel}(R)} \quad (\text{EQ 2.55})$$

where K_{\perp}^{\parallel} is the calibration factor of the system. It is evident therefore that all the instrumental and extinction effects disappear and δ depends only on the volume backscattering properties of the atmosphere (Pal 1973).

For single scattering by either Rayleigh particles or Mie particles (perfect sphere), the polarization of the incident wave is retained in the backscattering. Thus, since a linearly polarized wave is launched, the return should also be linearly polarized if only those mechanisms are present (apart from the very small molecular depolarization component that would have a value of only 2%). As a result, any measured value greater than 0.02 immediately indicates that a process is involving scattering mechanisms other than Rayleigh or Mie scattering. Thus the most probable source of the observed depolarization would be a result of the variable particle shape, chemical composition and physical characteristic. If the aerosol number density is high enough, the multiple-scattering process, even from spherical particles, could introduce some depolarization (Pal 1973; McNeil 1975; Pal 1978; Sassen 1994).

2.13. Retrieval of microphysical aerosol parameters

As it was pointed out in ‘‘Aerosol direct effects on climate’’, p 13, the aerosol size distribution and the chemical composition are the key parameters. Lidars deliver information on particle extinction and backscatter coefficients at multiple wavelengths. This information can be used

to derive physical particle properties as particle size, number, surface-area, and volume concentration, as well as the complex refractive index. The problem of determining those properties by multispectral lidar measurements, belongs to a class of inverse ill-posed problems. Several methods were developed to solve this problem: the singular value decomposition method (Yoshiyama 1996), the iterative method (Rajeev 1998), the regularization method (Detlef 1999; Detlef 1999; Detlef 2000) and the hybrid regularization method (Böckmann 2001; Böckmann 2001).

Within the frame of the EARLINET project, the participants have the opportunity to use the program developed in the Institute of Mathematic of the University of Postdam (IMP) based on the hybrid regularization method. The IMP mathematical model, which relates the optical and the physical particle parameters, consists of a system of two Fredholm integral equations of the first kind for the backscatter and extinction coefficients given by (EQ 2.34). This set of equation is reformulated into a more specific and more solid form

$$\begin{aligned} \mathbf{a}_p^{ex} &= \int_{R_{\min}}^{R_{\max}} \frac{3}{4r} Q_{ex} v(r) dr = \int_{R_{\min}}^{R_{\max}} K_p^{v,ext} v(r) dr \\ \mathbf{b}_p^p &= \int_{R_{\min}}^{R_{\max}} \frac{3}{4r} Q_p v(r) dr = \int_{R_{\min}}^{R_{\max}} K_p^{p,ext} v(r) dr \end{aligned} \quad (\text{EQ 2.56})$$

where $v(r)$ is the volume concentration distribution [$\mu\text{m}^3\text{cm}^{-3}\mu\text{m}^{-1}$], K is the volume extinction (or backscatter) kernel and R_{\min} , R_{\max} are the minimum and maximum radius of the distribution. To choose ranges for the radius, it must be observed that only particles with radii of the order of the magnitude of the measurement wavelengths (355 to 1064nm) possess particle-size-depend scattering efficiencies and therefore are suitable for inversion. Thus the range of particle size distribution is limited.

A hybrid regularization method is applied that uses variable projection dimension and variable B-spline order as well as truncated singular-value decomposition (TSVD) simultaneously for that ill-posed inversion (Böckmann 2001; Böckmann 2001). This method can be used with a known or an unknown refractive index. In the latter case, by using a refractive index grid between suitable limits, this method is performed for each grid point and the solution or set of solutions is the one which minimizes the errors between the input extinction and backscatter coefficients and the calculated coefficients using Mie theory. The minimizations are based on the absolute error, the relative error and a combination of the relative and absolute error. Thus three solutions are given per inversion.

The one key parameter that best describes the radiative properties of a given size distribution is the surface-area weighed effective radius r_e which is defined as

$$r_e(z) = \frac{\int n(r, z) r^3 dr}{\int n(r, z) r^2 dr} \quad (\text{EQ 2.57})$$

where r_e [μm] is the effective radius at altitude z and $n(r, z)$ [$\text{cm}^{-3}\mu\text{m}^{-1}$] is the aerosol number concentration distribution at altitude z . The total surface-area concentration a_t [$\mu\text{m}^2\text{cm}^{-3}$] the total volume concentration v_t [$\mu\text{m}^3\text{cm}^{-3}$], and the number concentration of particles [cm^{-3}] are given, respectively by

$$\begin{aligned} a_t &= 4\mathbf{p} \int n(r) r^2 dr \\ v_t &= \frac{4\mathbf{p}}{3} \int n(r) r^3 dr \\ n_t &= \int n(r) dr \end{aligned} \quad (\text{EQ 2.58})$$

This method can handle the inversion with only one extinction and three backscatter coefficients up to 10% of noise. In general, it was found that inversion errors increase with the reduction of measurement data and that higher accuracy of the reduced data set is required for a successful inversion (Böckmann 2001). Simulations with the IMP algorithm showed that for noiseless data the mean and integral parameters of the particle size distribution, (effective radius, total surface-area concentration, total volume concentration and number concentration of particles), except the number concentration, can be limited to 7% error in the case of three backscatter and two extinction coefficients.

2.14. Conclusion

This chapter describes the lidar equations involved in the multiple-wavelength lidar system. A special attention have been carried out to the Rayleigh and Mie scattering theories. Those theories link the aerosol size distribution and the refractive index to the measured parameters by lidar. The depolarization ratio is a good indicator of the shape of the aerosols and allows the assumption of spherical aerosols in the case of low ratios.

The retrieval of the aerosol microphysical aerosol parameters is performed by the IMP algorithm. For that, at least one extinction coefficient and three backscatter coefficients are needed. As it will be explain in the next chapter, this is the minimal configuration of this lidar system. Thus, the mean and integral parameters of the particle size distribution can be determinated with an uncertainty on the aerosol parameters smaller than 10%. The advantages of this algorithms are no *a priori* information of the shape of the size distribution and refractive index.

2.15. References

- Ansmann, A., M. Riebesell, et al. (1992). "Combined Raman Elastic-Backscatter Lidar for Vertical Profiling of Moisture, Aerosol Extinction, Backscatter, and Lidar Ratio." Applied Physics B-Photophysics and Laser Chemistry **55**(1): 18-28.
- Ansmann, A., M. Riebesell, et al. (1990). "Measurement of Atmospheric Aerosol Extinction Profiles with a Raman Lidar." Optics Letters **15**(13): 746-748.
- Barrell, H. and J. E. Sears (1939). "The refraction and Dispersion of Air for the Visible Spectrum." Phil. Trans. Roy. Soc. London **A238**: 1-64.
- Bates, D. R. (1984). "Rayleigh scattering by air." Planetary Space Science **32**: 785-790.
- Bey, I., and al. (2001). "Global modeling of tropospheric chemistry with assimilated meteorology: Model description and evaluation." In press, J. Geophys. Res.
- Böckmann, C. (2001). "Hybrid regularization method for the ill-posed inversion of multiwavelength lidar data in the retrieval of aerosol size distribution." Applied Optics **40**(9): 1329-1342.
- Böckmann, C., and Wauer, J. (2001). "Algorithms for the inversion of light scattering data from uniform and non-uniform particles." Aerosol Science **32**: 49-61.
- Bodhaine, B. A. (1999). "On Rayleigh Optical Depth Calculations." American Meteorological Society **16**: 1854-1861.
- Bohren, C. F., and Huffman, D. R. (1983). Absorption and scattering of light by small particles. New-York, Wiley.
- Charlson, R. J., and Heintzenberg, J. (Eds.) (1995). Aerosol forcing of climate. New-York, John Wiley & Sons, Ltd.
- Cooney, J. (1968). "Measurements of the Raman component of Laser Atmospheric backscatter." Applied Physics Letters **12**(2): 40-42.
- Cooney, J. (1969). "Measurements Separating the Gaseous and Aerosol Components of Laser Atmospheric Backscatter." Nature **224**: 1098-1099.
- CRC (1997). Handbook of chemistry and Physics, CRC Press.
- Deepak, A., and Gerber, H. E. (Eds) (1983). Report on the experts meeting on aerosols and their climatic effects. Williamsburg, VA, WMO.
- Detlef, M., Wagner, F., Wandiger, U., Ansmann, A., Wendisch, M., Althausen, D., and Hoyningen-Huene, W. (2000). "Microphysical particle parameters from extinction and backscatter lidar data by inversion with regularization: experiment." Applied Optics **39**(12): 1879-1892.
- Detlef, M., Wandiger, U., and Ansmann, A. (1999). "Microphysical particle parameters from extinction and backscatter lidar data by inversion with regularization: simulation." Applied Optics **38**(12): 2358-2368.

- Detlef, M., Wandiger, U., and Ansmann, A. (1999). "Microphysical particle parameters from extinction and backscatter lidar data by inversion with regularization: theory." Applied Optics **38**(12): 2346-2357.
- DLR (1998). UV/Vis Atmospheric Constituents, Atmos User Center.
- Edlén, B. (1953). "The Dispersion of Standard Air." Journal of the Optical Society of America **43**: 339-344.
- Edlén, B. (1966). "The Refractive Index of Air." Metrologia **2**(2): 71-80.
- Esposito, F., Pavese, G., Santoro, M., Serio, C., and Cuomo, V. (1998). "Ozone correction to the aerosol optical depth in the Chappuis band." Journal of Aerosol Science **29**(10): 1219-1124.
- Fenner, W. R., H. A. Haytt, et al. (1973). "Raman cross sections of simple gases." Journal of the Optical Society of America **63**(1): 73-77.
- Harrison, R. M., and van Grieken, R. E. (1998). Atmospheric particles. New-York, John Wiley & Sons. Ltd.
- Hinkley, E. D. (1976). Laser Monitoring of the Atmosphere, Springer-Verlag.
- HITRAN (1996).
- Inaba, H. and T. Kobayashi (1969). "Laser-Raman Radar for Chemical Analysis of Polluted Air." Nature **224**: 170-172.
- Inaba, H. and T. Kobayashi (1972). "Laser-Raman Radar -Laser-Raman scattering methods for remote detection and analysis of atmospheric pollution-." Opto-Electronics **4**: 101-123.
- Klett, J. D. (1981). "Stable analytical inversion solution for processing lidar returns." Applied Optics **20**: 211-220.
- Klett, J. D. (1985). "Lidar inversion with variable backscatter/extinction ratios." Applied Optics **24**(11): 1638-1643.
- Krichbaumer, W. and C. Werner (1994). "Current state of-the-art of LIDAR inversion methods for atmospheres of arbitrary optical density." Applied Physics B-Lasers and Optics **59**: 517-523.
- Lazzarotto, B. (2000). Ozone and water vapor measurements by Raman lidar in the planetary boundary layer. Génie rural. Lausanne, EPFL: 200.
- Leonard, D. A. (1967). "Observation of Raman Scattering from the Atmosphere using a Pulsed Nitrogen Ultraviolet Laser." Nature **216**: 142-143.
- Liu, H., Jacob, D. J., Bey, I., and Yantosca, R.M. (2001). "Constraints from 210Pb and 7Be on wet deposition and transport in a global three-dimensional chemical tracer model driven by assimilated meteorological fields." Journal of Geophysical Research-Atmospheres **106**: 12109-12128.
- Mc Cartney, E. J. (1976). Optics of the Atmosphere, Wiley.
- McNeil, W. R., and Carswell, A. I. (1975). "Lidar polarization studies of the troposphere." Applied Optics **14**(9): 2158-2168.

- Measures, R. M. (1992). Laser Remote Sensing. Fundamentals and Applications. New-York, Krieger.
- Melfi, S. H. (1972). "Remote Measurements of the Atmosphere Using Raman Scattering." Applied Optics **11**(7): 1605-1610.
- Melfi, S. H., J. D. Lawrence, et al. (1969). "Observation of Raman Scattering by Water Vapor in the Atmosphere." Applied Physics Letters **15**(9): 295-297.
- Melfi, S. H. and D. Whiteman (1985). "Observation of Lower-Atmospheric Moisture Structure and Its Evolution Using a Raman Lidar." Bulletin of the American Meteorological Society **66**(10): 1288-1292.
- Owens, J. C. (1967). "Optical Refractive Index of Air : Dependence on Pressure, Temperature and Composition." Applied Optics **6**(1): 51-59.
- Pal, S. R., and Carswell, A. I. (1973). "Polarization properties of lidar backscattering from clouds." Applied Optics **12**(7): 1530-1535.
- Pal, S. R., and Carswell, A. I. (1978). "Polarization properties of lidar scattering from clouds at 347nm and 694nm." Applied Optics **17**(15): 2321-2328.
- Peck, E. R. and K. Reeder (1972). "Dispersion of Air." Journal of the Optical Society of America **62**: 958-962.
- Penndorf, R. (1957). "Tables of the refractive index for standard air and the Rayleigh scattering coefficient for the spectral region between 0.2 and 20.0 μm and their application to atmospheric optics." Journal of the Optical Society of America **47**: 176-182.
- Rajeev, K., and Parameswaran, k. (1998). "Iterative method for the inversion of multiwavelength lidar signals to determine aerosol size distribution." Applied Optics **37**(21): 4690-4700.
- Rothermel J., B., D. A., Vaughan, J.M., and Post, M. J. (1989). "Evidence of a Tropospheric Aerosol Backscatter Background Mode." Applied Optics **28**(6): 1040-1042.
- Sasano, Y., and Browell, E., V. (1989). "Light scattering characteristics of various aerosol types derived from multiple wavelength lidar observations." Applied Optics **28**(9): 1670-1679.
- Sasano, Y., Browell, E., V., and Ismail S. (1985). "Error caused by using a constant extinction/backscattering ratio in the lidar solution." Applied Optics **24**(22): 3929-3932.
- Sassen, K. (1994). "Advances in polarization diversity lidar for cloud remote sensing." Proceedings of the Ieee **82**(12): 1907-1914.
- Seinfeld, J. H. and S. N. Pandis (1998). Atmospheric Chemistry and Physics, Wiley Interscience.
- Sherlock, V. (1998). Evaluation de la technique du lidar Raman en vue de l'étude climatologique de la vapeur d'eau dans la moyenne et haute stroposphère, Université Paris VI.
- Warneck, P. (1988). Chemistry of the Natural Atmosphere, Academic Press.

- Whiteman, D. N., S. H. Melfi, et al. (1992). "Raman Lidar System for the Measurement of Water-Vapor and Aerosols in the Earths Atmosphere." Applied Optics **31**(16): 3068-3082.
- Wright, M. L., Proctor, E. K., Gasiorek, E., Liston, E. M. (1975). A preliminary study of air pollution measurement by active remote-sensing techniques, Final report, NASA contract NAS1-11657.
- Yoshiyama, H., Ohi, A., and Ohta, K. (1996). "Derivation of the aerosol size distribution from a bistatic system of a multiwavelength laser with the singular value decomposition method." Applied Optics **35**(15): 2642-2648.

This chapter describes the experimental setup of the lidar system. First, a general description is given, starting from the transmitter to the data acquisition system. Second, the simulation of the receivers is presented in more details. For this purpose, a ray tracing software was used to calculate the characteristics of the receiving optics and to test the possible influence of the decenter and defocalisation effects on the detectors. Finally some tests of the Hamamatsu photosensor modules used in this lidar system are described. Those tests include measurements of the photomultiplier tube uniformity, linearity and after pulse effect. As a conclusion, the future upgrade of the lidar system are discussed.

A complete description of the components of the lidar system and their characteristics is given in “Lidar specification table”, p 194.

3.1. System description

The Figure 3-1 shows the general layout of the multiplewavelength lidar system. The main technical characteristics are presented in “Lidar specification table”, p 194.

The transmitter is a pulsed Nd:YAG laser, equipped with two non-linear crystals (BBO) for second and third harmonic generation. The pulse repetition rate of the laser can be tuned continuously up to 100Hz. At the output of the third harmonic generator the three wavelengths (1064, 532 and 355nm) are separated by two beamsplitters and are expanded by a factor of five before being transmitted into the atmosphere. This is done by three beamexpanders optimized for each wavelength and the resulting divergence is 0.14mrad for each emitted wavelength in the atmosphere. The expanded beams are directed into the atmosphere by dielectric mirrors mounted on piezoelectric controlled stages. In order to control precisely the polarization state of the transmitted 532nm radiation, an air-spaced Glan-Thompson prism is inserted into the 532nm optical path.

After atmospheric interactions, the elastic backscattered radiations at 355, 532 parallel, 532 perpendicular, 1064nm, and the Raman shifted backscattered signals at 387nm (nitrogen shift from 355nm), 408nm (water vapor shift from 355nm) and 607nm (nitrogen shift from 532nm) are collected by two telescopes in a Newtonian and a Cassegrain configurations. The telescopes are dedicated to tropospheric and stratospheric-mesospheric measurements, respectively. The separations between the transmitter axes and the receiver axes of the Newtonian and the Cassegrain telescope are 300 and 1500mm, respectively. This dual receiver configuration is employed in order to reduce the dynamic range of the signals, i.e. to improve the signal to noise ratio of the signals.

The Newtonian telescope was bought from the firm Vixen (type R200SS). It has a 20cm paraboloid prime mirror and its aperture ratio has a value of $f/4$ (0.8m equivalent focal length). This telescope is mounted in a vertical position and can be tilted with an angle of 5° off the zenith for a coarse alignment of the receiver. Its fine alignment uses the piezoelectric controlled stages of the transmitter. The Cassegrain telescope was formerly used for star photometry measurements and from time to time, is still used in a Coudé configuration for FTIR measurements. This telescope has a paraboloidal primary mirror with a diameter of 76cm and an hyperboloid secondary mirror. This combination gives a aperture ratio of $f/15$ (11.4m equivalent focal length). Its mounting is provided with motorized focusing adjustment. The telescope is mounted in an equatorial position and both polar axis and declination axis are controlled by slow motion drives which are used for the alignment of the system.

The two filter polychromators used for the spectral separation of the optical signals are mounted directly to the focal plane of the telescopes. They are build up around a set of beamsplitters and custom design thin band pass filters with high out-of-band rejection. The polychromators are shown in more details latter in this chapter. Due to the low wintry temperatures they are thermocontrolled to keep up with the operating range of the optics and to avoid condensation. The backscattered signals at 355, 387, 408, 532 and 607nm are detected by photomultiplier tubes. They have fast response, high gain and high enough quantum efficiency and relatively low noise levels. However, they are essentially unavailable at wavelength beyond about 1000nm. Avalanche photodiodes are used for detection of the signal at 1064nm.

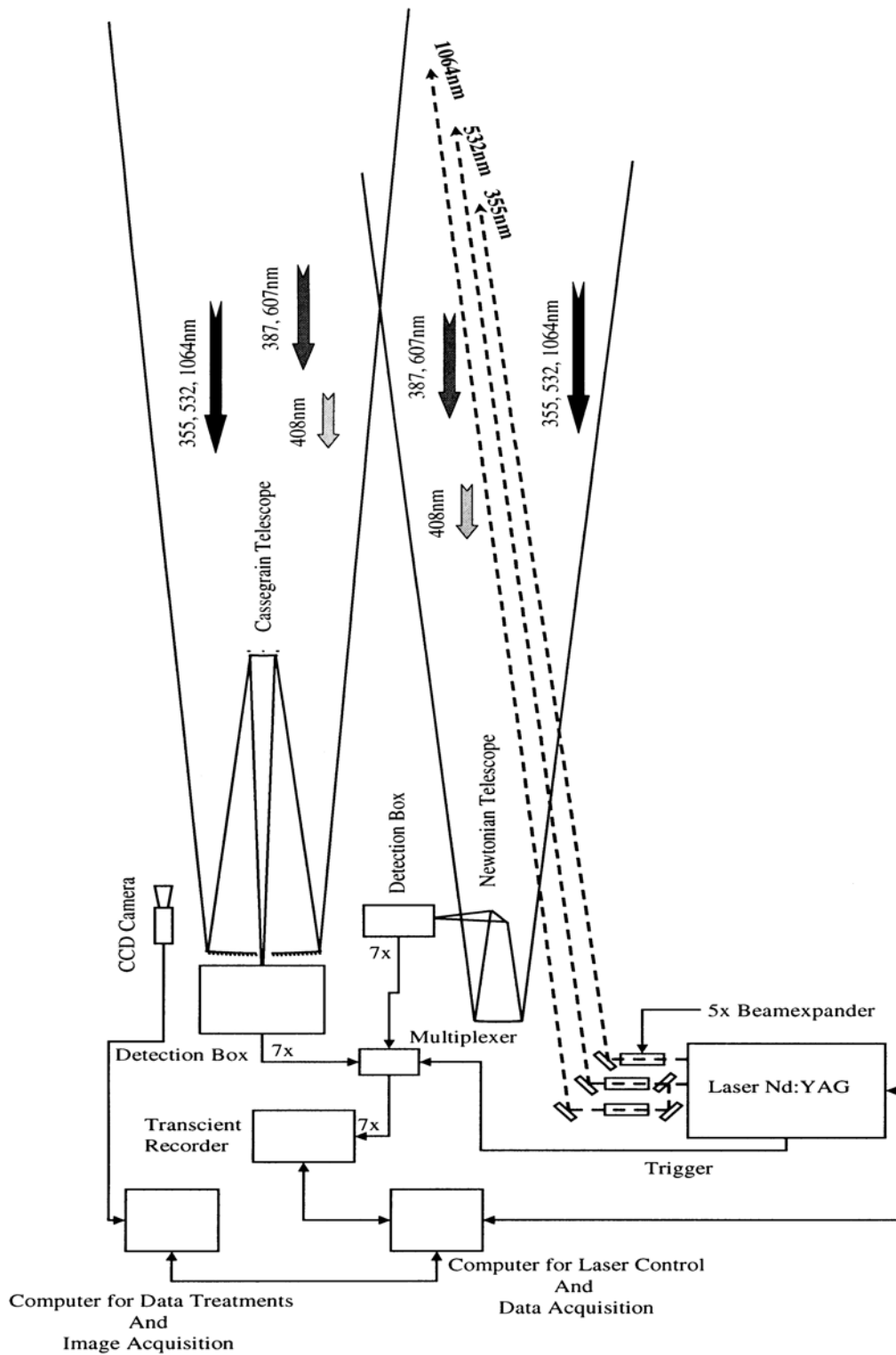


FIGURE 3-1. The experimental layout of lidar system installed at the Jungfraujoch.

The signals from the two receivers are alternatively digitized by transient recorders. The data acquisition system, build by Licel GbR (Berlin, Germany), is suited to fast repetitive signals which are recorded simultaneously in analog and photoncounting modes. By using this combination of analog and photon counting detection, the dynamic range of the signal is extended.

For analog mode detection, the signals are amplified according to the input range selected, and signals below a frequency of 10MHz are passing an anti-alias filter and digitized by a 12Bit-20MHz analog to digital converter. Each signal is written to a fast memory which is readout after each shot and added to the summed signal in a 24Bit wide RAM (up to 4096 shots). Depending on the trigger input, signal is added to one of the two RAM, which allows acquisitions of two channels if these signals can be measured sequentially. At the same time the signal part in the high frequency domain above 10MHz is amplified and a 250MHz fast discriminator detects single photon events above a selected threshold voltage. Two different settings of the preamplifier can be controlled by software together with 64 different discriminator levels. Again the signal is written to a fast memory and added to the 16Bit wide summation RAM after each acquisition cycle.

Seven transient recorders are controlled via a NI-DAQ (National Instruments) card installed in a PC and running under a LabView (National Instruments) program. The recorders are triggered synchronously with the Q-switch of the laser. A fast multichannel analog multiplexer is used to switch alternatively the signals from the two receivers into the transient recorders.

3.2. Ray tracing analysis

The first part of the ray tracing analysis of the receiver configuration is dedicated to the overlap function that provides the theoretical ranges of measurement of the two telescopes and thus a series of model runs have been performed in order to optimize the receiver optical configuration. They are described below.

3.2.1. Overlap function

The theoretical development of the overlap function also called the geometrical probability factor is given in (Measures 1992). This factor depends on the telescope field of view and primary diameter, the laser beam divergence and diameter in function of the altitude, and the angle and the distance between the axes of the laser beams and the receiver axis. Here are presented some results obtained by a simple model of this function. The most simple configuration is when the axis of the laser beam and the axis of the telescope are parallel, thus the inclination angle is set to zero and the field of view of the telescope is between 0.1 and 2mrad. Figure 3-2 and Figure 3-3 show the results obtained for the Newtonian and Cassegrain telescopes respectively. The X-axis gives the value of the overlap function. This value is equal to zero where the laser beam is not inside the field of view of the telescope and is equal to unity where the laser beam is completely inside the field of view of the telescope. Usually, the Fernald and the Raman algorithms are only performed where this function is equal to unity. Otherwise systematic error is induced. The Y-axis gives the altitude above the lidar system. Both figures show the inadequacy of taking the field of view (FOV) of the telescope smaller than the divergence of the laser beam (0.14mrad) because the overlap function is never equal to the unity. The ideal

lidar is a lidar with the smallest possible field of view of the telescope to reduce to the minimum the sky background with no inclination angle to avoid the laser beam to go out of the field of view of the telescope at high altitude.

Overlap Function vs. Field of View of the Newtonian Telescope

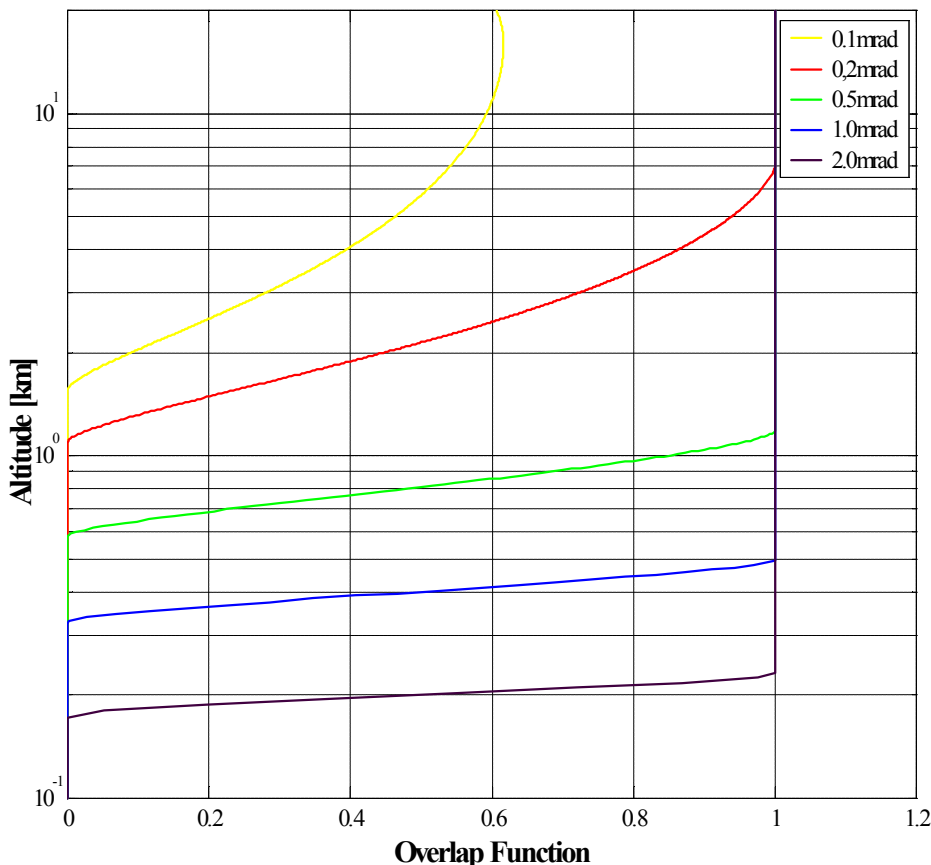


FIGURE 3-2. Overlap function according to the field of view of the Newtonian telescope for a laser beam divergence of 0.14mrad and no inclination angle between the axis of the laser beam and the axis of the telescope.

Measurements with the Newtonian telescope has to be done as low as possible, ideally, less than 100 meter above the station and up to the tropopause. FOV of 0.2, 0.5, 1 and 2mrad provide a minimum altitude of 7000, 1200, 500 and 230m (see Figure 3-2). One possibility to reduce the minimum altitude is to tilt the laser beam towards the telescope axis. The inclination angle can be set to a maximum value equal to half of the difference between the divergence of the laser beam (0.14mrad) and the field of view (FOV) of the telescope. For example with a FOV of 2mrad, the maximum angle is 0.9mrad and thus insures that the laser does not go out of the field of view of the telescope at bigger distances. Unfortunately, the minimum altitude with those parameters is still high. To reach the desired range, another possible way is to increase the FOV to a value of 3mrad and to work with an inclination angle of 1.4mrad. Thus the full overlap is reached under 100m.

Overlap Function vs. Field of View of the Cassegrain Telescope

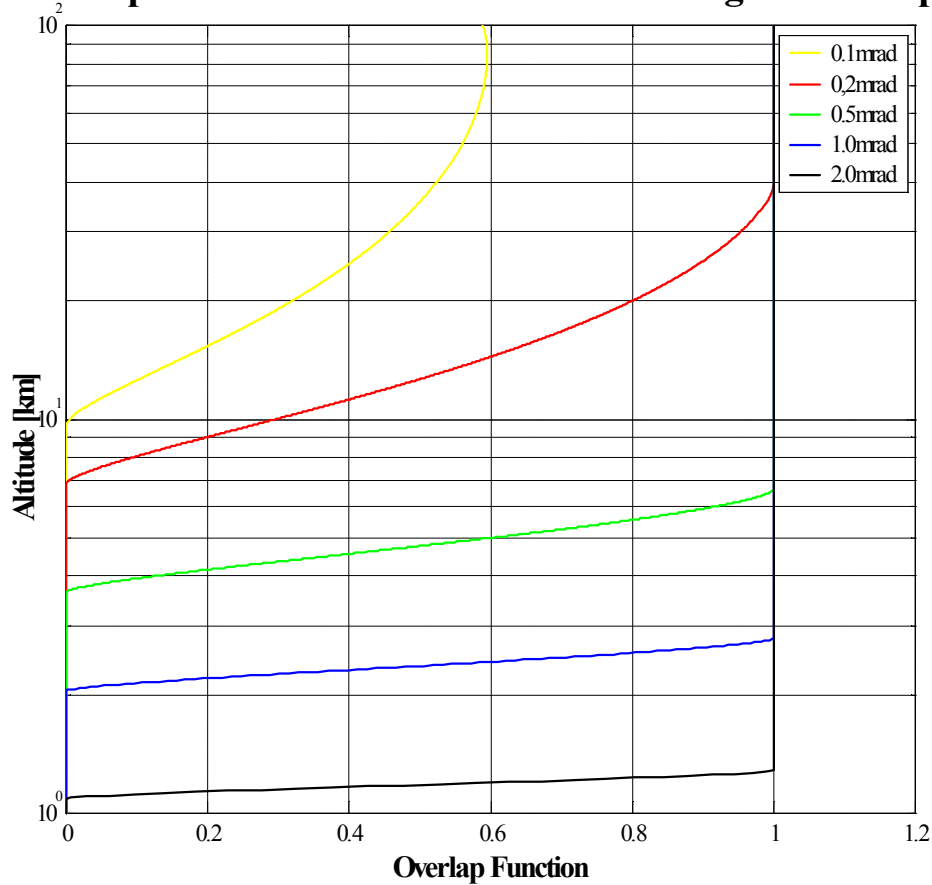


FIGURE 3-3. Overlap function according to the field of view of the Cassegrain telescope for a laser beam divergence of 0.14mrad and no inclination angle between the axis of the laser beam and the axis of the telescope.

The Cassegrain telescope is dedicated to stratospheric measurements and its operating range starts around 7km above the lidar system. The configuration with parallel axes and a 0.5mrad FOV provides a minimum altitude of 6500m that fulfils those conditions. This minimum can be reduced to 4100m if an inclination angle of 0.1mrad is set.

Those studies have shown that the Cassegrain telescope has no limitation inside its operating range while the Newtonian telescope configuration presents some restrictions for the very low altitude measurements.

3.2.2. Simulation of the detection part

The position of the input optics and the influence of the decenter and the defocusing effects due to the geometrical configuration of the lidar system (see Figure 10-3, p 201) are determined by using a ray tracing software (Optics Software for Layout & Optimization, OSLO5, Sinclair Optics).

The Hamamatsu PMT holders are designed to focus a 10mm parallel beam on the active area of the detector and this size is the key parameter for setting the position of the collimating lens. The other detectors have an effective cathode size of 45mm and do not pose restriction on the beam size and the same is valid for the effective aperture of the 45° beamsplitters of which value is 35mm, and for the filters of which diameter is 25mm.

Figure 10-4, p 202 in annex, shows the spot size of the laser beam versus the altitude for an transmitted beam with a diameter of 25mm and a divergence of 0.14mrad. Those sizes are used as object size in OSLO and the decenter to the axis of the telescope is given by the distance between the axis of the telescope and the center of the laser beam. This distance is taken height-constant (i.e. no inclination angle) in the following examples and its value is 300 and 1500mm for the Newtonian and Cassegrain telescope respectively.

3.2.2.a. Newtonian receiver

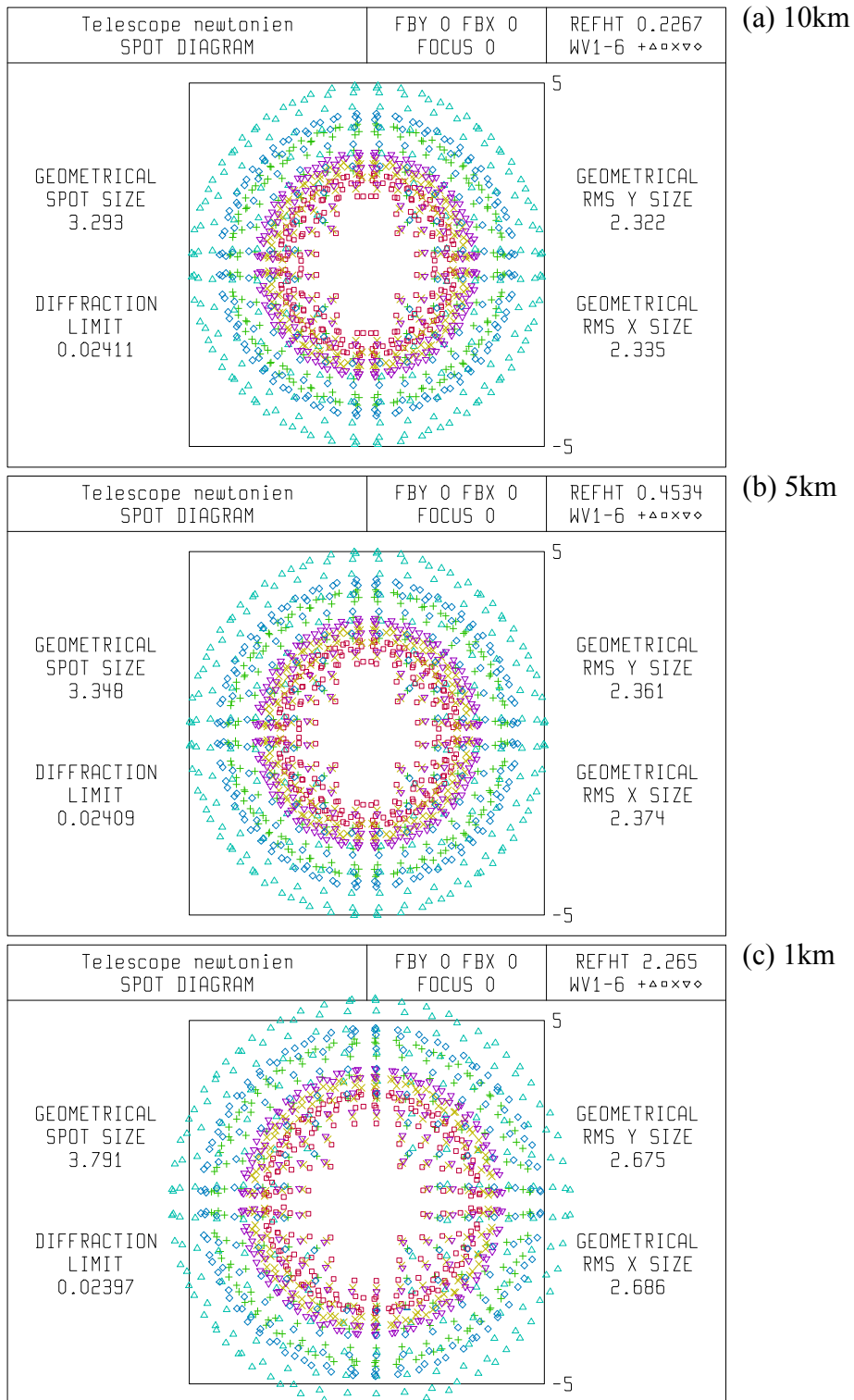
The light coming from the Newtonian telescope is collimated by a simple plano-convex lens. The diameter of the collimated beam is 10mm. The lens has a diameter of 25.4mm (1 inch) and an effective focal length (EFL) of 40mm. The characteristics of the telescope are known and its modelisation allows to determinate the exact position of the focal plane with regard to the axis of the telescope and an object at the infinity. The first step of the modelisation consists of an autofocus algorithm for determining the best spot size along the optical axis without the lens, to fix the lens at the right position and then to observe the image of the initial object at distances corresponding to the different positions of the detectors because the optical length is not the same for all the wavelengths. The second step is to see the defocalisation and the decenter effect versus the altitude. Finally, the position of this lens is changed in order to keep the spot size of the laser beam within a diameter less than 10mm for each altitude.

The general concept of spot diagram analysis involves tracing enough rays so that the data for any particular ray can be treated statistically. In the study of random variables, a much used concept is that of moments, or average values. Each ray is considered to carry a weight w_i proportional to the area of its cell in the aperture of the system and has transverse aberrations (DX_i , DY_i) in the plane of the image. Then the position of the first moment, relative to the point of intersection of the reference ray with the image surface is

$$\langle x \rangle = \frac{\sum w_i DX_i}{\sum w_i} \quad \langle y \rangle = \frac{\sum w_i DY_i}{\sum w_i}$$

(EQ 3.1)

The root-mean-square (RMS) spot size in x and y are the square root of the variances of the two terms in (EQ 3.1) and are labeled as geometrical RMS x size and geometrical RMS y size on the diagram. Finally, the radial RMS spot size is the square root of the sum of the two variances.



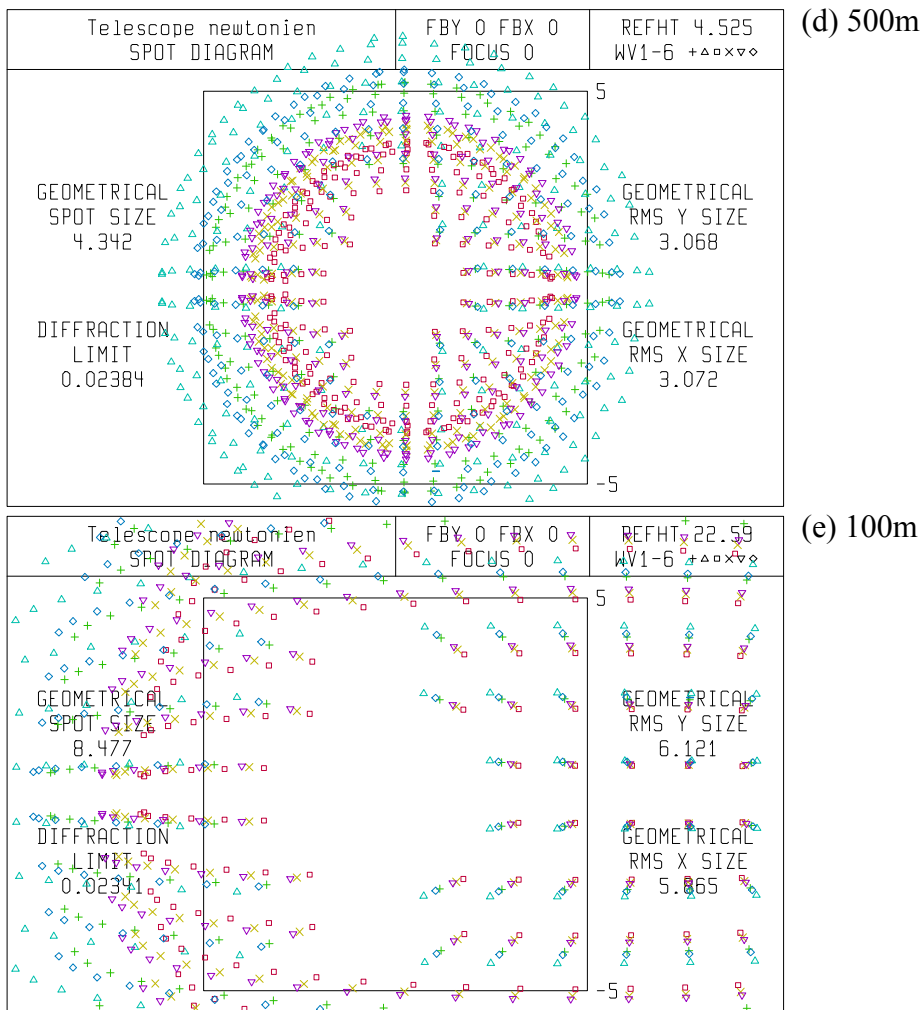


FIGURE 3-4. Spot diagram of the laser beam in the 532nm filter plane from different altitude (a) 10km, (b) 5km, (c) 1km, (d) 500m and (e) 100m. The receiver optics is optimized for object at an altitude of 10km above the system.

Figure 3-4 shows the spot diagrams of the laser beam collected by the Newtonian telescope at the 532nm filter plane (corresponding to F4 in Figure 3-7) for different altitudes. Those altitudes are 10km, 5km, 1k, 500m and 100m for the Figure 3-4 (a), (b), (c), (d) and (e), respectively. Each symbol represents the intersection of one ray with the image surface and the plus (+), the triangle, the square, the cross (x), the inverse triangle and the diamond (◇) symbols correspond to 523, 1064, 355, 387, 408 and 607nm respectively. Also presented are the geometrical RMS sizes of the spot diagram and the diffraction limit of the optical system. This limit is the radius of the equivalent Airy disk for the system. The big black square labeled from -5 to +5 gives the scale of the spot size in millimeter and its center is the optical axis of the system. Any ray outside of this square is not detected by the photosensor module. The position of the input lens (L1) is set to optimized the image from 10km (Figure 3-4(a)). Unfortunately, at low altitude, the radius of the image is larger than 10mm and thus some parts of the signal are lost (Figure 3-4(c), (d) and (e)).

Figure 3-5 presents the spot diagrams for another position of the input lens. This position is chosen in order to optimized the image from 100m above the lidar system as it is shown in Figure 3-5(b). But again this configuration is not optimized for all the altitudes, in particular above 5km (Figure 3-5(a)).

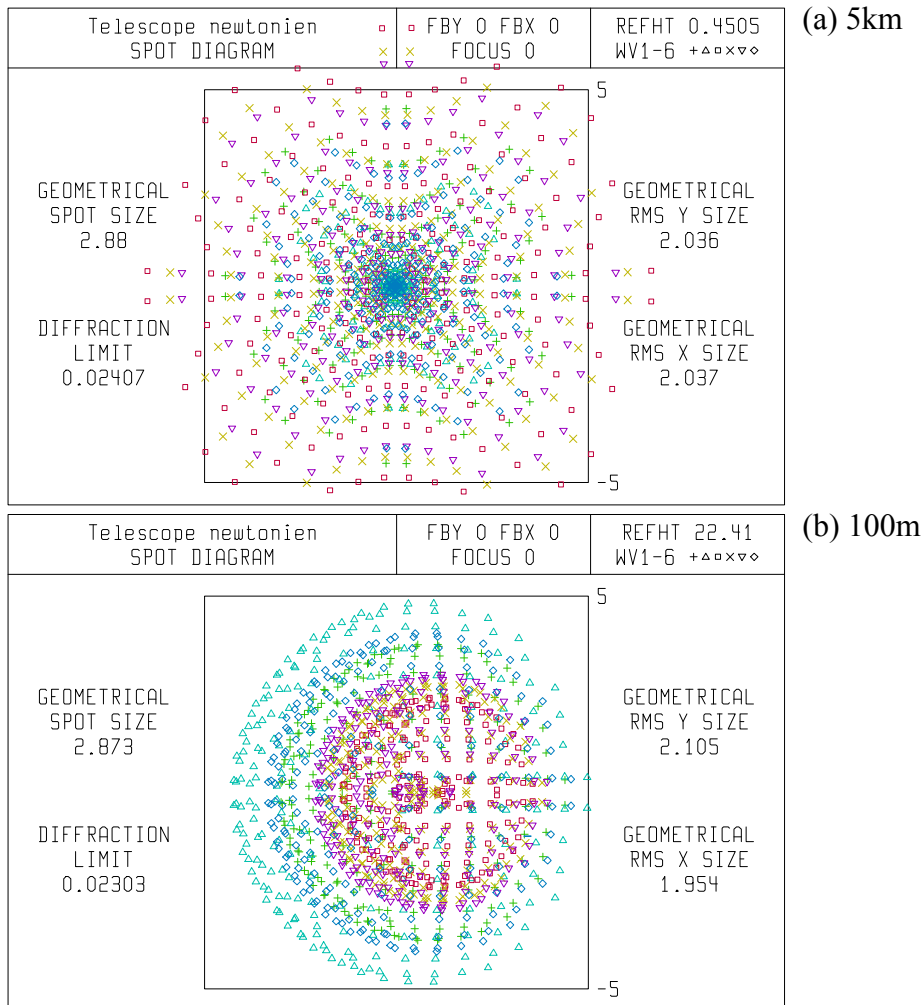
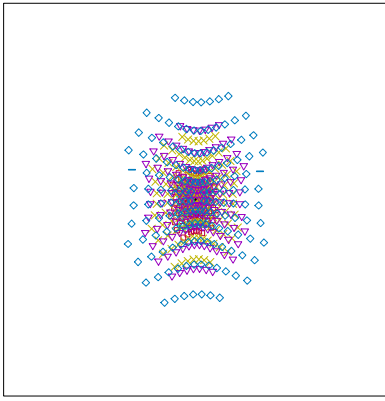
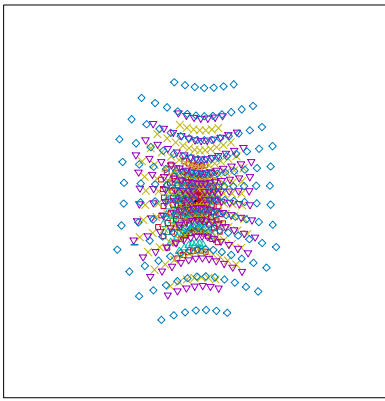
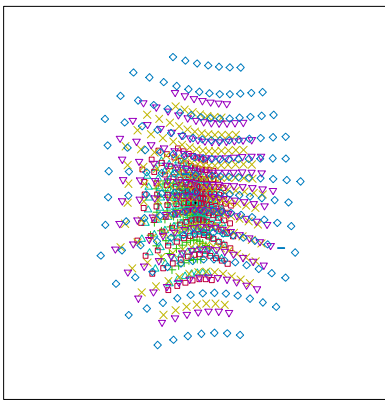


FIGURE 3-5. Spot diagram of the laser beam in the 532nm filter plane from different altitude (a) 5km, (b) 100m. The receiver optics is optimized for object at an altitude of 100m above the system.

In relation to the position of the previous case, this second position of the lens is further of the focal point of the telescope in order to reduce the defocalisation effect. Those studies demonstrate the impossibility of measuring simultaneously the lower part (100 to 5000m) and the upper part (5000 to 10000m) of the operating range of the Newtonian telescope. Depending of the position of the lens, either one part or the other is preferred.

3.2. Ray tracing analysis

3.2.2.b. Cassegrain receiver

| | | | | |
|------------------------------------|---|------------------------|-----------------------------|-------------------------------------|
| telescope SPOT DIAGRAM | | FBY 0 FBX 0 FOCUS 0 | REFHT 164.2 WV1-6 +▲□×▽◇ | (a) 50km |
| GEOMETRICAL SPOT SIZE 0.9197 |  | | 5 | GEOMETRICAL RMS Y SIZE 0.7628 |
| DIFFRACTION LIMIT 0.0158 | | | -5 | GEOMETRICAL RMS X SIZE 0.5137 |
| telescope SPOT DIAGRAM | | FBY 0 FBX 0 FOCUS 0 | REFHT 162.9 WV1-6 +▲□×▽◇ | (b) 20km |
| GEOMETRICAL SPOT SIZE 1.145 |  | | 5 | GEOMETRICAL RMS Y SIZE 0.9475 |
| DIFFRACTION LIMIT 0.01553 | | | -5 | GEOMETRICAL RMS X SIZE 0.6431 |
| telescope SPOT DIAGRAM | | FBY 0 FBX 0 FOCUS 0 | REFHT 160.9 WV1-6 +▲□×▽◇ | (c) 10km |
| GEOMETRICAL SPOT SIZE 1.518 |  | | 5 | GEOMETRICAL RMS Y SIZE 1.248 |
| DIFFRACTION LIMIT 0.01398 | | | -5 | GEOMETRICAL RMS X SIZE 0.8649 |

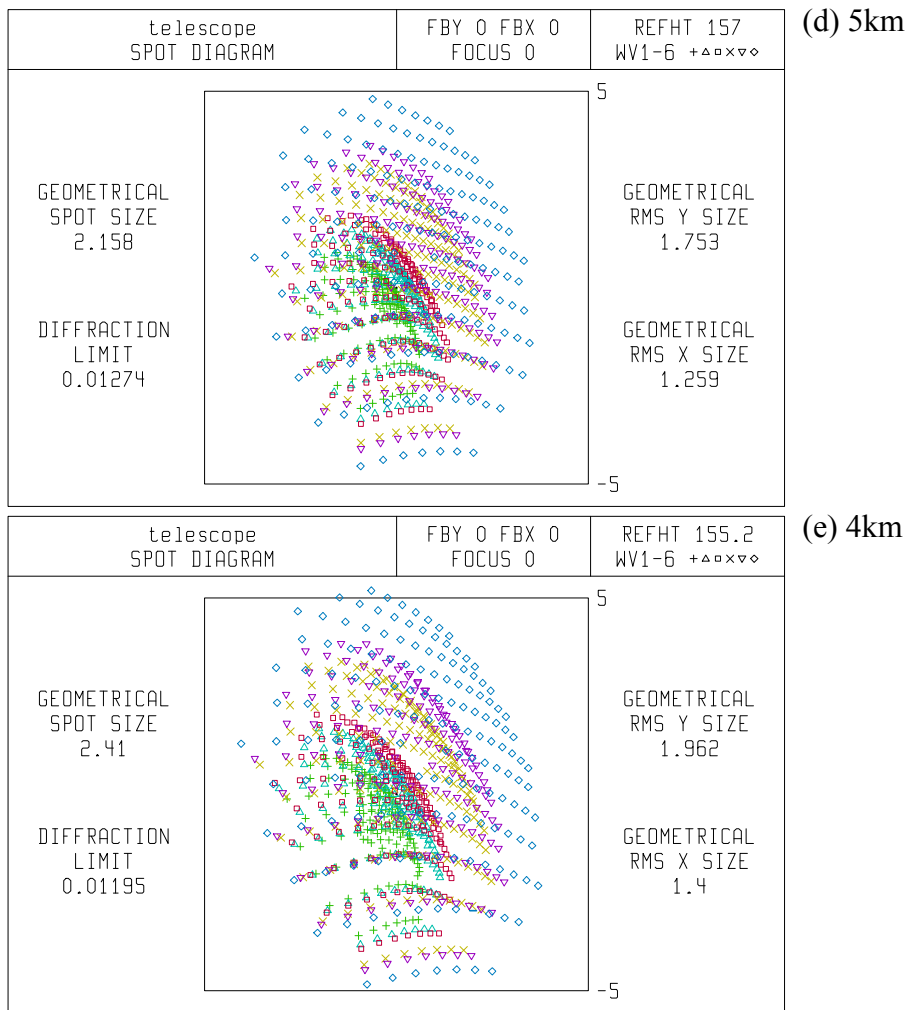


FIGURE 3-6. Spot diagram of the laser beam in the 532nm filter plane from different altitude (a) 50km, (b) 20km, (c) 10km, (d) 5km and (e) 4km. The receiver is optimized at 5km.

Contrary to the Newtonian case, the light coming from the Cassegrain telescope is collimated by using two lenses. The main limitations here are the vertical and lateral height requirements of the detection box. The maximum distance between the back of the telescope and the floor is 800mm and the maximum lateral distance to the polar axis of the telescope is around 500mm. Thus the first plano-convex lens reduces the focal length of the system and the second plano-convex lens collimates the incoming light on the beamsplitter into a 10mm diameter beam. Both lenses have a diameter of 50.8mm (2 inches) and a focal length of 62.9mm. The studies of the Cassegrain receiver follow the same formalism than the Newtonian telescope described in the previous section.

Figure 3-6 shows the spot diagrams of the laser beam collected by the Cassegrain telescope at the 532nm filter plane (corresponding to F4 in Figure 3-8) for different altitudes. The first lens L4 is fixed and only the position of the second lens can be changed in order to optimize the

image from 5km (Figure 3-6(d)). This position is suitable for all the altitudes above 5km as it is seen in Figure 3-6(a), (b), and (c) and also for the image from 1km below Figure 3-6(e). *A priori* the Cassegrain telescope is less influenced by the defocalisation effects due to a bigger focal length.

The combination of the two telescopes enables to measure over a huge operating range without any drop-out, but one has to keep in mind that those results are theoretical and can differ from the experimental one. Indeed, all the simulations were computerized with specific parameters which can not be exactly set in the reality as the inclination angle.

3.3. Filter polychromators

The Figure 3-7 and Figure 3-8 show the schematic representation of the filter polychromators dedicated to the tropospheric measurements from the Newtonian telescope and the stratospheric-mesospheric measurements from the Cassegrain telescope, respectively. Those polychromators use the same spectral separation principle which is based on beamsplitters and filters.

3.3.1. Newtonian filter polychromator

The following paragraph explains the tropospheric detection system. The light from the Newtonian telescope first encounters a diaphragm and is then collimated by the positive plano-convex lens (**L1**) to a 10mm diameter. This diaphragm close to the focal point of the telescope sets the field of view of the receiver. The set of beamsplitters (**BS1-BS5**) separate the light by wavelength into different channels: Raman scattering from nitrogen (387 and 607nm) and water vapor (408nm), and Mie-Rayleigh scattering (355, 532 and 1064nm). The beamsplitters, optimized for the different wavelengths, operate at a 45° angle of incidence and their coatings work for both parallel and perpendicular polarization. Elements after the beamsplitters consist of sets of broadband and narrowband interference filters (**F1-F6**) and neutral density filters (**ND**) which are employed to adapt the light intensity of the signals to the corresponding PMT sensitivity. On the 532nm channel, a Wollaston prism (**WP**) separates the parallel polarized backscattered signal from the perpendicular polarized one with an extinction ratio of 10^{-5} . The angle of separation of the two outgoing beams is wavelength dependent: at 532nm the value of this angle is about 12°. A 2x beam compressor (**L1+L2**) adapts the incoming beam size to the prism aperture. The Wollaston prism, the beam compressor and the two detecting PMTs are mounted on a holder that can be rotated precisely around the common optical axis of the elements. This design allows precise alignment and an easy way of calibrating the depolarization ratio by circular permutation of the «parallel» and «perpendicular» PMTs.

Those detectors, as well as the detector at 355nm are photomultiplier tubes (**PMT1**) from Hamamatsu (H6780-06 series). The positive plano-convex lens (**L1**) focuses the incoming beam on the 5mm active surface of the PMT. To improve the PMT spatial uniformity, one plano-convex lens (**L3**) and one optical diffuser (**D**) are positioned in front of the photocathode. More details are given in (Simeonov, Larchevêque et al. 1999). The detection on the Raman channel is assured by PMT from Thorn Emi, QA9829 series (**PMT2**) at 387 and 408nm, and B9202 series (**PMT3**) at 607nm. And finally, an Si-Avalanche photodiode from

EG&G, C30954/5E series (APD) is used at 1064nm.

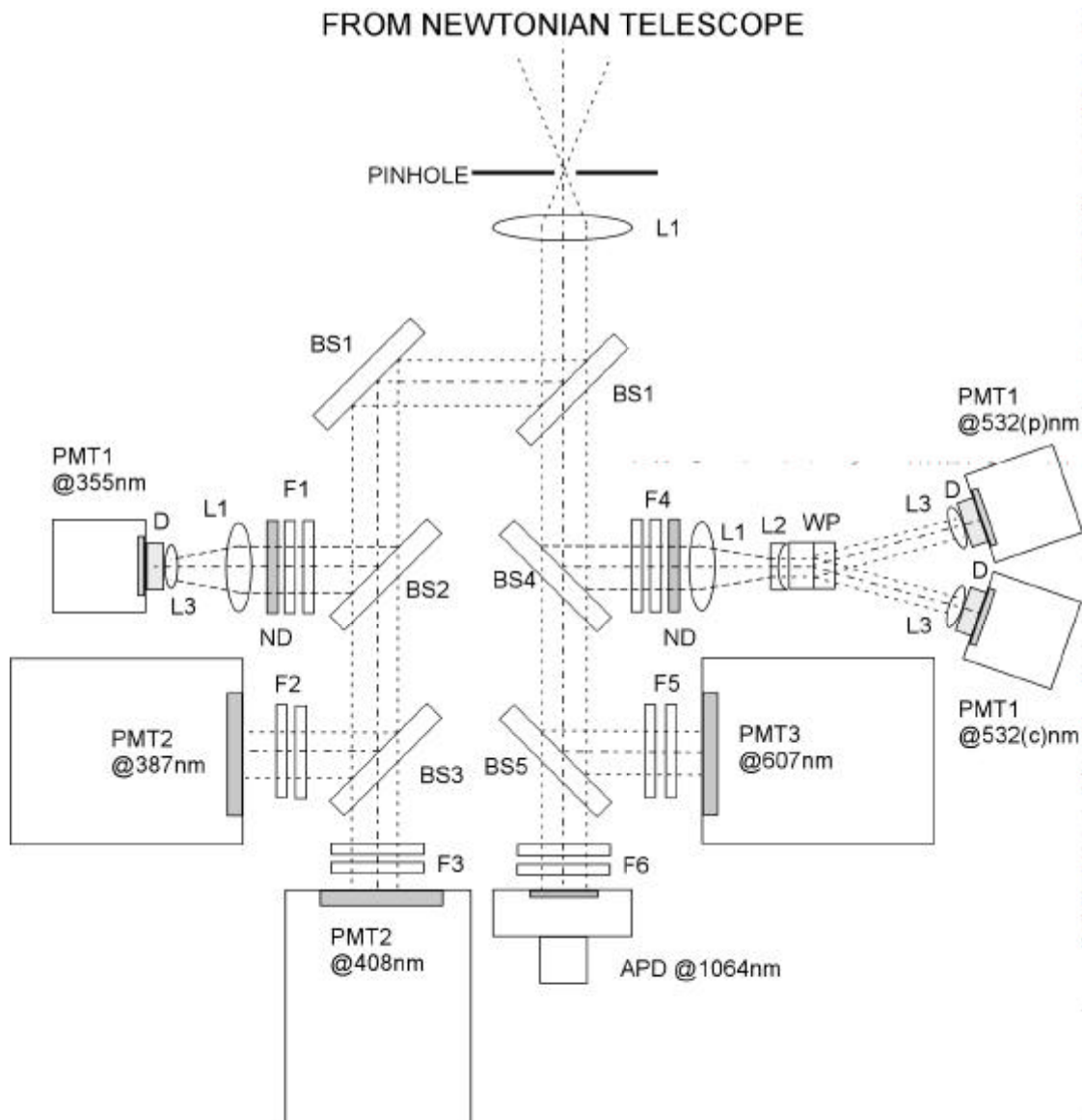


FIGURE 3-7. Schematic representation of the filter polychromator dedicated to the tropospheric measurements from the Newtonian telescope.

3.3.2. Cassegrain filter polychromator

The main differences between the Cassegrain and the Newtonian filter polychromators are in the input lenses, the choice of the detectors, instead of PMT Hamamatsu H6780-06, Thorn-Emi QA9829 series PMT (**PMT2**) are used, and especially the available room due to the different configuration of the telescope. Due to a longer effective focal length and the possibility to add a chopper close to the focal plane of the system, two positive plano-convex lenses are used to collimate the incoming light from the telescope. The rest of the optical elements is the same except that two mirrors are inserted on the 408 and 1064nm channels in order to reduce

the vertical height requirement of the polychromator.

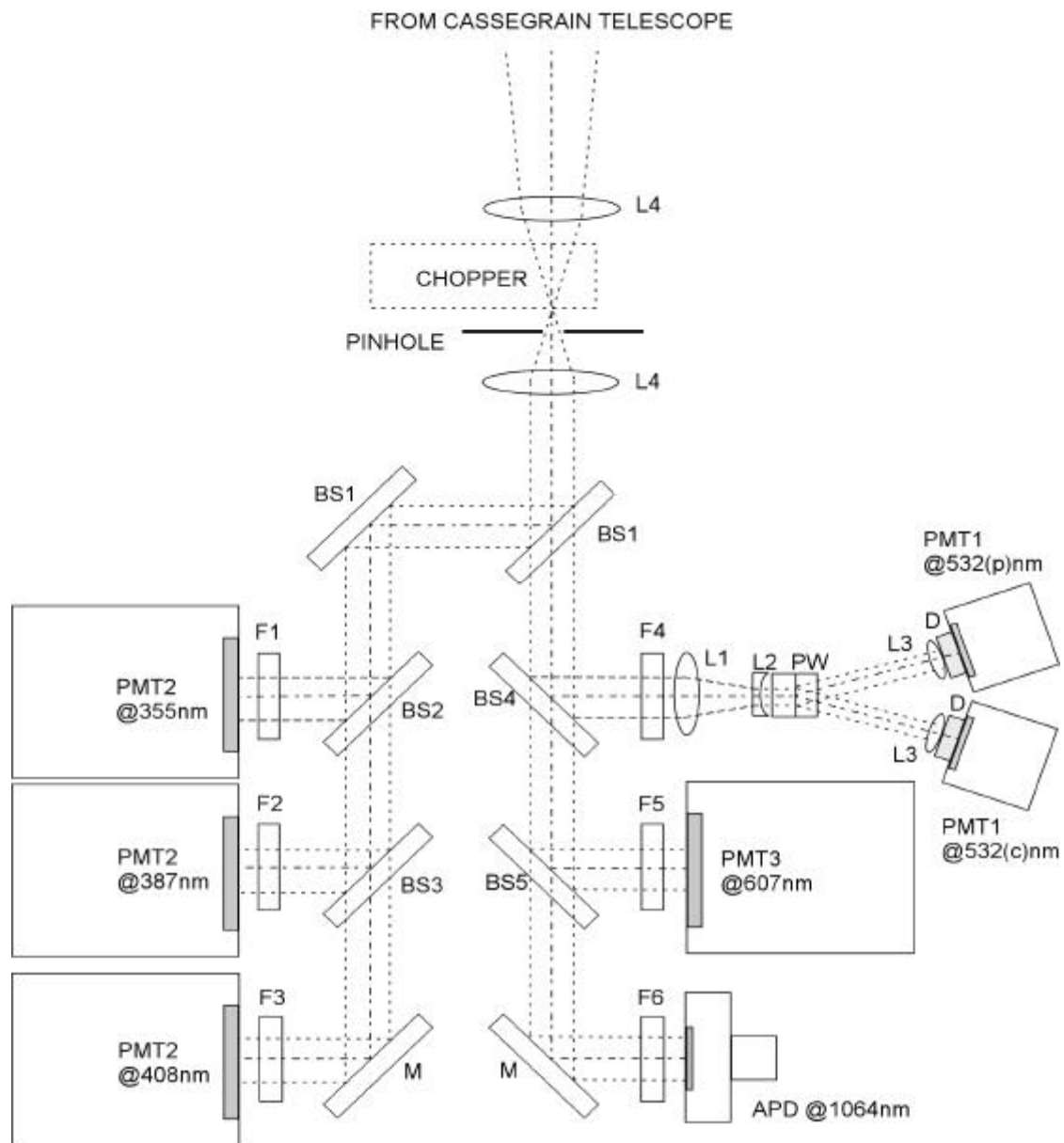


FIGURE 3-8. Schematic representation of the filter polychromator dedicated to the stratospheric-mesospheric measurements from the Cassegrain telescope

3.4. Detectors

The basic instrumental characteristics in determining the choice of a photodetector include the spectral response, quantum efficiency, frequency response, gain, and dark current. In most cases, the wavelength of the signal to be detected constitutes the primary factor in selecting the class of photodetector to be employed in any applications. For wavelengths that range between

200 and 1000nm photomultipliers are generally preferred because of their high gain and low noise. For the near-infrared wavelengths, photodiodes and in particular avalanche photodiode are a good compromise. Those avalanche photodiodes are similar to photomultipliers in the sense that their sensitivity is no longer determined by thermal noise of the detector and output circuit (Measures 1992). Four different detectors are used in the lidar system

- PMT, Hamamatsu photosensor modules
- PMT, Thorn Emi, QA9829 series
- PMT, Thorn Emi, B9202 series
- Si-Avalanche photodiode, EG&G, C30954/5E series

The advantages of the Hamamatsu photosensor modules are described in the next section. The Thorn Emi PMT QA9829 series has a higher gain than the Hamamatsu PMT and thus is used on the Raman wavelengths at 387 and 408nm while the Thorn Emi PMT B9202 has a higher sensitivity at 607nm and is used on the Raman wavelength. Concerning the detectors of the receiver dedicated to the stratospheric-mesospheric measurements, the Hamamatsu of the 355nm channel is substituted by a Thorn Emi PMT QA9829 series. The others are the same. The next section presents some tests on the spatial uniformity and the linearity of the Hamamatsu photosensor module. More details are in (Simeonov, Larchevêque et al. 1999).

3.5. The Hamamatsu photosensor modules

A large number of factors may contribute to the accuracy of a LIDAR measurements (Measures 1992; Schoulepnikoff, Van den Bergh et al. 1998). One of the most important sources of errors in such measurements is the photodetection unit which in most cases is a photomultiplier tube (PMT). Many studies have examined the influence of the PMT linearity, the dynamic range and the signal induced noise on the quality of the lidar signal (Cairo 1966; Pettifer 1975; Swinesson 1991) generally there was less concern about the effect of the PMT spatial uniformity on the signal.

The spatial uniformity of the PMT is defined as the variation of its sensitivity with the position of incident light on the photocathode. In LIDAR applications the image of the air volume illuminated by the laser beam is projected on the PMT photocathode by the receiving telescope. This image in biaxial lidar has a "cometlike" shape with a "head" corresponding to the signal from a short distance and a "tail" corresponding to the signal from longer distances. The use of a PMT with spatial nonuniformity for detecting lidar signals can cause artifacts because different areas of the photocathode detect the signal from different distances. The lidar systems receiving signals from short and very short distances are affected more by this PMT nonuniformity because of the faster "traveling" of the image over the photocathode.

In the last few years, a new type of PMTs: the Hamamatsu 5600 series (Hamamatsu Photonics 1994; Kyushima 1994) have attracted the attention of the lidar community (Brenner 1996), due to their very small size, excellent linearity, fast response and lack of detectable signal-induced noise.

3.5.1. Anode spatial uniformity

An example of the Hamamatsu PMT response as a function of the light source position is shown in Figure 3-9. The measured values were normalized to the average of 10X10 central points (2X2mm). The nonuniformity observed in the sensitivity can be explained by the new type of electron multiplier configuration -Metal Channel Dynode (Kyushima 1994) used in this PMT. This configuration is similar to that used in a venetian blind type one and is equal to sixteen, eight-stage electron multipliers working in parallel.

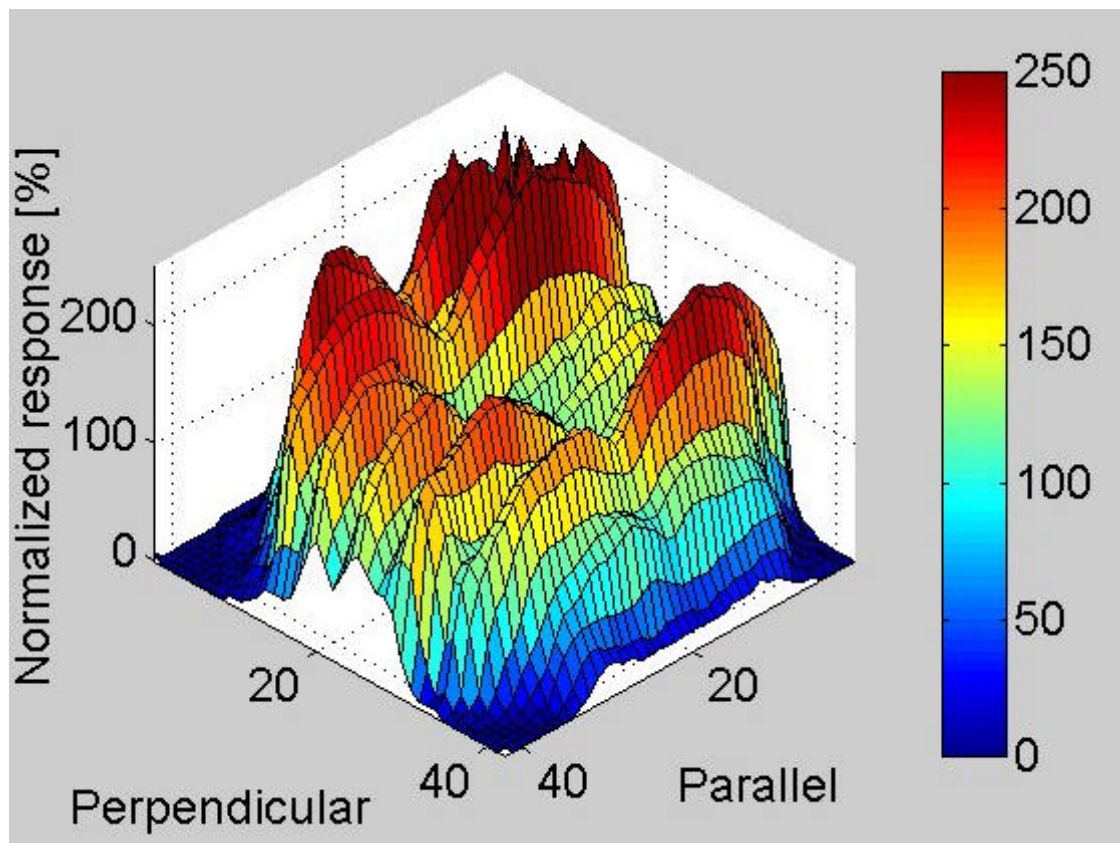


FIGURE 3-9. Anode spatial uniformity of the Hamamatsu H5783-06

The results show that the normalized spatial uniformity of the active area with a diameter of 8mm can vary from 0.2 to 2.8 times the average value defined for the central part of the PMT (10X10 points). For the central part with a diameter of 2mm these variations range from 0.7 to 1.4

A standard way to reduce the spatial nonuniformity of the PMT would be to change the electrical potentials between the PMT electrode (dos Santos, Veloso et al. 1996). This is not applicable because the high voltage power supply, the voltage divider, and the PMT itself are sealed together in one block.

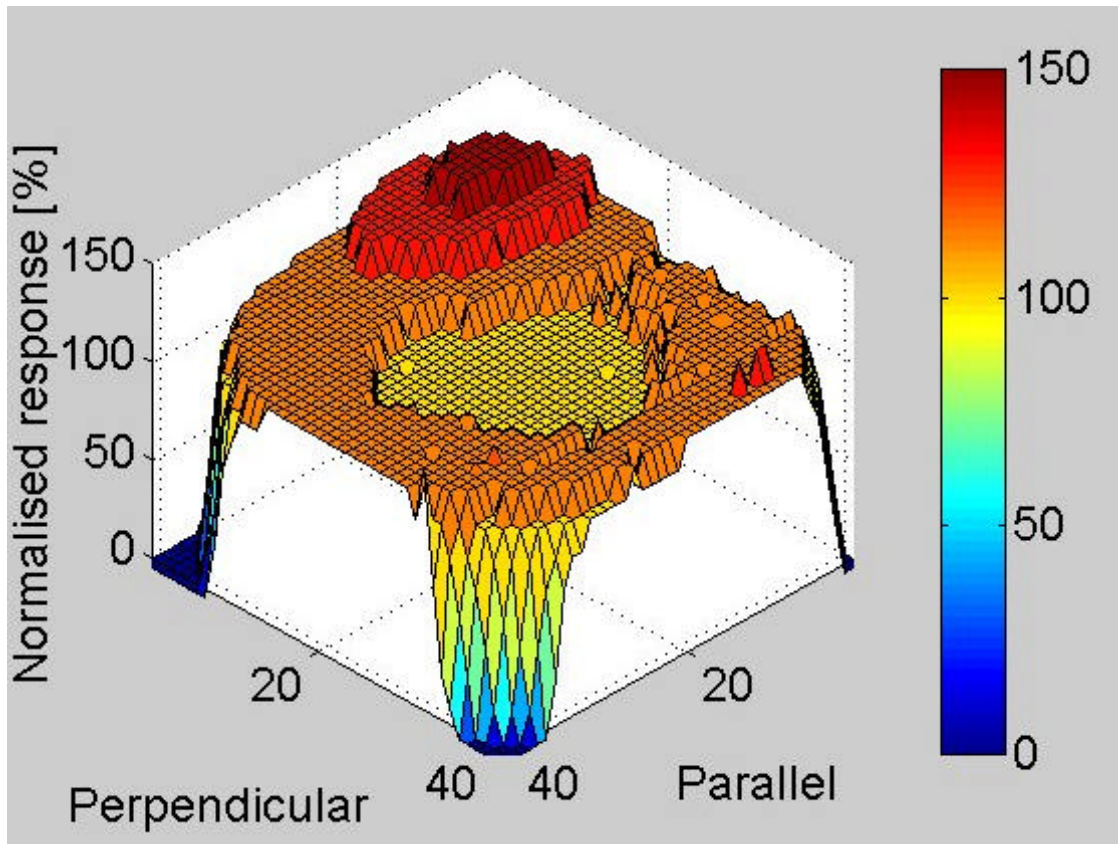


FIGURE 3-10. Anode spatial uniformity of the photosensor module with an additional 3mm thick surface diffuser plus a lens with a 16mm focal length.

Therefore, to improve the PMT spatial uniformity, an optical diffuser is used to spread the incoming light more homogeneously over the photocathode surface. Such a diffuser is placed in front of the PMT, in direct contact with its entrance window. It is made of a fused silica plate with a diameter equal to the PMT entrance window (10mm) polished on one side, and ground on the other (abrasive mesh 600). A further improvement in the PMT uniformity was achieved by using a short focal length lens. The lens is a plano-convex one made of fused silica with a focal length of 16 mm and a diameter of 10 mm. It is placed with its flat surface directly on the diffuser. This lens concentrates the incoming light into the most homogeneous central part of the photocathode. The result from a PMT scan with a lens and a 3 mm thick diffuser is shown in Figure 3-10. The central part with a diameter of approximately 3mm has excellent uniformity with variations less than 2%. A ring with an outer diameter of roughly 7mm and approximately 10% higher efficiency surrounds this part. The variations in the uniformity of this area are between 0.9 and 1.45 times the average of the central zone. The use of a lens and a diffuser reduces the total PMT efficiency by about 45%. This reduction was evaluated by comparing the responses of the PMT with and without lens/diffuser combination from an active area with a diameter of 7mm. The reduction is not only due to the optical losses caused by the uncoated surfaces and scattering from the diffuser, but also due to the lower efficiency of the central part of the PMT photocathode.

3.5.2. Linearity of the photosensor

It is usually assumed that the signal output of an PMT is linearly proportional to the input light intensity and that when no light is present there is only a small electrical output, known as dark current. While this is true for low light intensities, the PMT output is nonlinear for high input intensities.

The Hamamatsu PMT is mainly dedicated to the low altitude range and, a good linearity and no after pulse effect are statutory for such kind of measurements. The linearity was tested, using the fact that the response of the PMT should be the sum of each contribution when five LEDs (Light Emitting Diode) illuminate it. This way of making eliminates the nonlinearity between the input voltage of the LED and its light intensity. Three tests were performed on one photosensor module. The first one was made at the maximum control voltage (0.99V) of the photosensor according to the following method:

- Each of the LEDs is tuned to give the same output value of the tested PMT.
- One LED is switched on and the PMT response is recorded
- A second LED is switched on and the response is recorded
- And so on until the five LED are switched on.
- This last value becomes the new value of each LED and a new set of measurements is done. As long as the response does not reach the maximum allowed value of 4V, those iterations are done.

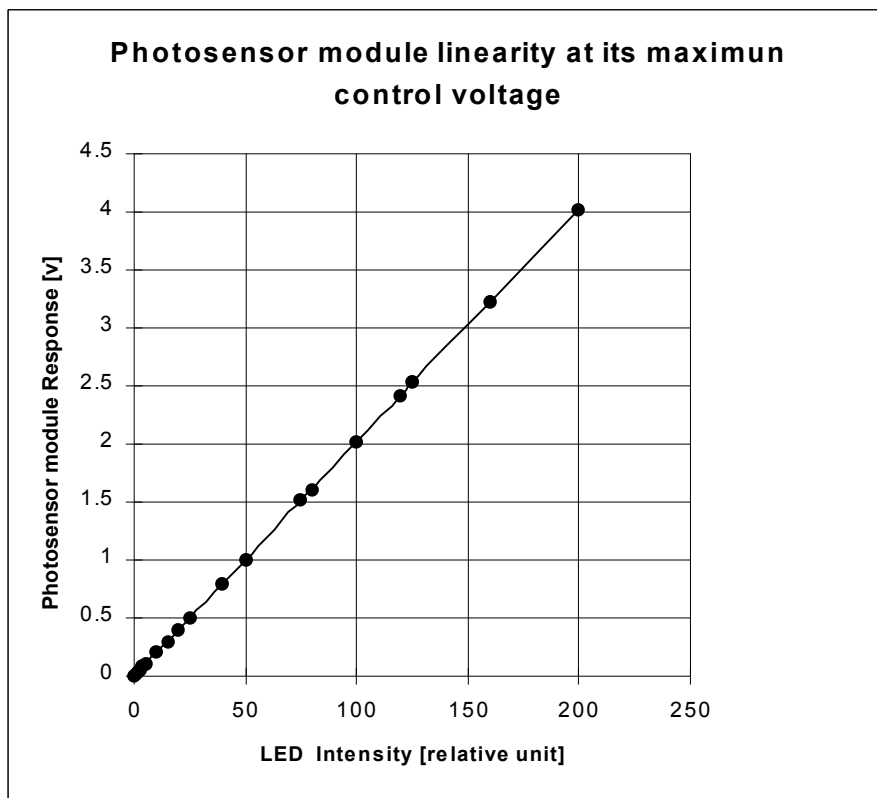


FIGURE 3-11. Hamamatsu photosensor module linearity at its maximum control voltage (0.99V).

Figure 3-11 shows the results of this first test. The photosensor module has a linear response at its maximum control voltage over the range of measurements observed.

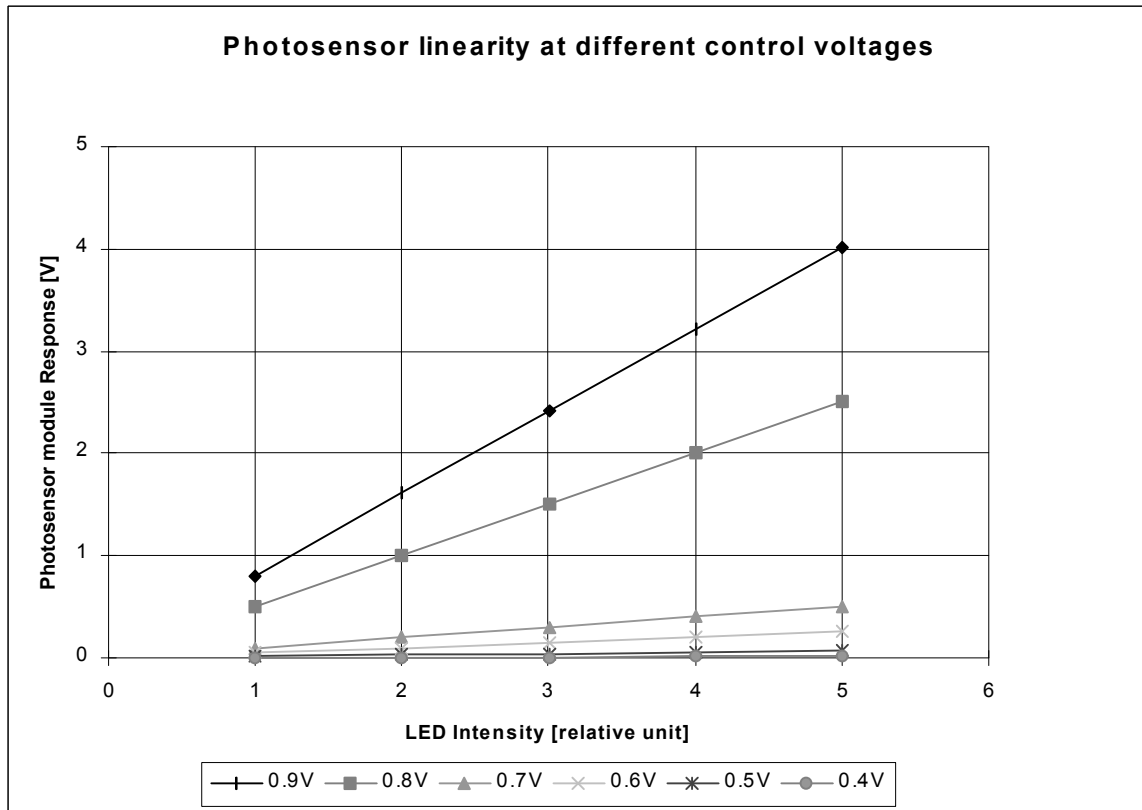


FIGURE 3-12. Hamamatsu photosensor module linearity in function of its control voltage. The LED intensities are not constant from one case to the other one.

The second test is performed at different control voltages and thus will be determined if the linearity of the photosensor is control voltage dependent. Unfortunately, it was impossible to scan the same range of responses from 0.5 to 4V with control voltages from 0.4 to 0.9V. For this reason, the initial values of the LEDs are different for each control voltage and only one incrementation is done. Figure 3-12 shows that the linearity of the photosensor is control voltage independent in this operating range.

The third and last test was performed at different control voltage but with the same LED intensity during all the experiment. It is only possible between 0 and 5mV. This will validate the second test with constant parameters.

The PMT provides the same response whatever the control voltage, see Figure 3-13.

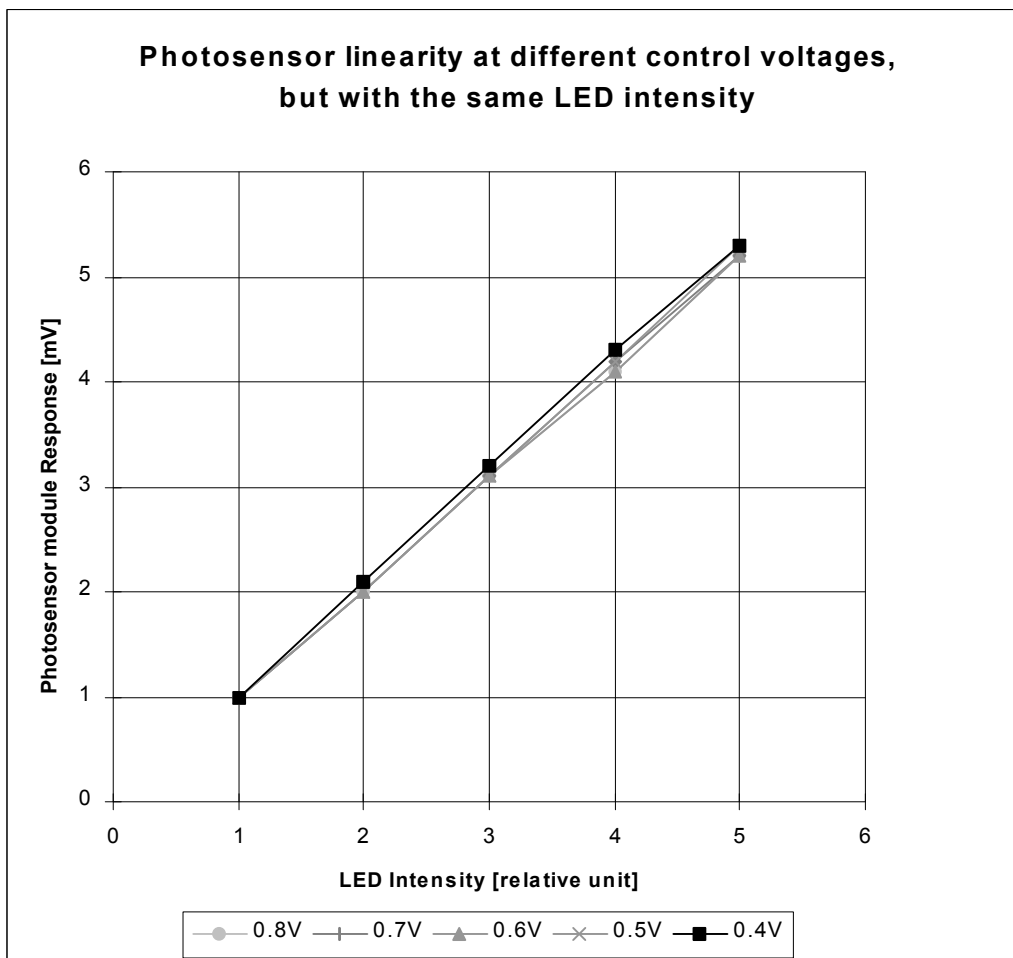


FIGURE 3-13. Hamamatsu photosensor module linearity in function of its control voltage with the same LED intensity for the five cases.

3.5.3. After pulse effect

When a PMT is exposed to momentary high intensities, the output does not return to the dark current level immediately but instead decays slowly. This effect is called after pulse effect or signal-induced-noise (SIN).

The pulsed light is generated by a quadrupled Nd:YAG laser and its intensity is reduced by a set of neutral density filters. A polychromator ensures the rejection of the background light and an optical fiber collects and transmits the laser pulse to the photosensor module whose control voltage is set to its maximum (0.9V). The PMT response is recorded by an oscilloscope. Figure 3-14 shows the shape of the laser pulse detected by the two different photosensor module. Two traces are presented on each picture the white curve is the response of the PMT while the yellow one is the trig of the oscilloscope. The X-axis is the time in nanosecond and the Y-axis is the PMT response in millivolt.

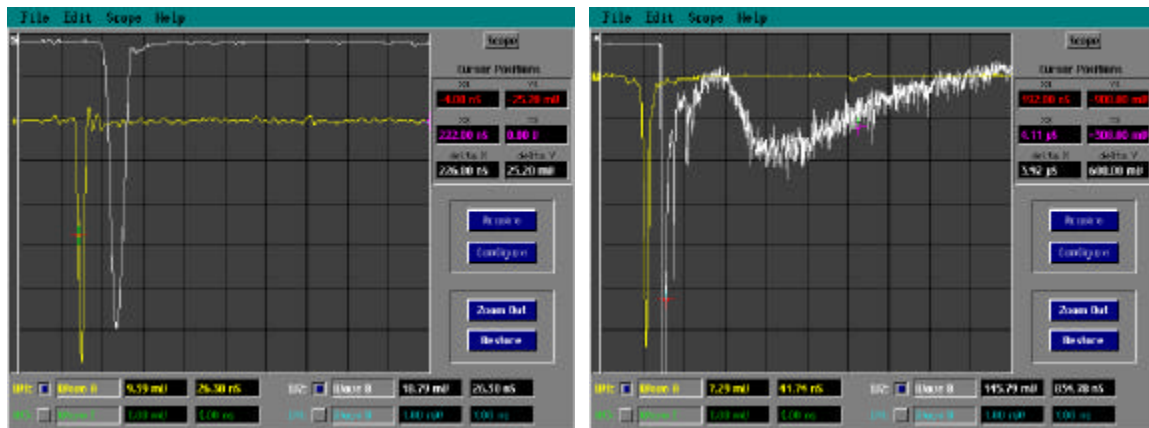


FIGURE 3-14. Pictures of the laser pulses recorded by the two photosensor modules. No significant after pulse effect are observed (left panel) and presence of artefacts (right panel).

The left panel shows a photomodule without any after pulse effect whereas it is not the case for the second one. This effect can be induced by oversaturation of the photocathode by direct exposition to the solar light and not only induces by after pulse effect. No improvements were observed after some days while the voltage was applied under dark conditions. This module was returned to the supplier.

3.5.4. Conclusion

The Hamamatsu photosensor module has a good linearity, no after pulse effect and with the adds of a diffuser and a lens its nonuniformity can be overcome. The choice of this PMT for the elastic tropospheric measurements is obvious.

3.6. Conclusion

The simulation of the receiver part highlights the defocalisation and decenter effect of the off-axis lidar system and encountered problems of very low altitude measurements with such configuration. The operational range of the Newtonian telescope is set between 400m and 9km above the station until the Cassegrain is still not in operation.

This configuration allows the retrieval of the backscattered light at 355, 387, 408, 532 parallel, 532 perpendicular, 607 and 1064nm. The combination of those signals provides aerosol extinction and backscatter profiles, linear depolarization ratio and water vapor mixing ratio. Also possible is the determination of the temperature beyond 90km by Rayleigh scattering (usually at 532nm) (Meriwether 1994), but aerosol interference cannot be tolerated. Thus much of the system are for the measurement of temperature above 30km, where aerosol is negligible. To reject this interference, the comparison of the received rotational Raman scattering signal in two frequency bands allows temperature measurements (Arshinov and Bobrovnikov 1983; Arshinov, Bobrovnikov et al. 1983). The rotational Raman technique (RRT) rely on the detec-

tion of signals with opposite temperature dependence within the pure rotational Raman spectrum of nitrogen molecules whose spectral separation is usually ensured by interferometer. To put this in a concrete form, most of the light at 532nm can be collected before the beamcompressor and transmits to the interferometer by an optical fiber or a third telescope can be especially dedicated to this measurements.

Another upgrade of the system is the ozone measurements using the differential absorption technique (DIAL). In absence of a strong aerosol load in the stratosphere, the on- and off-lines may be chosen far from one another, typically at 308 and 355nm, respectively, inside and outside the ozone absorption band (Stefanutti 1992). The 355nm channel is already recorded and the 308nm channel can be generate by a XeCl excimer laser. The 308nm channel can be add on the 355nm channel with few modification of the detections boxes. But the present beamsplitter 355/387-408nm transmits 308nm and thus is not suitable for this configuration.

With few modifications and one additional laser, the present system can be upgraded to a more sophisticated lidar system which can measure ozone, temperature, aerosol and water vapor mixing ratio profiles.

3.7. References

- Arshinov, Y. F. and S. M. Bobrovnikov (1983). "Remote-Sensing of the Atmospheric-Temperature Using Pure Rotational Raman Lidar." Izvestiya Akademii Nauk Sssr Fizika Atmosfery I Okeana **19**(4): 431-434.
- Arshinov, Y. F., S. M. Bobrovnikov, et al. (1983). "Atmospheric-Temperature Measurements Using a Pure Rotational Raman Lidar." Applied Optics **22**(19): 2984-2990.
- Brenner, P., Reitebuch, O., Schäfer, K., Trickl, T., and Stichternath, A. (1996). A novel mobile vertical-sounding system for ozone studies in lower troposphere. 18th International Laser Radar Conference, Berlin.
- Cairo, F., Congeduti, F., Poli, M., Centurioni, S., and Di Donfrancesco, G. (1966). "A survey of the signal-induced noise in photomultiplier detection of wide dynamics luminous signals." Review of scientific instrument **67**: 3275-3280.
- dos Santos, J. M. F., J. F. C. A. Veloso, et al. (1996). "A simple method to improve the spatial uniformity of venitian-blind photomultiplier tubes." Ieee Transactions of Nuclear Science **43**(3): 1335-1340.
- Hamamatsu Photonics, K. K. (1994). Metal package photomultiplier tube R5600 series. Shizuoka 438-01, Japan.
- Kyushima, H., Hasegawa, Y., Atsumi, A., Nagura, K., Yokota, H., Ito, M., Takeuchi, J., Oba, K., Matsuura, H., and Suzuki, S. (1994). "Photomultiplier tube of new dynode configuration." Ieee Transactions of Nuclear Science **41**: 725-729.
- Measures, R. M. (1992). Laser Remote Sensing. Fundamentals and Applications. New-York, Krieger.

- Meriwether, J. W., Dao, P. D., McNutt, R. T., and Klementi, W. (1994). "Rayleigh lidar observations of mesosphere temperature structure." Journal of Geophysical Research-Atmospheres **16**: 16973-16987.
- Pettifer, R. E. W. (1975). "Signal induced noise in lidar experiments." J. Atmos. Terr. Phys. **37**: 669-673.
- Schoulepnikoff, L., H. Van den Bergh, et al. (1998). Tropospheric air pollution monitoring, lidar. Encyclopedia of environmental analysis and remediation, John Wiley & Sons.
- Simeonov, V., G. Larchevêque, et al. (1999). "The influence of the photomultiplier spatial uniformity on lidar signals." Applied Optics **38**: 5186-5190.
- Stefanutti, L., Castagnoli, F., Del Guasta, M., Morandi, M., Sacco, V. M., Zuccagnoli, L., Godin, S., Megie, G., and Porteneuve, J. (1992). "The Antarctic Ozone LIDAR System." Applied Physics B-Lasers and Optics **55**: 3-12.
- Swinesson, J. A., and Apituley, A. (1991). RIVM tropospheric ozone lidar. Bilthoven, the Netherlands, RIVM Rep. No. 222201006 (National Institute of Public Health and Environmental Protection).

This chapter presents the numerical scheme of the Fernald and the Raman inversions developed in the chapter “Theory”, p 21. Starting from the raw data, all the important steps are discussed, in particular the influence of the lidar ratio in the elastic inversion. The sources of uncertainties are pointed out and error analysis of the two algorithms is described, just as the errors of the depolarization ratio. The error sources on the water vapor mixing ratio are presented in the chapter “Advances in global change research Article”, p 151. A determination of the Angstrom coefficient based on three wavelengths instead of two is also presented in this chapter.

4.1. Data treatment

This section is dedicated to the numerical scheme that is used to retrieve aerosol extinction and backscatter coefficients by the Fernald algorithm or by the Raman algorithm. Figure 4-1 shows the flow chart of the numerical scheme. Before any data treatment, a noise file obtained with the telescope closed is subtracted from the raw data. Normally, such noise files are recorded every half an hour. The sky background is determined by the last bins of the data and then subtracted from those data. The result is called corrected data after being corrected for the time delay between the Q-switch and the laser pulse. Before inversions can be applied to measured signals, they are averaged over time interval of interest (typically half an hour) and spatially averaged (smoothed) in order to increase the signal to noise ratio. The initial spatial resolution of the system is 7.5m and generally, no profiles are given at this resolution because the signals are noisy. First, profiles are smoothed with a sliding average of which window has a parabolic variation, thus the resolution can be reduced significantly (typically 90m in analog mode and 150m in photon counting mode).

The molecular number density is needed to calculate the Rayleigh scattering coefficients or the Raman scattering coefficients in the Fernald and Raman inversion schemes. Temperature and pressure profiles, needed for density profile computation, are determined from a standard atmosphere model fit to measured ground-level values, or are taken from radiosonde data when available. Those profiles are calculated with the same resolution than the signal resolution. In any case, all the wavelengths are recorded but Raman shifted wavelengths are used in principle for nighttime measurements. As a rule, the Fernald inversion is used for daytime measurements while the Raman inversion is applied for nighttime measurements.

4.1.1. Fernald inversion

The inversion of the elastic lidar equation given by (EQ 2.44) is replaced with the backward numerical calculation scheme of Fernald-Sasano (Sasano 1985) and the total backscattering coefficient $\beta_p + \beta_m$ is given by

$$\mathbf{b}_p(I-1) + \mathbf{b}_m(I-1) = \frac{S_p(I-1)PR^2(I-1)\exp[A(I, I-1)]}{\frac{PR^2(I)}{\mathbf{b}_p(I) + \mathbf{b}_m(I)} + \{S_p(I)PR^2(I) + S_p(I-1)PR^2(I-1)\exp[A(I, I-1)]\}\Delta R} \quad (\text{EQ 4.1})$$

where $PR^2(I)$ is the range corrected signal at the altitude I , S_p is the lidar ratio, ΔR is the resolution and $A(I, I-1)$ is defined as

$$A(I, I-1) = \left\{ [S_p(I-1) - S_m] \mathbf{b}_m(I-1) + [S_p(I) - S_m] \mathbf{b}_m(I) \right\} \Delta R \quad (\text{EQ 4.2})$$

where S_m is the molecular extinction to backscatter ratio, β_m is the molecular backscatter coef-

ficient. The term $A(I, I-1)$ is used to replace the exponential terms that incorporate the effects of the aerosol extinction between adjacent data points range ΔR apart.

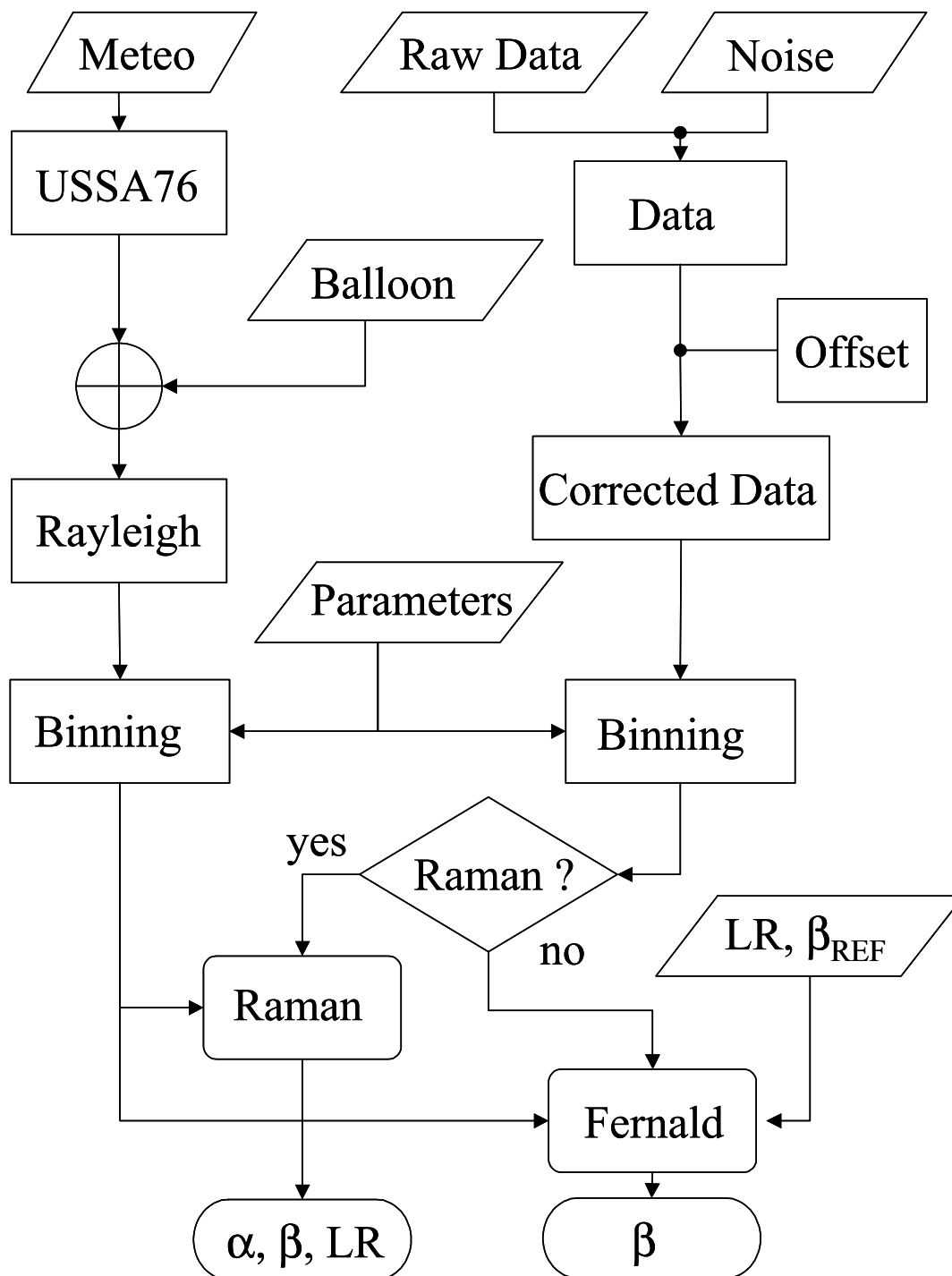


FIGURE 4-1. Flow chart of the numerical scheme for the retrieval of the backscatter coefficient or the extinction coefficient, backscatter coefficient and lidar ratio by Fernald or Raman inversion, respectively.

As it was highlighted in the theoretical chapter, two unknown quantities, the particle lidar ratio and the particle backscatter coefficient at a suitable reference altitude, have to be known in order to determine the particle backscatter coefficient profile. Usually, the lidar ratio is chosen to $50 \pm 10 \text{sr}$ and $10 \pm 5 \text{sr}$ in aerosol layers and cirrus clouds (if present), respectively (Vaughan 1998). To find an appropriate reference altitude and value, a Rayleigh signal is calculated from temperature and pressure profiles of a balloon or a model and compared to the range corrected lidar signal. If the slope of both, the calculated and the measured signal, agree over a sufficient range, it is assumed that negligible aerosols are present in this range, and thus the total backscatter coefficient is assumed to be equal to the molecular coefficient. The reference value is set to zero and a first inversion is applied and the total backscatter coefficient is compared to the molecular coefficient in the range of interest. If the former is less than the later, that has no physical meaning, the difference between the two values is added to the reference value and a new inversion is applied.

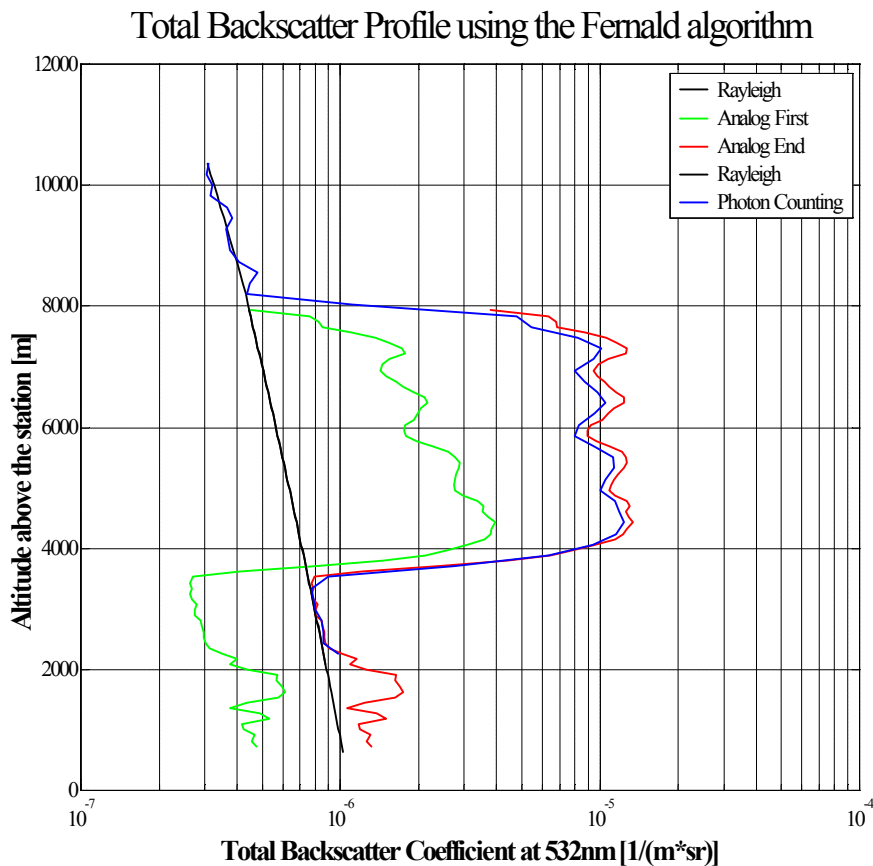


FIGURE 4-2. A typical example of a total backscatter coefficient at 532nm retrieved by the Fernald algorithm with a lidar ratio of 15sr.

Those iterations are done until the difference is less than 1% of the molecular coefficient or until the number of iterations is bigger than 150. This formalism is very useful when the upper part of the lidar signal is inside a cloud. Indeed, the signal recorded in analog mode is generally too noisy after passing the cloud. Figure 4-2 shows one example of a 532nm signal; the X-axis

gives the total backscatter coefficient and the Y-axis the altitude. The green line (Analog First) is the analog profile with no aerosol contribution at 8000m, the red line (Analog End) is the same after iterations and the blue line (Photon Counting) is the photon counting profile. Also shown is the Rayleigh backscatter profile (black line). In the analog mode, the reference altitude is set at 8000m, the lidar ratio is 15sr and the resolution is 90m. In the photon counting mode, the reference altitude is 10500m with the same lidar ratio and the resolution is 180m. The molecular range is between 2500 and 3500m. The minimum altitude of those two profiles is 600 and 2200m in analog and in photon counting mode, respectively. Those two profiles show no significant difference, proof that the iteration formalism provides good results and can be the basic scheme of an automatic data treatments. But, in the case of a high particle load throughout the whole range of measurement, this formalism can not be applied.

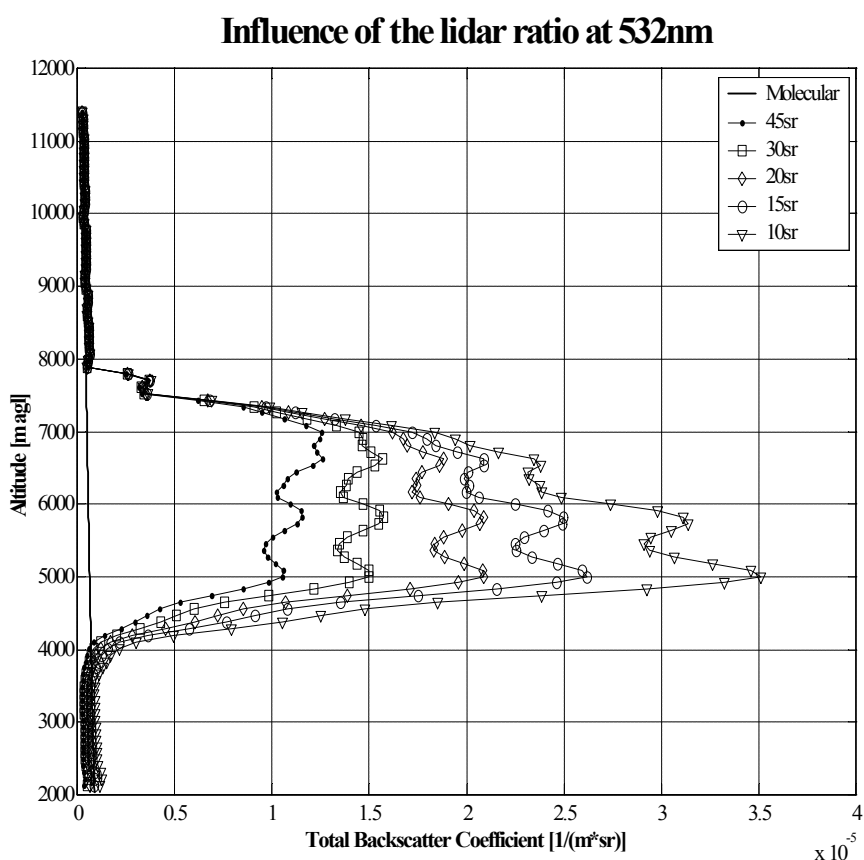


FIGURE 4-3. Influence of the lidar ratio on the retrieval of the total backscatter coefficient using the Fernald algorithm in presence of hazy layers. The lidar ratio is set to 45, 30, 20, 15 and 10sr, respectively. A molecular reference is chosen at 11000m.

Nevertheless the lidar ratio is still not known and its influence on the retrieval of the backscatter profile, at 532nm, is highlighted in Figure 4-3 and Figure 4-4 for two different cases, in presence of hazy layers and with low aerosol load, respectively. In the former case, using a higher lidar ratio underestimates the total backscatter profile and can provide smaller value

than the molecular profile (45sr and 30sr). In the latter case, this effect is smoothed due to the less influence of the aerosol on the total backscatter profile. The influence of the lidar ratio becomes more important as the wavelength decreases.

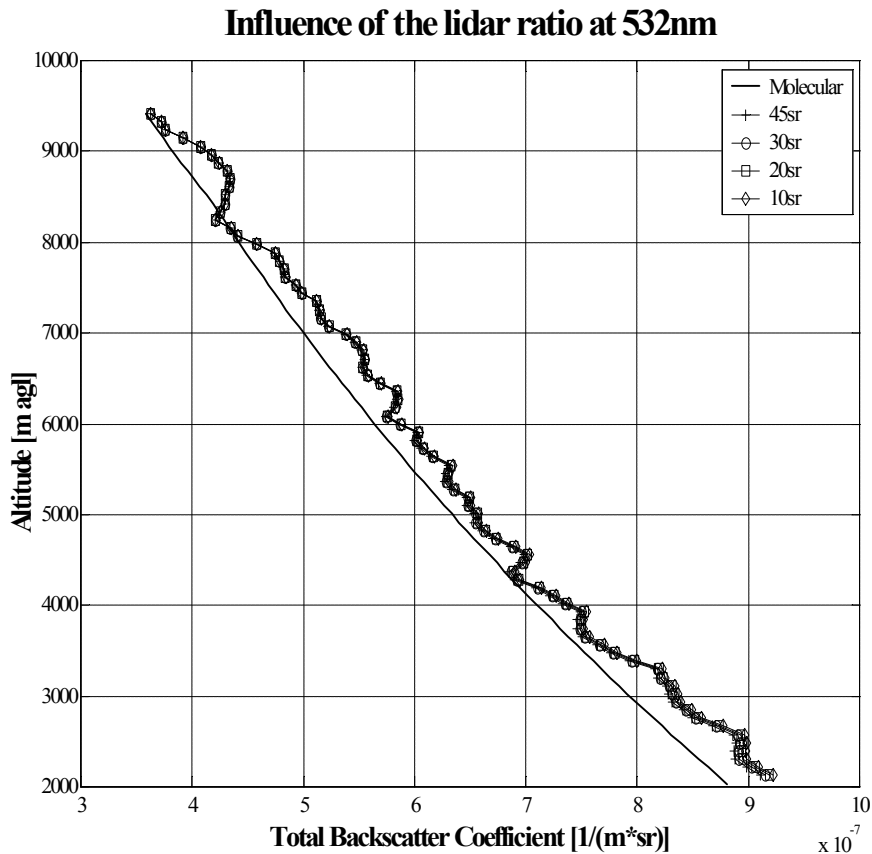


FIGURE 4-4. Influence of the lidar ratio on the retrieval of the backscatter coefficient using the Fernald algorithm in presence of low aerosol load. The lidar ratio is set to 45, 30, 20 and 10sr, respectively. A molecular reference is chosen at 9000m.

The combination of the analog and photon counting regime is useful to retrieve the backscatter profile since two different reference values can be applied and that the results have to be similar throughout the overlap region of the two detection regimes as it is well seen in Figure 4-2 between 2000 and 8000m agl. This overlap region is so huge due to the low energy pulse of the laser and no saturation of the photon counting at low altitude. This latter is possible mostly because of the PMT parameters (short pulse duration) and the high counting rate of the counter.

4.1.2. Raman inversion

Before the signal profile is vertically smoothed, the time-averaged lidar signals $P(z)$ are corrected for range and molecular scattering and extinction, in order to leave only the dependence on aerosol extinction (Ansmann, Wandinger et al. 1992).

$$\begin{aligned} \frac{P(R, \mathbf{I}_L, \mathbf{I}_R) R^2}{\exp\left[-\int_0^R \mathbf{a}_m(\mathbf{I}_L, r) + \mathbf{a}_m(\mathbf{I}_R, r) dr\right]} &= P^*(R) \\ &= K(\mathbf{I}_R) \mathbf{x}(R) N(R) \frac{d\mathbf{s}(\mathbf{I}_L, \mathbf{I}_R, \mathbf{p})}{d\Omega} \exp\left[-\int_0^R \mathbf{a}_p(\mathbf{I}_L, r) + \mathbf{a}_p(\mathbf{I}_R, r) dr\right] \end{aligned} \quad (\text{EQ 4.3})$$

where $K(\lambda_R)$ is the all range-independent system parameters at wavelength λ_R , and $\xi(R)$ is the overlap function. Assuming $\alpha_p \sim \lambda^k$ dependence with $\Delta\lambda/\lambda_L \ll 1$, rearranging the terms, taking the logarithm and then the derivative gives

$$\mathbf{a}_p(\mathbf{I}_L, R) = \frac{1}{1 + \left(\frac{\mathbf{I}_L}{\mathbf{I}_R}\right)^k} \frac{d}{dR} \ln \left\{ \frac{\mathbf{x}(R) N(R)}{P^*(R)} \right\} \quad (\text{EQ 4.4})$$

Again the inversions can be applied to the altitude region where the lidar system overlap function is unity.

$$\begin{aligned} \mathbf{a}_p(\mathbf{I}_L, R) &= \frac{1}{1 + \left(\frac{\mathbf{I}_L}{\mathbf{I}_R}\right)^k} \frac{d}{dR} \ln \left\{ \frac{N(R)}{P^*(R)} \right\} \\ &= \frac{1}{1 + \left(\frac{\mathbf{I}_L}{\mathbf{I}_R}\right)^k} \frac{d}{dR} \ln \{ \tilde{P}(R) \} \end{aligned} \quad (\text{EQ 4.5})$$

For a correct application of (EQ 4.5), it is necessary to calculate the derivative of the logarithm of the ratio of two quantities, i.e. the atmospheric number density $N(R)$ and the corrected N_2 Raman lidar signal $P^*(R)$. The derivative is usually taken by a least-squares technique, by fitting the Raman lidar data by means of linear or quadratic functions. For a correct statistical approach to the problem, the χ^2 confidence test has to be used to assess both the best model and the measurement error (Whiteman 1999). The careful application of statistical analysis techniques is required to accurately estimate the aerosol extinction and the aerosol extinction

error (Pappalardo 2000).

4.2. Error analysis

As with any experimental technique, lidar measurements are subject to a number of experimental uncertainties, arising both from the measurement *per se* and from the assumptions or uncertain values that enter into the data analysis. These uncertainties depend on a number of factors, including the laser wavelength and other lidar system parameters, the background light, the aerosol concentration, the accuracy, resolution, and proximity of the nearest molecular density measurement, the validity of lidar calibration procedures, and the uncertainty of the atmospheric transmission profile at the lidar profile (Russell 1979). In general, the total measurement uncertainty depends on these factors in a complicated and often counterintuitive way. Nevertheless, it is important that quantitative estimates of those uncertainties be derived, both as a means of assigning error bars to lidar-derived data products, and as a tool in designing and estimating future lidar systems for improved measurements or different operating conditions.

Errors can be divided into two broad and rough but useful classes: **systematic** and **random**. **Systematic errors** are errors which tend to shift all measurements in a systematic way so their mean value is displaced. Those errors can be induced by misalignment of either the transmitter or the receiver, inadequate value of the lidar ratio, calculation of the molecular backscatter coefficient and so on. But small systematic errors will always be present. For instance, no instrument can ever be calibrated perfectly.

Random errors are errors which fluctuate from one measurement to the next. They yield results distributed about some mean value. Random errors displace measurements in an arbitrary direction whereas systematic errors displace measurements in a single direction. The main source of those errors is associated with signal detection.

Some systematic error can be substantially eliminated (or properly taken into account). Random errors are unavoidable and must be lived with.

4.2.1. Error propagation

Frequently, the result of an experiment will not be measured directly. Rather, it will be calculated from several measured physical quantities (each of which has a mean value and an error). What is the resulting error in the final result of such an experiment?

For a function F , derived from several measured variables x, \dots, z , which have independent errors, the uncertainty in $F(x, \dots, z)$ can be approximated as (Taylor 1997)

$$dF = \sqrt{\left(\frac{\partial F}{\partial x} dx\right)^2 + \dots + \left(\frac{\partial F}{\partial z} dz\right)^2} \quad (\text{EQ 4.6})$$

where δx is the uncertainty in measured variable x .

4.2.2. Errors of the Fernald inversion

The sources of uncertainties in the estimate of the aerosol backscatter coefficient are represented by:

- The statistical error due to signal detection (Theopold 1988).
- The systematic error associated with the estimate of the lidar ratio (Godin 1987).
- The systematic error associated with the estimate of the molecular backscatter coefficient (Russell 1979).
- The systematic error associated with the estimate of the total backscatter coefficient at the reference altitude (Godin 1987).
- The systematic error associated with the multiple-scattering (Ansmann, Wandinger et al. 1992; Wandinger 1998; Whiteman 2000).
- The error introduced by operational procedures such as signal averaging during varying atmospheric extinction and scattering conditions (Ansmann, Wandinger et al. 1992; Bosenberg 1998).

Fernald inversions can be applied to the altitude region where the lidar system overlap function is unity. In the altitude region where this condition is not accomplished a further systematic error source has to be accounted for if no corrections are applied.

The aerosol backscatter coefficient is calculated by the subtraction of the molecular backscatter coefficient to the total backscatter coefficient β_t given by (EQ 2.44).

4.2.2.a. Statistical error due to signal detection

The uncertainty of the statistical error due to signal detection on the aerosol backscatter coefficient is given by the partial derivative of aerosol backscatter coefficient with regard to the range corrected signal

$$\frac{\partial \mathbf{b}_p}{\partial PR^2} dPR^2 = \frac{\mathbf{b}_t}{PR^2} \left[1 + 2\mathbf{b}_t S_p \int_{R_f}^R \exp \left(-2 \int_{R_f}^R (S_p - S_m) \mathbf{b}_m dr' \right) dr \right] dPR^2 \quad (\text{EQ 4.7})$$

where δPR^2 is the error on the range corrected signal. The measured signal P_m is the result of the contributions of the backscattered signal P' , the background signal P_{bg} , and a noise term P_n . If the lidar signal is acquired in photon counting regime, then P' follows the Poisson distribution (Taylor 1997). In analog regime, a tension is measured and not a number of counts as in photon counting regime. There is a relationship between the signal S_b in mV and the number of photoelectrons n (Inaba and Kobayashi 1972; David 1995) given by

$$S_b = \left(\frac{2^b}{V_{\max}} q G_{PM} G_A R \right) n \quad (\text{EQ 4.8})$$

where b [-], is the number of digit of the analog-to-digital convertor, V_{\max} [mV], is the maxi-

imum voltage of the signal input range, q [C], is the electron charge, G_{PM} [-], is the gain of the detector, G_A [-], is the gain of the amplifier, and R [Ω], is the resistor.

The quantity used in lidar data analysis is $P' = P_m - \langle P_{bg} + P_n \rangle$, with P' not equal to P generally. P has a complex statistical distribution (Bosenberg 1998) and can have negative values at low signal-to-noise levels. For large values of the signal-to-noise ratio $P'(z) = P(z)$ can be assumed. In this case only the simple statistical error (Poisson distribution) due to the signal noise is taken into account. Otherwise, the error is calculated by the standard deviation of some profiles.

4.2.2.b. Systematic error associated with the estimate of the lidar ratio

The uncertainty of the lidar ratio on the aerosol backscatter coefficient is given by the partial derivative of β_t with regard to the lidar ratio

$$\frac{\partial \mathbf{b}_p}{\partial S_p} dS_p = \left[\begin{array}{l} \mathbf{b}_t \frac{\int_{R_f}^R PR^2 \exp\left(-2 \int_{R_f}^R (S_p - S_m) \mathbf{b}_m dr'\right) dr}{PR^2 \exp\left(-2 \int_{R_f}^R (S_p - S_m) \mathbf{b}_m dr'\right)} \\ 2\mathbf{b}_t + \mathbf{b} \frac{S_p \int_{R_f}^R PR^2 \left(-2 \int_{R_f}^R \mathbf{b}_m dr'\right) \exp\left(-2 \int_{R_f}^R (S_p - S_m) \mathbf{b}_m dr'\right) dr}{PR^2 \exp\left(-2 \int_{R_f}^R (S_p - S_m) \mathbf{b}_m dr'\right)} \\ - \int_{R_f}^R \mathbf{b}_m dr \end{array} \right] dS_p \quad (\text{EQ 4.9})$$

where δS_p is the error on the lidar ratio. The values of the lidar ratio are mainly derived from literature sources and therefore a 10% uncertainty on the lidar ratio is assumed

4.2.2.c. Systematic error associated with the estimate of the molecular backscatter coefficient

The uncertainty of the molecular backscatter coefficient on the aerosol backscatter coefficient is given by the partial derivative of β_t with regard to the molecular backscatter coefficient

$$\frac{\partial \mathbf{b}_p}{\partial \mathbf{b}_m} d\mathbf{b}_m = \begin{bmatrix} -2\mathbf{b}_t \int_{R_f}^R (S_p - S_m) dr \\ -4 \frac{\mathbf{b}_t^2}{PR^2 \exp \left\{ -2 \int_{R_f}^R (S_p - S_m) \mathbf{b}_m dr \right\}} \int_{R_f}^R S_p PR^2 \exp \left\{ -2 \int_{R_f}^R (S_p - S_m) \mathbf{b}_m dr' \right\} \int_{R_f}^R (S_p - S_m) dr' dr \\ -1 \end{bmatrix} d\mathbf{b}_m \quad (\text{EQ 4.10})$$

where $\delta\beta_m$ is the error on the molecular backscattering coefficient. Since the Rayleigh cross section is known with a good accuracy, the uncertainty at the reference value results essentially from uncertainties in the molecular density profile $N(R)$. (Russell 1979) gives a relative error on the molecular density of 3% when density models or interpolations are used. In order to reduce this source of error, the use of simultaneous radiosonde profile instead of a standard atmosphere profile is recommended. At the location and time of a radiosonde measurement, molecular density can typically be determined with an uncertainty of less than 1% (Hoxit 1973; Lenhard 1973). Other studies of spatial and temporal variability above the boundary layer (Planet 1979) indicate that, within about 100km and 6h of the radiosonde measurements, this uncertainty increases only about 1%, provided there are no intervening frontal air mass movements.

4.2.2.d. Systematic error associated with the estimate of the total backscatter coefficient at the reference altitude

The uncertainty of the total backscatter coefficient at the reference altitude on the aerosol backscatter coefficient is given by the partial derivative of β_t with regard to the reference value

$$\frac{\partial \mathbf{b}_p}{\partial \mathbf{b}_{R_f}} d\mathbf{b}_{R_f} = \left(\frac{\mathbf{b}_t}{\mathbf{b}_{R_f}} \right)^2 \left(\frac{PR^2}{(PR^2)_{R_f}} \right) \exp \left\{ 2 \int_{R_f}^R (S_p - S_m) \mathbf{b}_m dr \right\} d\mathbf{b}_{R_f} \quad (\text{EQ 4.11})$$

where $\delta\beta_R$ is the error on the total backscattering at the reference altitude. Generally, the value is only given by the molecular backscattering coefficient. Thus the relative error on the molecular coefficient is given in the previous section.

4.2.2.e. Systematic error associated with the multiple-scattering

The two way extinction term of the single-scattering lidar equation (EQ 2.42) is written under

the assumption that all scattered photons except those scattered in the direct backward direction are permanently removed from the transmitted and received laser beams. But some photons that are scattered out of the lidar beam may later be scattered back in. Thus, the actually received lidar signal $P(R)$ includes photons that haven't been scattered more than once. The effective value of the extinction coefficient is somewhat smaller than the single-scattering value. In addition to increasing the received power, multiple-scattering can also affect its polarization (Sassen 1994).

The effects of multiple-scattering depend on the atmosphere scattering and absorption coefficients, the size of the scattering particles, the time after pulse transmission and the widths of the transmitted and received lidar beams.

(Whiteman 2000) evidenced that in most circumstances multiple-scattering effects from tropospheric aerosol are negligible. Those effects tend to be much more important in fog and cloud.

4.2.2.f. Error introduced by operational procedures

Time Averaging of Data

When only $P(R)$ varies during the measurement averaging period, direct averaging of signals is correct (Bosenberg 1998). Whereas when only $\alpha_p(R)$ varies during the averaging time the inversion has to be computed before averaging. (Ansmann, Wandinger et al. 1992) showed that the error associated with time averaging of data can be sensitively reduced by dividing the total measurement time period into intervals with constant particle extinction conditions. For an appropriate division of the total time into intervals, signal profiles must be stored with high temporal resolution.

4.2.2.g. Total error of the elastic inversion

The uncertainty on the backscatter coefficient profile without multiple-scattering effects is given by

$$db_p = \left\{ \left(\frac{\partial b_p}{\partial PR^2} dPR^2 \right)^2 + \left(\frac{\partial b_p}{\partial S_p} dS_p \right)^2 + \left(\frac{\partial b_p}{\partial b_m} db_m \right)^2 + \left(\frac{\partial b_p}{\partial b_{R_f}} db_{R_f} \right)^2 \right\}^{1/2} \quad (\text{EQ 4.12})$$

To show the contribution of each term of (EQ 4.12), two cases are presented here based on real signals recorded at the Jungfraujoch: one is at clear sky condition and the other is at hazy sky condition. The error analysis is based on the two aerosol backscatter coefficient profiles shown in Figure 4-5. The profiles are recorded in photon counting mode at 532nm, averaged over half an hour or 36000 shots, and retrieved with a spatial resolution of 90m, a lidar ratio of 10sr (Hazy sky) or 43sr (Clear sky) and the molecular value at 11000m agl are taken as reference value.

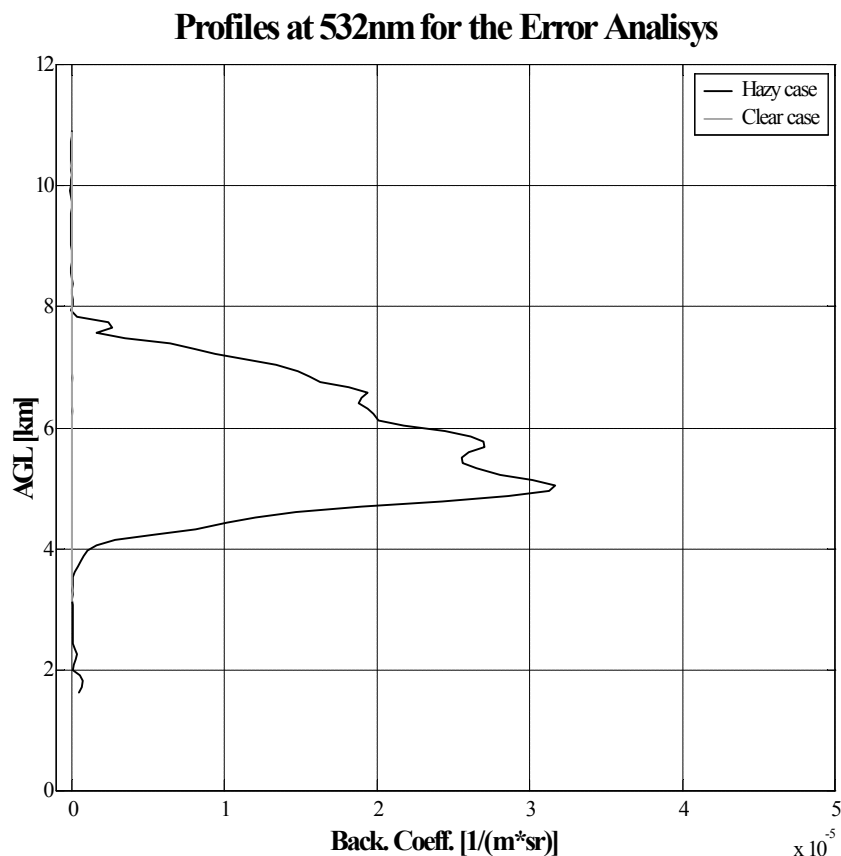


FIGURE 4-5. Aerosol backscatter coefficient profiles in clear sky (gray line) and hazy sky (black line) conditions for the error analysis.

(EQ 4.7), (EQ 4.9) - (EQ 4.11) are applied to those profiles, assuming no multi-scattering effect, a Poisson distribution in both case, 10% uncertainty on the lidar ratio and 3% uncertainty on the molecular profile.

Figure 4-6 shows the total relative error of the measurement taken in clear sky condition and also the contributions associated with the signal detection, (EQ 4.7), the lidar ratio (EQ 4.9), the molecular backscatter coefficient (EQ 4.10) and the reference value (EQ 4.11). In this case the total relative error is less than 10% below 10km agl and is mainly due to the molecular error below 8km agl and than to the detection noise. The contribution of the errors on the lidar ratio and on the reference value are negligible throughout the profile.

Figure 4-7 shows the results of the second case where the total relative error reaches 20% at 10km asl. Below 8km agl or inside the hazy region, the main component of the relative error comes from the lidar ratio whereas the molecular component is negligible. Above this region, the detection noise becomes dominant due to a strong attenuation of the signal.

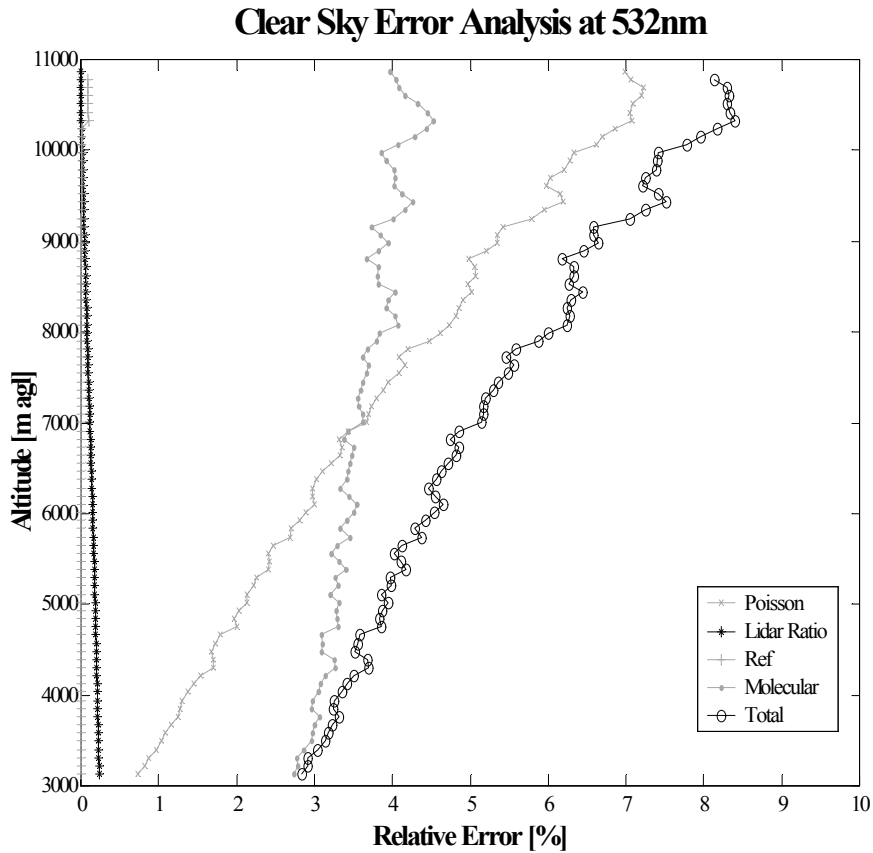


FIGURE 4-6. Error analysis of the clear sky case. The different curves show the contribution of the relative error associated to the detection (Poisson), the lidar ratio (Lidar Ratio), the reference value (Ref), the molecular backscatter coefficient (Molecular) with regard to the total error (Total).

In both case, the relative error on the aerosol backscatter coefficient associated with the reference value is negligible and this relatively small effect of a poor reference value estimate was already pointed out by Klett (Klett 1981).

Those examples highlight the different behaviors of the error components depending on the atmospheric conditions. As a result, the molecular uncertainty is the main uncertainty in clear sky (or low aerosol load) condition whereas the lidar ratio becomes more important with increasing the aerosol load. The influence of the lidar ratio increases at shorter wavelengths.

The molecular backscattering profile can be calculated with a good accuracy but it is not the case for the lidar ratio which is more and less guessed. This is the main drawback of the elastic lidar.

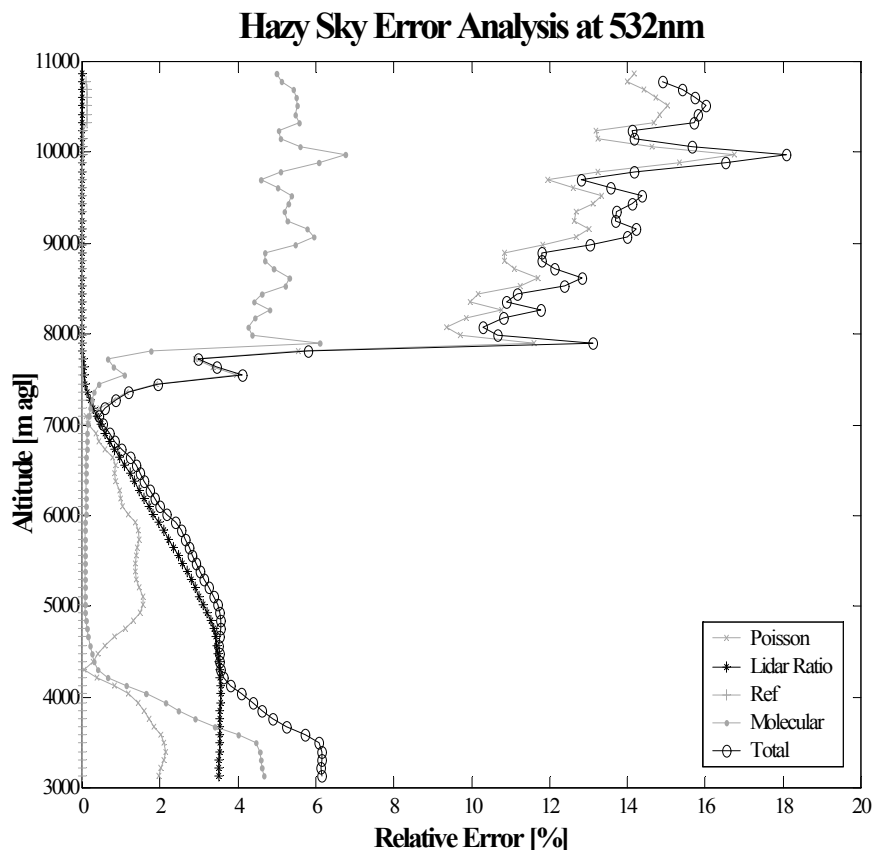


FIGURE 4-7. Error analysis of the hazy sky case. The different curves show the contribution of the relative error associated to the detection (Poisson), the lidar ratio (Lidar Ratio), the reference value (Ref), the molecular backscatter coefficient (Molecular) with regard to the total error (Total).

4.2.3. Errors of the Raman inversion

The part of the error analysis dedicated to the extinction coefficient has been investigated in details within the EARLINET community (Pappalardo 2000) and are reproduced here with the permission of the first author, Pappalardo Gelsominia, Istituto di Metodologie Avanzate di Analisi Ambientale, Potenza, Italy.

The sources of uncertainties in the estimate of the aerosol extinction coefficient are represented by:

- The statistical error due to signal detection (Theopold 1988).
- The systematic error associated with the estimate of temperature and pressure profiles (Ansmann, Wandinger et al. 1992).
- The systematic error associated with the wavelength dependence parameter k (Ansmann, Wandinger et al. 1992; Whiteman 2000).

- The systematic error associated with the multiple-scattering (Ansmann, Wandinger et al. 1992; Wandinger 1998; Whiteman 2000).
- The error introduced by operational procedures such as signal averaging during varying atmospheric extinction and scattering conditions (Ansmann, Wandinger et al. 1992; Bosenberg 1998).

Raman inversion can be applied in the altitude region where the lidar overlap function is unity. In the altitude region where this condition is not accomplished a further systematic error source has to be accounted for.

4.2.3.a. Statistical error due to signal detection

Taking into account the random errors that are due to signal noise, it is possible to derive the uncertainty on the aerosol extinction coefficient from (EQ 4.5):

$$\frac{\partial \mathbf{a}_p}{\partial P^*} dP^* = \frac{\frac{dP^*(z)}{dz}}{\left(1 + \left(\frac{\mathbf{I}_0}{\mathbf{I}_R}\right)^k\right) P^{*2}(z)} dP^* \quad (\text{EQ 4.13})$$

where δP^* is the error on the range corrected signal corrected for the molecular contribution. This error is the sum of the statistical error due to signal detection,

$$\frac{\partial P^*}{\partial PR^2} dPR^2 = \frac{dPR^2}{\exp\left[-\int_0^R \mathbf{a}_m(\mathbf{I}_L, r) + \mathbf{a}_m(\mathbf{I}_R, r) dr\right]} \quad (\text{EQ 4.14})$$

where δPR^2 is the error on the range corrected signal, and of the systematic error on the molecular coefficients,

$$\frac{\partial P^*}{\partial \mathbf{a}_m(\mathbf{I}_X)} d\mathbf{a}_m(\mathbf{I}_X) = (P^*)^2 \frac{\exp\left[-\int_0^R \mathbf{a}_m(\mathbf{I}_L, r) + \mathbf{a}_m(\mathbf{I}_R, r) dr\right]}{PR} d\mathbf{a}_m(\mathbf{I}_X) \quad (\text{EQ 4.15})$$

where $\delta \alpha_m(\lambda_X, r)$ is the error on the molecular extinction coefficient at wavelength X of which relative uncertainty is 3% (Russell 1979). Thus the error on the molecular and range corrected signal is written as

$$dP^* = \left\{ \left(\frac{\partial P^*}{\partial PR^2} dPR^2 \right)^2 + \left(\frac{\partial P^*}{\partial \mathbf{a}_m(I_R)} d\mathbf{a}_m(I_R) \right)^2 + \left(\frac{\partial P^*}{\partial \mathbf{a}_m(I_L)} d\mathbf{a}_m(I_L) \right)^2 \right\}^{1/2}$$

(EQ 4.16)

4.2.3.b. Systematic error associated with the estimate of nitrogen profile

The use of standard pressure and temperature profiles instead of the real ones leads to systematic errors in presence of gradients. While pressure gradients are always limited, temperature gradients are large especially in the case of strong inversion layers. The computation of the term $d/dz \{\ln[N(z)]\}$ in (EQ 4.5) is directly affected by the temperature gradient dT/dz ; in fact:

$$\frac{d}{dz} \{\ln[N(z)]\} = \frac{1}{N} \frac{dN}{dz} \cong \frac{1}{T} \frac{dT}{dz}$$

(EQ 4.17)

$$\frac{\partial \mathbf{a}_p}{\partial N} dN \cong -\frac{1}{T^2} \frac{dT}{dz} dT$$

(EQ 4.18)

where δT is the error on the temperature. A 3% uncertainty on the temperature is assumed (Russell 1979).

Thus, a significant systematic uncertainty on α_p can result from an error in the estimate of strong temperature gradients. A temperature gradient of 13K/km has been found to determine an error $\delta\alpha_p = 0.32 \times 10^{-3} \text{m}^{-1}$ (Ansmann, Wandinger et al. 1992) but gradient of this magnitude are seldom in the free troposphere.

4.2.3.c. Systematic error associated with the wavelength dependence parameter k

For what concerns the wavelength dependence parameter k, (Ansmann, Wandinger et al. 1992) reported for cirrus clouds a relative uncertainty smaller than 2% and 4% for a deviation of 0.5 or 1 between the true value of k and the one used in (EQ 4.5), respectively. (Whiteman 2000) reported a value of $\delta\alpha_p/\alpha_p < 6-8\%$ for a k variability in the range 0-2 in the boundary layer. In order to reduce this error source k can be estimated from two-wavelength N_2 Raman back-scattering measurements.

4.2.3.d. Systematic error associated with the multiple-scattering

An additional systematic error associated with multiple scattering has to be accounted for, primarily in presence of clouds. There are contradictory estimations of this error. (Ansmann, Wandinger et al. 1992) estimated that multiple scattering contribution to the overall error is smaller than 10% at the cloud base and around 5% within the cloud. (Wandinger 1998) showed

that multiple-scattering error is of the order of 50% at the bases of both water and ice clouds and decrease with increasing penetration depth to below 20%. (Whiteman 2000) evidenced that in most circumstances multiple-scattering effects from tropospheric aerosol are negligible.

4.2.3.e. Error introduced by operational procedures

Time Averaging of Data

Because of the occurrence of the logarithm, (EQ 4.5) represents a non-linear relationship between the aerosol extinction coefficient $\alpha_p(R)$ on the one hand and both the lidar signal $P(R)$ and the atmospheric number density $N(R)$ on the other hand. This implies that appropriate precautions need to be applied for time averaging of the data.

(Ansmann, Wandinger et al. 1992) estimated that the potential error caused by an inappropriate addressing of this problem can lead to $\delta\alpha_p/\alpha_p=10\%$ and $=30\%$ for cirrus clouds at the base and top, respectively, and to $\delta\alpha_p/\alpha_p=10\%$ for thin cirrus.

When only $P(R)$ varies during the measurement averaging period, direct averaging of signals is correct (Bosenberg 1998). Whereas when only $\alpha_p(R)$ varies during the averaging time the logarithm has to be computed before averaging.

For high values of the signal-to-noise ratio the Poisson and Gaussian distribution are indistinguishable and this implies that the systematic error caused by the exchange of logarithm and averaging operators decreases quadratically with the relative standard deviation (Bosenberg 1998); hence, in the general case all quantities vary during the averaging time, for high signal-to-noise ratio values the order of application of the operators is indifferent. For most application $\alpha_p(R)$ varies more slowly than $P(R)$; it is then preferable to first average the signals $P(R)$ till the systematic error caused by switching the operator is small; at this SNR level it is safer to continue with forming the logarithm before averaging (Bosenberg 1998).

Averaging the logarithms of the signals, although theoretically leading to correct results, is in practice leading to systematic errors at low signal-to-noise levels, where $P(R)$ can assume negative values which are disregarded in the computation of the logarithm (Theopold 1988). (Ansmann, Wandinger et al. 1992) showed that the error associated with time averaging of data can be sensitively reduced by dividing the total measurement time period into intervals with constant particle extinction conditions. For an appropriate division of the total time into intervals, signal profiles must be stored with high temporal resolution. Time sections of nearly constant particle extinction can then be determined from the time series of elastic-backscatter profiles.

Vertical smoothing of the data

Before the signal profile is vertically smoothed, the time-averaged lidar signals $P(R)$ are corrected for range and molecular scattering and extinction, in order to leave only the dependence on aerosol extinction (Ansmann, Wandinger et al. 1992).

(Godin 1999) evidenced that algorithms using different vertical resolutions applied to the same synthetic data lead to results deviating up to 30%, with larger errors generally occurring as data become noisier. Vertical smoothing of the data can be performed through a sliding average. It is necessary to be take care when filtering procedures of data are applied.

The problem still needs to be properly addressed.

4.2.3.f. Total error on the aerosol extinction profile

The uncertainty on the extinction coefficient profile without multi-scattering effects and wavelength dependence is given by

$$d\mathbf{a}_p = \left\{ \left(\frac{\partial \mathbf{a}_p}{\partial P^*} dP^* \right)^2 + \left(\frac{\partial \mathbf{a}_p}{\partial N} dN \right)^2 \right\}^{1/2}$$

(EQ 4.19)

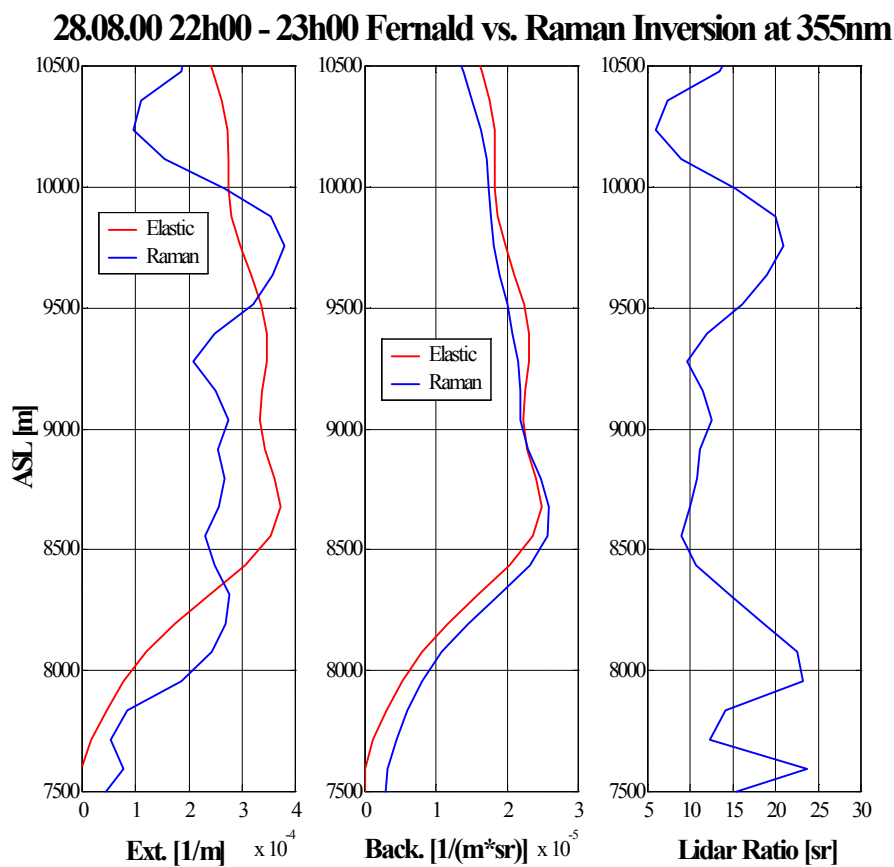


FIGURE 4-8. August 28th 2000 extinction, Backscatter and Lidar Ratio profiles retrieved by Raman Lidar and compared to elastic profiles obtained with lidar ratio of 15sr. The Raman profiles are used in the error analysis of the extinction, backscatter coefficients and the associated lidar ratio.

To demonstrate the influence of the errors associated with the signal detection and with the estimate of the nitrogen profile, (EQ 4.19) is applied to one case, recorded on August 28th 2000, obtained with a parabolic gliding average from 225 to 900m and then a reduction of the spatial resolution to 180m. The wavelength dependence is set to zero and the altitude reference

at 11000km asl. Figure 4-8 shows the extinction, backscatter and the lidar ratio profiles obtained by the Raman algorithm and also the extinction and the backscatter profiles obtained by the Fernald algorithm with a constant lidar ratio of 15sr. The backscatter profiles show similar behavior while the choice of a constant lidar ratio is the source of the discrepancies between the extinction profiles.

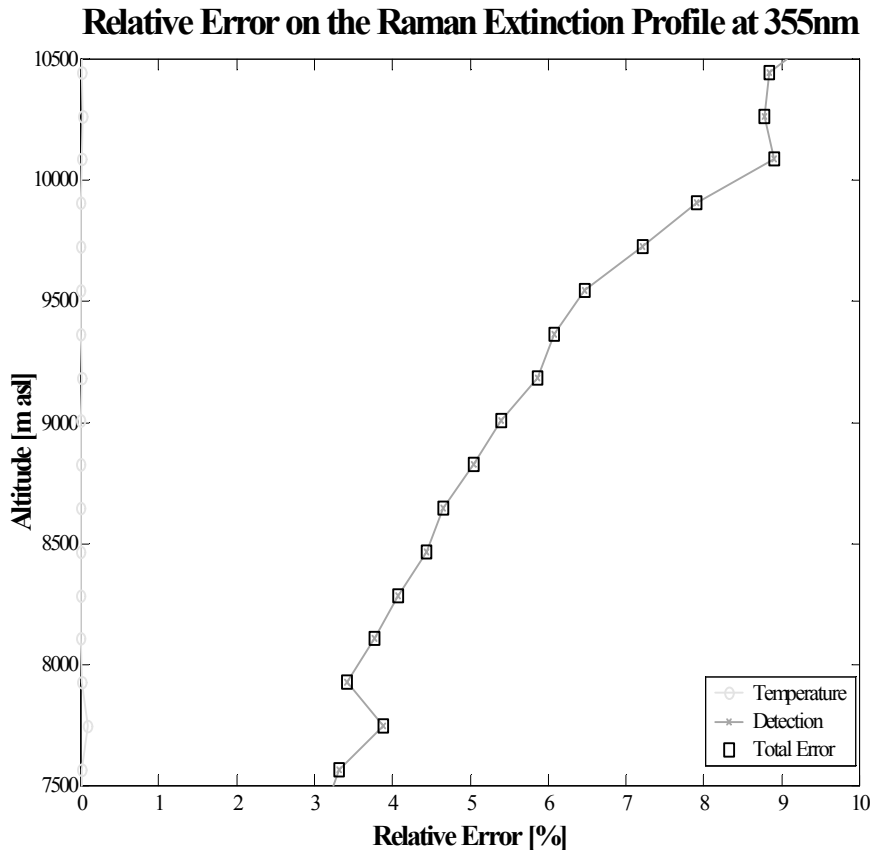


FIGURE 4-9. Errors analysis on the extinction profile retrieved by Raman inversion. The relative error related to the signal detection and temperature gradient are labeled detection and temperature, respectively and are given with regard to the total relative error.

Figure 4-9 shows the relative errors associated with the signal detection (EQ 4.16), temperature gradient (EQ 4.18) and the total relative error from (EQ 4.19). The Poisson distribution is assumed and the temperature profile is determined by model with an expected uncertainty of 3%.

In this case, the uncertainty on the extinction profile is mainly due to the statistical error on the detection at the Raman wavelength. The error on the number density is negligible while no inversion layers are present. The total error is less than 10% throughout the profile due to a larger sliding average and reduction of the spatial resolution.

4.2.4. Error of the backscatter profile

Rewriting (EQ 2.51) with the normalized profiles $P^\#$ at the reference height gives

$$\frac{\mathbf{b}_p(R, \mathbf{I}_L) + \mathbf{b}_m(R, \mathbf{I}_L)}{\mathbf{b}_m(R, \mathbf{I}_L)} = \frac{P^\#(R, \mathbf{I}_L)}{P^\#(R, \mathbf{I}_L, \mathbf{I}_R)} \times \frac{\exp\left\{-\int_R^{R_f} [\mathbf{a}_p(\mathbf{I}_R, r) + \mathbf{a}_m(\mathbf{I}_R, r)] dr\right\}}{\exp\left\{-\int_R^{R_f} [\mathbf{a}_p(\mathbf{I}_L, r) + \mathbf{a}_m(\mathbf{I}_L, r)] dr\right\}} \quad (\text{EQ 4.20})$$

The sources of uncertainties in the estimate of the aerosol backscatter coefficient are represented by:

- The statistical error due to signal detection (Theopold 1988).
- The systematic error associated with the estimate of the molecular backscatter coefficient.
- The systematic error associated with the estimate of the molecular extinction coefficient.
- The systematic error associated with the estimate of the particular extinction coefficient.

Aerosol backscatter profile can be calculated to the altitude region where the lidar system overlap function is different to unity assuming that the overlap functions are identical at the pump and Raman shifted wavelengths.

4.2.4.a. Total error of the backscatter profile

The total error is given by

$$db_p(\mathbf{I}_L) = \left[\begin{aligned} & \left(\frac{\partial \mathbf{b}_p(\mathbf{I}_L)}{\partial P^\#(\mathbf{I}_R)} dP^\#(\mathbf{I}_R) \right)^2 + \left(\frac{\partial \mathbf{b}_p(\mathbf{I}_L)}{\partial P^\#(\mathbf{I}_L)} dP^\#(\mathbf{I}_L) \right)^2 \\ & + \left(\frac{\partial \mathbf{b}_p(\mathbf{I}_L)}{\partial \mathbf{b}_m(\mathbf{I}_L)} d\mathbf{b}_m(\mathbf{I}_L) \right)^2 \\ & + \left(\frac{\partial \mathbf{b}_p(\mathbf{I}_L)}{\partial \mathbf{a}_p(\mathbf{I}_L)} d\mathbf{a}_p(\mathbf{I}_L) \right)^2 + \left(\frac{\partial \mathbf{b}_p(\mathbf{I}_L)}{\partial \mathbf{a}_p(\mathbf{I}_R)} d\mathbf{a}_p(\mathbf{I}_R) \right)^2 \\ & + \left(\frac{\partial \mathbf{b}_p(\mathbf{I}_L)}{\partial \mathbf{a}_m(\mathbf{I}_L)} d\mathbf{a}_m(\mathbf{I}_L) \right)^2 + \left(\frac{\partial \mathbf{b}_p(\mathbf{I}_L)}{\partial \mathbf{a}_m(\mathbf{I}_R)} d\mathbf{a}_m(\mathbf{I}_R) \right)^2 \end{aligned} \right]^{\frac{1}{2}} \quad (\text{EQ 4.21})$$

The details of each partial derivative are given in “Error on the backscatter coefficient determined by Raman lidar”, p 203. Figure 4-10 shows the resulting uncertainty of the backscatter profile of the Figure 4-8 and also the seven individual contributions of (EQ 4.21). Those errors are the error on the Raman signal and the elastic signal, the error on the aerosol extinction coefficient at the Raman wavelength and at the elastic wavelength, the error on the molecular extinction coefficient at the Raman and at the elastic wavelengths, and the molecular backscatter coefficient at the elastic wavelength. The molecular terms are based on an expected uncertainty of 3%, the detection terms are calculated with the Poisson distribution and the aerosol terms come from (EQ 4.19).

In this case, the total error is mainly due to the error on the aerosol extinction profile at the Raman and the elastic wavelengths. Except the values below 7750m, the total error throughout the profile is less than 20%.

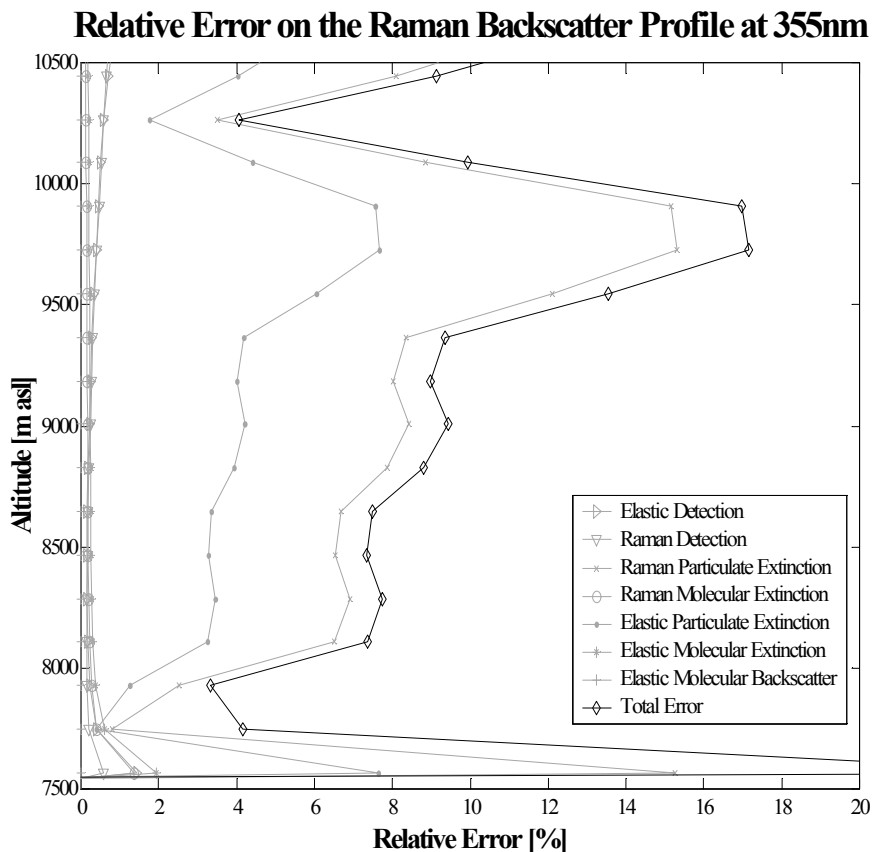


FIGURE 4-10. Errors analysis on the backscatter profile retrieved by Raman inversion. The errors are associated with the signals detection, the aerosol and molecular extinction coefficients at the Raman and the elastic wavelengths, and also with the molecular backscatter coefficient at the elastic wavelength.

In the case of low aerosol load (not shown here), the errors on the detection become the main components as in the elastic inversion scheme.

4.2.5. Error on the Lidar ratio

The sources of uncertainties in the estimate of the Lidar ratio are represented by:

- The error due to the aerosol extinction coefficient profile.
- The error associated with the estimate of the aerosol backscatter coefficient profile.

Lidar ratio profile can be determined to the altitude region where the lidar system overlap function is unity because of the aerosol extinction profile. In the altitude region where this condition is not accomplished a further systematic error source has to be accounted for.

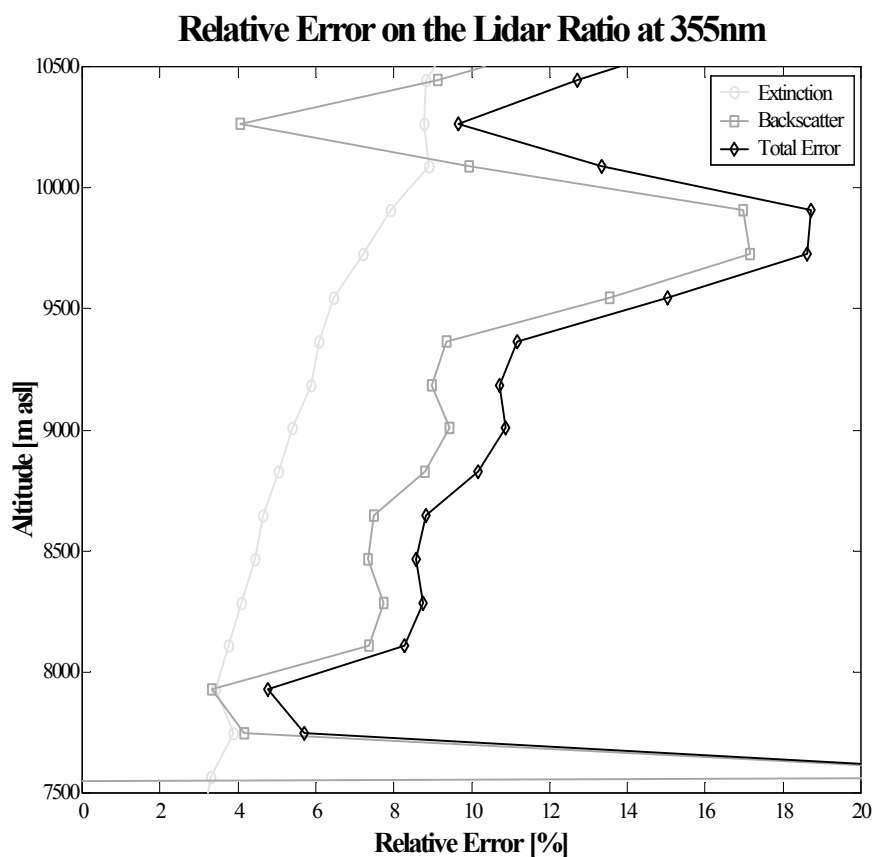


FIGURE 4-11. Errors analysis on the lidar ratio profile retrieved by Raman inversion. The errors are associated with the aerosol extinction and aerosol backscatter coefficients at the elastic wavelength.

4.2.5.a. Error due to the aerosol extinction profile

This error is described in details in the section 4.2.3. p 97.

4.2.5.b. Error due to the aerosol backscatter profile

This error is described in details in the section 4.2.4. p 103.

4.2.5.c. Total error on the Lidar ratio

The total relative error on the Lidar ratio is given by

$$\frac{dS_p}{S_p} = \left\{ \left(\frac{da_p}{a_p} \right)^2 + \left(\frac{db_p}{b_p} \right)^2 \right\}^{1/2}$$

(EQ 4.22)

Figure 4-11 shows the relative error on the lidar ratio and it is not a surprise that the error on the backscatter coefficient is stronger than the extinction one.

4.2.6. Error on the depolarization ratio

The sources of uncertainties in the estimate of the depolarization ratio are represented by:

- The statistical error due to signal detection (Theopold 1988).
- The systematic error associated with the estimate of the calibration constant.

Depolarization ratio can be calculated to the altitude region where the lidar system overlap function is different smaller than unity, because this function is the same for the two signals.

4.2.6.a. Statistical error due to signal detection

This error is described in details in the section 4.2.2.a. p 91.

4.2.6.b. Systematic error associated with the estimate of the calibration constant

The calibration of the two depolarized channels is done by circular permutation of the «parallel» and «perpendicular» PMTs assuming that the atmospheric conditions remain constant during all the period. This is generally true under clear sky condition. This calibration is not an absolute one but a relative one, indeed, one PMT intensity is corrected to record the same intensity as the other one. The calibration constant K has a value of 1.20 ± 0.04 . This uncertainty is calculated by the standard deviation on the mean value.

Due to the good linearity of the PMTs, this constant is not voltage control dependent if the ratio of the two control voltages is constant.

4.2.6.c. Total error on the depolarization ratio

The uncertainty on the depolarization ratio is given by

$$\frac{d(d)}{d} = \left\{ \left(\frac{dP^\perp}{P^\perp} \right)^2 + \left(\frac{dP^\parallel}{P^\parallel} \right)^2 + \left(\frac{dK}{K} \right)^2 \right\}^{1/2}$$

(EQ 4.23)

where $K [-]$, is the calibration constant of the system.

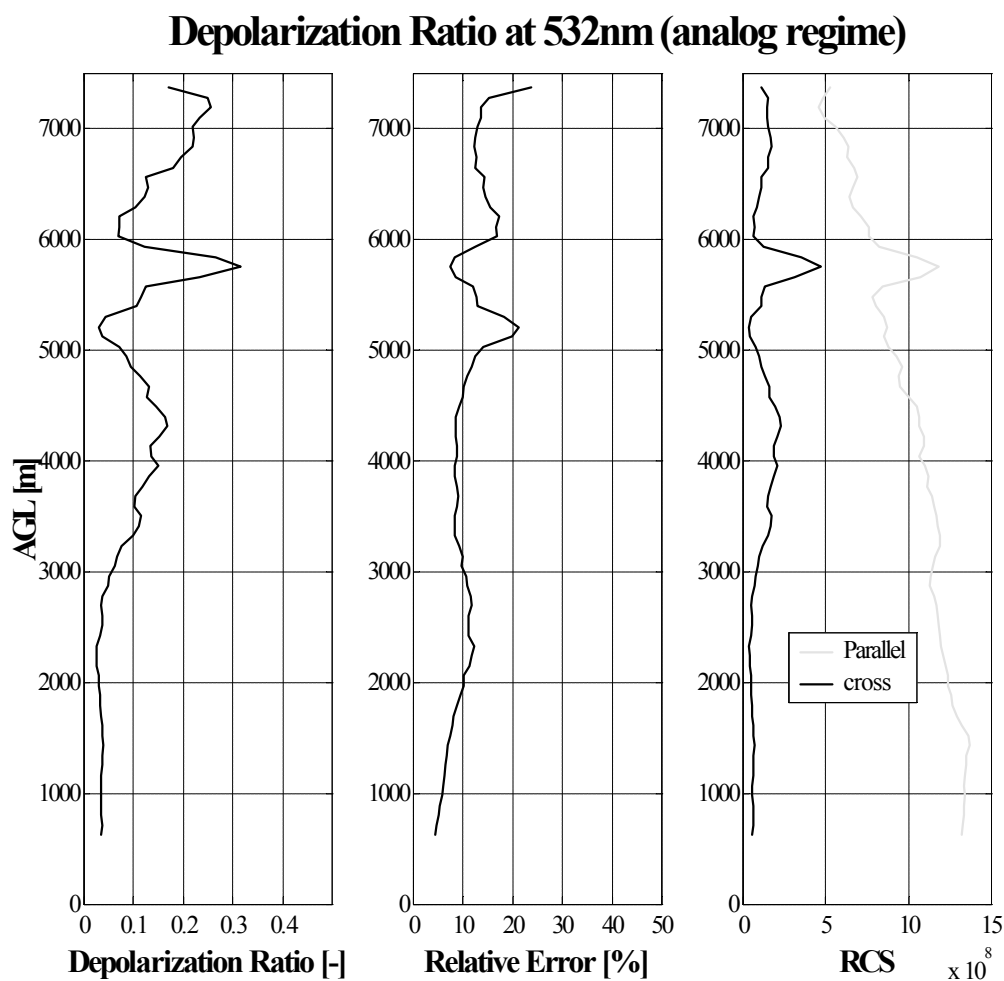


FIGURE 4-12. Depolarization ratio and its relative error. The parallel and the perpendicular signals are recorded in analog mode.

Figure 4-12 shows one example of depolarization ratio profile with its relative error. The parallel and perpendicular signals are detected in analog mode and smoothed with a sliding average (from 37.5 to 112.5m) and with a reduced resolution of 45m. Again the Poisson distribution is assumed for the error associated with the signal detection. At low altitude, this ratio is close to the molecular and spherical aerosol value (3%). The error of the depolarization ratio is smaller than 15% and reaches a maximum value of 20% at higher altitudes.

4.3. Angstrom exponent

The Angstrom exponent given by (EQ 2.35) is related to the Junge or power law size distribution (Junge 1955) by $\alpha=v-2$, where

$$\frac{dN}{d \ln(r)} = Cr^{-n} \quad (\text{EQ 4.24})$$

is the differential number density for which the radius extends from zero to infinity. However, the size distribution of aerosols typically do not follow the Junge distribution nor have radii extending from zero to infinity, and that departure from those conditions often introduces curvature in the logarithms ratio. Therefore a second-order polynomial fit of the following form is used

$$\ln[\mathbf{a}(I)] = \mathbf{a}(I_0) + b_1 \ln(I) + b_2 \ln(I)^2 \quad (\text{EQ 4.25})$$

to account for the curvature (Eck 1999), where $\alpha(\lambda_0)$ is the instantaneous extinction coefficient at the wavelength λ_0 , b_1 is the Angstrom exponent itself and b_2 is the variation of this exponent in relation to $\ln(\lambda)$.

4.4. Conclusion

This chapter has highlighted the main sources of errors on both inversion schemes and thus provided the limitation of the system. The statistical error due to the signal detection is the upper limit in clear sky condition whereas the errors associated with the lidar ratio and the aerosol extinction profiles become important with increasing aerosol load. The errors associated with the Raman detection can be reduced using a higher repetition rate of the laser.

The time averaging is also important for reducing the statistical errors in varying conditions, time sections of nearly constant particle extinction can then be determined from the time series of elastic-backscatter profiles and thus reduced the systematic error introduced by operational procedures.

4.5. References

Ansmann, A., U. Wandinger, et al. (1992). "Independent Measurement of Extinction and Backscatter Profiles in Cirrus Clouds by Using a Combined Raman Elastic-Backscatter Lidar." *Applied Optics* **31**(33): 7113-7131.

Bosenberg, J. (1998). "Ground-based differential absorption lidar for water vapor and temperature profiling: methodology." *Applied Optics* **37**(18): 3845-3860.

- David, C. (1995). Etude des nuages stratosphériques polaires et des aérosols volcaniques en régions polaires par sondage laser., Université Paris VI.
- Eck, T. F., Holben, B. N., Reid, J. S., Dubovik, O., Smirnov, A., O'Neill, N. T., Slutsker, I. and Kinne, S. (1999). "Wavelength dependence of the optical depth of biomass burning, urban, and desert dust aerosols." Journal of Geophysical Research-Atmospheres **104**(D24): 31333-31349.
- Godin, S. (1987). Etude expérimentale par télédétection laser et modélisation de la distribution verticale d'ozone dans la haute stratosphère, Université Paris 6.
- Godin, S., and al. (1999). "Ozone differential absorption lidar algorithm intercomparison." Applied Optics **38**(30): 6225-6236.
- Hoxit, L. R., and Henry, R. H. (1973). J. Atmos. Sci. **30**: 922.
- Inaba, H. and T. Kobayashi (1972). "Laser-Raman Radar -Laser-Raman scattering methods for remote detection and analysis of atmospheric pollution-." Opto-Electronics **4**: 101-123.
- Junge, C. E. (1955). "The size distribution and aging of natural aerosols as determined from electrical and optical measurements in the atmosphere." J. Meteorol. **12**: 13-25.
- Klett, J. D. (1981). "Stable analytical inversion solution for processing lidar returns." Applied Optics **20**: 211-220.
- Lenhard, R. W. (1973). Am. Meteorol. Soc. **54**: 691.
- Pappalardo, G. (2000). "Retrieval of the aerosol extinction coefficient from N₂ Raman lidar signals." EARLINET internal note.
- Planet, W., and Laver, J. (1979). NOAA-NESS; personal communication.
- Russell, P. B., Swissler, T. J., and McCormick, M. P. (1979). "Methodology for error analysis and simulation of lidar aerosol measurements." Applied Optics **18**(22): 3783-3797.
- Sasano, Y., Browell, E., V., and Ismail S. (1985). "Error caused by using a constant extinction/backscattering ratio in the lidar solution." Applied Optics **24**(22): 3929-3932.
- Sassen, K. (1994). "Advances in polarization diversity lidar for cloud remote sensing." Proceedings of the Ieee **82**(12): 1907-1914.
- Taylor, J. (1997). An Introduction to Error Analysis, University Science Books.
- Theopold, F., and Bosenberg, J. (1988). "Evaluation of DIAL measurement in presence of signal noise." proceedings of the 14th ILRC.
- Vaughan, J. M., Geddes, N. J., Flamant, P. H., and Flesia, C. (1998). Establishment of a backscatter coefficient and atmospheric database, DERA, UK.
- Wandinger, U. (1998). "Multiple-scattering influence on extinction- and backscatter- coefficient measurements with Raman and high-spectral- resolution lidars." Applied Optics **37**(3): 417-427.
- Whiteman, D., and al. (2000). "Raman lidar measurements of water vapor and cirrus clouds during the passage of hurricane Bonnie." accepted in J. of Geophys. Res.

Whiteman, D. N. (1999). "Application of statistical methods to the determination of slope in lidar data." Applied Optics **38**(15): 3360-3369.

For the purpose of using data from different stations in joint studies, and for the reliability of the database as a whole it is important that the quality of the measurements taken by the different systems is compared. Data quality depends on system hardware as well as evaluation software. Tests have been performed for both areas separately and for overall performance. Within the frame of the EARLINET project, intercomparisons of the retrieval algorithms have been performed using synthetic data for a number of situations of different complexity whereas the system comparison have been performed with well-calibrated mobile systems.

This chapter presents the results of the elastic and Raman algorithms intercomparisons and the intercomparison between the mobile micro-lidar of the Observatoire Cantonal de Neuchâtel and the Jungfrauoch lidar system.

5.1. Elastic algorithm

This section presents the intercomparison of the elastic algorithm within the frame of the EARLINET network. The complete results of this intercomparison are discussed in more details in (Böckmann 2001). Here is presented the contribution of the EPFL-Lidar group to this work with the permission of the first author, Christine Böckmann, Institute of Mathematics, University of Postdam, Germany.

5.1.1. Data simulation

Synthetic lidar signals were used for the algorithm intercomparison. In this way, the numerical correctness and accuracy of the algorithms as well as the experience of the groups and the limits of the method itself could be tested for examples with different degree of difficulty. The synthetic lidar signals were calculated with the IFT lidar simulation model. This software permits one to simulate and to evaluate elastically and inelastically backscattered lidar signals of arbitrary wavelengths in dependence on a variety of system parameters for a variable model atmosphere with arbitrary aerosol and cloud layers. Sky background, background noise, and signal noise are considered as well. Atmospheric input parameters are profiles of temperature and pressure to calculate Rayleigh scattering and profiles of extinction coefficients and lidar ratios for the simulation of aerosol and cloud layers.

For the algorithm intercomparison three different data sets of elastic backscatter signals at wave-lengths of 355, 532, and 1064nm were simulated. A US standard atmosphere (United States Committee on Extension to the Standard Atmosphere, 1976) with a ground pressure of 1013 hPa and a ground temperature of 0°C, a tropopause height of 12.0km, and isothermal conditions above were assumed. The signal profiles were simulated without signal noise. An incomplete overlap of laser beam and receiver field of view below 250m was introduced. Typical system parameters (laser power, telescope diameter, etc.) were used for the calculations. However, they are not of importance for the algorithm intercomparison. In all cases, only boundary-layer aerosols in heights below 4.5km were simulated. Minor particle scattering in the free troposphere and the stratosphere was introduced and no clouds were considered. The three simulation cases represent different atmospheric conditions with increasing degree of difficulty in data evaluation:

Case 1: The first case assumes very unrealistic atmospheric conditions. The extinction coefficient was independent of wavelength and changed stepwise from $3.0 \times 10^{-4} \text{m}^{-1}$ below 1500m to $3.5 \times 10^{-4} \text{m}^{-1}$ between 1500 and 2000m and $4.0 \times 10^{-4} \text{m}^{-1}$ between 2000 and 2440m, and decreased to values below $1.0 \times 10^{-6} \text{m}^{-1}$ above. The lidar ratio had a constant value of 50sr for all heights and all wavelengths.

Case 2: In the second case, significant aerosol load up to 4000m was simulated, see Figure 5-1. A more realistic, height-dependent extinction coefficient was assumed. In addition, the extinction coefficient changed with wavelength, with highest values for the shortest wavelength and lowest values for the longest wavelength. The lidar ratio was height-independent in the aerosol layer, but took different values of 64sr for 355nm, 62sr for 532nm, and 42sr for 1064nm. Above 4500m the lidar ratio was 45sr for all wavelengths.

Case 3: In case 3, significant aerosol load up to 3300m was simulated, see Figure 5-1. Realistic, height-dependent extinction coefficients and lidar ratios were introduced. The extinction coefficient varied quite differently with wavelength in different heights. The lidar ratio took values between 24 and 69sr, but did not vary with wavelength. Above 3600m the lidar ratio was again 45sr for all wavelengths.

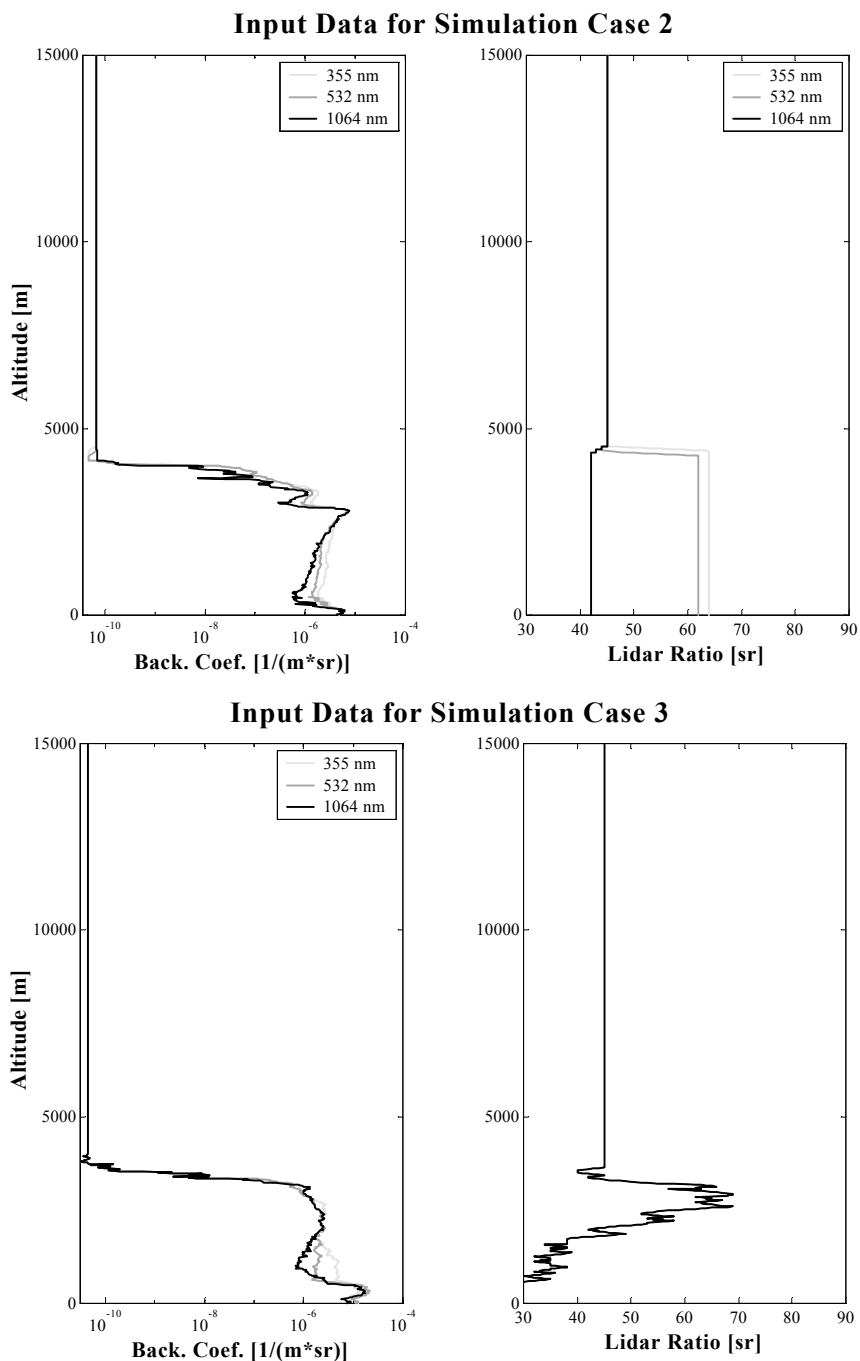


FIGURE 5-1. Backscatter coefficients and lidar ratios as input data for simulation case 2 and simulation case 3.

For the first case the input profiles of extinction coefficient and lidar ratio were provided to the participants to allow an exercise with known solutions. Cases 2 and 3 were used for the inter-comparison and the results are discussed here. The procedure of the algorithm intercomparison was as follows.

Stage 1: The simulated signals were distributed to all groups without any information on the input parameters, except the used standard atmosphere. Each group calculated particle backscatter coefficient profiles using its own algorithm.

Stage 2: Information for the correct lidar ratio profile was provided to all groups. Evaluation was repeated.

Stage 3: The reference value at calibration height was also provided. Evaluation was repeated.

The first stage was the most difficult and most realistic one, because lidar-ratio profiles and reference values were unknown. Therefore, not only the correctness and accuracy of the algorithms was proven but also the dependence of the solution on estimates of the lidar ratio and the reference value. In the third and final stage all parameters are known, so it proves definitively the numerical correctness, i.e., the accuracy and stability of the algorithms depending on the noise level and other circumstances.

5.1.2. Intercomparison results

The following figures and tables show only the results of the EPFL Lidar group, no comparisons are made with the other participating groups in the intercomparison, but they will appear as the mean values in the tables. The different input parameters of the three cases are summarized in Table 5-1. For the first stage of the three cases, the reference altitude is set between 14000 and 15000m and the reference value is given by the molecular backscatter coefficient at that altitude. A height-constant lidar ratio of 45sr is taken as it is proposed in (Vaughan 1998). For the second stage, the reference altitude and the reference value are the same than is the first case.

TABLE 5-1 Input parameters of the three cases

| Stage | Case 1 | | Case2 | | Case 3 | |
|-------|--|---|--|-------------|--|-------------|
| | Reference Values | Lidar Ratio | Reference Values | Lidar Ratio | Reference Values | Lidar Ratio |
| 1 | Molecular at 15000m | 45sr | Molecular at 1500m | 45sr | Molecular at 15000m | 45sr |
| 2 | Molecular at 15000m | 28sr (355nm) 39sr (532nm) 77sr (1064nm) | Molecular at 15000m | Variable | Molecular at 15000m | Variable |
| 3 | $4 \times 10^{-10} [\text{m}^{-1} \text{sr}^{-1}]$ at 9000m | 28sr (355nm) 39sr (532nm) 77sr (1064nm) | 6.6667×10^{-11} [$\text{m}^{-1} \text{sr}^{-1}$] at 9000m | Variable | 4.4444×10^{-11} [$\text{m}^{-1} \text{sr}^{-1}$] at 9000m | Variable |

Figure 5-2 shows the retrieved aerosol backscatter coefficient profiles between 0 and 4500m at 355nm in comparison to the simulation input profile of case 1 concerning all the three stages

(from left to right: stage 1, stage 2 stage 3). The results at the three wavelengths are also given in the annex: Figure 10-5, p 205, Figure 10-6, p 206 and Figure 10-7, p 207.

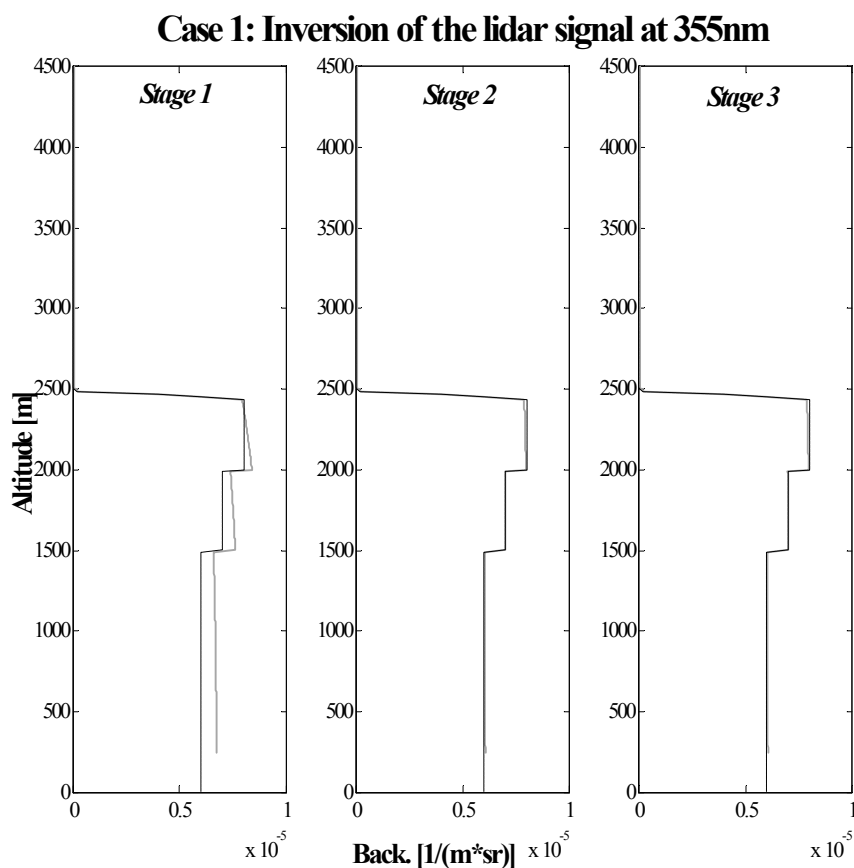


FIGURE 5-2. Retrieved aerosol backscatter coefficient at 355nm (gray line) in comparison to the simulation input profile (black dot-line) for the case1. The left, middle and right panels give the stage 1, stage 2 and stage 3, respectively.

The first stage of this first case highlights the importance of the lidar ratio compared to the reference value. Indeed, no differences are observed below 4500m between the stage 2 and the stage 3. In this case, a constant lidar ratio of 45sr overestimates the backscatter coefficient below 4500m.

The results for case 2 are shown in details for the three wavelengths in Figure 10-8, p 208, Figure 10-9, p 209, Figure 10-10, p 210, and as well as in the first column of Table 5-2, Table 5-3 and Table 5-4. Those tables give the mean relative errors between 300 and 3500m and between 300 and 3000m for the case 2 and the case 3, respectively and also the mean absolute error between 3500 and 15000m and between 3000 and 15000m for the case 2 and case 3, respectively. The mean values are the average values of the participant groups. In Figure 5-3, the retrieved backscatter coefficient profiles at 355nm are given between 0 and 3500m in the left column and the relative error in the right column. In the first stage the relative errors from

the correct solution are below 70%, 35% and 6% at 355, 532 and 1064nm, respectively. Especially for the wavelength 355nm the deviations are very large whereas with increasing wavelength the relative errors become smaller. This is explained by the decrease of the molecular backscatter coefficient with increasing wavelength and by the smaller sensitivity of the lidar ratio at longer wavelength. The mean errors over all groups for the wavelengths of 355, 532, and 1064nm are about 65%, 30% and 15%, respectively. In the second stage with known lidar-ratio profile but still unknown reference value the relative errors from the correct solution are smaller and are below 7%, 3% and 5% at 355, 532 and 1064nm. The mean errors over all groups for the wavelengths of 355, 532, and 1064nm are about 7%, 5% and 8%, respectively. In stage 3, with increasing knowledge on the input parameters (stages 2 and 3), the errors are below 5% for all wavelengths in the range between 300 and 3500m. The mean error over all groups stays well below 2% for all wavelengths. In the range from 3500 to 15000km the mean absolute error over all groups is smaller than $1 \times 10^{-8} \text{m}^{-1} \text{sr}^{-1}$. Both facts indicate that the EPFL algorithm works well and can in general reproduce the simulated profiles of case 2 if all input parameters are known.

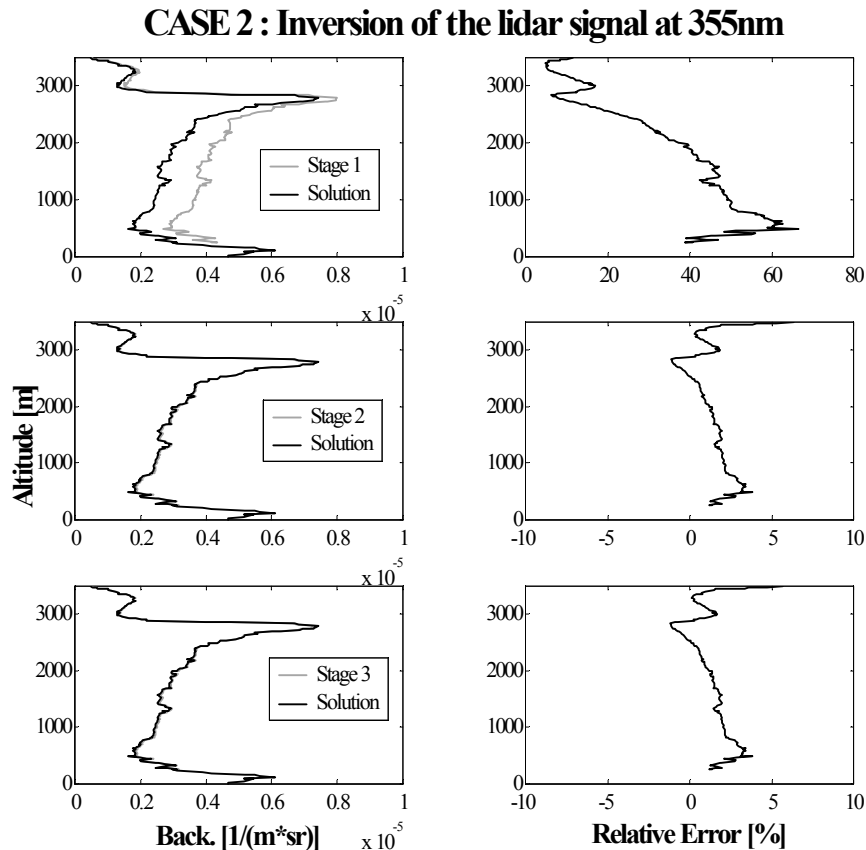


FIGURE 5-3. Retrieved aerosol backscatter coefficient at 355nm (gray line) in comparison to the simulation input profile for the case2 (black line). The right column gives the relative errors with regard to the simulation input profile.

The results for example 3, which is a more realistic one with a height-dependent lidar ratio but still without statistical noise and without clouds, are shown in Figure 10-11, p 211, Figure 10-12, p 212, Figure 10-13, p 213 and in the second column parts of Table 5-2, Table 5-3 and Table 5-4. Figure 5-4 shows the results at 355nm, for the stage 1, stage 2 and stage 3 and their relative errors. Those relative errors are more or less in the same ranges as for case 2. In detail, the relative errors for the first stage are below 50%, 10% and 10% at 355, 532 and 1064nm, respectively. Moreover, for stage 2 the respective errors are about 10% at the three wavelengths. For the third stage the errors are somewhat larger than for the third stage of case 2, which is mainly caused by the height-dependent lidar ratio. In the range between 300 and 3000 m, the mean error over all groups stays well below 5% for all wavelengths and in the range from 3000 to 15000km the mean absolute error over all groups is smaller than $1 \times 10^{-8} \text{m}^{-1} \text{sr}^{-1}$.

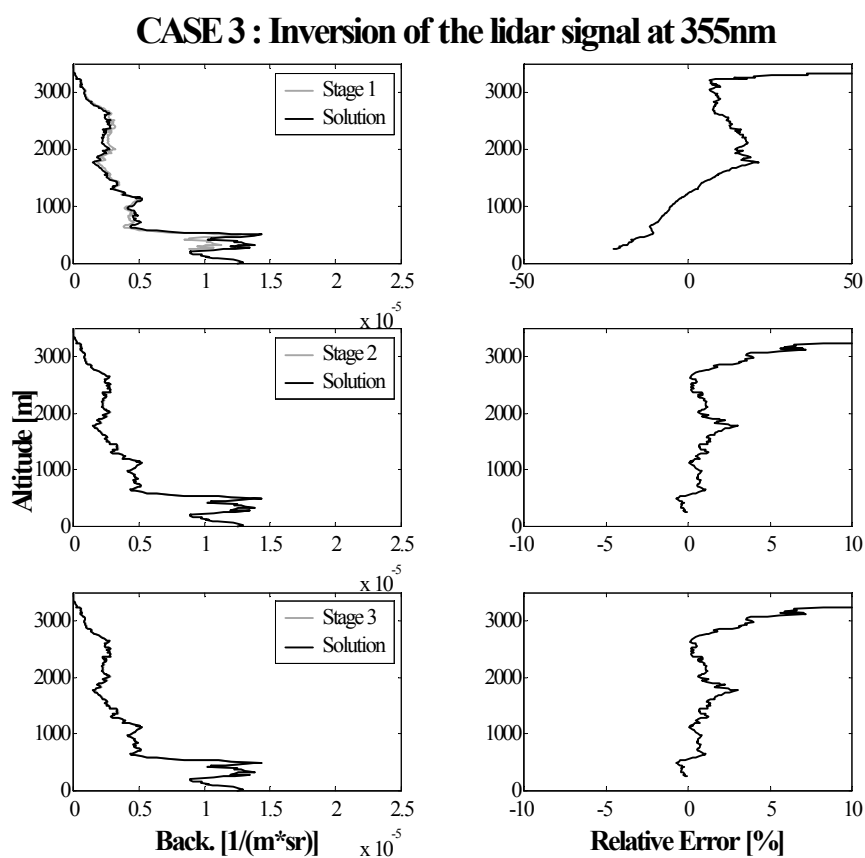


FIGURE 5-4. Retrieved aerosol backscatter coefficient at 355nm (gray line) in comparison to the simulation input profile for the case2 (black line). The right column gives the relative errors with regard to the simulation input profile.

The algorithm intercomparison showed that in general the data evaluation schemes of the different groups work well. Differences in the solutions can mainly be attributed to differences in the estimate of the input parameters. If the input parameters are known, remaining errors are of the order of a few percent. The unknown height-dependent lidar ratio had the largest influence

on the solutions, which demonstrates the need for independent measurements of the particle extinction coefficient, e.g., with the Raman method.

The unknown reference value was of minor importance for the examples presented here, because height regions with dominating Rayleigh scattering were present in all cases. It should be mentioned, however, that this is not necessarily the case under real atmospheric conditions. Especially at 1064nm, particle scattering often dominates the signals in the entire measurement range, which may cause additional errors that were not discussed here.

TABLE 5-2 Mean errors for the wavelength 355nm in stage 3

| Stage 3: 355nm | | | | |
|----------------|-------------------------|---|-------------------------|---|
| Group | Case 2 | | Case 3 | |
| | Mean Relative Error [%] | Mean Absolute Error [$\text{m}^{-1}\text{sr}^{-1}$] | Mean Relative Error [%] | Mean Absolute Error [$\text{m}^{-1}\text{sr}^{-1}$] |
| | 0.3075 - 3.4875km | 3.5025 - 15.0675km | 0.3075 - 3.0075km | 3.0025 - 15.0675km |
| EPFL | 1.54±0.91 | 1.54x10 ⁻⁸ ±0.91x10 ⁻⁸ | 1.01±0.84 | 1.85x10 ⁻⁸ ±1.41x10 ⁻⁸ |
| Mean values | 1.68 | 1.33x10 ⁻⁸ | 3.93 | 1.78x10 ⁻⁸ |

TABLE 5-3 Mean errors for the wavelength 532nm in stage 3

| Stage 3: 532nm | | | | |
|----------------|-------------------------|---|-------------------------|---|
| Group | Case 2 | | Case 3 | |
| | Mean Relative Error [%] | Mean Absolute Error [$\text{m}^{-1}\text{sr}^{-1}$] | Mean Relative Error [%] | Mean Absolute Error [$\text{m}^{-1}\text{sr}^{-1}$] |
| | 0.3075 - 3.4875km | 3.5025 - 15.0675km | 0.3075 - 3.0075km | 3.0025 - 15.0675km |
| EPFL | 0.91±0.72 | 9.68x10 ⁻¹⁰ ±1.00x10 ⁻⁹ | 1.36±0.39 | 1.24x10 ⁻⁹ ±1.80x10 ⁻⁹ |
| Mean values | 1.48 | 3.83x10 ⁻⁹ | 3.13 | 4.4x10 ⁻⁹ |

TABLE 5-4 Mean errors for the wavelength 1064nm in stage 3

| Stage 3: 1064nm | | | | |
|-----------------|-------------------------|---|-------------------------|---|
| Group | Case 2 | | Case 3 | |
| | Mean Relative Error [%] | Mean Absolute Error [$\text{m}^{-1}\text{sr}^{-1}$] | Mean Relative Error [%] | Mean Absolute Error [$\text{m}^{-1}\text{sr}^{-1}$] |
| | 0.3075 - 3.4875km | 3.5025 - 15.0675km | 0.3075 - 3.0075km | 3.0025 - 15.0675km |
| EPFL | 2.88±0.60 | 1.18x10 ⁻¹⁰ ±7.26x10 ⁻¹⁰ | 3.05±0.39 | 7.02x10 ⁻¹⁰ ±5.10x10 ⁻⁹ |
| Mean values | 1.38±1.74 | 5.12x10 ⁻¹⁰ ±8.59x10 ⁻¹⁰ | 2.02±2.63 | 1.06x10 ⁻⁹ ±1.56x10 ⁻⁹ |

5.2. Raman algorithm

This section presents the intercomparison of the Raman algorithm. The complete results of this intercomparison are discussed in more details in (Pappalardo 2001). Here is presented the contribution of the EPFL-Lidar group to this work with the permission of the first author, Pappalardo Gelsominia, Istituto di Metodologie Avanzate di Analisi Ambientale, Potenza, Italy.

5.2.1. Data simulation

Simulated nitrogen Raman data, produced at IFT were distributed together with results as a training case for the intercomparison of Raman algorithms. Raman signals were simulated for a simple stepwise changing extinction profile with the values $0.3 \times 10^{-3} \text{m}^{-1}$ below 1500m, $0.35 \times 10^{-3} \text{m}^{-1}$ between 1500 and 2000m, $0.4 \times 10^{-3} \text{m}^{-1}$ between 2000 and 2445m, and a decrease to $2.0 \times 10^{-7} \text{m}^{-1}$ above 2500m, $2.0 \times 10^{-8} \text{m}^{-1}$ above 7500m and $2.0 \times 10^{-9} \text{m}^{-1}$ above 10000m at a wavelength of 532nm. The wavelength dependence parameter (or Angstrom coefficient), k , between the emitted light at 532nm and the received Raman nitrogen light at 607nm was set $k=1.5$. A constant lidar ratio of 50sr was used. Three different signals, one without noise, one with a shot noise for 10000 and one with a shot noise for 1000 laser pulses were simulated. The introduction of noise was the major difference to the former EARLINET simulations. Again, a US standard atmosphere with a ground pressure of 1013hPa and a ground temperature of 0°C , a tropopause height of 12.0km, and isothermal conditions above were assumed. An incomplete overlap of laser beam and receiver field of view below 250m was introduced. The goal of this first case is to select appropriate spatial averaging to obtain a statistical error on the aerosol extinction coefficient of $<10\%$ in the height range from 500 to 2000m.

The case 1 is similar to the training case, but is divided into 15 profiles with 3600 laser shots each (corresponds to 2 minutes averages with 30Hz system). The goal of this case is to select appropriate spatial averaging for temporal averages of 10, 20 and 30 minutes to obtain a statistical error on the aerosol extinction coefficient below 10% in the height range from 500 to 2000m.

The case 2 has unknown solution and both elastic and Raman data are divided into 20 profiles with 3600 laser shots (corresponds to 2 minutes averages with 30Hz system). The goal of this case is to determinate the mean extinction, the mean backscatter and the mean lidar ratio profiles for the entire time period.

As the data are simulated, the Poisson distribution provides negligible errors and cannot be applied in this intercomparison. Thus the error associated with the signal detection is based on the square root of the variance (standard deviation). The error related to the determination of the nitrogen profile is calculated with an uncertainty of 3% on the temperature.

5.2.2. Intercomparison results

For the training case, a parabolic gliding average with an initial windows of 5 bins and a final one of 10 bins is applied first. The resolution is reduced from 15 to 30m and from 15 to 60m, for the 10000 shots case and the 1000 shots case respectively. Table 5-5 and Table 5-6 show

the mean deviation and root-mean-square (RMS) deviation from the solution calculated at three different range heights corresponding to the first three altitude ranges present in the solution, from 250 to 1492.5m, from 1507.5 to 1987.5m and 2002.5 to 2437.5m, respectively. The RMS deviations are 2.75%, 3.46% and 8.75% for the 10000 shots case and, 3.55%, 2.88 and 5.92% for the 1000 shots cases. The final resolution of the 1000 shots case is larger than the 10000 shots case in order to counteract the increase of the noise in the second case and provides better RMS deviation at high altitude.

TABLE 5-5 Deviations from the solution for the case with 10000 laser shots

| 10000 laser shots | | | | | |
|--------------------|-------------------|--------------------|-------------------|--------------------|-------------------|
| 250 - 1492.5m | | 1507.5 - 1987.5m | | 2002.5 - 2437.5m | |
| Mean Deviation [%] | RMS Deviation [%] | Mean Deviation [%] | RMS Deviation [%] | Mean Deviation [%] | RMS Deviation [%] |
| 1.90 | 2.75 | 0.11 | 3.46 | -4.42 | 8.75 |

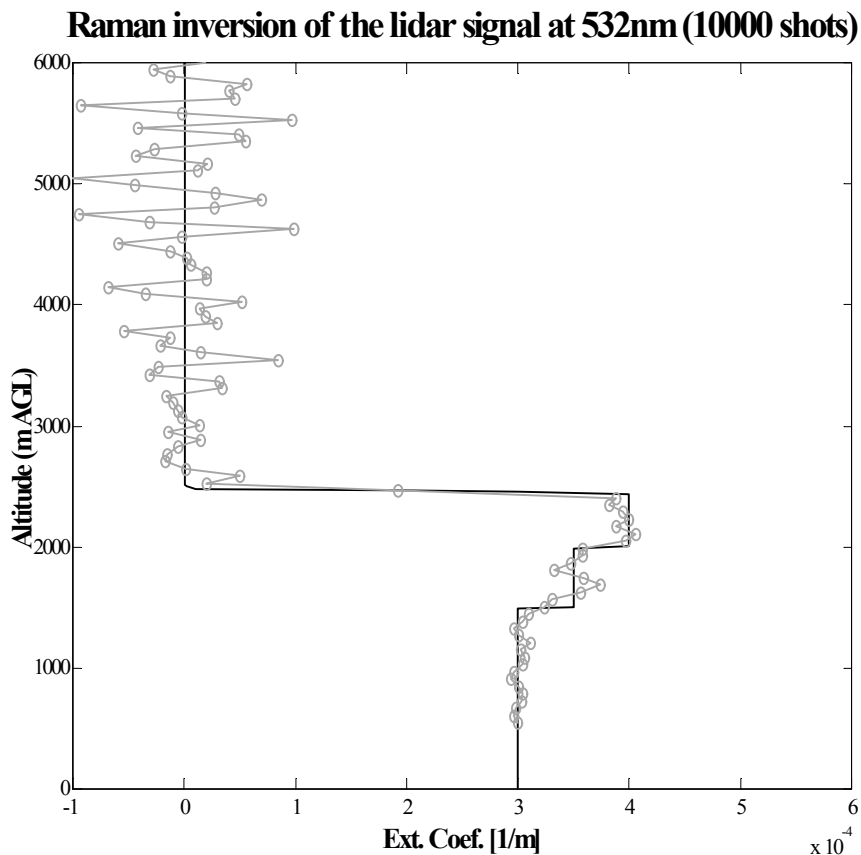


FIGURE 5-5. Retrieved aerosol extinction profile of the Raman training case (gray line), corresponding to 10000 shots, compared with the given solution (black line).

TABLE 5-6 Deviations from the solution for the case with 1000 laser shots

| 1000 laser shots | | | | | |
|------------------|-----------|------------------|-----------|------------------|-----------|
| 250 - 1492.5m | | 1507.5 - 1987.5m | | 2002.5 - 2437.5m | |
| Mean | RMS | Mean | RMS | Mean | RMS |
| Deviation | Deviation | Deviation | Deviation | Deviation | Deviation |
| [%] | [%] | [%] | [%] | [%] | [%] |
| 3.55 | 4.91 | -0.66 | 2.88 | -1.80 | 5.92 |

Figure 5-5 and Figure 5-6 show the results of the Raman training case (gray line), corresponding to 10000 laser shots and the case of 1000 laser shots, respectively and are compared with the given solution (black line).

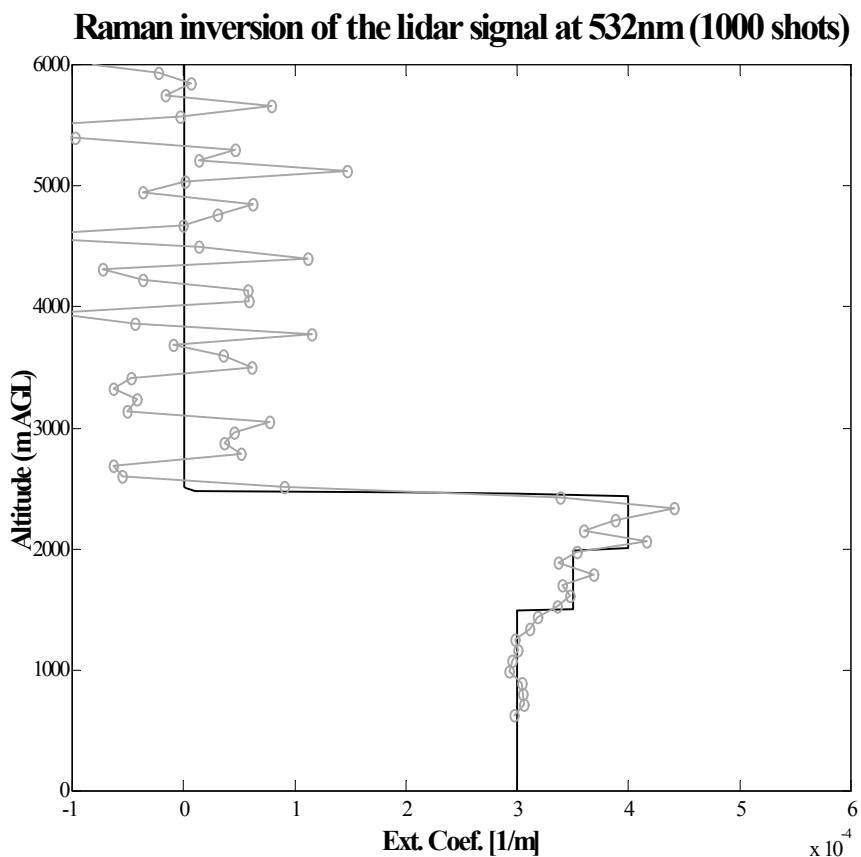


FIGURE 5-6. Retrieved aerosol extinction profile of the Raman training case (gray line), corresponding to 1000 shots, compared with the given solution (black line).

For the case 1, the signals are smoothed with a gliding average of 75 to 900m between 300 and 14000m and then reduces to a resolution of 30m. The pure molecular region is set to 14000m.

Figure 5-7 shows the extinction, backscatter and lidar ratio profiles of the Raman case 2 for temporal average of 30 minutes or 54000 laser shots. Also shown are the given solution and the elastic extinction and backscatter profiles obtained by Fernald inversion with a constant lidar ratio of 40sr. The Raman profile is framed by two red lines that represent the absolute error of this profile whose maximum is below 10% at 2500m.

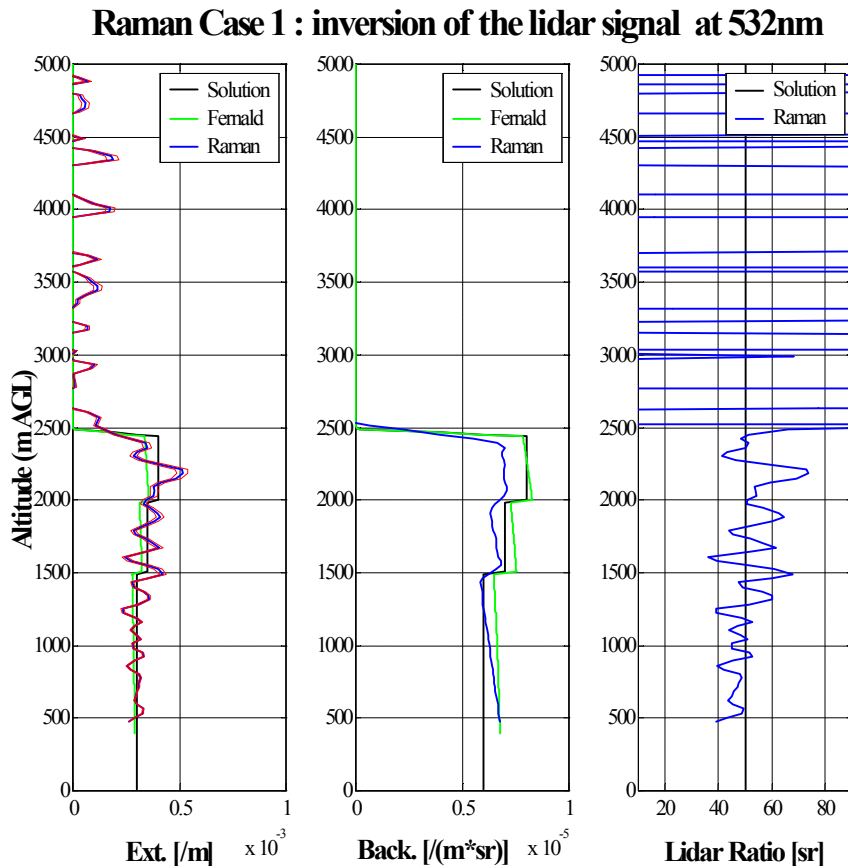


FIGURE 5-7. Retrieved aerosol extinction, backscatter and lidar ratio profiles of the Raman case 1 for temporal average of 30 minutes or 54000 laser shots, compared with the given solution and the Fernald inversion of the elastic signals with a constant lidar ratio of 40sr.

The case 2 presents varying atmospheric conditions and must be divided into two time periods of 15 minutes each. The signals are smoothed with this with the same input parameters than in the previous case. Figure 5-8 shows the retrieved aerosol extinction and its relative error, backscatter and lidar ratio of the Raman case 3 for temporal average of 15 minutes or 36000 laser shots (gray square and gray round lines) and 30 minutes (black line). The latter is the mean value of the two former, except for the error which is the square root of the sum of the variances. Again the relative error on the extinction profile is below 10% below 2500m for the three temporal averages.

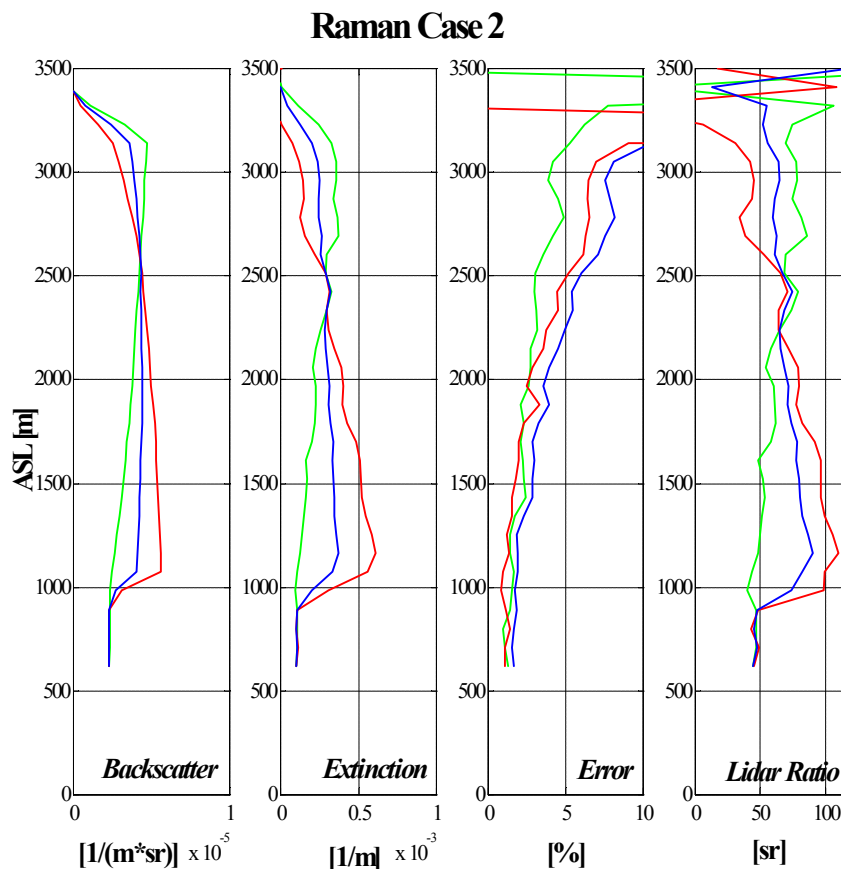


FIGURE 5-8. Retrieved aerosol extinction and its relative error, backscatter and lidar ratio profiles of the Raman case 2 for temporal average of 15 minutes (green and red lines) and 30 minutes (blue line).

The case 1 and case 2 are still to be evaluated in the frame of the EARLINET project.

5.3. System intercomparison

Lidar systems are rather complex, involving several subsystems, and their performance is critically dependent on a number of adjustments that are not easily standardized. To achieve comparable performance at many stations which are widely spread over Europe it is therefore mandatory to perform direct intercomparisons at system level. For EARLINET these intercomparisons required a rather big effort because many of the systems are not transportable. It is why it was impossible to organize a single central intercomparison campaign. To keep the effort manageable for the participating groups the main part of the intercomparisons were made against the two transportable systems: the lidar of the Meteorologisches Institut der Ludwig-Maximilians-Universität München (MIM), and the lidar of the Max-Planck-Institut für Meteorologie Hamburg (MPI). Both systems emit three laser wavelengths in the ultraviolet (355nm), green (532nm) and infrared (1064nm). The MIM system additionally has a scanning

capability, the MPI system is additionally equipped with a Raman channel at 387nm. The goal of each intercomparison experiment was to derive several aerosol extinction and backscatter profiles from all participating lidar systems under different meteorological conditions. It was considered desirable to perform intercomparisons for four different episodes under conditions without low clouds on at least two different days, but deviations from this are tolerable if the results that could be achieved in the given time are convincing. The lidar systems were located very close together with a horizontal distance less than 500m. Each compared profile has been averaged over typically 15-30 minutes in time and 50-300m in space. Comparisons could best be made if the amount of aerosol in the atmosphere was moderate. Since it was impossible to deliver either of the two transportable lidar systems at the Jungfraujoch, a comparison with the micro-lidar of the Observatoire Cantonal de Neuchâtel (OCN) was performed. This micro-lidar is very small and can be easily transported. It has been compared to the MPI system in September 2000 with good results, especially at nighttime the performance of the system is comparable to lidars with much more powerful lasers. However the intercomparisons are restricted to elastic detection at 532nm and the retrieve of the backscatter profiles is made using only the OCN algorithm in order to avoid introducing systematic errors.

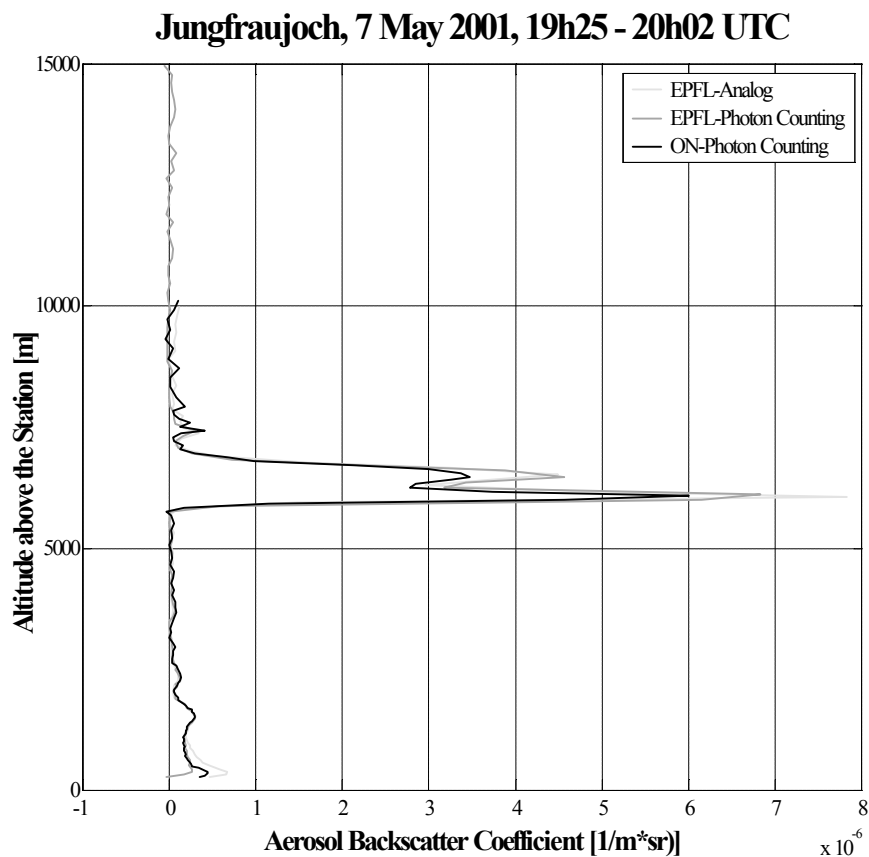


FIGURE 5-9. Intercomparison of aerosol backscatter profiles at 532 nm between OCN and EPFL in presence of aerosol and cirrus clouds. Measurements were taken on May 7, 2001.

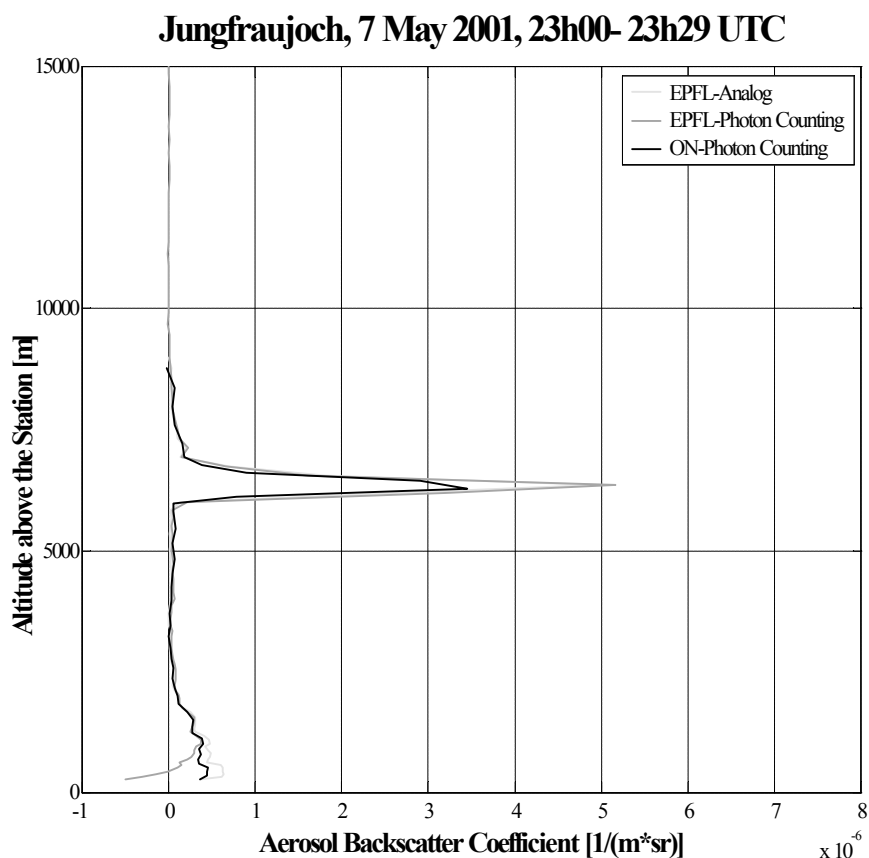


FIGURE 5-10. intercomparison of aerosol backscatter profiles at 532 nm between OCN and EPFL in presence of aerosol and cirrus clouds. Measurements were taken on May 7, 2001

Measurements have been taken on May 7 and 8, 2001, all measurements were at nighttime to extend the intercomparison range to higher altitudes. Although the measured aerosol backscatter was quite small, as expected, on May 7 some aerosol has been detected up to altitudes of 1500m above the Station (see Figure 5-9 and Figure 5-10). Additionally, cirrus clouds were present and they can be regarded as “aerosol” for the purpose of this study. But cirrus is usually much more inhomogeneous than other aerosol layers, so one has to be very careful when comparing cirrus backscatter from different lidar systems against each other. The systems have different field of views and point to different parts of the atmosphere, which can lead to higher deviations between the measured profiles than expected. On May 8 the atmosphere was very clean and the whole measurement range can be regarded as within the free troposphere (see also the changed scale for aerosol backscatter in Figure 5-11). For the calculation of the deviations, from the EPFL only the analog channel has been chosen. Photon counting and analog channel showed generally very good agreement, only in the near range the photon counting channel was saturated and could not be used for the calculation of aerosol backscatter profiles. Cases with moderate or high aerosol load have not been required at this site because of the high altitude of the station.

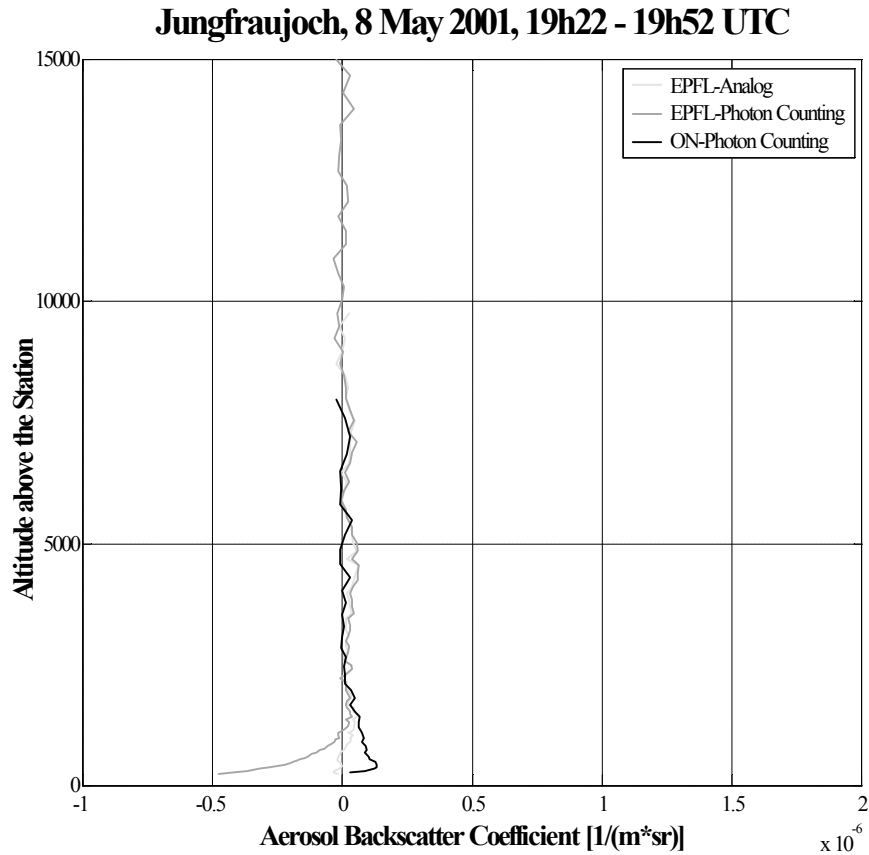


FIGURE 5-11. Intercomparison of aerosol backscatter profiles at 532 nm between OCN and EPFL under low aerosol conditions. Measurements were taken on May 8, 2001.

TABLE 5-7 Mean deviations and standard deviations for the three intercomparison between the OCN and the EPFL lidar at 532nm.

| Date [UTC] | Wavelength [nm] | Height Range [m asl] | Mean Dev. $\times 10^7$ [$\text{m}^{-1}\text{sr}^{-1}$] | Standard Dev. $\times 10^7$ [$\text{m}^{-1}\text{sr}^{-1}$] |
|-----------------------------|--------------------|-------------------------|--|--|
| 2001/05/07 19h25 - 20h02 | 532 | 4000 - 5400 | -0.6 (-20.9%) | 0.9 (32.5%) |
| | | 5600 - 9000 | 0.1 | 0.3 (22%) |
| | | 9600 - 10600 (Ci) | -5.7 (-16.6%) | 7.5 (22%) |
| 2001/05/07 23h00 - 23h29 | 532 | 4000 - 5200 | -0.9 (-21.1%) | 1.1 (25.4%) |
| | | 5700 - 9100 | 0.1 | 0.2 |
| | | 9700 - 10400 (Ci) | -5.9 (-25.9%) | 7.2 (31.5%) |
| 2001/05/08 19h22 - 19h52 | 532 | 4000 - 11600 | -0.15 | 0.5 |

All deviations between the profiles are much below the $5 \times 10^{-7} \text{m}^{-1} \text{sr}^{-1}$ margin, within the aerosol layer detected on 7 May. They even are in the range of the allowed relative values. In the cirrus clouds the deviations are little higher than they would be allowed for aerosol layers. Considering the difficulties that are connected with the inhomogeneity of cirrus clouds, this result can be regarded as sufficiently accurate to prove the quality of the systems also under conditions of high aerosol backscatter.

5.4. Conclusion

After this chapter, it is now evident that Fernald algorithm gives good results with no numerical errors. Generally, the main source of discrepancies is the data treatment (binning, reference values,...) and the inversion scheme is dependent on such errors. The Raman algorithm inter-comparison is still in progress but until now, no crude error have been detected. The hardware intercomparison allows to conclude that the Jungfraujoch lidar system has no evident systematic error.

The main conclusion of the combination of this chapter and the previous one dedicated to the data treatment and error analysis is that this lidar system can provide good measurements with a 10% and 20% error during daytime and nighttime measurements respectively.

5.5. References

- Böckmann, C., and al. (2001). "Algorithm intercomparison of the backscatter lidar." in EARLINET: Quality Assurance Report. internal note: 8-18.
- Pappalardo, G., and al. (2001). "Algorithm intercomparison of the Raman lidar." in EARLINET: Quality Assurance Report. internal note: 18-25.
- Vaughan, J. M., Geddes, N. J., Flamant, P. H., and Flesia, C. (1998). Establishment of a backscatter coefficient and atmospheric database, DERA, UK.

This chapter presents the submitted article to *Applied Optics*. This article deals with the general characteristics of the lidar system installed at the Jungfraujoch Observatory. Aerosol backscatter and extinction profiles from the both methods are shown, as well as depolarization ratio and water vapor mixing ratio profiles.

This article has to be seen as a card of the present system lidar system at the Jungfraujoch observatory. Thus it is like a abstract of the previous chapters.

Submitted to Applied Optics, October 2001

**Development of a multiwavelength aerosol and water vapor lidar at the Jungfraujoeh
Alpine Station (3580m ASL) in Switzerland**

Gilles Larchevêque, Ioan Balin, Remo Nessler, Philippe Quaglia, Valentin Simeonov, Hubert
van den Bergh, and Bertrand Calpini

Air Pollution Laboratory, Swiss Federal Institute of Technology
CH – 1015 Lausanne, Switzerland

Abstract

The Jungfraujoeh Research Station (46.55°N, 7.98°E, ASL: 3'580m) has since decades contributed in a significant manner to the systematic observation of the earth atmosphere both with in situ measurements and trace gas column detection. This paper reports on the development of a lidar system bringing the measurement potential of highly resolved atmospheric parameters both in time and space with the goal of achieving long term monitoring of atmospheric aerosol optical properties and water vapor content. From the simultaneously detected elastic-backscatter signals at 355, 532 and 1064nm, Raman signals from nitrogen at 387nm and 607nm and water vapor at 407nm, the aerosol extinction and backscatter coefficients at three wavelengths and water vapor mixing ratio are derived. Additional information about particle shape is obtained by depolarization measurements at 532nm Water vapor measurements using both nitrogen and water vapor Raman returns from the 355nm laser beam are demonstrated with a vertical range resolution of 75m and an integration time of 2 hours. The comparison to the water vapor profile derived from balloon measurements (Snow White technique) showed excellent agreement. The system design and the results obtained by its operation are reported.

Introduction

The world's scientific community agrees upon the fact that human activities have an impact on the climate. Global warming and the induced climate change are among the most important environmental issues nowadays [1]. The enhanced greenhouse effect due to human activities emitting carbon dioxide, methane, nitrous oxide, chlorofluorocarbons (CFCs), or ozone, is investigated in great details today. This is not the case for water vapor and aerosols essentially because of their non-homogeneous distributions both in space and time. They are considered as the largest uncertainty in the understanding of the earth radiation budget [2]. Water vapor is the primary greenhouse gas and despite its small amount in the free troposphere and stratosphere, recent studies have shown that it may play an essential role in the earth climate [3-6]. Aerosols affect the heat balance of the earth both directly by reflecting and absorbing solar radiation and by absorbing and emitting some terrestrial infrared radiation, and indirectly by influencing the properties and processes of clouds and possibly by changing the heterogeneous chemistry of reactive greenhouse gases [2, 3].

For global atmosphere model prediction, direct radiative forcing can be accurately calculated at least in principle once the optical constants, size distribution, and atmospheric concentration of the aerosols are known. However aerosol radiative properties are sensitive functions of particle size, optical depth, and composition, and they exhibit strong variation with wavelength in both the visible and thermal regions of the spectrum. Further determination of the indirect aerosol effect is more difficult since this involves complex physical interactions that are not fully understood yet [2].

Well-calibrated instruments with a long-term monitoring capability are needed to measure changes in stratospheric and tropospheric aerosols concentrations and radiative properties, changes in atmospheric water vapor and changes in cloud covering and cloud radiative properties. In situ aircraft measurements, sun photometer, radar and lidar (ground based, airborne or in space) are among the different possibilities. This paper focuses on describing the current configuration and ability of a combined multi-wavelength Raman elastic-backscatter lidar system installed since 1999 at the Jungfraujoch Research Station (Lat: 46.55°N, Long: 7.98°E, ASL: 3'580m). Because of its location the station is above the planetary boundary layer most of the time and the aerosol load and the humidity levels are extremely low. These are unique conditions for high altitude lidar observations in central Europe, reducing the signal dynamic range, the attenuation and the induced noises well below the values of other similar facilities in Europe. Furthermore the Jungfraujoch observatory is a world known atmospheric monitoring station with observations since the 50's [7-11]. It is an essential part of different international networks for monitoring of the atmosphere and many different instruments, providing well-established quality data are installed there.

The Jungfraujoch lidar station was designed as a multifunctional system allowing multi-wavelength aerosol measurements by elastic and Raman methods, depolarization measurements at 532nm and water vapor mixing ratio measurements by Raman technique. The specifications of the Jungfraujoch lidar system are given in Table 1. Future implementation of pure rotational Raman temperature measurements for the lower altitudes completed with Rayleigh temperature measurements for the higher altitudes and a DIAL tropospheric and stratospheric ozone channel will expand the capability of the instrument. The results will be compared with the data of instruments for column and *in situ* measurements of similar atmospheric parameters already installed at the station. The lidar is included into the European Aerosol Research Lidar NETwork (EARLINET) project that incorporates 19 aerosol lidars all over Europe. The network was established to perform studies of the general characterization of the vertical aerosol distribution and its dependence on season, weather regime, diurnal cycle and local effects, and also to investigate the temporal and spatial development of the aerosol properties over Europe [12].

Methodology

The advantages and drawbacks of aerosol lidars for deriving optical aerosol parameters have been widely discussed in the literature [13, 14]. There are two similar approaches for solving the ill posed problem of determining aerosol extinction coefficient from a single wavelength lidar, the Fernald or the Klett inversion algorithms. Another approach is to use Raman scattering from atmospheric nitrogen as an additional signal with a well-known backscatter coefficient [15, 16]. The disadvantage of this method is the very low efficiency of the spontaneous vibrational Raman scattering resulting in low signal level thus suitable predominantly for nighttime measurements. In our data treatment we have used Fernald and Raman techniques to retrieve the aerosol extinction and backscatter coefficients. Using the spontaneous vibrational Raman signals from atmospheric nitrogen and water vapor, the range resolved water vapor mixing ratio is retrieved, a technique that has become a standard procedure for nighttime water vapor measurement [17].

If the atmosphere is probed by a polarized laser beam the backscatter light will maintain the polarization within a limit of 2-3% if the scattering is due to molecules (Rayleigh scattering) or homogeneous spherical particles (Mie scattering) in the single scattering approximation, whereas non-spherical particles or multiple scattering will induce some degree of depolarization. The degree of depolarization in lidar applications is measured usually by the depolarization ratio that is the ratio between the intensities of the returned cross-polarized and parallel-polarized signals. Analyzing the depolarization ratio, information about particle shape and phase or presence of multiple scattering can be derived [18, 19].

As already mentioned, the aerosol size distribution is a key parameter. Its retrieval is possible if independent measurements of aerosol extinction and backscatter coefficient are available at only a few lidar wavelengths [20, 21]. The Jungfraujoch lidar enables to determinate three backscatter coefficients and two extinction coefficients. Table 1 summarizes the different wavelengths and measured parameters that are currently performed at the Jungfraujoch together with their respective limit of detection.

TABLE 1. Specifications of the Jungfraujoch Lidar system. Tropospheric and stratospheric measurements.

| Measured parameter | Wavelength of the signal used (nm) | Complementary information needed | Range | Vertical resolution | Temporal resolution | Night/Day measure |
|-------------------------------|------------------------------------|---|-------|---------------------|---------------------|-------------------|
| extinction 355 | 387 | Pressure profile Wavelength dependence parameter | 30km | 100 - 200m | 30mn | night |
| extinction 532 | 607 | Pressure profile Wavelength dependence parameter | 30km | 100 - 200m | 30mn | night |
| backscattering 355 | 355 | Extinction profile at 355nm | 30km | 100 - 200m | 30mn | night |
| backscattering 532 | 532 | Extinction profile at 532nm | 30km | 100 - 200m | 30mn | night |
| extinction 355 | 355 | Lidar ratio at 355nm | 30km | 100 - 200m | 30mn | night/day |
| backscattering 355 | 355 | Lidar ratio at 355nm | 30km | 100 - 200m | 30mn | night/day |
| extinction 532 | 532 | Lidar ratio at 532nm | 30km | 100 - 200m | 30mn | night/day |
| backscattering 532 | 532 | Lidar ratio at 532nm | 30km | 100 - 200m | 30mn | night/day |
| extinction 1064 | 1064 | Lidar ratio at 1064nm | 30km | 100 - 200m | 30mn | night/day |
| backscattering 1064 | 1064 | Lidar ratio at 1064nm | 30km | 100 - 200m | 30mn | night/day |
| depolarisation 532 | 532// + 532L | | 30km | 100 - 200m | 30mn | night/day |
| H ₂ O mixing ratio | 408 + 387 | Calibration value | 12km | 100 - 200m | 2h | night |

System description

The Jungfraujoch lidar is based on a two-telescope configuration in order to cover a maximum operating range. The system was mounted in the astronomical dome of the Jungfraujoch Station. The lidar receiving optics and electronics are placed on the second floor of the dome and the transmitting optics, the computers for controlling the laser source and the acquisition system together with the laser cooling unit are installed on the first floor as shown in Figure 1a. Figure 1b is a picture of the Jungfaujoch lidar in operation.

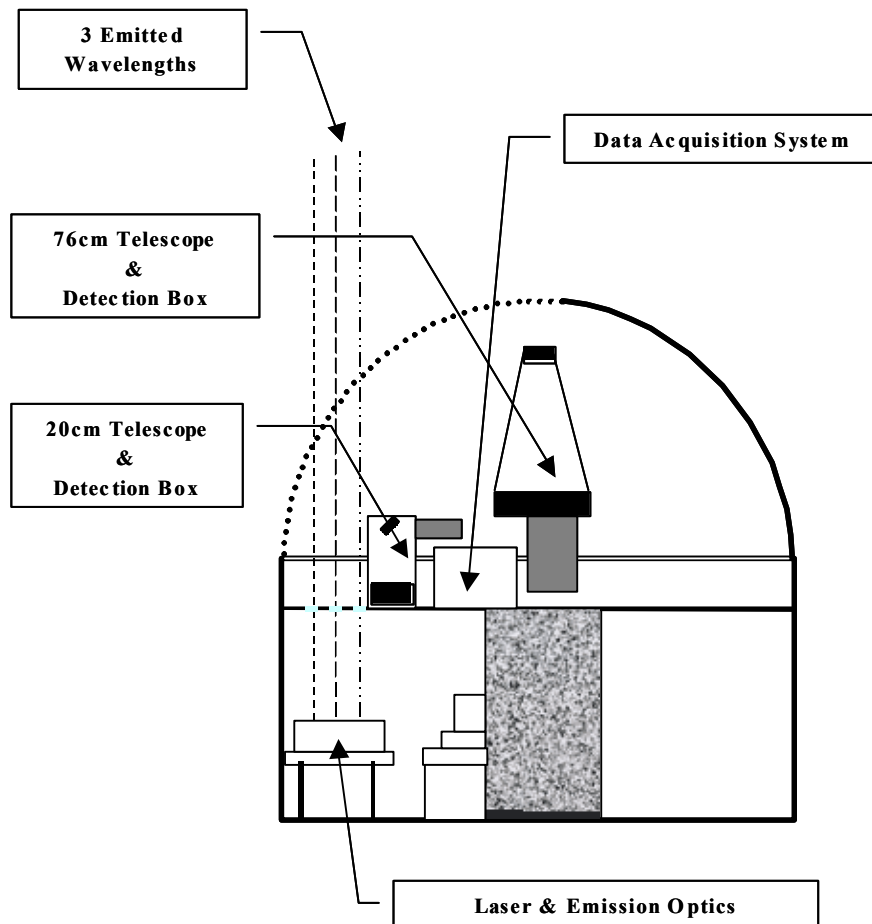


FIGURE 1a. Schematic of the Jungfraujoch lidar installation in the astronomical cupola.

The laser transmitter is based on a tripled Nd: YAG laser (Infinity, Coherent). The laser produces 3.5ns pulses with energies of up to 400mJ at 1064nm. Due to the original scheme of the amplifier that employs a phase-conjugated mirror for thermal lensing correction, the laser repetition rate can be tuned continuously from 2 to 100Hz. The laser parameters are specified in Table 2. Two BBO crystals perform the frequency doubling and tripling of the fundamental frequency. Dichroic mirrors separate the three output wavelengths -1064nm, 532 nm, and 355nm. The corresponding beams are expanded by three 5X beam expanders and directed onto three dichroic steering mirrors. These mirrors are controlled independently by piezoelectric driven x-y mounts to align the laser beams within the field of view of the telescopes. In order to control precisely the polarization state of the transmitted 532nm radiation, an air-spaced Glan-Thompson prism is inserted into the optical path of the 532nm beam.

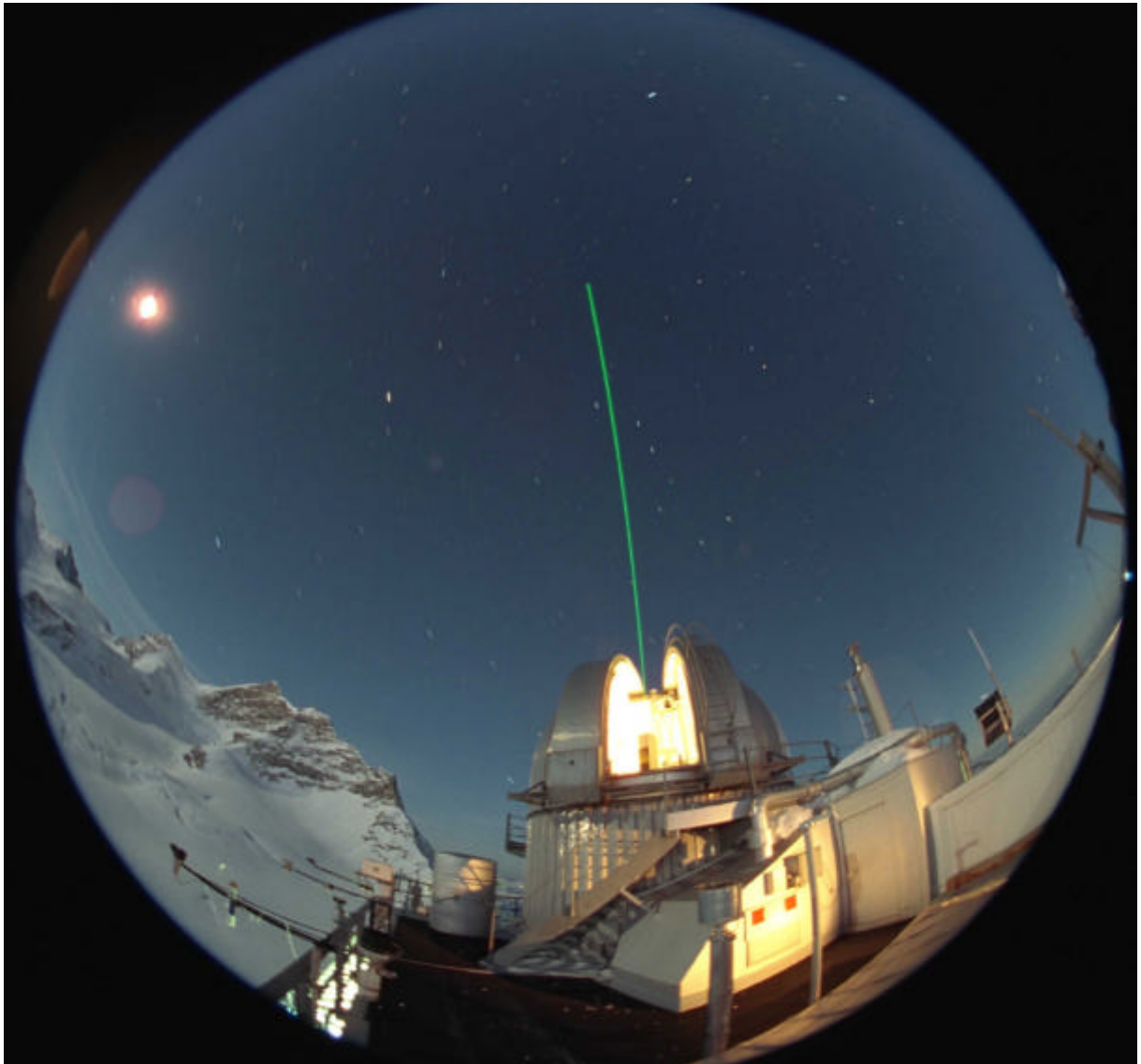


FIGURE 1b. Nighttime picture of the EPFL lidar system at Jungfrauoch.

TABLE 2. Technical data of the lidar

| Transmitter | |
|---|--|
| Laser | |
| Type | Nd:YAG |
| Model | Coherent Infinity 40-100 |
| Wavelength | 1064, 532, 355nm |
| Repetition rate | 0.1 – 100Hz |
| Divergence | 0.7mrad |
| Beam expander | |
| Magnification | 5x |
| Divergence of the expanded laser beam | 0.14mrad |
| Receiver | |
| Telescope tropospheric | |
| Geometry | Newtonian |
| Main mirror | 200mm, f/4 |
| Field of view | 0.2 - 3.8mrad |
| Telescope stratospheric | |
| Geometry | Cassegrain |
| Main mirror | 760mm, f/15 |
| Field of view | 0.2 – 0.4mrad |
| Dispersion system | Beam splitters and bandpass filters |
| Dispersion system of the short range telescope | |
| Channel 355nm | |
| Beamsplitters efficiency | 88% |
| Filters transmission | 33% |
| Out-of-band filters transmission | 10^{-8} (relative to the peak transmission) |
| Detector | PMT Hamamatsu H6780-06 |
| Channel 387nm | |
| Beamsplitters efficiency | 63% |
| Filters transmission | 51% + 10% neutral density |
| Out-of-band filters transmission | 10^{-10} (relative to the peak transmission) |
| Detector | PMT Thorn Emi, QA9829 |
| Channel 408nm | |
| Beamsplitters efficiency | 74% |
| Filters transmission | 37% |
| Out-of-band filters transmission | 10^{-8} (relative to the peak transmission) |
| Detector | PMT Thorn Emi, QA9829 |
| Channel 532nm | |
| Beamsplitters efficiency | 84% |
| Filters transmission | 30% + 10% neutral density |
| Out-of-band filters transmission | 10^{-8} (relative to the peak transmission) |
| Detector | PMT Hamamatsu H6780-06 |
| Channel 607nm | |
| Beamsplitters efficiency | 77% |
| Filters transmission | 42% |
| Out-of-band filters transmission | 10^{-9} (relative to the peak transmission) |
| Detector | PMT Thorn Emi, B9202 |
| Channel 1064nm | |
| Beamsplitters efficiency | 73% |
| Filters transmission | 58% |
| Out-of-band filters transmission | 10^{-8} (relative to the peak transmission) |
| Detector | APD EG&G, C30954/5E |
| Data acquisition system | |
| Type | 7 input-channels in analog and photoncounting mode with 2 triggers |
| Model | Licel |
| Maximum count rate (photon counting mode) | 200MHz |
| Maximum voltage (analog mode) | 20, 100, 500mV |
| Minimum time-bin width | 50ns |
| Number of time bins | 16'000 |

dynamic range of the signals. A Newtonian, 20 cm telescope with an aperture ratio of F/4 covers the lower range from 400 to 12'000m altitude above ground level (AGL). The telescope is pointed vertically and can be tilted at 5° from the vertical. The astronomical telescope originally installed into the dome and used earlier for stellar photometry will provide stratospheric and mesospheric measurements. It is a Cassagrain type with a main mirror diameter of 760mm and an aperture ratio of F/14. It has German equatorial mounting with slow motion drives on both (polar and elevation) axes that we use to align the telescope versus the laser beams. Even though preliminary tests have been performed with this telescope and lidar signals from altitudes up to 60 km AGL were detected, regular measurements are still not being carried out.

At the present moment the received wavelengths for each telescope include three elastically scattered wavelengths, and two spontaneous Raman signal from nitrogen and water vapor respectively. The optical signals received by each of the telescopes are separated spectrally by two filter-polychromators. They are built using an identical optical layout for both telescopes but differ by physical size and the way of optical coupling to the respective telescope. The filter-polychromators and coupling optics are designed and optimized using a ray tracing analysis (OSLO 6 software). The optical layout of the short-range receiver without the receiving telescope is schematically depicted in Figure 2. The different wavelengths are separated by dichroic beam-splitters and then filtered by sets of broadband (typically 4nm) and narrowband (typically 0.5nm) interference filters specific for each wavelength. Neutral-density filters are employed to adapt the light intensity of the signals to the corresponding PMT sensitivity. The important optical parameters of the filter-polychromators together with the photodetectors efficiencies are summarized in Table 2.

Two different polarization states with planes of polarization parallel and perpendicular to the polarization plane of the transmitted beam are separated from the 532nm signal by a Wollaston prism in order to define the depolarization ratio. A 2X beam-compressor adapts the size of the incoming beam to the prism aperture. The Wollaston prism, the beam-compressor and the two detecting PMTs are mounted on a holder that can be rotated precisely around the common axis of the optical elements. This design allows precise alignment and an easy way of calibrating the depolarization block by reversing the position of the "parallel" and "perpendicular" PMTs.

Photomultiplier tubes perform the detection of the optical signals for the UV and visible signals and by Si-avalanche photodiodes (C30954/5E from EG&G) for 1064nm signals. Elastically backscattered signals at 355 and 532 nm (with parallel and perpendicular polarization) are detected by photosensor modules (Hamamatsu – 5783-06). The new, metal-channel dynode configuration of the PMT used in this module ensures short pulse duration and good pulse-height distribution which in turn make possible both the analogue and photon-counting mode of detecting the signals. Despite these excellent features, the PMT shows none-negligible spatial non-uniformity. An improvement of the PMT uniformity leading to variations of less than 2% in the sensitivity of the central part of the photocathode was achieved by adding a lens and a diffuser before the PMT, as described in [22]. The Raman wavelengths are detected by two types of PMTs for 387nm and 408nm (Thorn-EMI QA9829A), and for 607nm (B9202A) signals. The PMTs used in the Raman channels were specially selected to work in a photon-counting mode.

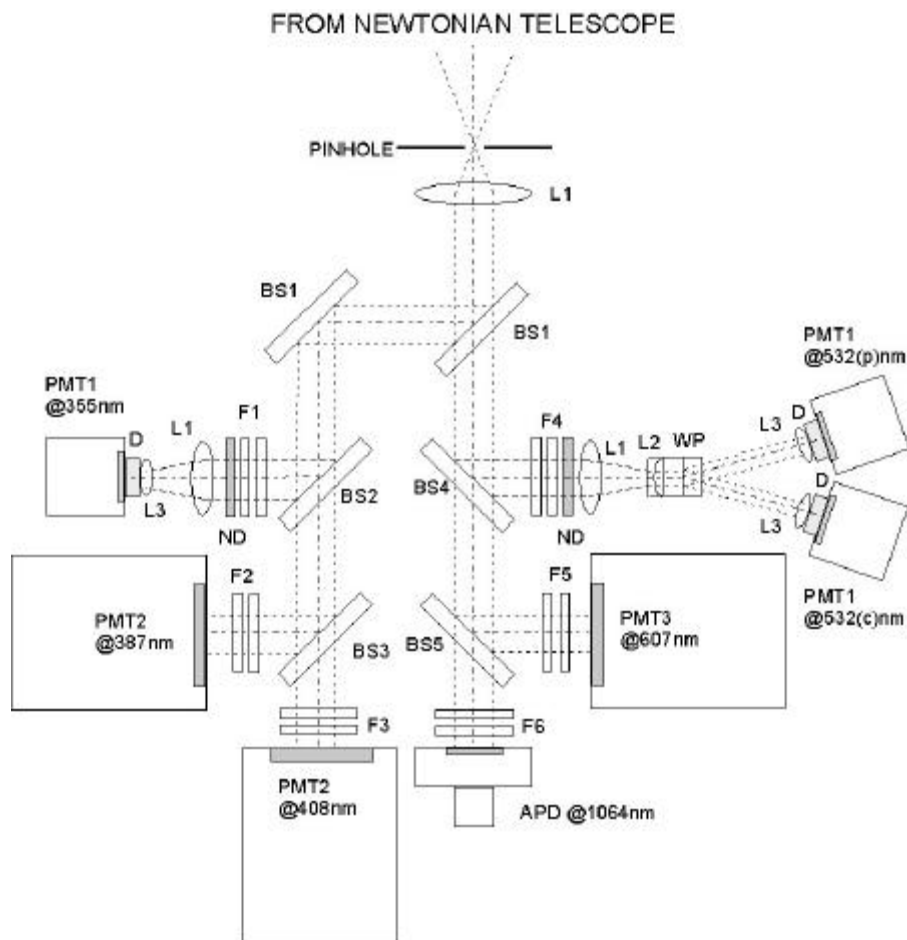


FIGURE 2. Schematic of the lidar detection setup (lens L, beam splitter BS, filter F, Wollaston prism WP, photomultiplier tube PMT, avalanche photodiode APD)

The acquisition of the signals is performed by seven transient recorders (Licel GmbH). Each transient recorder combines a 200MHz photon-counting unit with a 12 bit 20 MHz analogue-to-digital converter. A low repetition rate alternating storing of the data is possible for each of the transient recorders by using two sets of memories consisting of a 24bit and a 16bit RAMs for the analogue and for the photon-counting data correspondingly.

The data stream is directed to one of these memory sets depending on the states of two external triggers. This feature of the device allows us to record the data from the Newtonian and the Cassagranian telescopes by turns using a single acquisition system. The control over the transient recorders, as well as, the preliminary and final treatment of the data is performed on a PC using LabVIEW and Matlab programs.

Results

In the framework of the EARLINET project the lidar has been operating every other week since April 2000. Examples of data recorded with the tropospheric telescope during this period will be discussed here in some details.

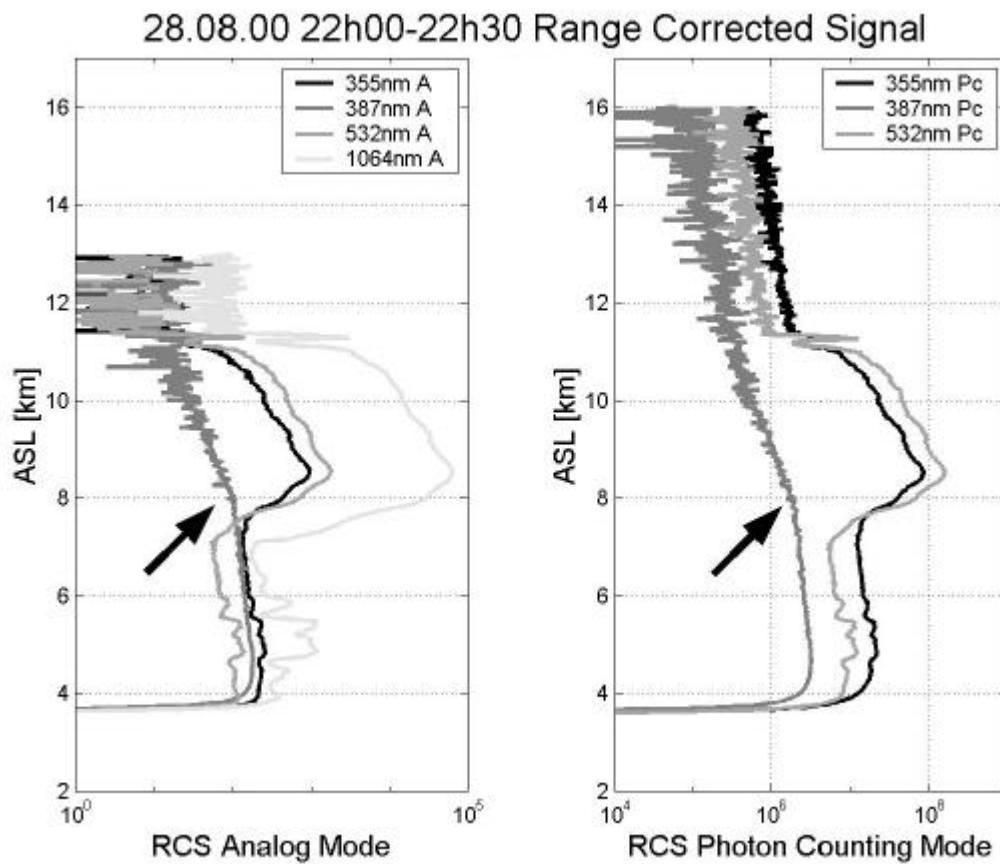


FIGURE 3. Range corrected signals at 355, 387, 532 and 1064nm in analogue mode (left panel) and photon counting mode (right panel). Arrows mark the break in slope of the Raman channel due to the aerosol extinction in the cloud.

Range corrected signals (RCS, lidar signals multiplied by the square of the distance) at the three elastic-backscatter wavelengths and the Raman wavelength at 387nm are shown in Figure 3. RCS signals in analog mode recorded on August 28th 2000 between 22h00 and 22h30 are shown in the left panel, whereas the right panel shows the same set of data but acquired in photon counting mode. Note the logarithmic scale used for the RCS intensity on the horizontal scale. In this lidar configuration, the three laser beams are emitted off axis with respect to the telescopes. It implies that at short distance where a full overlap of the laser light with the telescope field of view is not achieved the measurements cannot be used. Thus the data shown in Fig. 3 are valid only from a lower altitude of approximately 4 km ASL. A strong aerosol layer between approximately 7 and 11km is well outlined on the RCS at the elastic wavelengths. The same layer is seen in the Raman channel as a change of the slope of the RCS due to the increased optical thickness. An arrow in the figure points the breaking point of the RCS at the bottom of the layer. The fact that this relatively strong layer does not give a rise to the Raman signal is a proof for the good rejection of the elastic-backscatter light in the Raman channel of the system.

The vertical profiles of the aerosol backscatter coefficients at 355, 532 and 1064nm calculated by the Fernald inversion method from the already presented RCS are shown in Figure 4. The backscatter coefficients for each of 355nm and 532nm wavelengths when calculated using analog and photon-counting signals show very good agreement. In the Fernald formalism, the weak point is that a lidar ratio must be postulated at each wavelength *a priori*, thus retrieving these coefficients more like relative rather than absolute values. Based on *in situ* observation at Jungfraujoch [23] and also in accordance with [24], a reasonable value of 15 for the lidar ratio was selected for each wavelength, a value that was kept constant at any altitude considered in these examples. We will see later that this value is also in good accordance with the value retrieved in the case of the Raman formalism applied to the 355 nm elastic lidar signal for which the nitrogen Raman channel at 387 nm was used as an additional channel thus avoiding any hypothesis about the lidar ratio. The data was smoothed by a variable gliding average (from 37.5m to 150m in analog mode, 75m to 225m in photon counting mode) prior inversion. The integration time was 30 minutes. In the profiles shown in Fig. 4, two space regions with different light scattering properties can be distinguished. In the region between 8 and 11 km ASL, the values of the aerosol backscatter coefficients for the three wavelengths are equal and of the order of $1.5 \cdot 10^{-5} \text{ m}^{-1} \text{sr}^{-1}$ and indicates that the aerosol particles are large compared to any of the emitted wavelengths. In this case the scattering efficiency is almost independent of the wavelength and the aerosol contribution is larger than the molecular contribution. The second type of aerosol light scattering is seen at altitude region between 4 and 7 km ASL where the laser wavelengths are of the same order of magnitude as the aerosol mean size, Here a key parameter that governs this scattering effect is the ratio between the particle size and the laser wavelength. It is obvious that the three aerosol backscatter coefficients differ significantly. For example at an altitude of 5 km ASL, the backscatter coefficient is equal to $2 \cdot 10^{-6} \text{ m}^{-1} \text{sr}^{-1}$, $1 \cdot 10^{-6} \text{ m}^{-1} \text{sr}^{-1}$ and $0.5 \cdot 10^{-6} \text{ m}^{-1} \text{sr}^{-1}$ respectively at 355, 532 and 1064nm. In that case the molecular scattering is prevailing over the aerosol scattering.

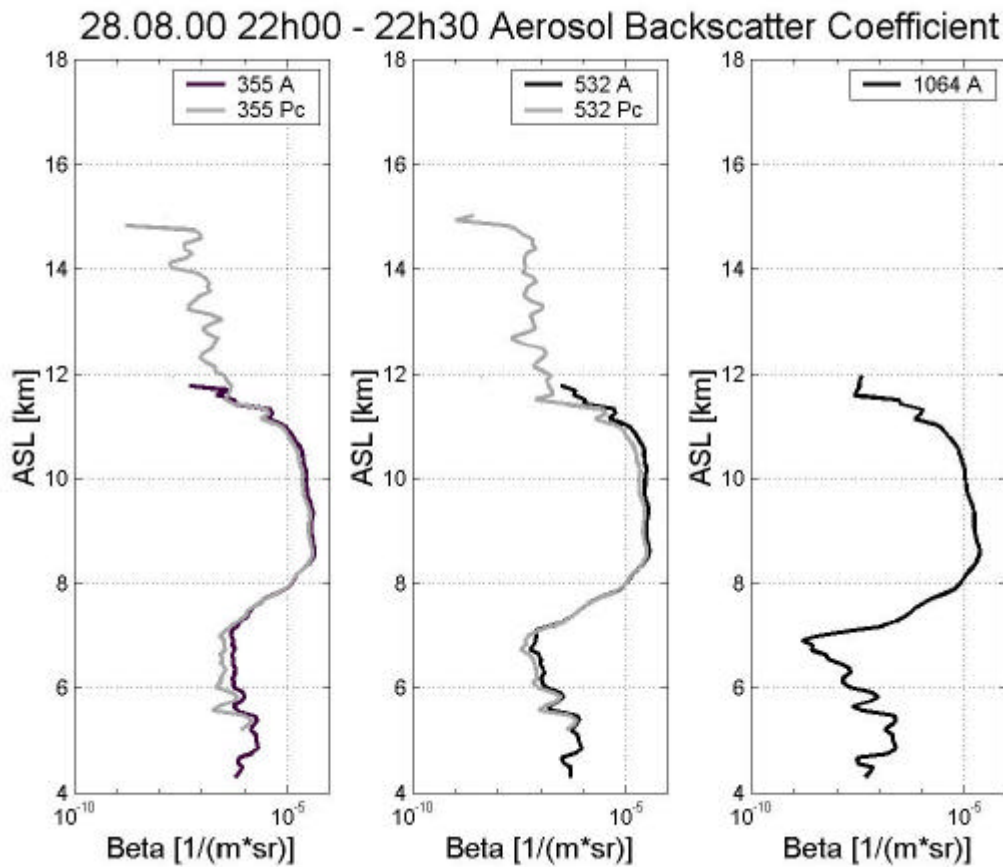


FIGURE 4. Aerosol backscatter coefficients in analogue (A) and photon counting (Pc) mode retrieved from the data in Fig. 3 applying the Fernald inversion formalism and assuming a lidar ratio of 15.

Figure 5 shows the comparison between the aerosol extinction and the backscatter coefficients obtained using in one case the Fernald inversion at 355nm (denoted as “Elastic” in the figure) with a constant lidar ratio of 15 (average value from the Raman lidar ratio) and in the other case the inversion algorithm using the Raman nitrogen signal at 387nm combined with the elastic lidar signal at 355nm (denoted as “Raman” in the figure). Due to the weaker Raman signals, the averaging time is one hour, a larger variable gliding average (300 to 900m) is used and the comparison is shown here only in photon counting mode, since the Raman nitrogen signal intensity is more than three orders of magnitude lower than the elastic one. The profiles are compared in the cloud region between 7.5 and 10.5 km ASL. An Angström parameter equal to zero (no wavelength dependence) is taken and the molecular atmosphere is assumed at an altitude of 14km ASL to retrieve the backscatter coefficient. The density profile is calculated using a US standard atmosphere fitted to the temperature and pressure measured at the Jungfraujoch station. The extinction and backscatter coefficients obtained are in good agreement. Between 8.5 and 9.5 km, the retrieved coefficients are also similar to the values proposed in [24] for cirrus conditions with an extinction coefficient of $1.4 \cdot 10^{-5} \text{ m}^{-1}$, a backscattering coefficient of $2 \cdot 10^{-4} \text{ m}^{-1} \text{ sr}^{-1}$ and a lidar ratio of 13.5 sr^{-1} .

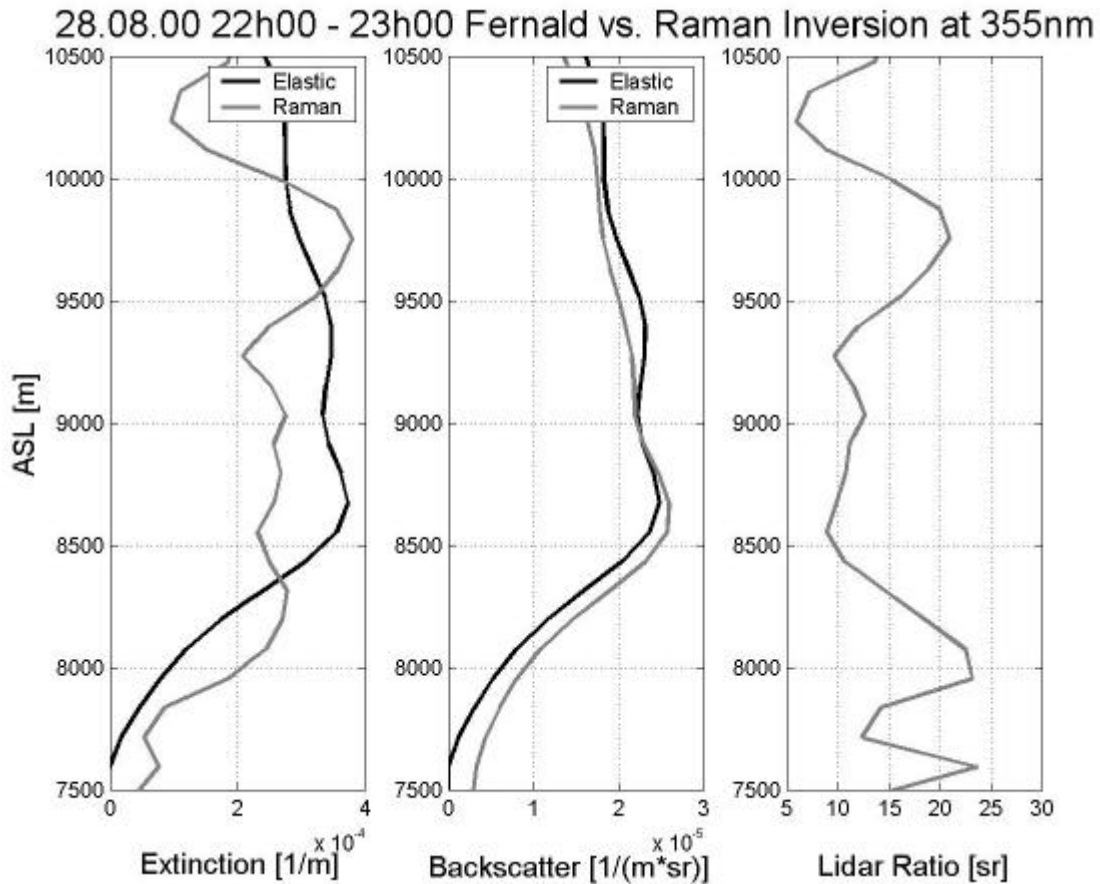


FIGURE 5. Aerosol extinction and backscatter coefficients at 355nm obtained with the Fernald formalism (Elastic) and by combinations of Raman and elastic signals (Raman). The corresponding lidar ratio of the Raman profiles is given in the right panel.

The temporal evolution of the aerosol backscatter coefficients on August 28th 2000 between 16h00 and 24h00 local time calculated by the Fernald inversion method at 355 and 1064nm is shown in Fig.6 a and b correspondingly. The time resolution is half an hour and the lidar ratio is chosen equal to 15. The blank parts on the plot are due to strong extinction inside the cloud. The top of the aerosol layer is around the tropopause while its bottom decreases in time down until an altitude of 2km above the Jungfraujoch lidar station. During these measurements, a Saharan dust event was recorded simultaneously by a network of 19 lidar stations all over Europe within the frame of the EARLINET EU program [25]. In particular the enhanced aerosol backscatter values extending from 4 to 7 km ASL were shown to be linked to the presence of Saharan dust particles. Pronounced peaks of the order of $1.5\text{--}5.5 \cdot 10^{-6} \text{m}^{-1} \text{sr}^{-1}$ were observed by several lidar systems in EARLINET operating at 355nm [25]. Similar values were detected from our system as shown in Fig. 4. Note that in this case at 1064nm, the presence of these particles exhibits a weaker contribution on the aerosol backscatter coefficient. This is another example of the strong wavelength dependence of the backscatter coefficient.

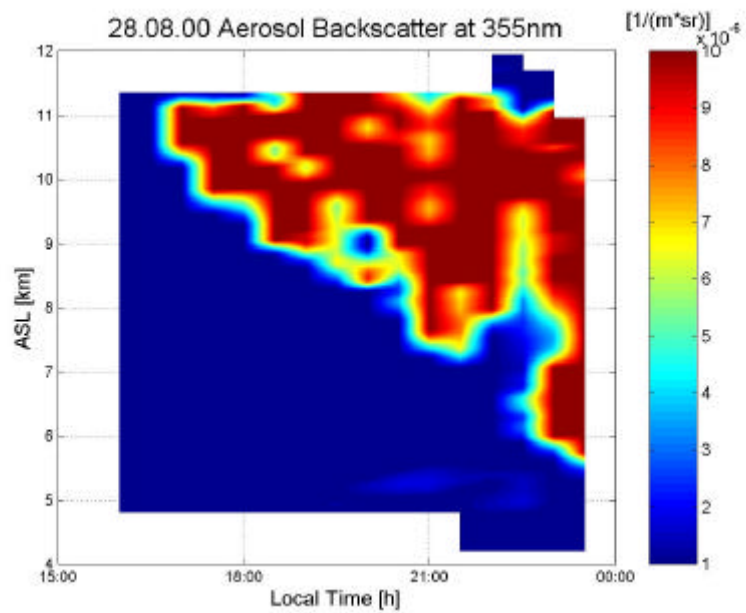


FIGURE 6(a). Temporal evolution of the aerosol backscatter coefficient at 355nm on August 28th 2000 between 16h00 and 24h00 LT.

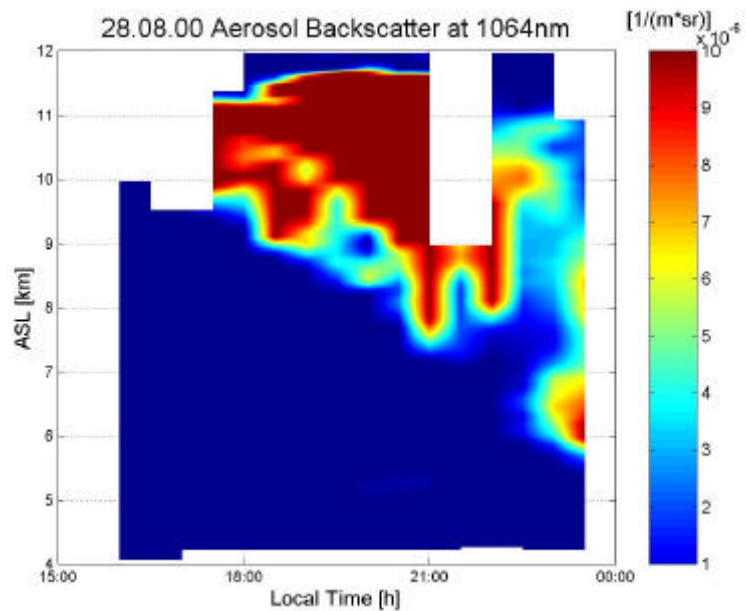


FIGURE 6(b). Temporal evolution of the aerosol backscatter coefficient at 1064nm on August 28th 2000 between 16h00 and 24h00 LT.

The sources of uncertainties in the estimate of the aerosol backscatter coefficient by the Fernald inversion are investigated in Figure 7. Here we consider only the error sources that are associated with the statistical error due to the signal detection [26], the systematic errors linked with the estimate of the lidar ratio [27], the total backscatter coefficient at the reference altitude [27] and the molecular backscatter coefficient [28]. They are taken into account using the Taylor approximation [29] and reported in the figure as the ratio of the uncertainty divided by the aerosol backscatter coefficient itself. Additional error sources due to multiple scattering [30, 31] or misalignment of the lidar transmitter are not considered here.

The relative error on the backscatter profiles is calculated from the data samples shown in Fig. 4 assuming a Poisson distribution [32] for the statistical error due to the signal detection, an uncertainty of 3% on the molecular coefficient and 10% on the lidar ratio. The relative error on the aerosol backscatter ratio remains below 8% up to an altitude of 11km ASL (below the cirrus cloud layer) while at higher altitude the statistical error on the signal detection increases due to a poor signal to noise ratio.

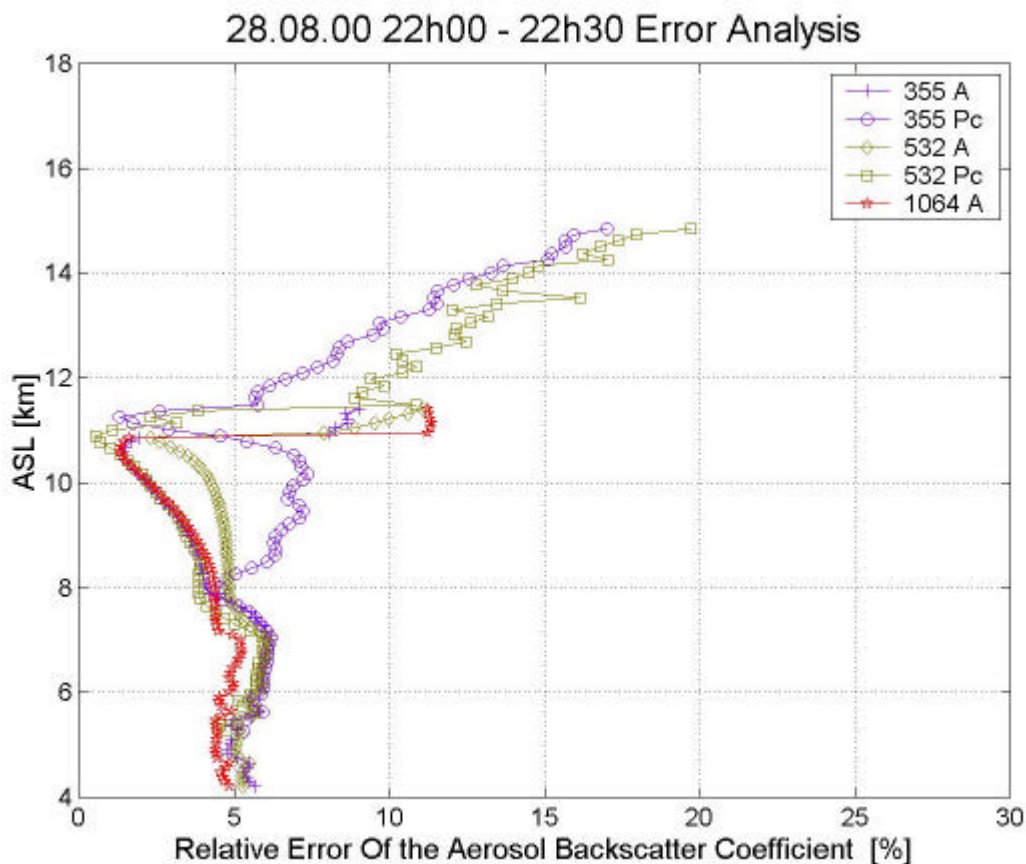


FIGURE 7. Relative error on the aerosol backscatter coefficients in analogue (A) and photon counting (Pc) modes calculated from the data in Fig. 4.

The depolarization ratio brings additional information on the aerosol shape (spherical versus non spherical particles). In Figure 8 a typical measurement of the depolarization ratio is shown. It exhibits values below the cloud layer of the order of 2% that is indicative of an aerosol free atmosphere. This low baseline value of the depolarization ratio is obtained because of the special design of the detection unit using a Wollaston prism as polarizer. In Fig. 8 a cloud layer is seen between 6.5 and 8.5 km ASL with a maximum depolarization ratio around 7.8 km. A first break in the vertical profile of the depolarization ratio around 6.5 km ASL indicates that part of the water vapor was condensed and frozen in the form of small crystallites thus causing this increase of the depolarization ratio. The latter has a value that is close to its detection limit (<2%) at 6.5 km ASL and increases almost linearly to 9% at 7.2 km ASL. It is assumed to be a region of the cloud characterized by a mixture of water droplets and small ice particles. At 7.2 km ASL a second break in the profile is observed followed by a maximum depolarization ratio of the order of 40% at 7.8 km ASL. It is indicative of a cloud layer containing only frozen particles (crystallites) in this case. The aerosol backscatter coefficients that were simultaneously recorded (only the $\beta_{532\text{ nm}}$ vertical profile is shown in Fig. 8 for clarity) had values of the order of $4 \cdot 10^{-7}$, $2 \cdot 10^{-7}$ and $1 \cdot 10^{-8} \text{ m}^{-1} \text{ sr}^{-1}$ at 355, 532 and 1064 nm below the cloud (< 6.5 km ASL). Increasing scattering toward shorter wavelengths is a general characteristic of non-absorbing particles that are small compared to the wavelength of the laser light [33]. At 7.8 km ASL, these coefficients reached maximum values of the order of $3 \cdot 10^{-6}$, $2 \cdot 10^{-6}$ and $7 \cdot 10^{-7} \text{ m}^{-1} \text{ sr}^{-1}$. In this case the different backscattering values are depicting a wavelength dependence that is totally different to the one presented in Fig. 5.

Since August 2000, nighttime measurements of the water-vapor mixing ratio were performed on a regular basis in the middle and upper troposphere [34]. The water vapor is measured by Raman lidar taking advantage of the spontaneous vibrational Raman scattering of an incident laser beam by atmospheric N_2 and H_2O molecules. The third harmonic of the Nd:YAG laser at 355 nm is used, with the Raman shifted wavelengths at respectively 387 nm from N_2 and 408 nm from H_2O . In first approximation the water vapor mixing ratio $\text{H}_2\text{O}(z)$ defined in units of [g/kg dry air] is proportional to the ratio of the two Raman backscattered signals assuming a constant mixing ratio for N_2 . The lidar system efficiency is not known *a priori* and a reference value must be used as calibration point for retrieving an absolute water vapor profile by the Raman lidar.

Figure 9 shows the water vapor measured by Raman lidar from Jungfraujoch for a total integration time of two hours and a vertical resolution of 75 m. The lidar profile is compared with parallel balloon measurements using a chilled cooled mirror hygrometer (i.e. Snow White) launched from the Swiss Meteorological Station in Payerne (located at about 80 km West from the Jungfraujoch station). At the altitude of 4.75 km ASL, the absolute water vapor content measured by balloon is used as reference value for the lidar profile. Both profiles are in good agreement, especially if one recalls here that the lidar measurements were performed with the short-range telescope (primary diameter of only 20 cm). Error sources in the water vapor lidar measurements were presented in details elsewhere [17] with an overall uncertainty of below 5% for clear sky conditions, but that may reach 20% in case of hazy conditions.

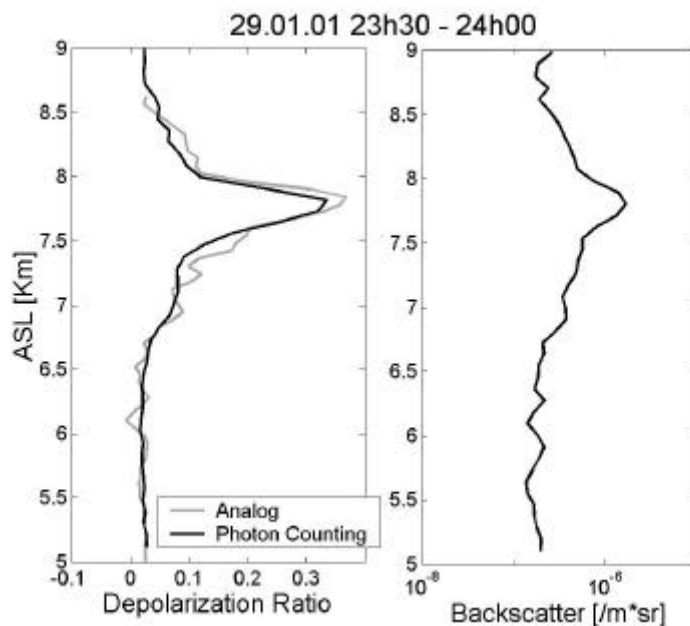


FIGURE 8. Depolarization ratio at 532nm in analogue and photon counting modes. The backscatter coefficient at 532nm using the Fernald inversion formalism and assuming a lidar ratio of 15 is shown for direct comparison.

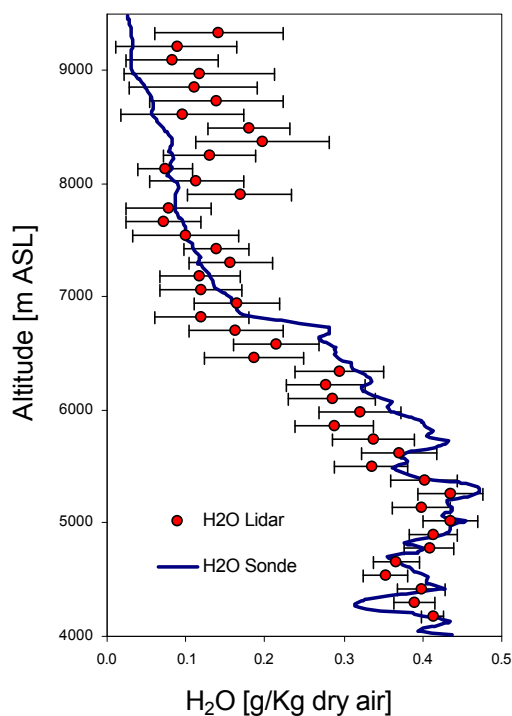


FIGURE 9. Water vapor mixing ratio measured by Raman lidar and by balloon (Snow White sonde, Swiss Meteorological station in Payerne). The calibration point for the Raman lidar data is used at an altitude range of 4.75 km ASL.

Conclusion

The multiwavelength aerosol lidar constructed at the Jungfraujoch Alpine station in Switzerland was presented with the purpose of providing extinction and backscatter profiles at 355 and 532nm, backscatter profiles at 1064nm and depolarization measurements at 532nm. Even if the experimental conditions on site are harsh with some extreme atmospheric conditions (temperature ranging from -50 to $+20$ degrees Celsius, maximum wind speed up to 200 km/hr, 2/3 of the atmospheric pressure at sea level) the system has shown reliable results with measurements on a regular basis. The data acquisition is performed both in analogue and photon counting modes, thus allowing the aerosol retrieval over a higher vertical range. The depolarization that is a good indicator of the aerosol shape in the atmosphere was demonstrated with an excellent rejection ratio (essentially no optical cross-talks in the detection box between the parallel and perpendicular channels) thanks to the use of a Wollaston prism as polarizer. Range resolved water vapor measurements were demonstrated as well with an achievable range that will soon be achieved up to the tropopause when using the 76 cm Cassagrain telescope.

First measurements in the stratosphere and lower mesosphere have been already achieved at 355 and 532nm. Regular measurements will soon be performed using both telescopes simultaneously (see Fig. 1), thus significantly increasing the range of observation for both the aerosol and the water vapor content in the higher atmosphere.

A new temperature channel at 532nm based on pure rotational Raman method will be implemented. The use of an additional laser source will furthermore allow the regular measurements of ozone in the free troposphere and lower stratosphere using the differential absorption lidar (DIAL) method in the UV. The final combination of range resolved data including water vapor and ozone around the tropopause region together with an accurate determination of the aerosol content and the temperature will bring essential information for our understanding of the atmospheric dynamics at this transition zone between the troposphere and the stratosphere.

Acknowledgements

The authors kindly thank the Foundation Jungfraujoch Gornergrat for the different research facilities at Jungfraujoch, the Swiss Meteorological Institute (Payerne Station) for the radio sounding data and the use of meteorological data from Jungfraujoch, the Swiss National Foundation and the Swiss Federal Office for Education and Science for financial support.

References

1. Houghton, J., *Global Warming: the complete briefing*. 1997: Cambridge University Press.
2. Charlson, R.J., and Heintzenberg, J. (Eds.), *Aerosol forcing of climate*. Dahlem Workshop Reports, ed. R.J. Charlson, and Heintzenberg, J. Vol. Environmental Sciences Research Report 17. 1995, New-York: John Wiley & Sons, Ltd.
3. IPCC, *Climate change 1994*. 1995, Cambridge: Press Syndicate of the University of Cambridge.
4. Chahine, M.T., *The hydrological cycle and its influence on climate*. Nature, 1992(359): p. 373.
5. Starr, D.O., and Melfi, S. H. (Eds.), *The role of water vapor in climate: a strategic research plan for the proposed GEWEX, water vapor project (GVaP)*. 1991: NASA Conf. Publ.
6. Rind, D., *Just add water vapor*. Nature, 1998(281): p. 1152-1153.
7. Baltensperger, U., Gäggeler, H. W., Jost, D. T., Lugauer, M., Schwikowski, M., Weingartner, E., and Seibert, P., *Aerosol climatology at high-alpine site Jungfraujoch, Switzerland*. Journal of Geophysical Research-Atmospheres, 1997. D102: p. 19707-19715.
8. Delbouille, L., and Roland, G., *High resolution solar and atmospheric spectroscopy from the Jungfraujoch high altitude station*. Optical Engineering, 1995. 34: p. 2736-2739.
9. de Mazière, M., van Roozendaal, M., Hermans, C., Simon, P. C., Demoulin, P., and Roland, G., *Quantitative evaluation of the post-Pinatubo NO₂ reduction and recovery, based on 10 years of FTIR and UV-visible spectroscopic measurements at the Jungfraujoch*. Journal of Geophysical Research-Atmospheres, 1998. 103: p. 10849-10858.
10. Heimo, A., and al., *The Swiss atmospheric radiation monitoring network CHARM*. paper presented at the WMO technical conference on meteorological and environmental instruments and methods of observation (TECO-98), Casablanca, Morocco, 1998.
11. Maier, D., and al., *EMCOR radiometer: calibration and first tests*. Proceedings of SPIE, 1998. SPIE's First International Asia-Pacific Symposium on remote sensing of the atmosphere, environment and space: p. 362-373.
12. Bösenberg, J., and al., *A lidar network for the establishment of an aerosol climatology*. in the proceedings of the 19th ILRC, Annapolis MA, USA, 1998. NASA/CP-1998-207671/PT1: p. 23-24.
13. Grant, W.B., et al., *Selected papers on Laser Applications in Remote Sensing*. 1997: SPIE Milestone series.
14. Measures, R.M., *Laser Remote Sensing. Fundamentals and Applications*, ed. J.W.a. Sons. 1992, New-York: Krieger. 510.
15. Ansmann, A., M. Riebesell, and C. Weitkamp, *Measurement of Atmospheric Aerosol Extinction Profiles with a Raman Lidar*. Optics Letters, 1990. 15(13): p. 746-748.
16. Ansmann, A., et al., *Combined Raman Elastic-Backscatter Lidar for Vertical Profiling of Moisture, Aerosol Extinction, Backscatter, and Lidar Ratio*. Applied Physics B-Photo-

-
- physics and Laser Chemistry, 1992. 55(1): p. 18-28.
17. Whiteman, D.N., S.H. Melfi, and R.A. Ferrare, *Raman Lidar System for the Measurement of Water-Vapor and Aerosols in the Earths Atmosphere*. Applied Optics, 1992. 31(16): p. 3068-3082.
 18. Pal, S.R., and Carswell, A. I., *Polarization properties of lidar backscattering from clouds*. Applied Optics, 1973. 12(7): p. 1530-1535.
 19. McNeil, W.R., and Carswell, A. I., *Lidar polarization studies of the troposphere*. Applied Optics, 1975. 14(9): p. 2158-2168. I., *Po*
 20. Böckmann, C., and Wauer, J., *Algorithms for the inversion of light scattering data from uniform and non-uniform particles*. Aerosol Science, 2001. 32: p. 49-61.
 21. Böckmann, C., *Hybrid regularization method for the ill-posed inversion of multiwavelength lidar data in the retrieval of aerosol size distribution*. Applied Optics, 2001. 40(9): p. 1329-1342.
 22. Simeonov, V., et al., *The influence of the photomultiplier spatial uniformity on lidar signals*, Applied Optics, 1999. 38: p. 5186-5190.
 23. Nyeki, S., and al., *The Jungfraujoch high-alpine research station (3454m) as a background clean continental site for the measurement of aerosol parameters*. Journal of Geophysical Research-Atmospheres, 1998. 103: p. 6097-6107.
 24. Vaughan, J.M., Geddes, N. J., Flamant, P. H., and Flesia, C., *Establishment of a backscatter coefficient and atmospheric database*. 1998: DERA, UK.
 25. Papayannis, A., and al., *Continental-scale vertical profile measurements of free tropospheric Saharan dust particles performed by a coordinated ground-based european lidar network (EARLINET project)*. to be submitted to the Journal of Geophysical Research.
 26. Theopold, F., and Bosenberg, J., *Evaluation of DIAL measurement in presence of signal noise*, proceedings of the 14th ILRC, 1988.
 27. Godin, S., and al., *Ozone differential absorption lidar algorithm intercomparison*. Applied Optics, 1999. 38(30): p. 6225-6236.
 28. Russell, P.B., Swissler, T. J., and McCormick, M. P., *Methodology for error analysis and simulation of lidar aerosol measurements*. Applied Optics, 1979. 18(22): p. 3783-3797.
 29. Taylor, J., *An Introduction to Error Analysis*. 2nd edition ed. 1997: University Science Books.
 30. Ansmann, A., et al., *Independent Measurement of Extinction and Backscatter Profiles in Cirrus Clouds by Using a Combined Raman Elastic-Backscatter Lidar*. Applied Optics, 1992. 31(33): p. 7113-7131.
 31. Whiteman, D., and al., *Raman lidar measurements of water vapor and cirrus clouds during the passage of hurricane Bonnie*. accepted in J. of Geophys. Res, 2000.
 32. Bosenberg, J., *Ground-based differential absorption lidar for water vapor and temperature profiling: methodology*. Applied Optics, 1998. 37(18): p. 3845-3860.

33. Mc Cartney, E.J., *Optics of the Atmosphere*. 1976: Wiley. 408.
34. Balin, I., Larchevêque, G., Quaglia, P., Simeonov, V., van den Bergh, H., and Calpini, B., *Water vapor profile by Raman lidar in the free troposphere from the Jungfraujoch Alpine Station*, in *Advances in global change research*. 2001, Kluwer Academic Publisher.

This chapter presents an article about the water vapor mixing ratio measurements performed with the lidar system of the Jungfraujoch Station. The Raman method is presented in more details than in “Water vapor mixing ratio”, p 50, as well as a discussion about the error sources of the method.

This article was presented to The International Workshop on ” Climatic Change, Implications for the Hydrological Cycle and for Water Management” (September 22 - 29, 2000, Wengen-CH) and is accepted to ADVANCES IN GLOBAL CHANGE RESEARCH, Kluwer Academic Publishers, Dordrecht (The Netherlands) and Boston (USA), vol.9, 2001.

Water vapor vertical profile by Raman lidar in the free troposphere from the Jungfraujoch Alpine Station

Ioan Balin, Gilles Larchevêque, Philippe Quaglia, Valentin Simeonov, Hubert van den Bergh,
and Bertrand Calpini

Authors' affiliation:

Laboratory of Air Pollution (LPAS)

Swiss Federal Institute of Technology – Lausanne (EPFL) 1015 Switzerland

Abstract

The water vapor content in the atmosphere is an important criteria for the validation of predictive results obtained from global scale atmospheric models. Due to its non-homogeneous distribution in the troposphere, both in space and time, the water vapor content in the atmosphere may still be considered today as the largest uncertainty in our understanding of the earth radiation budget. This paper presents new results obtained by Raman lidar measurements as one of the attractive method for long-term continuous observation of the water vapor content in the atmosphere. A powerful pulsed laser beam at 355 nm is emitted and the inelastic back-scatter signals (Raman shift) from nitrogen and water vapor are recorded respectively. The ratio between the water vapor Raman shifted wavelength at 408nm and the nitrogen at 387nm gives a first estimate of the relative water vapor mixing ratio with good vertical resolution. The absolute water vapor vertical profiles are retrieved using an additional *in situ* external reference value directly obtained from the Jungfraujoch meteorological station. The Raman lidar operation located at an altitude of 3'580 m above sea level in the Swiss Alpine region is discussed, together with two typical water vapor vertical profiles obtained in clear sky and in cloudy conditions, and directly compared with radio sounding measurements performed by the Swiss Meteorological Station from Payerne (80km West). A first estimate of the statistical (signal to noise) and systematic error sources is presented.

Key words:

Light **D**etection and **R**anging (LIDAR), Raman inelastic back-scatter, free troposphere, water-vapor, global climate change, Jungfraujoch Alpine Research Station

1 Introduction

Water vapor (H_2O) is the primary greenhouse gas and is a crucial atmospheric constituent. It induces the natural atmospheric greenhouse effect [1] and the hydrological cycle [2]. Atmospheric trace gases such as carbon dioxide (CO_2), methane (CH_4), nitrous oxide (N_2O), or chloro-fluorocarbons (CFC) are among the most important anthropogenic greenhouse gases. Both, natural water vapor and these above mentioned gases contribute to the fragile thermodynamics equilibrium of the atmosphere by trapping long-wave (infrared) terrestrial re-radiation.

Water vapor averages about one per cent by volume in the atmosphere, but is much variable in time and space: it comprises about 4 percent of the atmosphere by volume near the surface, but only 3-6 ppmv (parts per million by volume) above 10 to 12 km. The annual average precipitation over the globe is about 1 meter while the water-vapor column density (precipitable water) averages about 5 cm in the tropical region and less than 1 mm at the poles. Nearly 50% of the total atmospheric water is trapped into the planetary boundary layer (PBL, from 0 to 1-2 km) while less than 6 % of the water is above 5 km, and only 1 % above 12 km in the stratosphere. Despite this small amount of water vapor in the free troposphere (above 2 km), recent studies have shown that the middle and upper troposphere water vapor content is the main source of the OH radical and play an essential role for the earth climate [1,2,3]. The upper troposphere and low stratosphere water vapor more accurate and at high-resolution measurements are needed to cover the lack of knowledge of the tropopause phenomena, of the vertical dynamic, of the nucleation processes and of the cirrus formation. It will make also possible the monitoring water vapor content in the lower stratosphere (e.g. its already observed increasing being partially related to the CH_4 oxidation). In addition these data are necessary for initializing the Numerical Weather Prediction (NWP) and Global Climate models.

Different measurement techniques are used to estimate the water vapor content in the atmosphere, with various spatial coverage (horizontal and vertical resolution) and temporal resolution, as well as detection limits and costs [3]. These methods may also be identified by their principle (sampling detector or remote sensing), by their location (balloons, satellites, aircraft or ground based method). Among these, the Raman lidar (**Lidar Detection And Ranging**) is a remote sensing technique with high vertical resolution (tens to hundreds of meters), good temporal resolution (typically one hour per vertical profile) and the potential for long-term continuous measurements. On the other hand this method will not bring information in terms of spatial coverage, as is the case for airborne lidar or satellite observation. Water vapor measured by Raman lidar is limited to a maximum altitude range of typically 15 km, but combined with the passive microwave techniques, a method with lower range resolution but possible data retrieval up to the mesosphere [4]. These combined methods appear to give an ideal tool for 2D continuous water vertical profile throughout the atmosphere. Here we will focus on the development of a Raman lidar system at the Jungfraujoch Research Station (3'580 m ASL) in order to measure with high vertical resolution the water-vapor content in the free troposphere, present the first nighttime water-vapor profiles measurements and error sources, and give indications about the final configuration of the system.

2. Raman lidar

2.1 Principle

A lidar instrument is composed of a transmitting and a receiving section. The transmitter emits the pulsed laser beam in the atmosphere. This beam interacts with the atmospheric constituents upon propagation, and the back-scattered light is collected by a telescope, spectrally resolved, and recorded by a detection unit. The light interacts with atmospheric gases and aerosols by a multitude of phenomena like Rayleigh (or molecular), Mie (or aerosol), Fresnel, and Raman scattering, as well as by inducing fluorescence, so as to provide the source of the lidar signal for atmospheric monitoring. A picture of the Jungfraujoch lidar system in operation at night is given in Figure 1.



Figure 1:
The EPFL lidar in operation at night from Jungfraujoch.

The Raman lidar measurement of the water vapor takes advantage of the spontaneous vibrational Raman scattering of an incident laser beam by atmospheric N_2 and H_2O molecules. In this experiment the third harmonic of a Nd:YAG laser at 355nm is used. The Raman shifted wavelengths are respectively 387 nm from N_2 and 408 nm from H_2O . The water-vapor mixing ratio $H_2O(z)$ defined in units of [g/kg dry air] is calculated from these back-scattered signals assuming a constant mixing ratio for N_2 [8, 9, 12-15]. It is expressed as:

$$H_2O(z) = \left[\frac{N_{H_2O}(z) - b_{H_2O}}{N_{N_2} - b_{N_2}} \right] C \cdot \Gamma(z, I_{H_2O}, I_{N_2}) \quad (1)$$

where $N(z)$ is the total number of photons detected for the H_2O and N_2 Raman signals respectively from an altitude z , and b is the background intensity due to the skylight and the detector noise.

The correction term $\Gamma(z, \lambda_{H_2O}, \lambda_{N_2})$ takes into account the differential extinction of the atmosphere at the water vapor (408 nm) and nitrogen (387 nm) Raman shifted wavelengths on the return path due to the total extinction coefficient α . It can be written as:

$$\Gamma(z, I_{H_2O}, I_{N_2}) = \frac{\exp\left[-\int_{z_0}^z a(I_{N_2}, r) dr\right]}{\exp\left[-\int_{z_0}^z a(I_{H_2O}, r) dr\right]} \quad (2)$$

where:

$$\alpha = \alpha_{molec} + \alpha_{aerosol} + \alpha_{abs} \quad (3)$$

The total extinction term (α) is the sum of the molecular extinction (α_{molec}), the aerosol extinction ($\alpha_{aerosol}$) and the molecular absorption (α_{abs}) [9] and is wavelength dependent [7]. The altitude of the Jungfraujoch lidar site (z_0) is 3'580 m ASL. This optical extinction corresponds to an integrative effect over the entire range from the lidar site z_0 to the altitude of interest z .

The calibration coefficient C in Equ. 1 can be expressed as:

$$C = \frac{L_{N_2}(I) \sigma_{N_2}(I) M_{H_2O} n_{N_2}}{L_{H_2O}(I) \sigma_{H_2O}(I) M_{dry, air} n_{dry, air}} \quad (4)$$

where L is the instrument constant that takes into account the transmitter and receiver optical efficiency and the quantum efficiency of the detectors for the two channels, σ is the Raman back-scatter cross section, and M and n are the molecular mass and number density of the water vapor and nitrogen respectively. As this calibration constant C depends upon the lidar system efficiency L , it cannot be measured directly. This is why in Equ. 1, the value of the water vapor mixing ratio is only retrieved as a relative value and an external calibration point must be added to the lidar measurements.

Let us recall here that the main difficulty in this water-vapor measurement in the middle and upper troposphere by Raman lidar relies on the rather weak Raman water vapor signal intensity: On one hand in the free troposphere, the water vapor concentration is very low and decreases by 2-3 orders of magnitude from 2 to 12 km, and on the other hand the water vapor Raman cross section (which is similar to the nitrogen Raman cross section) induces a back-scattered signal that is typically three orders of magnitude lower than the elastic back-scattered signal in clear sky or molecular condition [12].

2.2. Raman lidar setup at the Jungfraujoch Alpine Research Station

A multi-wavelength lidar system was installed in 1999 at the Jungfraujoch Research Station (Lat: 46.55°N, Long: 7.98°E, ASL 3'580m) in the astronomic dome in order to probe the atmosphere above the Swiss Alps [17]. The simplified optical layout of the lidar system is shown in Figure 2. The transmitter of the system is based on a Nd:YAG laser (Spectra Physics, Infinity) with a maximum energy of 400 mJ at 1064 nm equipped with two non-linear crystals for second (532 nm) and third (355 nm) harmonic generation. Because of the use of a phase-conjugated mirror, the laser can be operated with repetition rates ranging from 20 to 100Hz. Dichroic mirrors at the laser output separate the three laser wavelengths and each beam is expanded 5 times in order to reduce the laser divergence from 0.7 to 0.14 mrad. These expanded beams are emitted to the atmosphere using 45° dielectric mirrors mounted on piezoelectric-driven stages (M). The typical output energy emitted into the atmosphere is 70 mJ at 355 nm, 60 mJ at 532 nm, and 45 mJ at 1064 nm. The lidar system is working on the vertical axis. The lidar emitter is off-axis from the lidar receiver and the first data analysis can only be performed at an altitude higher than 250 m above the ground, an altitude where a full overlap of the laser beam into the telescope field of view is achieved. In its actual configuration the system is equipped with a ϕ 20 cm primary mirror diameter Newtonian telescope with a focal length of 80 cm. This small size telescope enables measurements up to 12-15 km above the lidar site. The Jungfraujoch astronomical telescope, a ϕ 76 cm primary mirror diameter Cassegrain telescope, will made available simultaneous operation and lidar detection in the upper troposphere and stratosphere.

The elastic backscatter signals at 355 nm, 532 nm with parallel and perpendicular polarization and 1064 nm as well as the Raman shifted signals from N₂ at 387 nm and H₂O at 408 nm (pumped at 355 nm) and N₂ at 607 nm (pumped at 532 nm) are simultaneously recorded. They are used to estimate the aerosol back-scatter/extinction coefficients and the water vapor content.

Here we used only the 355 nm beam to extract the water vapor mixing ratio from the Raman back-scatter from H₂O at 408 nm and N₂ at 387 nm. The back-scattered light is collected by the telescope and spectrally separated by a set of dichroic mirrors and filters. Two sets of interference filters at each of the signal output are used to reduce the sky background light and suppress the residual elastically back-scattered light in the Raman channels. This combination of filters acts as an equivalent narrow band filter with 0.5 nm FWHM at 408 nm and 387 nm respectively and a rejection ratio of better than 10^{-7} between 200 to 1200 nm. Two head-on photomultiplier tubes (type EMI 9829 QA) are used in photon-counting mode. The acquisition unit has a maximum counting rate of 250 MHz with a sampling rate of 20 MHz.

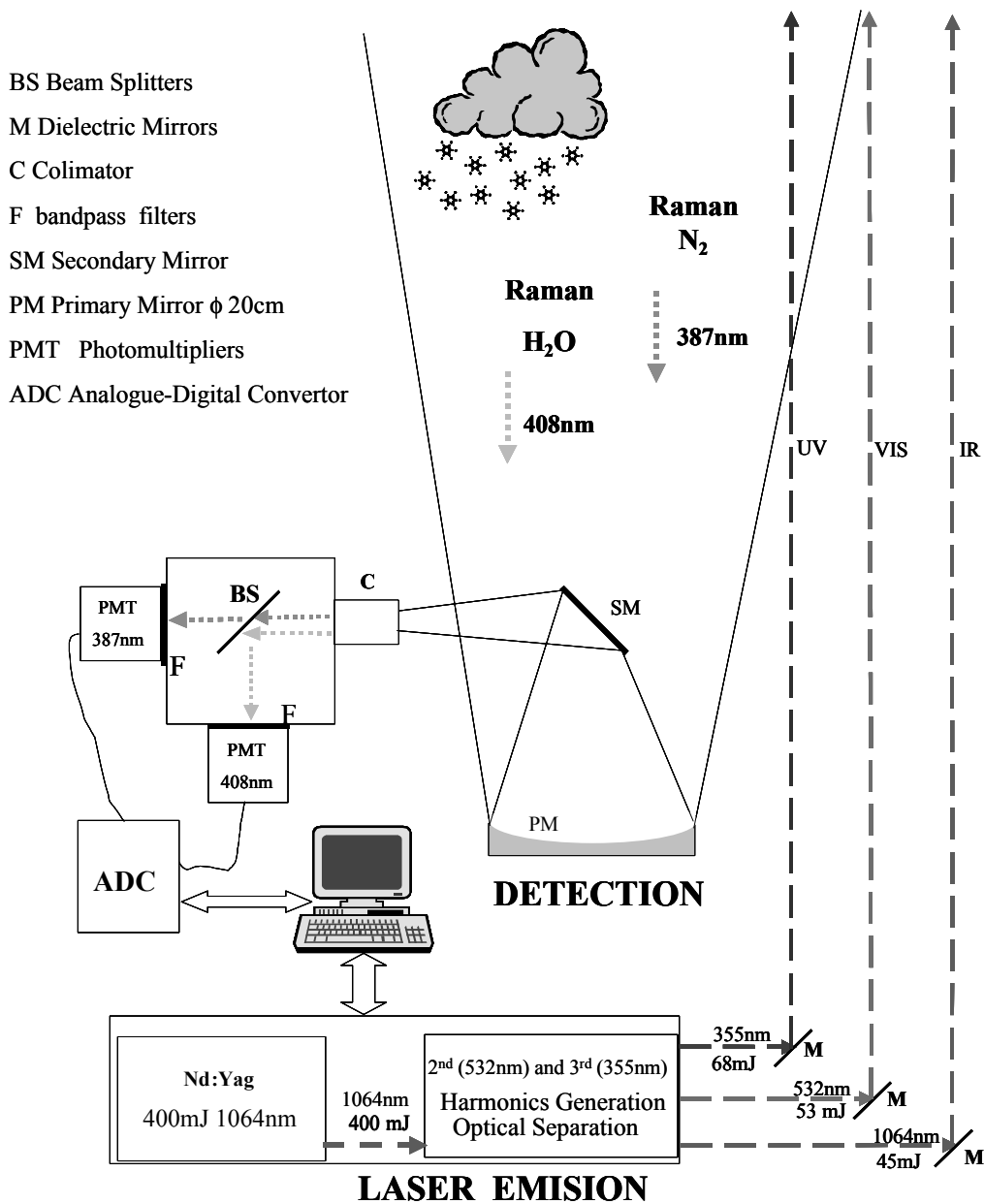


Figure 2:
Raman lidar setup at Jungfraujoch

2.3 Measurement procedure

The lidar signals for H₂O and N₂ are acquired in files of 4000 laser shots each with a typical repetition rate of 50 Hz or an integration time of less than 2 minutes per file. The acquisition unit is used with 3'000 channels at 50 ns per channel or an equivalent maximum altitude range of 22.5 km above the Jungfraujoch lidar site. A LabView routine allows processing the two Raman signals for retrieving the water vapor mixing ratio according to Equ. (1).

This routine also allows visualizing file by file each of the two recorded signals, calculating the signal to noise ratio and detection limit, estimating the statistical error and selecting the right temporal and spatial averaging conditions. The background value (b) of each signal is calculated as an average of the last 1'000 channels (i.e. 7'500 m), which is subtracted afterwards from the raw signal. As the system constant C in Equ. (1) is unknown, a ground reference H₂O [g/kg] value is calculated using the relative humidity RH [%], the air pressure P_{air} [mbar] and the temperature T [°C] values that are permanently measured by Swiss Meteorological Institute (ISM) at Jungfraujoch. The ISM hygrometer used for these measurements is a Meteolabor type VTP6 (±0.15°K, 0.1% RH). This ground-based value is used as a calibration for the first H₂O Raman lidar data at an altitude of 250 m above the lidar site. This implies that the assumption of an homogeneous water vapor mixing ratio is made over this range of 250 m in the free troposphere. This assumption may in special atmospheric conditions induce some error. It will be soon investigated in more details using additional tethered balloon measurements. Radiosonde measurements launched at ~80 km West from the ISM meteorological station in Payerne are used as independent comparisons with the lidar profiles. The water vapor content from the radiosonde was calculated based on the temperature and the dew point measurements (VIZ hygistor detector).

Finally, the location of this lidar system at Jungfraujoch is rather unique: at an altitude of 3'580 m ASL, the system is essentially all year long in the free troposphere, thus avoiding the complex interferences of the planetary boundary layer photochemistry and meteorology. Furthermore as Jungfraujoch is far away from the brightly lit main urban areas, it has therefore very little "light pollution".

2.4 Error sources:

The differential atmospheric transmission factor $\Gamma(z, \lambda_{\text{H}_2\text{O}}, \lambda_{\text{N}_2})$ includes the extinction contributions due to the molecular (Rayleigh), the aerosol (Mie) and the trace gas absorption. According to Whiteman et al., [9] the correction factor related to the differential atmospheric transmission at these wavelengths (N₂: 387nm and H₂O: 408nm) is mainly due to the Rayleigh molecular diffusion ($\alpha_{\text{molec}} \sim \lambda^{-4}$) in clear sky conditions (no aerosols) and its contribution rises to 5 % at 7 km ASL. In Figure 3 the Rayleigh extinction coefficients from N₂ and H₂O and the H₂O Rayleigh correction factor are calculated from Jungfraujoch up to the tropopause. This is done using the molecular Rayleigh differential cross section [18] and considering real atmospheric parameters for the air number density based on temperature and pressure profiles measured directly by the radiosonde from Payerne. The results given in Figure 3 for a temperature of 1.5°C and a pressure of 669 mbar at Jungfraujoch show that for these wavelengths the error increases with the altitude and reaches ~ 4 % at the tropopause.

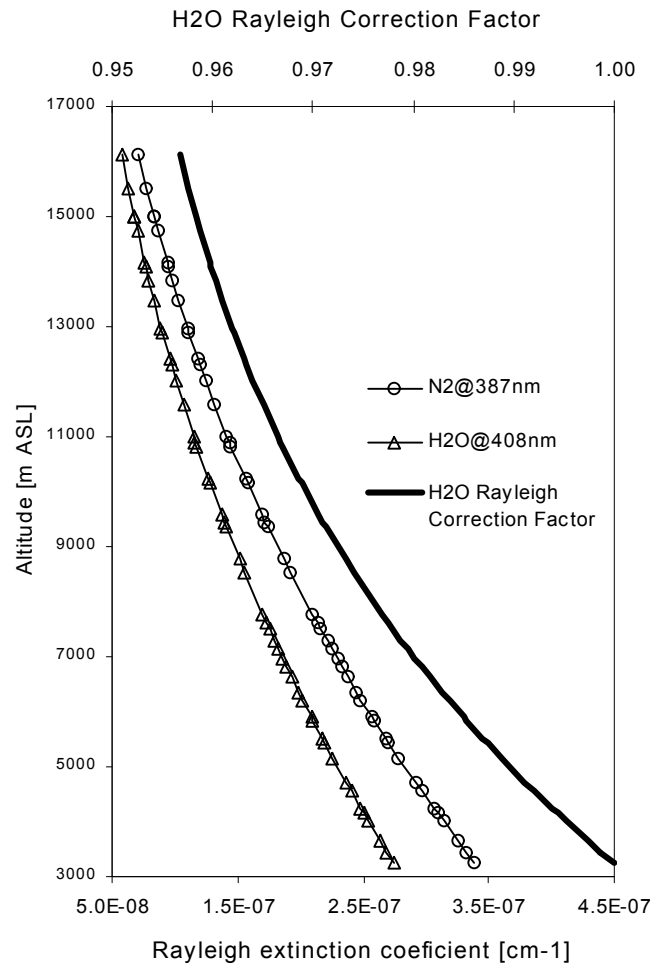


Figure 3:

Evolution of the error source due to the differential Rayleigh cross section in the troposphere: the Rayleigh extinction coefficient (lower scale) for the N₂ Raman shifted wavelength at 387 nm and the water vapor at 408 nm is shown versus altitude. The Rayleigh correction factor is shown on the upper scale.

Nevertheless in the case of cloud layers or hazy conditions, the aerosol or Mie scattering must be accounted for in $\Gamma(z, \lambda_{H_2O}, \lambda_{N_2})$. Here we used the elastic 355 nm lidar signal together with the N₂ Raman shifted signal following a data analysis proposed by Ansmann et al. [6] to retrieve the aerosol extinction coefficient at 355 nm initially. The 387 nm and 408 nm aerosol extinction coefficients are retrieved following the α_{aerosol} proportional to λ^{-1} law. Therefore the differential aerosol extinction coefficient between the two Raman shifted wavelengths can be directly taken into account in $\Gamma(z, \lambda_{H_2O}, \lambda_{N_2})$.

Finally $\Gamma(z, \lambda_{H_2O}, \lambda_{N_2})$ is also influenced by possible interference with trace gas absorption. While this is particularly true in the planetary boundary layer where most of the primary pollution is emitted and trapped, these absorption effects tend to be less significant in the free troposphere. Furthermore the molecular absorption (α_{abs}) by ozone and other trace gases can in first approximation be neglected at the 387 and 408 nm wavelengths [6,9,12].

The estimation of the statistical error takes into account two error sources: the shot noise on the PMT and the background noise (estimated from the last 1'000 channels of the lidar signals or 7'500m). The signal to noise ratio is considered as the ratio between the background subtracted signal and the average of these last 1'000 channels. The shot noise is expressed by a Poisson distribution (i.e. proportional to \sqrt{N}) and dominates when the signal to noise ratio is high, e.g. at low altitude, while the background noise is the principal source of the statistical error at low signal to noise ratio or high altitudes. The sum of these two contributions is given in the following equation:

$$\frac{d_{H_2O}}{H_2O} = \frac{1}{\sqrt{N_{H_2O}}} \sqrt{1 + \frac{R}{N_{bkg}}} \frac{1}{1-R} \quad (5)$$

where N_{H_2O} is the number of detected photons, N_{bkg} is the number of channels used to average the background signal (1'000 in this case) and R is the ratio of the average value of the background and the total signal [12].

For the systematic error sources, a careful control of the alignment of the lidar emitter/receiver was performed regularly. Since no misalignment was observed even over periods of some days of continuous measurements, this error source was no longer considered. Note that a systematic error would change the calibration constant C but this effect is also cancelled by considering for each H_2O profile the simultaneous external calibration value.

3. H₂O Measurements

Since August 2000, nighttime measurements of the water vapor content were performed by Raman lidar at Jungfraujoch on a regular basis. Two typical cases of water vapor lidar profiles in clear sky conditions (A) and in presence of a cloud layer (B) will be presented. The laser parameters and the meteorological conditions during these two periods of measurements are summarized in Table 1.

Table 1: Lidar parameters and meteorological conditions

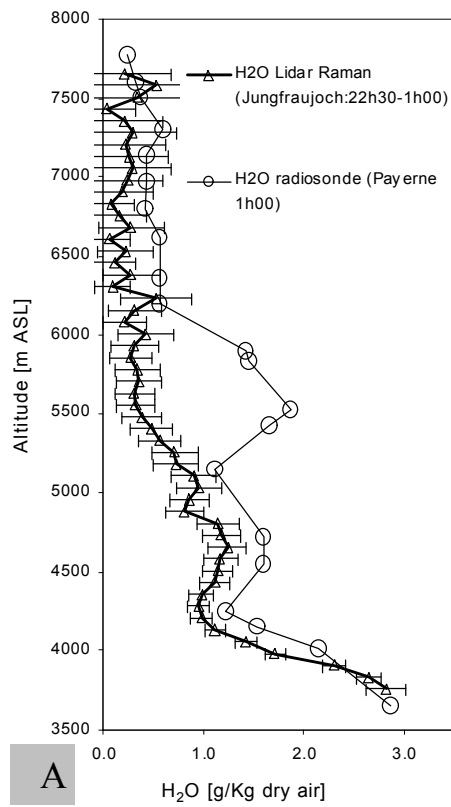
| Case | Date/Time Start | Int. Time [h] | Laser 355nm | Meteorological Conditions (Jungfraujoch site) | | | | |
|------|---------------------|---------------|-------------|---|-----------------------|---------------------|----------------------|------------------------|
| | | | | T _a [°C] | P _a (mbar) | RH _a [%] | WD _a [°N] | WS _a [km/h] |
| A | 01/08/2000 22:34 | 2:41 | 60mJ/20Hz | 1.4 | 668.9 | 39.9 | 307.9 | 33 |
| B | 29/08/2000 23:26 | 2:28 | 31mJ/20Hz | -0.4 | 664.4 | 61.2 | 307.3 | 30 |

The water vapor vertical profile obtained by Raman lidar in clear sky (A) conditions for an integration time of 2 h 41 min with a space resolution of 75 m is shown in the Figure 4a. This result is extracted from the lidar signals presented in Figure 4b where the range corrected signals RCS i.e. the raw lidar signals multiplied by the square of the distance for four different lidar channels are given. They correspond to the two Raman shifted signal at 408 nm (H₂O) and 387 nm (N₂) and the two elastic signals at 355 nm and 1064 nm. A water vapor profile obtained by meteorological balloon launched simultaneously from Payerne by ISM is shown for comparison in Fig. 4a. The reference value of the water vapor mixing ratio of the Raman lidar profile is directly measured at Jungfraujoch and considered as constant for the lidar calibration at the effective altitude of 3'700m ASL.

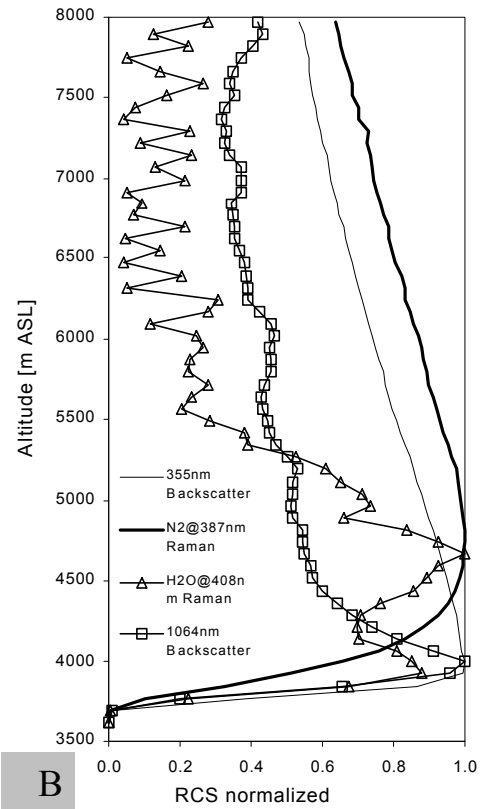
With the use of the 20 cm Newtonian telescope the measurement range is limited to typically 8 km ASL due to insufficient signal to noise ratio at higher altitude. The statistical error bars have been calculated according to Equ. (5). The H₂O Raman lidar profile appears in good agreement with the radiosonde profile up to about 5 km ASL. This comparison must nevertheless be considered with care since the balloon was launched from Payerne, which is located approximately 80 km west from Jungfraujoch at 490 m ASL. The rather large discrepancy between lidar and radiosonde data observed in the altitude range from 5-6 km is probably linked to the presence of cloud layers over Payerne and not at Jungfraujoch. Above 7 km both techniques indicates a water vapor content of less than 0.5 g/kg and the error on the lidar estimation increases due to the very low signal to noise ratio. Note that the water vapor column density estimated from the lidar data gives a value of 4 mm of precipitable water vapor above Jungfraujoch, or about 40% of the water vapor column density measured from Payerne.

The case (B) with a cloud layer uniformly developed over Switzerland is given in Figure 5. Fig. 5a shows a similar comparison between balloon and Raman lidar measurements as in Fig. 4a for a lidar integration time of 2 h 28 min and 75 m vertical resolution in the presence of a cloud layer around 5.5 km ASL. Here the profiles are shown only up to 6 km ASL due a strong attenuation of the laser light above the cloud. In this figure the molecular and the aerosol correction factors that are considered in $\Gamma(z, \lambda_{H_2O}, \lambda_{N_2})$ are also shown. Up to 5 km ASL the Raman lidar water vapor profile is in reasonable agreement with the radiosonde measurement. The lidar profile shows an increase of the water content in the cloud despite of its low relative optical thickness. The aerosols correction which is negligible below the cloud (no aerosols) reaches high values (20 %) in the cloud. For comparison the Rayleigh molecular correction has a contribution of less than 4 % at 6 km ASL.

In Fig. 5b the two elastic lidar signals at 355 and 1064 nm are strongly perturbed by the presence of the cloud layer. This is not the case for the measurement of the N₂ Raman shifted wavelength. This is indicative of a receiver optic with excellent rejection of the elastic signal and essentially no interference on the Raman channel. In the case of the Raman water vapor channel, even if the signal is also strongly attenuated by the cloud layer, there is a distinct increase of water vapor content measured in the cloud layer. Note that this study is performed without considering multi-scattering effects, water droplets absorption, or Raman scattering from liquid water [6].



A



B

Figure 4A:

Vertical profile comparison between water vapor mixing ratio measured by Raman lidar and by radiosonde in the case of clear sky condition (case A)

Figure 4B:

Range corrected signals for the two Raman wavelengths and the elastic 355 and 1064 nm.

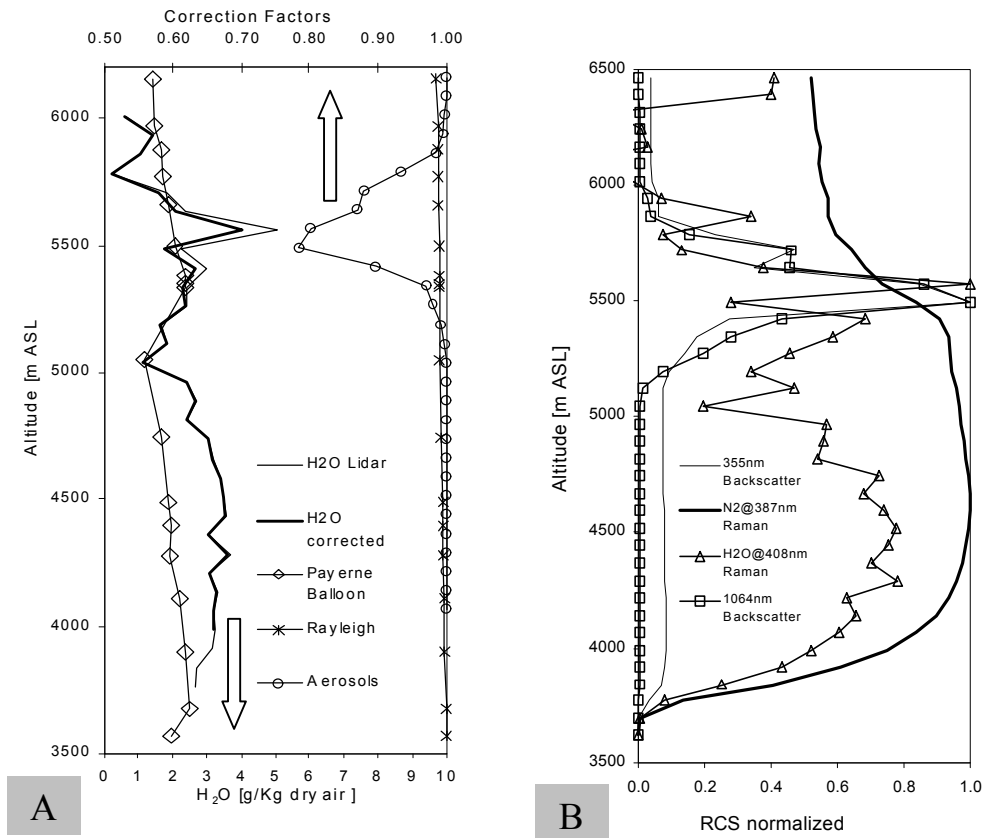


Figure 5a:

Vertical profile comparison between water vapor mixing ratio (lower scale) measured by Raman lidar and by radiosonde in the case of cloudy sky condition (case B). The correction factors (upper scale) for the water vapor content by Raman lidar are indicated both for the Rayleigh correction (less than 5%) and for the Mie scattering (up to 20 % in the cloud).

Figure 5b:

Range corrected signals for the two Raman wavelengths and the elastic 355 and 1064 nm. The cloud layer at an altitude of 5,5 km ASL is clearly shown on the two elastic signals, while the Raman signals are essentially not perturbed. This is indicative of an excellent rejection ratio of the elastically back-scattered light in the Raman channels.

These first results demonstrate the sensitivity of the method for both clear sky and cloudy conditions. The relatively small altitude range of the measurement is due to the small active area of the telescope. From simple model calculation, the use of the astronomical telescope will enhance our range of measurement of the water by Raman lidar over the entire troposphere.

Conclusion

At the Jungfraujoch Alpine Research Station in Switzerland, a new lidar system was operated since 1999 with continuous monitoring of the aerosol properties in the free troposphere since spring 2000. Water vapor measurements by Raman lidar have been demonstrated in this paper. These measurements are obtained in the free troposphere using an intense UV laser beam at 355 nm and detecting the range resolved Raman back-scattered signal by water molecules at 408 nm and nitrogen at 387 nm. With a calibration value measured directly at Jungfraujoch, the ratio of these two signals can be directly interpreted as a water vapor mixing ratio profile in the free troposphere. These measurements are obtained over a limited altitude range of typically 4-8 km ASL due to the initial use of a small size telescope (20 cm primary mirror diameter). The same method will soon be applied using the astronomical telescope (76 cm primary mirror diameter) and in this case simple model calculations have shown that water vapor profile up to the tropopause should be achieved, with a time resolution of less than one hour and an altitude range resolution of typically 100 meters. These predictions are done for nighttime measurements, while daytime Raman lidar observations are still limited by the availability of interference filters with higher daylight rejection ratio.

At Jungfraujoch, the water measurements obtained by lidar and combined with range resolved passive microwave detection in the stratosphere and mesosphere will provide a unique tool for the detection of the water vapor content throughout the earth atmosphere. These combined methods could ideally complement the regular (every six hours) balloon sounding performed by the Swiss Meteorological Institute from Payerne for example. Furthermore these new local and high vertical resolution water vapor measurements could be add to the satellite observations in order to contribute at the general effort of understanding better the water vapor variability and trends..

Once self-consistent calibrated and optimized this method could be considered like a benchmark of long-term monitoring of high vertically resolved water vapor content in the middle and upper troposphere. Finally the combination of *in situ* aerosol characterization [19], solar radiation monitoring [20], trace gas column density by FTIR [21, 22], and range resolved observation of water vapor and ozone by passive microwave [23] and lidar, as well as temperature by rotational Raman lidar [24], will make this primary site of observation of the NDSC (Network for Detection of Stratospheric Changes) [25] a unique place for the observation of global climate change issues.

Acknowledgements

The authors kindly thank Mr. P. Jeannet and Dr. A. Heimo from Swiss Meteorological Institute (Payerne station) for the radio sounding data and the use of meteorological data from Jungfraujoch, the Swiss National Foundation for the financial support and the Jungfraujoch Alpine Research Station for allowing us to use their research facilities.

References

- [1] Houghton, J.T., G.J. Jenkins, and J.J. Ephraim's (Eds.), *Climate Change: The IPCC Scientific Assessment*, Intergovernmental Panel on Climate Change, U.K. Meteorological Office, Bracknell, England, (1990).
- [2] Chahine, M.T., The hydrological cycle and its influence on climate, *Nature*, 359, 373, (1992).
- [3] Starr, D.O. and S.H. Melfi (Eds.), *The Role of Water-vapor in Climate: A Strategic Research Plan for the Proposed GEWEX , Water-vapor Project (GVaP)*, *NASA Conf. Publ.*, CP-3120, 50 pp., (1991).
- [4] England, M.N., R.A. Ferrare, S.H. Melfi, D.N. Whiteman, and T.A. Clark, Atmospheric water-vapor measurements: Comparison of microwave radiometry and lidar, *J.Geophys. Res.*, 97, 899, (1992).
- [5] Melfi, S.H., and Whitemann, D.N., "Observation of lower-atmospheric moisture structure and its evolution using a Raman lidar", *Bulletin of the American Meteorological Society*, 66(10), pp.1288-1292, (1985)
- [6] Ansmann, A., Riebesell, M., Wandinger, U., et al., "Combined Raman elastic-backscatter LIDAR for vertical profiling of moisture, aerosols extinction, backscatter and lidar ratio", *Applied Physics B: Photonics and Laser chemistry*, vol. 55, pp. 18-28 (1992)
- [7] B. Lazzarotto, M. Frioud, G. Larchevêque, V. Mitev, P. Quaglia, V. Simeonov, A. Thompson, H. van den Bergh, and B. Calpini "Ozone and water vapor measurements by Raman lidar in the planetary boundary layer: error sources and field measurements" in press, *Applied Optics*, (2001).
- [8] Melfi, S.H., Lawrence, J.D., and McCormick, "Observation of Raman Scattering by water vapor in the atmosphere", *Appl. Phys. Letters*, 15(9), pp. 295-297 (1969).
- [9] Whitemann, D.N., Melfi S.H., and Ferrare R. A., "Raman lidar system for the measurement of the water vapor content and aerosols in the Earth's atmosphere", *Appl. Opt.* 31, 3068-3082 (1992)
- [10] Keckhut, A. Hauchecorne, and M. L. Chanin, "A critical review of the database acquired for the long-term surveillance of the middle atmosphere of the French Rayleigh lidars," *J. Atm. Ocean. Techn.*, 10, 850--867, (1993).
- [11] Platt, C. M. R., J. C. Scott, and A. C. Dilley, "Remote sensing of high clouds. Part VI: Optical properties of midlatitude and tropical cirrus," *J. Atm. Sci.* 44, 729--747, (1987).
- [12] Sherlock, V., et al. "Implementation and validation of a Raman lidar measurement of middle and upper tropospheric water-vapor", *Applied Optics*, vol.38, No27, (September 1999).
- [13] Kwon, S.A. et al., "Vertical distribution of atmospheric particles and water-vapor densities in the free troposphere", *Atmospheric Environment*, vol.31, No. 10, (1997).
- [14] Sherlock, V., et al. "Methodology for the independent calibration of Raman backscatter water-vapor lidar system", *Applied Optics*, vol.38, No 27, (1999).
- [15] Johnathan Wayne Hair, "A high spectral resolution Lidar at 532nm for simultaneous measurement of atmospheric state and aerosols profiles using iodine vapor filters", thesis, (1999)
- [16] Lazzarotto B. , Simeonov V. , Quaglia P. , Larchevêque G. , van den Bergh H. , and Calpini B. "A Raman Differential Absorption Lidar for Ozone and Water-vapor Measurement in the Lower Troposphere"; *Intern. J. of Env. An. Chem.* , 74 (1-4), pp. 255-261, (1999).

-
- [17] P. Quaglia, I. Balin, G. Larchevêque, V. Simeonov, H. Van Den Bergh, and B. Calpini "A new LIDAR station at the Jungfraujoch alpine station for long term monitoring of aerosols, temperature and water vapor", Proclim - 1st *Global Swiss Change Day, Berne*, (April, 2000)
- [18] Collis, R.T.H., and Russell, P.B., "Lidar measurement of particles and gases by elastic backscattering and differential absorption", *Laser monitoring of the atmosphere*, E.D. Hinkley ed., Springer-Verlag, 71-151, (1976)
- [19] Baltensperger U., Gäggeler H.W., Jost D.T., Lugauer M, Schwikowski M., Weingartner E., Seibert P. : "Aerosol climatology at the high-alpine site Jungfraujoch, Switzerland", *J. Geo. Research*, D102, pp. 19707-19715, 1997
- [20] Heimo and al. : "The Swiss atmospheric radiation monitoring network CHARM", *proc. WMO Technical Conference on Meteorological and Environmental Instruments and Methods of Observation (TECO-98)*, Casablanca, Morocco, 13-15 May 1998.
- [21] Delbouille L., G. Roland:" High resolution solar and atmospheric spectroscopy from the Jungfraujoch high altitude station", *Opt. Eng.* , 34, pp. 2736-2739, 1995
- [22] De Mazière, M., M. Van Roozendael, C. Hermans, P.C. Simon, P. Demoulin, G. Roland:" Quantitative evaluation of the post-Pinatubo NO₂ reduction and recovery, based on 10 years of FTIR and UV-visible spectroscopic measurements at the Jungfraujoch", *Journal of Geophysical Research*, Vol. 103, pp. 10.849-10.858, 1998
- [23] Siegenthaler A., Lezeaux O., Feist D. G., and Kämpfer N. : "First water vapor measurements at 183 GHz from the high alpine station Jungfraujoch", *in press*, *IEEE Transactions on Geoscience and Remote sensing*.
- [24] Arshinov Yu., Bobrovnikov S. M., Zuev V. E., and Mitev V. M. : "Atmospheric temperature measurements using a pure rotational raman lidar", *Applied Optics*, 22, pp. 2984-2990, 1983.
- [25] <http://www.ndsc.ncep.noaa.gov/>

This chapter is divided into two sections. The first section presents a comparison between the aerosol optical depth from the sunphotometer of the Swiss Meteorological Institute and the integrated extinction profile from the lidar system. The second part of this chapter is dedicated to the study of one cirrus clouds event and size distributions below the clouds and at its tail. Extinction, backscatter, lidar ratio and depolarization ratio are shown.

8.1. Sunphotometer comparison

One very stimulant exercise is to compare results obtained by independent measurements such as the aerosol optical depth (AOD) derived from the sunphotometer of the Swiss Meteorological Institute and the integrated lidar extinction profile. For this purpose all the days with one hour lidar and one hour sunphotometer measurements between 11h and 14h local time were selected. This time interval is selected in order to avoid the effect of probing of different air mass by the two instruments since the sunphotometer AOD is projected on the zenith angle. The set of lidar elastic signals was uniformly treated with altitude ranging from 4.5 to 12km asl. The lowest value in the extinction profile is linearly extrapolated down to ground and then integrating the whole profile provides the AOD of the lidar. Figure 8-1 shows the intercomparison in the infrared region between the sunphotometer at 1024nm and the lidar at 1064nm.

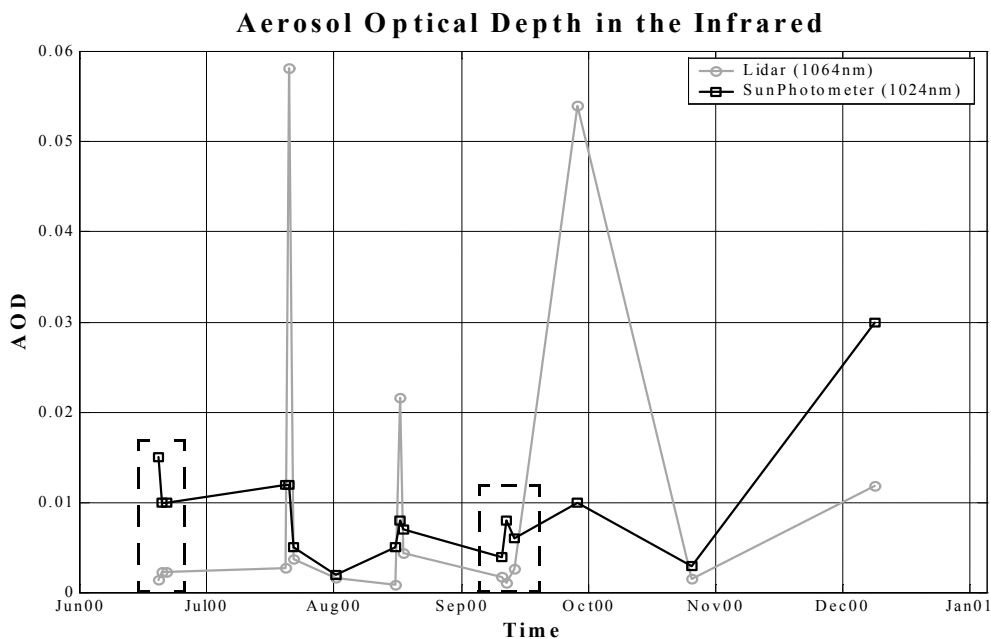


FIGURE 8-1. Intercomparison between sunphotometer and lidar aerosol optical depth (AOD) at 1024 and 1064nm, respectively, for one hour average profiles recorded between 11h and 14h local time. Dot-line rectangles can be subsidence effects from the valley.

No data of the sunphotometer is yet available for 2001 and the comparison is done from June 2000 to december 2000. During this period, negligible stratospheric AOD variation is assumed and thus do not influences the sunphotometer AOD. The aerosol optical depths of the lidar are in good agreement except the cloudy cases and when the lower layer is contaminated by subsidence from the valley especially during summer (dot-line rectangle). For the cloudy case, the lidar system is enable to measure while the sunphotometer is limited and does not provide results on the whole time period of one hour. Thus lidar AOD is larger than the sunphotometer AOD. For the second case, the lidar is blind at low altitude and do not detect the increasing aerosol load. Thus the lidar AOD do not show increasing values. This comparison proves the

capacity of this lidar system of providing reliable measurements.

Figure 8-2 shows the lidar AOD at the three elastic wavelengths for the entire set of signals between 11h and 14h local time.

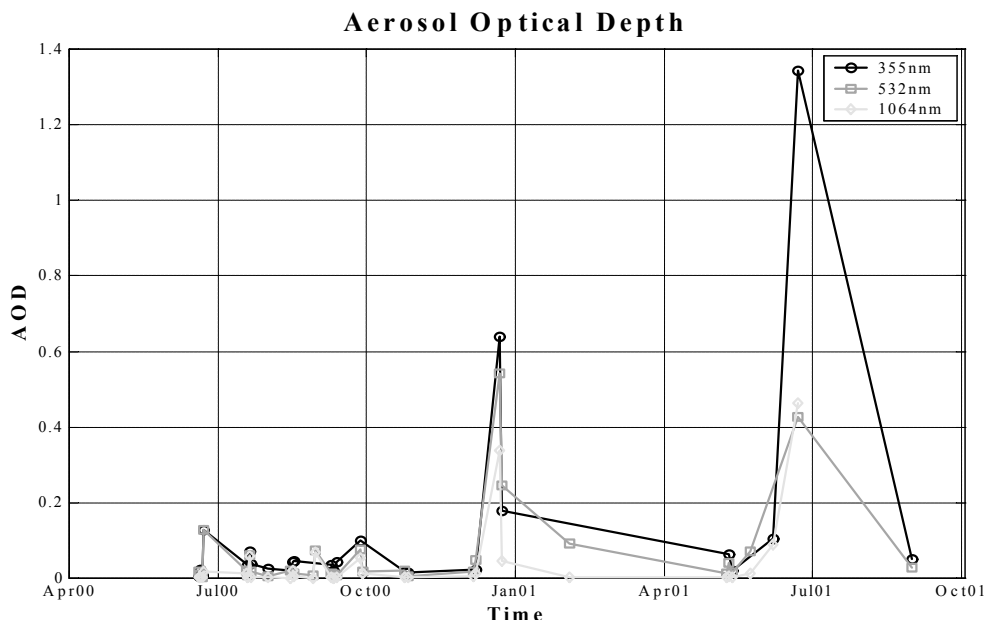


FIGURE 8-2. Lidar aerosol optical depth (AOD) at 355, 532 and 1064nm calculated between 5 and 12km asl for one hour average profiles recorded at 12h local time.

The general behavior out of the cloudy case, is decreasing AOD for the longer wavelengths induced by small particles. From this figure, no clear seasonal variation can be highlighted as for example the influence of the subsidence effects. For this, one have to focus measurements on the first 2km above the station but it is not possible with the present lidar configuration. For the free troposphere it is not reasonable to expect some reliable statistics only over one year. One have to be patient for such long term studies...

8.2. Cirrus study

This section presents the results obtained the June 20th 2001 between 21h00 and 24h00 local time. During this period, cirrus clouds were present at an mean altitude of 10km asl. Backscatter, extinction, depolarization ratio and lidar ratio profiles are presented and also a first attempt of size distribution retrieval below and at the tail of the clouds.

8.2.1. Meteorological conditions

The temperature, relative humidity (R.H.) and pressure at Jungfraujoch, recorded on June 20th 2001 by the Swiss Meteorological Institute, are given by Figure 8-3. During the measurement time period those parameters are stable with mean values of 270^oK, 22% and 663mbar, respectively.

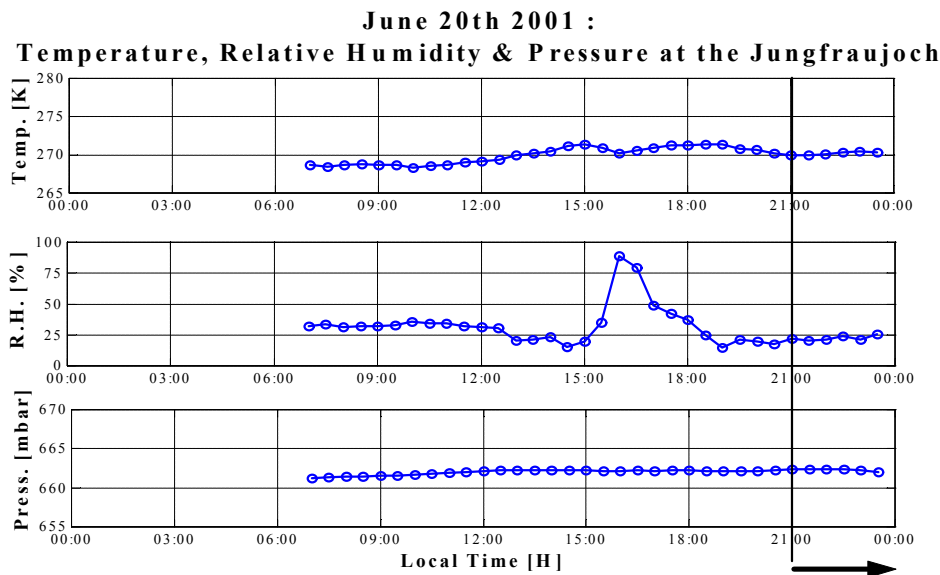


FIGURE 8-3. Temperature, relative humidity and pressure on June 20th 2001 at the Jungfraujoch.

The temperature and relative humidity profiles from a balloon launched at 24h00 from Payerne are shown in Figure 8-4 for comparison. The triangle symbol gives the corresponding three hours mean values measured at the Jungfraujoch Station and the rectangle gives the altitudes where the cirrus cloud is detected. The temperature profile and the pressure profile (not shown here) are not used for the inversions while the topographic influence at low altitude above the lidar system is not known. The problem is how to link the ground-level measurements to the balloon profiles?

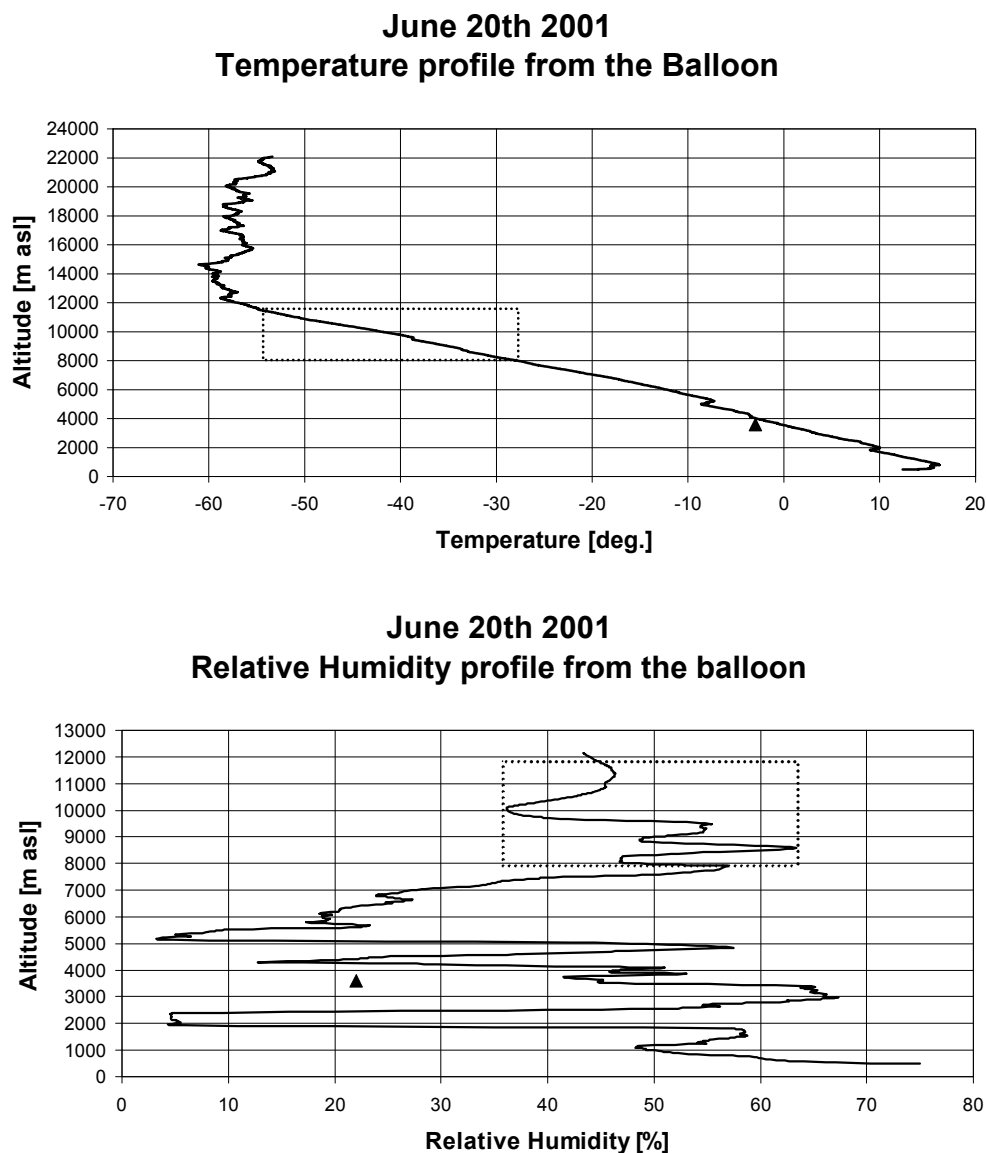


FIGURE 8-4. June 20th 2001 temperature (upper panel) and relative humidity (lower panel) profiles at midnight from a balloon launched at Payerne. The triangle symbol represents the measures at the Jungfraujoch Station while the dot rectangle is the cloudy zone of interest ranging from 8000 and 11500 m asl.

8.2.2. Lidar setup

During that period, the lidar configuration was 355, 387, 532(p), 532(c) and 1064nm. The 408 and 607nm were not available due to the loan of two transient recorders to the DIAL system involved in a field campaign in Marseille. The system at the Jungfraujoch was running with a 20Hz repetition rate of the laser and a 200mJ total energy. Figure 8-5 shows the range corrected signals at 355, 532(p) and 1064nm and Figure 8-6 shows the 532(p), 532(c) range cor-

rected signals and the corresponding depolarization ratio. Those signals are without any data treatment excepted the subtraction of a noise file. The spatial resolution is 7.5m and the temporal resolution is 200 seconds. The X-axis represents the local time, the Y-axis is the altitude above sea level in meter while the intensity of the signal is represented by the color code. The four elastic wavelengths show the same two clouds at an altitude between 8000 and 11500m asl with a vertical extension of each about 2000m.

If compare with the balloon data, the expected temperature at the base of the clouds is -27°C and -55°C at the top. The altitude ($>8000\text{m}$ asl) and the temperature ($<-25^{\circ}\text{C}$) are representative of cirrus clouds.

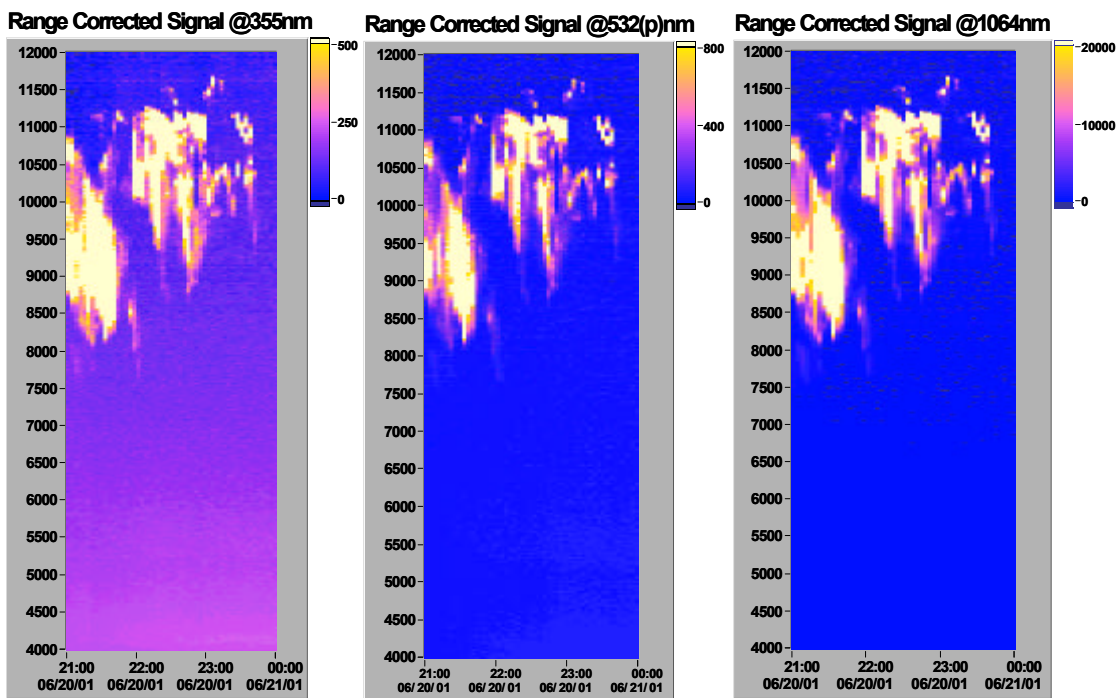


FIGURE 8-5. June 20th 2001, Range Corrected Signals at 355, 532(p) and 1064nm from 21h00 to 24h00. Spatial and temporal resolution of 7.5m and 200s respectively. Blue represents low backscattered signals while yellow is the contrary.

The depolarization ratio is generally less than 0.2 except at the base of the two clouds where the depolarization reaches a value about 0.5. The depolarization expected for ice layers are known to show values between 0.2 and 0.8, with frequent values between 0.4 and 0.5 (Sassen 1991). Lower depolarization have been sometimes observed in ice clouds. Further discussion about the depolarization ratio will be done later.

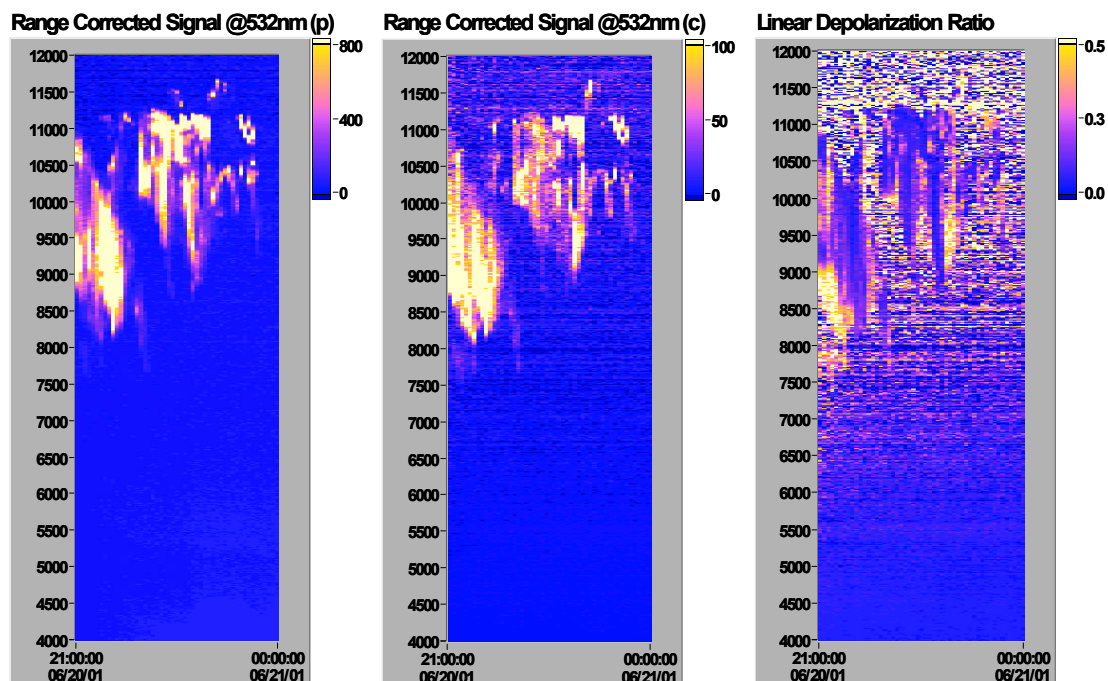


FIGURE 8-6. June 20th 2001, Range Corrected Signals at 532(p) and 532(c) from 21h00 to 24h00 and the corresponding depolarization ratio. Spatial and temporal resolution of 7.5m and 200s respectively. Blue represents low backscattered signals while yellow is the contrary.

As it is well explained in (Ansmann, Wandinger et al. 1992), systematic errors can be induced in strong varying atmosphere as it is the case in clouds. Therefore, one hour average profile is chosen as the mean value of three profiles (typ. 24000 laser shots) between 7 and 12km. Below 7km, the one hour average profile is the mean value of two profiles. Another additional error can be expected from the effect of multi-scattering inside clouds whose value can reach 10%. The Fernald inversion is performed with a sliding average with windows from 37.5 to 112.5m and a resolution of 45m in the analog mode and with a sliding average with windows from 75 to 262.5m and a resolution of 60m in the photoncounting mode. The former mode is dedicated to the lower part of the atmosphere (from 4500 to 8000m asl) with a constant lidar ratio of 45sr and a molecular value between 6800 and 7400m asl while the latter mode is dedicated to the cloudy altitudes (from 7500 to 12000m asl) with a constant lidar ratio varying from 3 to 30sr (depending on the time sampling) and a molecular value above 12000m asl. The infrared signal (1064nm) is only recorded in analog mode, but it is splitted into two regions and treated with the parameters described above. The depolarization ratio is determined from the ratio of the two signals at 532nm and is calculated from the smoothed signals. The Raman inversion is performed with an gliding average between 375m and 1125m, a reduced resolution of 45m in order to improve the signal to noise ratio, the wavelength dependence is taken to be equal to zero inside the clouds (photoncounting mode) and to unity lower down (analog mode). The aerosol free layer is supposed to be between 6800 and 7400m asl. Those parameters are set to provide an error of less than 20% on the backscatter and extinction

profiles from both algorithms.

8.2.3. Aerosol backscatter, extinction and lidar ratio profiles

Figure 8-7 shows the one hour average aerosol backscatter profiles at 355, 532 and 1064nm (upper panel) obtained by the Fernald inversion and the extinction profiles at 355nm (lower panel) obtained by the Raman algorithm. The aerosol backscatter profile at 355nm obtained by the Raman method is also shown. Discrepancies between the Raman and the Fernald results can be explained by the difference of the windows of the gliding averages and a unsuited lidar ratio applied in the Fernald inversion. Between 21 and 22h, the aerosol extinction profile above 7km is given in dot-line and is shown here for information. Its noisy behavior is due to sky background (sunset at 21h30).

Inside the cirrus clouds, the maximum aerosol backscatter value of $(2.4 \pm 0.4) \times 10^{-5} \text{m}^{-1} \text{sr}^{-1}$ at 355nm, from the Raman inversion, is reached at an altitude of 9.3km between 21h and 22h (a) and $(1.9 \pm 0.5) \times 10^{-5} \text{m}^{-1} \text{sr}^{-1}$ at 10.6km the next hour (b). The last profile shows a reduced value of $(3.1 \pm 0.9) \times 10^{-6} \text{m}^{-1} \text{sr}^{-1}$ for the tail of the clouds at an altitude of 10.6km (c). For comparison, the elastic backscatter values at 355nm are $(3.0 \pm 0.1) \times 10^{-5} \text{m}^{-1} \text{sr}^{-1}$, $(4.1 \pm 0.1) \times 10^{-5} \text{m}^{-1} \text{sr}^{-1}$, and $(5.5 \pm 0.4) \times 10^{-6} \text{m}^{-1} \text{sr}^{-1}$, respectively. The thin layer at 11km of the second hour is smoothed by the larger gliding average applied on the Raman signals. Unfortunately, a smaller resolution induces more noisy extinction profiles and by the way worst lidar ratio. The three corresponding maximum backscatter coefficients measured at 532nm are $(2.9 \pm 0.1) \times 10^{-5} \text{m}^{-1} \text{sr}^{-1}$, $(3.2 \pm 0.1) \times 10^{-5} \text{m}^{-1} \text{sr}^{-1}$, and finally $(4.3 \pm 0.4) \times 10^{-6} \text{m}^{-1} \text{sr}^{-1}$, while the infrared maximum values are $(2.1 \pm 0.1) \times 10^{-5} \text{m}^{-1} \text{sr}^{-1}$, $(2.9 \pm 0.1) \times 10^{-5} \text{m}^{-1} \text{sr}^{-1}$, and $(4.6 \pm 0.2) \times 10^{-6} \text{m}^{-1} \text{sr}^{-1}$, respectively. If those measurements are compared by wavelength per period, a wavelength dependency is observed in cirrus backscattering suggesting the presence of particles with a size of the same order of magnitude than the wavelengths. This can explain also the observed low depolarization values. This dependency is weak during the first time period and emphasizes during the two following hours.

The second region of interest is situated between 5 and 6km asl and is taken as a low aerosol load or clean atmosphere condition. Presented here are the mean values over this one kilometer region. The Raman method at 355nm provides the values of $(3.6 \pm 0.3) \times 10^{-7} \text{m}^{-1} \text{sr}^{-1}$, $(4.7 \pm 0.5) \times 10^{-7} \text{m}^{-1} \text{sr}^{-1}$ and $(7.0 \pm 0.6) \times 10^{-7} \text{m}^{-1} \text{sr}^{-1}$ corresponding to the first (a), second (b) and third time period of measurements (c), respectively, while the elastic backscatter coefficients are $(1.6 \pm 0.2) \times 10^{-7} \text{m}^{-1} \text{sr}^{-1}$, $(2.2 \pm 0.2) \times 10^{-7} \text{m}^{-1} \text{sr}^{-1}$ and $(2.0 \pm 0.2) \times 10^{-7} \text{m}^{-1} \text{sr}^{-1}$. The backscatter values at 532nm are $(8.5 \pm 0.9) \times 10^{-8} \text{m}^{-1} \text{sr}^{-1}$, $(1.5 \pm 0.1) \times 10^{-7} \text{m}^{-1} \text{sr}^{-1}$, and $(1.7 \pm 0.1) \times 10^{-7} \text{m}^{-1} \text{sr}^{-1}$, respectively and those at 1064nm are $(3.1 \pm 0.4) \times 10^{-8} \text{m}^{-1} \text{sr}^{-1}$, $(4.5 \pm 0.5) \times 10^{-8} \text{m}^{-1} \text{sr}^{-1}$, and $(5.4 \pm 0.6) \times 10^{-8} \text{m}^{-1} \text{sr}^{-1}$. All those values, except the last 355nm elastic value show an increase of the backscatter coefficients at low altitude. The strong wavelength dependence is characteristic of small particles that are expected in this region of a relatively clean atmosphere.

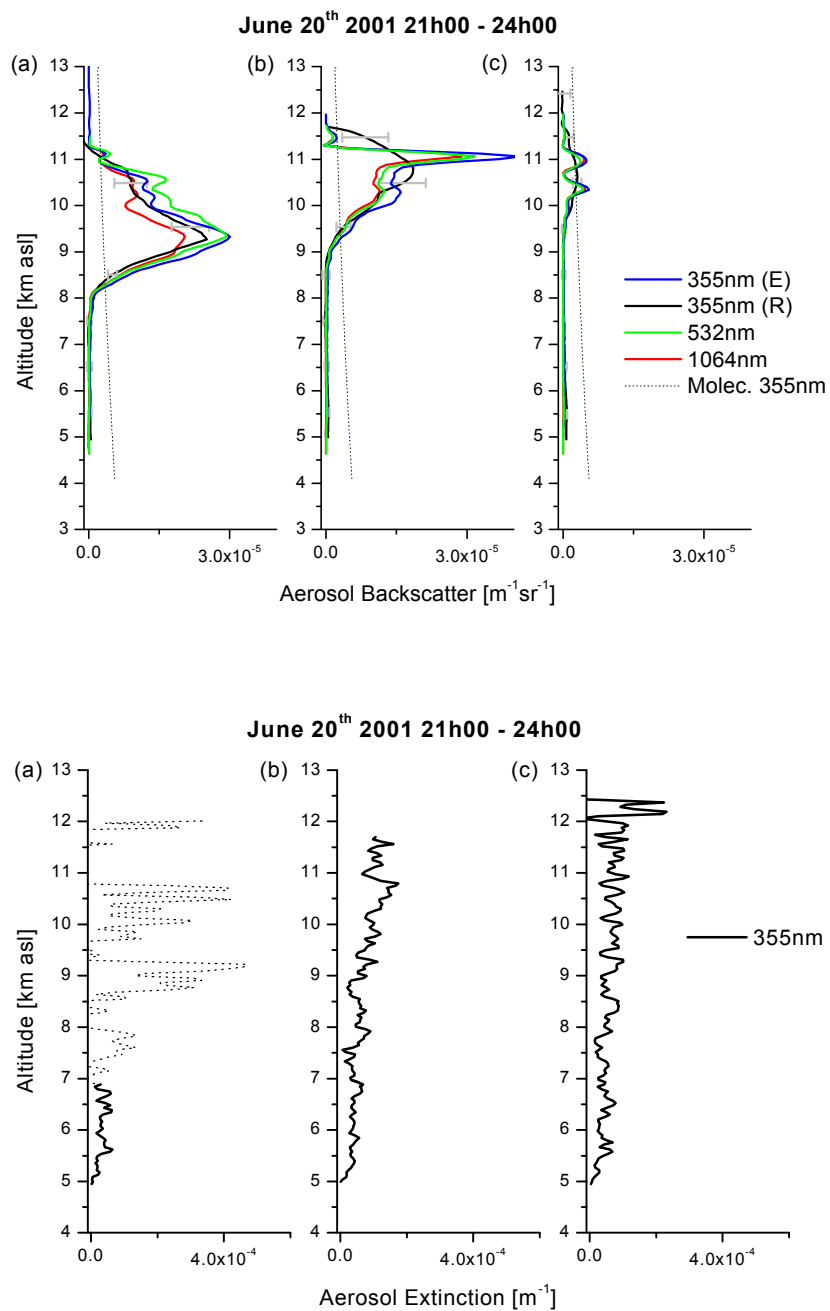


FIGURE 8-7. June 20th 2001 one hour average aerosol backscatter profiles at 355, 532 and 1064nm (upper panel) and one hour average aerosol extinction profiles at 355nm (lower panel). From left to right, profiles between (a) 21h and 22h, (b) 22h and 23h, and (c) 23h and 24h respectively. Subscript (E) and (R) stand for elastic and Raman respectively.

The aerosol extinction profiles at 355nm are obtained by the Raman inversion. The values corresponding to maximum backscatter are $(1.7\pm 0.1)\times 10^{-4}\text{m}^{-1}$ and $(1.0\pm 0.1)\times 10^{-4}\text{m}^{-1}$. Out of the cloud, the average value of the aerosol extinction coefficient is around $(3.0\pm 0.3)\times 10^{-5}\text{m}^{-1}$.

Those extinction and backscatter coefficients are representative of cirrus clouds. A second condition at 355nm is that only in cirrus clouds $\beta_p > 0.8\beta_m$ is satisfied (Reichardt 1999). Figure 8-8 shows the comparisons between the three Raman aerosol backscatter profiles and the 0.8 times molecular backscatter profile. This condition is fulfilled between 8.3 and 11.1km, between 9.5 and 11.7km, and between 10.2 and 11.0km for the first, second and third hour respectively. The 532nm elastic extinction profiles are used for the calculation of the optical depth inside the cloud for the two first hours. The obtained values are 0.38 between 8.0 and 11.3km, and 0.04 between 9.0 and 11.3km. A cirrus with an optical depth smaller than 0.05 is called subvisible cirrus while an optically thin ice cloud has an optical depth between 0.05 and 0.3 (Sassen 1989).

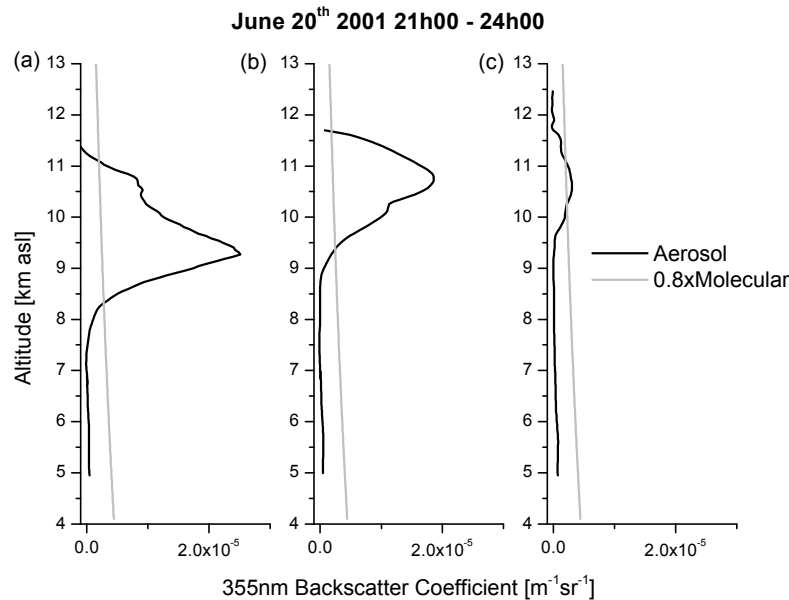


FIGURE 8-8. June 20th 2001 comparisons between the Raman aerosol backscatter coefficient at 355nm and the 0.8 times molecular backscatter coefficient between (a) 21h and 22h, (b) 22h and 23h and (c) 23h and 24h. Cirrus clouds satisfying the condition $\beta_p > 0.8\beta_m$.

Figure 8-9 shows the lidar ratio determined from the extinction and backscatter profiles at 355nm applying the Raman method. The lidar ratio can not be determined when the aerosol extinction coefficient is close to zero and the lidar ratios with a large error are not accounted for. So no lidar ratio are available between 6km asl and the base of the clouds. Below 6km asl, the lidar ratio values are between $(40\pm 3)\text{sr}$ and $(71\pm 20)\text{sr}$, $(40\pm 7)\text{sr}$ and $(83\pm 20)\text{sr}$, $(19\pm 1)\text{sr}$ and $(97\pm 27)\text{sr}$ during the first (a), the second (b) and the third hour (c), respectively. Those values are close to the expected values of 45sr (Vaughan 1998) or 57sr (Ackermann 1998).

The lidar ratio inside the cirrus during the second hour starts from a value of (66 ± 8) sr at an altitude of 9km and falls down to (3.9 ± 0.2) sr at 11.1km and has a value of (33 ± 2) sr at 11.7km. The minimal value is lower than the expected value of 13.5sr calculated for cirrus clouds (Vaughan 1998). And this is still observed during the last hour with a minimum lidar ratio of (10 ± 2) sr.

Numerical studies imply a decrease of the lidar ratio with a decreasing size of scattering ice crystals (Ansmann, Wandinger et al. 1992), Figure 8-9(b) shows a trend to smaller lidar ratio from 9.5 to 11km asl, indicating such behavior in parallel with a decreasing depolarization ratio (see Figure 8-10(b)). So the base of the cirrus could be composed of large depolarizing particles (ice crystals) while the upper part with smaller depolarization but strong backscattering may be composed of smaller particles.

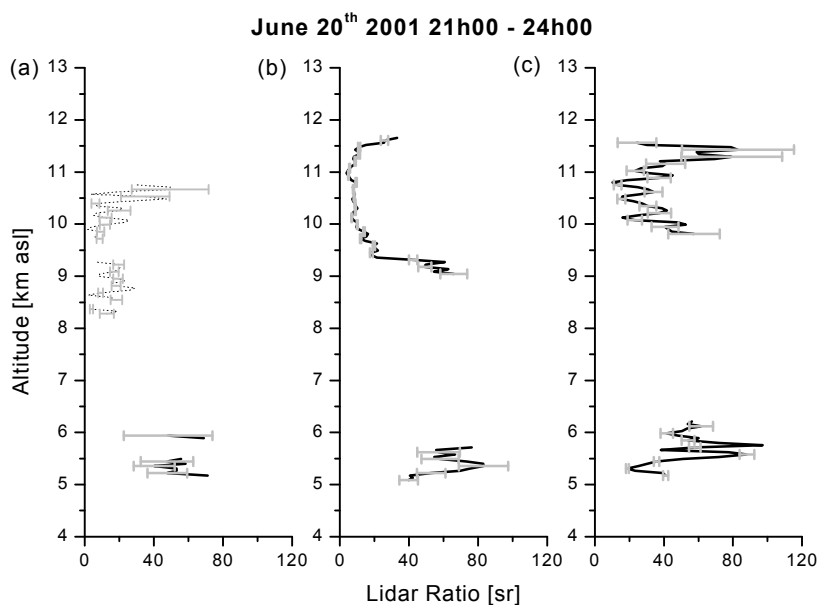


FIGURE 8-9. June 20th 2001 one hour average lidar ratio profiles at 355nm. From left to right, profiles between (a) 21h and 22h, (b) 22h and 23h, and (c) 23h and 24h respectively. The error bars are also shown.

Table 8-1 summarizes the backscatter and extinction values determined during this work inside a cirrus cloud for the second hour and at the tail of the cloud for the third hour. Some other values from (Ansmann, Wandinger et al. 1992) and theoretical results from (Vaughan 1998) are also shown. The last row of this table gives the values at the tail of the event and represents certainly a transient state.

TABLE 8-1. Comparison with other results of cirrus studies.

| Authors | Wavelength [nm] | Altitude [m asl] | Backscatter [$\text{m}^{-1}\text{sr}^{-1}$] | Extinction [m^{-1}] | Lidar ratio [sr] |
|-----------|--------------------|---------------------|--|-----------------------------------|---------------------|
| Ansmann | 308 | 9000 | 5×10^{-5} | 8×10^{-4} | 16 |
| Ansmann | 308 | 11200 | 4.5×10^{-5} | 4.5×10^{-4} | 10 |
| Ansmann | 308 | 8500 | 9×10^{-5} | 2×10^{-4} | 2 |
| Vaughan | 355, 532, 1064 | 7500 - 9500 | 1.4×10^{-5} | 2×10^{-4} | 13.5 |
| This work | 355 | 9300 | 1.9×10^{-5} | 1.7×10^{-4} | 9 |
| This work | 355 | 10600 | 0.3×10^{-5} | 1.0×10^{-4} | 33 |

8.2.4. Depolarization ratio

Figure 8-10 shows the depolarization ratio recorded in analog mode (black line) and in photon counting mode (gray line). Inside the cloud, the depolarization ratio reaches a maximum value of (0.24 ± 0.03) at 8.4km asl during the first hour, (0.13 ± 0.02) at 9.4km during the second hour and (0.18 ± 0.03) at 11.1km during the last hour. The altitudes of those two first ratio correspond to the altitude of the base of the cirrus while the altitude of the third one can be explained by the presence of a third layer between 11.0 and 11.5km whose linear depolarization has a value of (0.21 ± 0.01) and (0.28 ± 0.04) during the first and second hour respectively. Above the clouds, the average depolarization ratio is of order of 0.03, close to the molecular and pure spherical particles value.

When observed in cirrus, low depolarization values are often attributed to presence of big ($>100\mu\text{m}$) horizontally oriented plates (Platt 1978). Another answer to this behavior is the presence of liquid droplets and ice particles, together. Supercooled water is short living below -40°C , but in the presence of enhanced sulfuric aerosols, liquid droplets have been detected in cirrus colder than -50°C (Sassen 1992). The occurrence of particles smaller than $20\mu\text{m}$ in cirrus is not well assessed because of the lack of reliable in-situ probes. A third answer to this problem involves big ($r_{\text{eq}} \gg 1\mu\text{m}$) columnar ice particles only. Columns are supposed to be the most common crystal type at tropopause conditions (Pruppacher 1997).

Such low depolarization cirrus have been observed in many cases above Sodankyla ($67,4^\circ\text{N}$, Finland) (Del Guasta 1994; Del Guasta 1998) and above Geesthacht (53.5°N , 10.5°E , Germany) (Reichardt 1999).

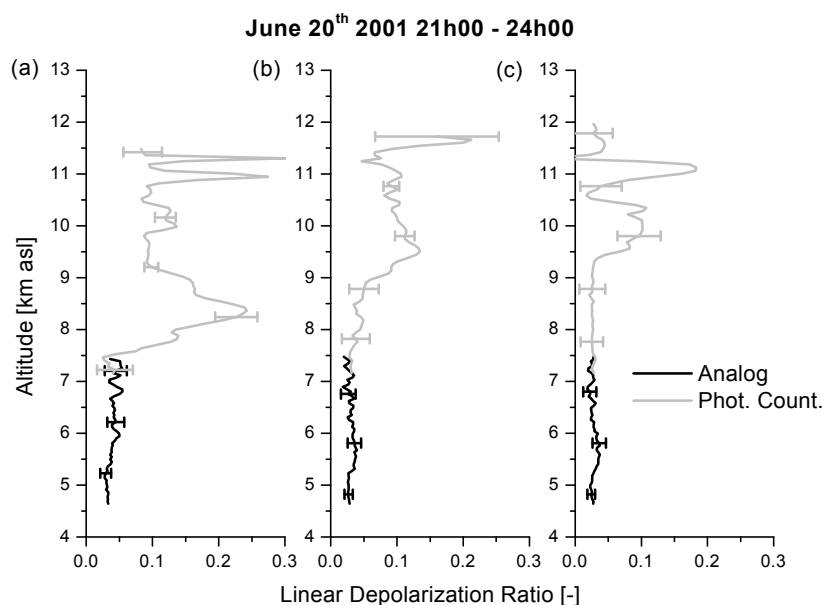


FIGURE 8-10. June 20th 2001 one hour average depolarization ratio profiles at 532nm. From left to right, profiles between (a) 21h and 22h, (b) 22h and 23h, and (c) 23h and 24h respectively. Subscript (An.) and (Ph.C.) stand for analog mode and photoncounting mode respectively. The error bars are also shown.

8.2.5. Size retrieval

This section presents the first attempt of size retrieval with real signals recorded at the Jungfraujoch. In an ideal case, three backscatter and two extinction coefficients with uncertainties smaller than 20% are needed for this retrieve. Since only one extinction is recorded in this case, the inversion is more unstable, but this can be overcome if the index of refraction is approximately known. For the region between 5 and 6km asl above the lidar system, the relative humidity is assumed to be close to the ground-level value (~22%). The chemical composition of dry aerosol performed by the Paul Scherrer Institut is dominated by ammonium sulfate (50%), carbonaceous particles (10%) and organic material (5%) (Weingartner 2001). The refractive indexes of those particles are $1.53-0.00i$, $1.75-0.45i$ and $1.40+0.00i$, respectively and if an internal melange is accounted for, the imaginary part of the bulk aerosol is around 0.05 and the expected real part is between 1.44 and 1.55. The former value is calculated with 35% of matter with a refractive index of $1.25+0.00i$ and the latter with 35% of matter with a refractive index of $1.55+0.00i$. For the cloudy region, the dry composition is no more adequate and thus the refractive index is taken as a hydrated aerosol and is set to $1.37+0.001i$ (IPCC 2001). The value of those refractive indexes are issue from (HITRAN 1996; IPCC 2001). The IMP algorithm is performed with the input parameters shown in Table 8-2.

TABLE 8-2. Input parameters for the IMP algorithm. The backscatter coefficients are given bottom down at 355, 532 and 1064nm and the extinction coefficient at 355nm.

| Case description | Radius range [μm] | Real part of the refractive index | Imaginary part of the refractive index | Extinction [m^{-1}] | Backscatter [$\text{m}^{-1}\text{sr}^{-1}$] |
|--------------------------------------|--------------------------------|-----------------------------------|--|--------------------------------|--|
| Case 1: 21h - 22h 5 - 6km | 0 - 2 | 1.44 - 1.55 in 11 steps | 0.04 - 0.05 in 5 steps | 2.8×10^{-5} | 3.6×10^{-7} 8.5×10^{-8} 3.1×10^{-8} |
| Case 2: 22h - 23h 5 - 6km | 0 - 2 | 1.44 - 1.55 in 11 steps | 0.04 - 0.05 in 5 steps | 3.3×10^{-5} | 4.7×10^{-7} 1.4×10^{-7} 4.5×10^{-8} |
| Case 3: 23h - 24h 5 - 6km | 0 - 2 | 1.44 - 1.55 in 11 steps | 0.04 - 0.05 in 5 steps | 3.3×10^{-5} | 7.0×10^{-7} 1.7×10^{-7} 5.4×10^{-8} |
| Case 4: 23h - 24h 9.7 - 10.6km | 0 - 10 | 1.37 in 1 step | 0.001 in 1 step | 7.2×10^{-5} | 2.0×10^{-6} 1.5×10^{-6} 1.8×10^{-6} |

Cases 1, case 2 and case 3 correspond to three sets of backscatter and extinction coefficients determined between 5 and 6km asl for the first, second and third hour, respectively. Case 4 is the set measured between 9.7 and 10.6km where the depolarization ratio is less than 0.1. The algorithm is based on the assumption of spherical particles. It is also possible to use it with elliptical or layered particles. The radius range is the lower and upper limits of the radius integration range of the IMP software. The real part and the imaginary part of the refractive index define the grid of calculation and the number of steps represents the resolution of the calculation. The extinction is the Raman extinction at 355nm, and the three backscatter values are given at 355, 532 and 1064nm respectively (bottom down).

Concerning the three cases at low altitude the radius range is set between zero and $2\mu\text{m}$ as suggested by in-situ measurements performed at Jungfraujoch (Baltensperger 1997). It is more difficult to select the correct radius range of the cloudy region. From the literature, authors stress the importance of particles sizes below the threshold of traditional crystal measurements ($20\mu\text{m}$) and give most important radius ranges between less than 2 and $4000\mu\text{m}$ (crystal length). As it was pointed out in theoretical chapter, the radius range is limited and an upper value of $10\mu\text{m}$ is selected. Thus only the last hour is selected for the size retrieval of the cloudy region.

8.2.5.a. Low altitude size distribution

Figure 8-11 shows the aerosol volume concentration distributions (dV/dr) of the three cases. The X-axis represents the radius of the particles and the Y-axis the volume distribution. The three curves per case give the best solution based on the different minimization methods. The indices of refraction of the best solution with regards to those methods are the label of those curves.

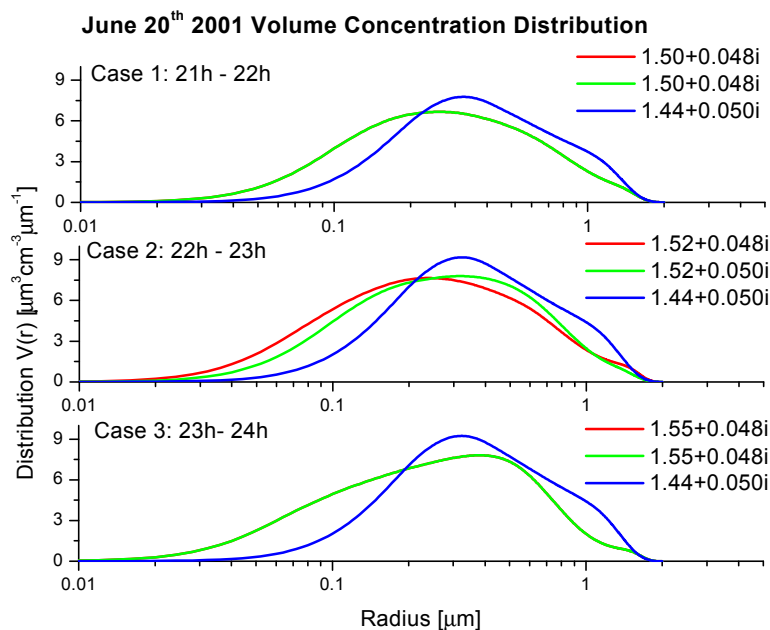


FIGURE 8-11. June 20th 2001 one hour average aerosol volume concentration distribution between 5 and 6km asl for case1: 21h - 22h, case2: 22h - 23h and case 3: 23h - 24h.

Those curves show that the accumulation range (0.05 to 1.25 μm) is the dominant range. Some particles are present in the Aitken Nuclei range ($<0.05\mu\text{m}$) while the coarse mode ($>1.25\mu\text{m}$) is almost empty.

Table 8-3, Table 8-4 and Table 8-5 summarize the integral parameters in the particle volume concentration distributions and the single-scattering albedo at 355nm of the case 1, case 2 and case 3, respectively. The last row of each table gives the mean values of the index of refraction, the effective radius, the surface concentration, the volume concentration, the particles concentration and the single scattering albedo, respectively.

In the three set of results, the third minimization method provides systematically the value of 1.44+0.050i while the two others methods gives the same values per set of data, except the second case, with an average value of 1.52+0.048i. The effective radius of the volume concentration distribution is almost constant during all the period with an average value of 0.38 μm . The surface concentration, the volume concentration and the number concentrations increase from

45 to $54\mu\text{m}^2\text{cm}^{-3}$, 5.7 to $6.6\mu\text{m}^3\text{cm}^{-3}$ and 206 to 408cm^{-3} . The extinction and backscatter coefficients increase during the period of observation and could be explain by the observed increase of the number concentration. The single-scattering albedo at 355nm has a value of 0.7. The critical single-scattering albedo that defines the boundary between cooling and heating effect depends on the surface albedo R_s and the upscatter fraction β (see(EQ 1.4) p 13).

TABLE 8-3. Case 1: Integral parameters of the particle size distribution

| Refractive index | Effective radius [μm] | Surface concentration [$\mu\text{m}^2\text{cm}^{-3}$] | Volume concentration [$\mu\text{m}^3\text{cm}^{-3}$] | Particle concentration [cm^{-3}] | Single scattering albedo at 355nm |
|------------------|------------------------------------|---|--|---|-----------------------------------|
| 1.50+0.048i | 0.35 | 45.3 | 5.3 | 261 | 0.70 |
| 1.50+0.048i | 0.35 | 45.3 | 5.3 | 261 | 0.70 |
| 1.44+0.050i | 0.44 | 43.0 | 6.3 | 96 | 0.68 |
| 1.48+0.048i | 0.38 | 44.5 | 5.6 | 206 | 0.69 |

TABLE 8-4. Case 2: Integral parameters of the particle size distribution

| Refractive index | Effective radius [μm] | Surface concentration [$\mu\text{m}^2\text{cm}^{-3}$] | Volume concentration [$\mu\text{m}^3\text{cm}^{-3}$] | Particle concentration [cm^{-3}] | Single scattering albedo at 355nm |
|------------------|------------------------------------|---|--|---|-----------------------------------|
| 1.52+0.048i | 0.33 | 55.3 | 6.1 | 490 | 0.71 |
| 1.52+0.050i | 0.36 | 52.8 | 6.3 | 294 | 0.70 |
| 1.44+0.050i | 0.44 | 50.8 | 7.5 | 114 | 0.68 |
| 1.49+0.049i | 0.38 | 53.0 | 6.6 | 299 | 0.70 |

TABLE 8-5. Case 3: Integral parameters of the particle size distribution

| Refractive index | Effective radius [μm] | Surface concentration [$\mu\text{m}^2\text{cm}^{-3}$] | Volume concentration [$\mu\text{m}^3\text{cm}^{-3}$] | Particle concentration [cm^{-3}] | Single scattering albedo at 355nm |
|------------------|------------------------------------|---|--|---|-----------------------------------|
| 1.55+0.048i | 0.33 | 55.4 | 6.1 | 555 | 0.71 |
| 1.55+0.048i | 0.33 | 55.4 | 6.1 | 555 | 0.71 |
| 1.44+0.050i | 0.44 | 51.1 | 7.5 | 115 | 0.68 |
| 1.52+0.048i | 0.37 | 54.0 | 6.6 | 408 | 0.70 |

Unfortunately, no in situ measurements of the size distribution were performed during this day what would be the most relevant validation of those results. The sum of two lognormal size distributions fitted on measurements performed at the Jungfraujoch (Weingartner 1999) for the clear-sky and free troposphere conditions is given in Figure 8-12. The lidar result of the case IIa (1.52+0.048i) gives an higher maximum volume concentration and is shifted in direction of

increasing radius. The particle number concentrations are 488cm^{-3} and 490cm^{-3} for the two lognormal distributions and the lidar distribution, respectively.

Knowing the two different conditions in which those measurements are performed (in-situ, $\text{R.H.} < 20\%$ and real atmosphere), this result can be regarded as good. Normally, the indoor size distribution must be corrected by a growth factor depending on the outdoor relative humidity.

June 20th 2001 Case 2: 22h - 23h Volume Concentration Distribution

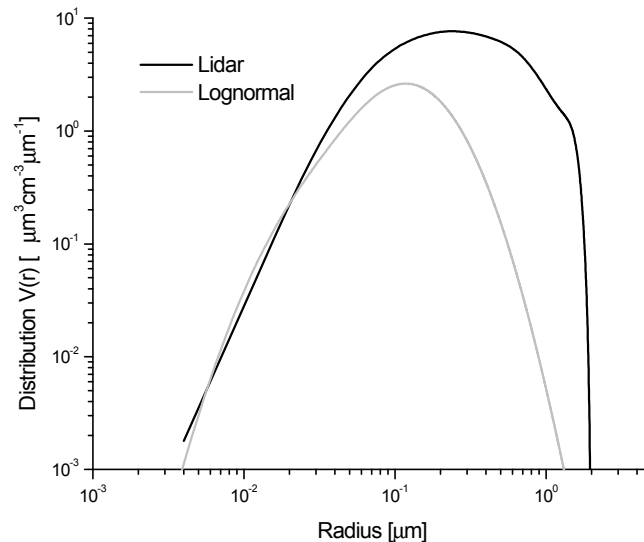


FIGURE 8-12. June 20th 2001 Comparison of the volume concentration distribution between the case 2 and the sum of two lognormal size distribution based on in-situ measurements.

To validate the retrieval of the size distribution, one field campaign is planned in summer 2002. The Paul Scherrer Institute will perform outdoor measurements and the lidar system will be upgraded in order to measure along a slant path in order to allow low altitude data collection.

8.2.5.b. Tail of cirrus size distribution

Figure 8-13 shows the one hour average volume concentration distribution of the case 4 between 9.7 and 10.6 km asl calculated with a refractive index of $1.37 + 0.001i$. Table 8-6 summarizes the integral parameters of the volume concentration distribution for this case. The effective radius of the volume concentration distribution has a value of $1.16\mu\text{m}$, three times the value of the other cases. The surface and the volume concentrations are also higher while the number concentration is smaller. The presence of larger particles induces such behavior.

This distribution is a bimodal one with one maximum around $0.5\mu\text{m}$ and the second one around $2.8\mu\text{m}$. The left part of this distribution corresponds to the accumulation range and has similar behavior than the distributions of the case 1, case 2 or case 3, but with a larger maximum volume concentration and shift in the increasing radius. That could be explained by some

in-cloud processes as scavenging and growth due to the aqueous phase reaction. The right part of this bimodal distribution could be the remain of the cirrus clouds of the previous hours.

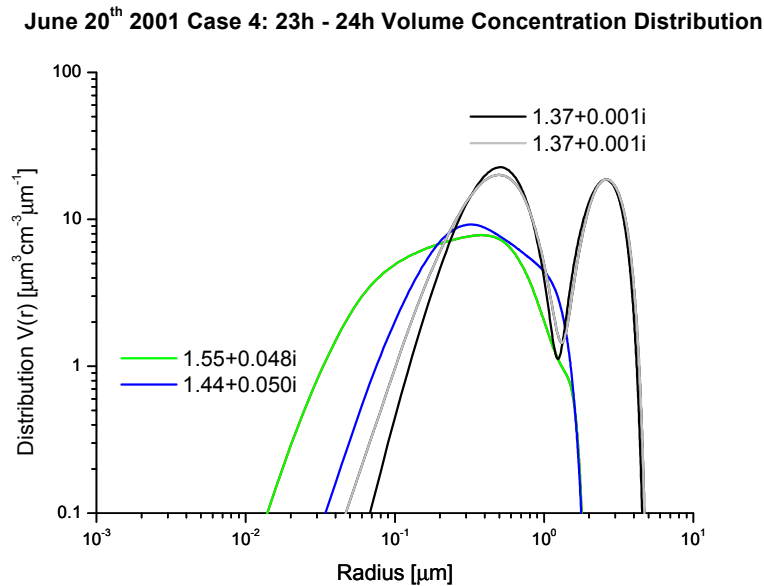


FIGURE 8-13. June 20th 2001 case 4: one hour average aerosol volume concentration distribution between 9.7 and 10.6 km asl for a refractive index of $1.37+0.001i$. The distribution of the case 2 are also shown and are labeled $1.55+0.048i$ and $1.44+0.050i$.

TABLE 8-6. Case 4: Integral parameters of the particle size distribution

| Refractive index | Effective radius [μm] | Surface concentration [$\mu\text{m}^2 \text{cm}^{-3}$] | Volume concentration [$\mu\text{m}^3 \text{cm}^{-3}$] | Particle concentration [cm^{-3}] | Single scattering albedo at 355 nm |
|------------------|------------------------------------|--|---|---|------------------------------------|
| $1.37+0.001i$ | 1.17 | 113.0 | 44.0 | 79 | 0.97 |
| $1.37+0.001i$ | 1.15 | 112.3 | 43.2 | 53 | 0.97 |
| $1.37+0.001i$ | 1.17 | 113.1 | 44.0 | 79 | 0.97 |
| $1.37+0.001i$ | 1.16 | 112.8 | 43.7 | 70 | 0.97 |

8.3. Conclusion

After hardware and software intercomparison, the comparison with the sunphotometer shows that similar trends are obtained by the both systems and is another check of the lidar system.

One cirrus event is described and its extinction, backscatter, lidar ratio, and depolarization ratio profiles are shown. Those results agree with the results of others lidar groups and theoretical values. Though the lidar ratio is smaller than the 15sr predicted value and this cloud presents low depolarization ratios. The origin of this low depolarization ratio is not well known due to the lack of *in situ* measurements.

One attempt of the retrieval of the volume concentration distribution at low altitude above the station provides results that are in the same order of magnitude than *in situ* measurements. And this, despite the fact that only one extinction and three backscatter coefficients are available. A second attempt at the tail of one cirrus event is performed and the comparison with the low altitude size distribution pointed out some in-cloud processes.

8.4. References

- Ackermann, J. (1998). "The extinction-to-backscatter ratio of tropospheric aerosol: a numerical study." Journal of Atmospheric and Oceanic Technology **15**: 1043-1050.
- Ansmann, A., U. Wandinger, et al. (1992). "Independent Measurement of Extinction and Backscatter Profiles in Cirrus Clouds by Using a Combined Raman Elastic-Backscatter Lidar." Applied Optics **31**(33): 7113-7131.
- Baltensperger, U., Gäggeler, H. W., Jost, D. T., Lugauer, M., Schwikowski, M., Weingartner, E., and Seibert, P. (1997). "Aerosol climatology at high-alpine site Jungfraujoch, Switzerland." Journal of Geophysical Research-Atmospheres **D102**: 19707-19715.
- Del Guasta, M., Morandi, M., Stefanutti, L., Balestri, S., Kyro, E., Rummukainen, M., Kivi, R., Rizi, V., Stein, B., Wedekind, C., Mielke, B., Matthey, R., Mitev, V., and Douard, M. (1998). "Lidar observation of spherical particles in a -65° cold cirrus observed above Sodankyla (Finland) during S.E.S.A.M.E." Journal of Aerosol Science **29**(3): 357-374.
- Del Guasta, M., Morandi, M., Stefanutti, L., Stein, B., Kolenda, J., Rairoux, P., Wolf, J. P., Matthey, R., and Kyro, E. (1994). "Multiwavelength lidar observation of thin cirrus at the base of the Pinatubo stratospheric layer during the EASOE campaign." Geophysical Research Letters **21**(13): 1339-1342.
- HITRAN (1996).
- IPCC (2001). Climate Change 2001: The Scientific Basis, Cambridge University Press.
- Platt, C. M. R., Abshire, N. L., McNice, G. T. (1978). "Some microphysical properties of an ice cloud from lidar observation of horizontally oriented crystals." Journal of Applied Meteorology **17**: 1220-1224.
- Pruppacher, H. R., and Klett J.D. (1997). Microphysics of Clouds and Precipitation, Kluwer Academic Publishers.

- Reichardt, J. (1999). "Optical and geometrical properties of northern midlatitude cirrus clouds observed with a UV Raman lidar." Physics and Chemistry of the Earth Part B-Hydrology Oceans and Atmosphere **24**(3): 255-260.
- Sassen, K. (1991). "The depolarization lidar technique for cloud research: a review and current assessment." Bulletin of the American Meteorological Society **72**(12): 1848-1866.
- Sassen, K. (1992). "Evidence for liquid-phase cirrus cloud formation from volcanic aerosols: climatic implications." Science **257**: 516-519.
- Sassen, K., Griffin, M. K., and Dodd, G. C. (1989). "Optical scattering and microphysical properties of subvisual cirrus clouds, and climatic implications." Journal of Applied Meteorology **28**: 91-98.
- Vaughan, J. M., Geddes, N. J., Flamant, P. H., and Flesia, C. (1998). Establishment of a back-scatter coefficient and atmospheric database, DERA, UK.
- Weingartner, E., Nyeki, S., and Baltensperger, U. (1999). "Seasonal and diurnal variation of aerosol size distributions ($10 < D < 750 \text{ nm}$) at a high-alpine site (Jungfraujoch 3580m asl)." Journal of Geophysical Research-Atmospheres **104**(21): 26809-26820.
- Weingartner, E. (2001). "Personal Communication"

As it is highlighted in the first chapter, the set of well-calibrated instruments have to be improved and this work focusses over the development of such device: one multi-wavelength lidar system at the Jungfraujoch observatory. This new system has to be regarded as a complementary tool to the present set of measurements at this station. Only the interactions of all those techniques can provide reliable data.

The combination of one Raman lidar and one standard backscatter lidar overcomes the drawbacks of the simple elastic lidar. The physical mechanisms linking the aerosol key parameters and the lidar signals are mainly described by the Mie and the Rayleigh theories. Information of the shape of the aerosol is provided by the depolarization ratio and allows the spherical aerosols assumptions in case of low depolarization values. Independent measurements of three backscatter and one extinction coefficients with up to 10% of noise allow the determination of the mean and the integral parameters of the particle size distribution: effective radius, total surface-area concentration, total volume concentration and number concentration of particles.

To reach this level of uncertainty, several tests have been performed. The receivers were modeled using a ray tracing software in order to evaluate the optimal operating range of each telescope. The intercomparison between the mobile micro-lidar of the Observatoire Cantonal de Neuchâtel and the Jungfraujoch lidar system has validated the good performances of this system. The elastic and Raman algorithms have been validated by the two software intercomparisons within the frame of the EARLINET project. And the comparison with the sunphotometer of the Swiss Meteorological Institute is an additional validation of the lidar system.

The sources of systematic and random errors are known and can be reduced to their minimum values. The main source of error is associated with the signal detection itself, but the knowledge of the lidar ratio and the molecular scattering coefficients are among the key parameters of the magnitude of the total error on the Fernald inversion. In the other side, the error introduced by operational procedures can be as significant as the other sources, especially in varying atmospheric conditions.

Up to now the system has shown reliable results and the ability of measuring on a regular basis. The filter polychromator of the Newtonian telescope presents no optical cross-talks between the elastic and the Raman channels and between the parallel and the perpendicular channels. This system provides reliable extinction and backscatter profiles at 355nm and backscatter profiles at 532 and 1064nm, and that with a maximum 20% of uncertainties up to the

tropopause. The depolarization ratio is demonstrated with an excellent rejection ratio. Values close to the molecular and pure spherical aerosol ratio are detected in clear sky condition. Nighttime measurements of water vapor mixing ratio have been also demonstrated. One attempt of the retrieval of the volume concentration distribution with three backscatter (355, 532 and 1064nm) and one extinction (355nm) profiles has demonstrated promising results. To confirm those results, one field campaign is planned in collaboration with the Paul Scherrer Institute. But the present system has to be improve, in particular the measurements at lower altitude. That can be carried out by tilting the system.

Other hardware upgrades of the system consist in measuring the ozone concentration and the temperature profile. The former needs one additional wavelength generated by a second laser and the later can be performed using the rotational Raman technique. The Cassegrain telescope is in its stage of evaluation and its employing will increase significantly the range of observation.

Concerning the software upgrades, the introduction of digital filters for the calculation of the derivative of the logarithm in the Raman algorithm is planned. Moreover the ozone retrieval algorithm is also based on the derivative of one logarithmic ratio and thus those digital filters are suitable for the core of the new algorithms. A more automated version of the present data treatment software is also being studied.

The future configuration of the lidar system at the Jungfraujoch will perform simultaneous measurement of the aerosol optical properties, the water vapor mixing ratio, the ozone concentration and the temperature profile.

10.1. Mie extinction and backscattering coefficients

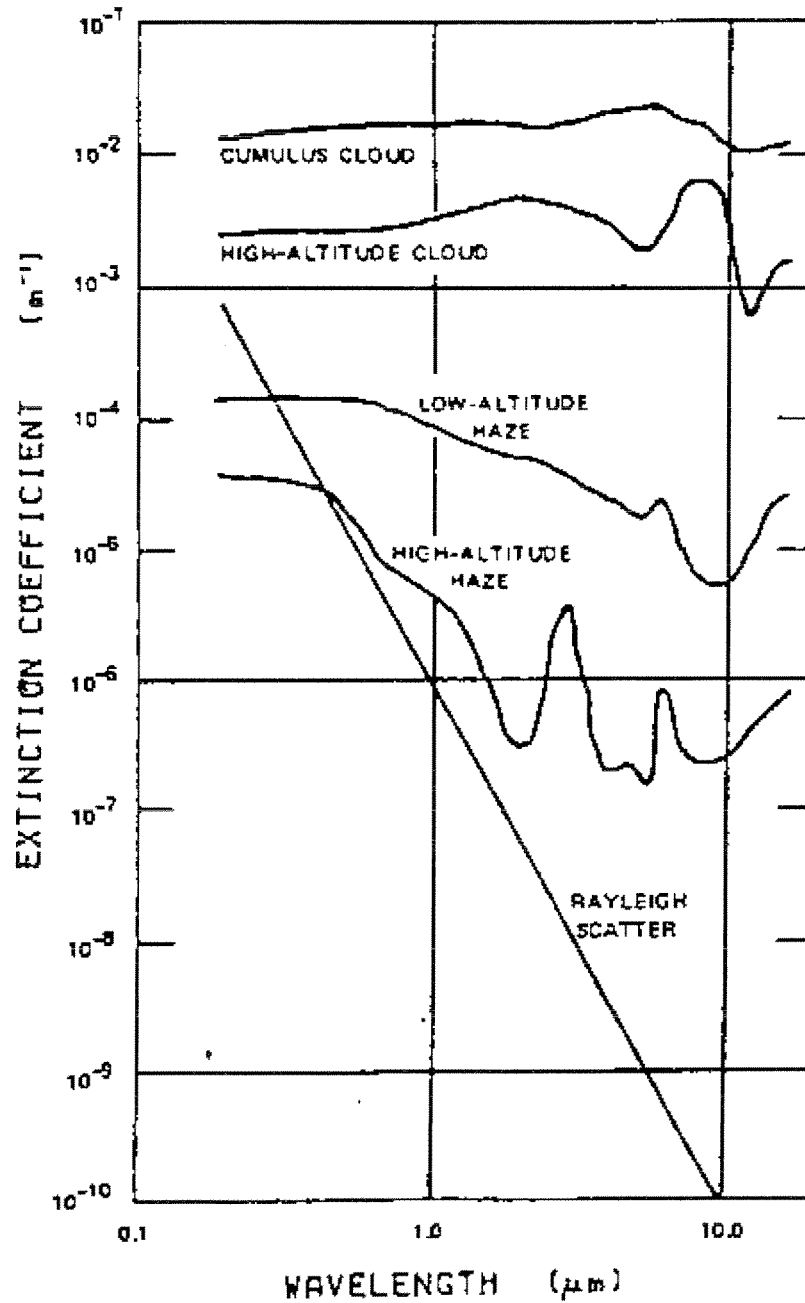


FIGURE 10-1. Extinction coefficients as a function of wavelength for various typical atmospheric conditions.

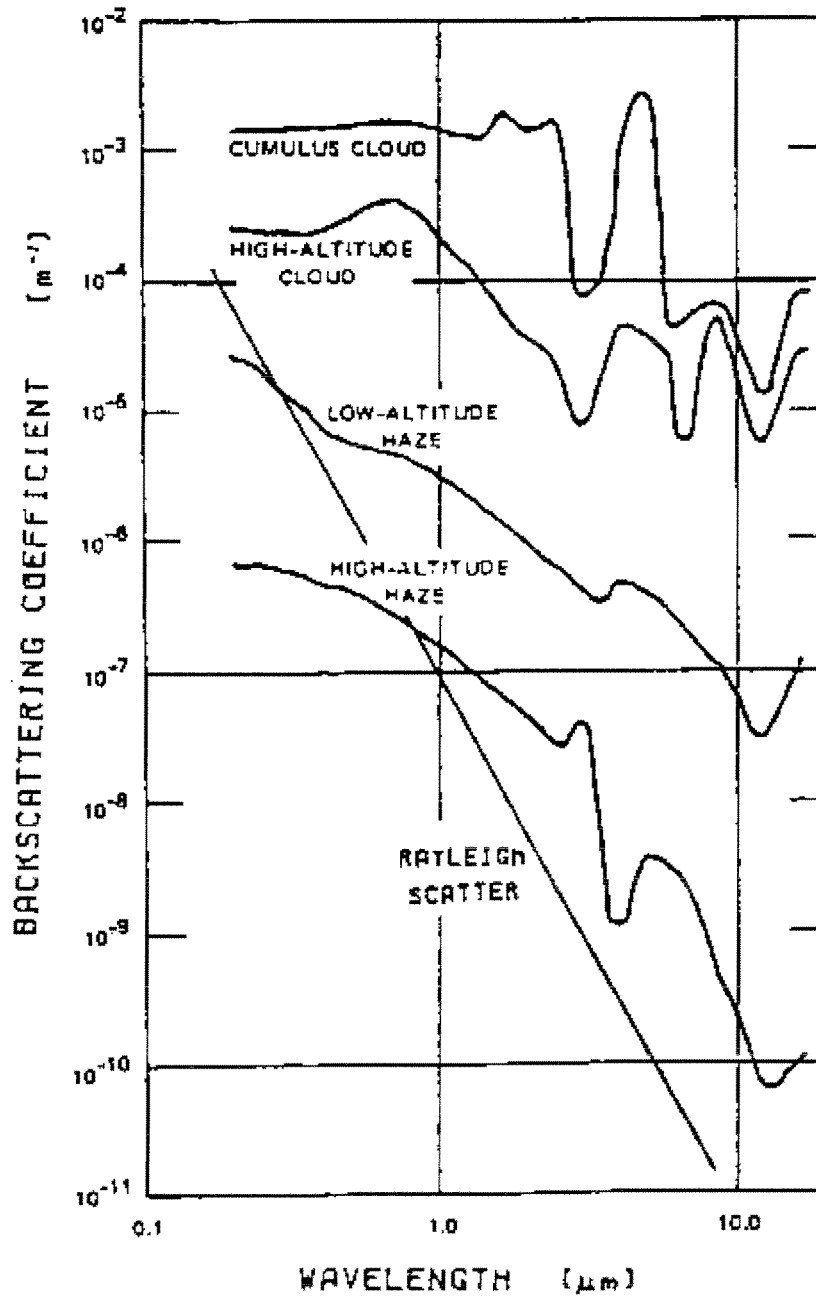


FIGURE 10-2. Backscattering coefficients as a function of wavelength for various typical atmospheric conditions.

10.2. Lidar specification table

10.2.1. Transmitter

Nd:YAG solid state laser

| | |
|----------------------------------|---|
| Manufacturer and model: | Coherent Infinity 40-100 |
| Wavelength: | 1064nm (fundamental) 532nm (second harmonic) 355nm (third harmonic) |
| Repetition rate: | up to 100Hz |
| Max. pulse energy @100Hz: | 400mJ @1064nm 200mJ @532nm 160mJ @355nm |
| Pulse to pulse stability @100Hz: | 1.7% @1064nm 2.5% @532nm 2.5% @355nm |
| Pulsewidth (typical): | 3.5ns @1064nm 3.0ns @532, 355nm |
| Linewidth (typical): | <250MHz (single shot) |
| Beam diameter (near-field): | >95% of pulse energy into 5.5mm diameter at SHG crystal plane |
| Beam diameter (far-field): | >84% of pulse energy into 0.7mrad divergence |
| Divergence (full-angle): | <0.7mrad |
| Timing jitter (rms): | <500 psec rms |

Glan-Thompson prism

| | |
|-------------------|---------------------|
| Manufacturer: | Optics for Research |
| Aperture: | 10mm |
| Transmittance: | 95% |
| Extinction ratio: | 5×10^{-5} |

Beam Expander

| | |
|--------------------------|---|
| Manufacturer: | ET «D & D», Sofia |
| Material: | Fused silica with antireflection coatings |
| Wavelength: | 1064nm |
| Magnification: | 5X |
| Input aperture diameter: | 6mm |

Beam Expander

| | |
|--------------------------|---|
| Manufacturer: | ET «D & D», Sofia |
| Material: | Fused silica with antireflection coatings |
| Wavelength: | 532nm |
| Magnification: | 5X |
| Input aperture diameter: | 6mm |

Beam Expander

| | |
|--------------------------|---|
| Manufacturer: | ET «D & D», Sofia |
| Material: | Fused silica with antireflection coatings |
| Wavelength: | 355nm |
| Magnification: | 5X |
| Input aperture diameter: | 6mm |

Flat laser dielectric mirror

| | |
|---------------------|----------------------|
| Manufacturer: | ET «D & D», Sofia |
| Material: | Fused silica, coated |
| Max. reflection at: | 1064nm |
| Diameter: | 2 inches |

Flat laser dielectric mirror

| | |
|---------------------|-------------------|
| Manufacturer: | ET «D & D», Sofia |
| Material: | BK7 glass, coated |
| Max. reflection at: | 532nm |
| Diameter: | 2 inches |

Flat laser dielectric mirror

| | |
|---------------------|----------------------|
| Manufacturer: | ET «D & D», Sofia |
| Material: | Fused silica, coated |
| Max. reflection at: | 355nm |
| Diameter: | 2 inches |

Motorized optical mount

| | |
|-------------------------|--|
| Manufacturer and model: | New Focus, model #8852 |
| Style: | Corner |
| Optics diameter: | 2 inches |
| Motorized axes: | 3 |
| Angular resolution: | 0.7 μ rad |
| Driver: | New Focus economical multi-axes driver model #8801 |

10.2.2. Receiver**Telescope**

| | |
|-------------------------|-------------------------------|
| Manufacturer and model: | Vixen, model R200SS |
| Configuration: | Newton |
| Primary mirror: | 200mm, parabolic multi-coated |
| Focal length: | 800mm |

Telescope

Manufacturer: Grubb Parsons & Co. Ltd.
Configuration: Cassegrain
Primary mirror: 30 inches, paraboloidal, glass type Duran 50, aluminized
Cassegrain convex mirror: 7.0 inches, hyperboloid, fused quartz type Herasil special, aluminized
Focal length: 11400mm

Beamsplitter (BS1)

Manufacturer: Barr Associates Inc.
Diameter: 2 inches
Angle of incident: 45°
Transmission: 88% @532nm, 90% @607,1064nm
Reflection: 95% @355, 387, 408nm

Beamsplitter (BS2)

Manufacturer: Omega Optical
Diameter: 2 inches
Angle of incident: 45°
Transmission: 70% @387nm, 85% @408nm
Reflection: 97% @355nm

Beamsplitter (BS3)

Manufacturer: Barr Associates Inc.
Diameter: 2 inches
Angle of incident: 45°
Transmission: 97% @408nm
Reflection: 99% @387nm

Beamsplitter (BS4)

Manufacturer: Barr Associates Inc.
Diameter: 2 inches
Angle of incident: 45°
Transmission: 90% @607,1064nm
Reflection: 95% @532nm

Beamsplitter (BS5)

Manufacturer: Barr Associates Inc.
Diameter: 2 inches
Angle of incident: 45°
Transmission: 90% @1064nm
Reflection: 95% @607nm

Bandpass filter (F1)

Manufacturer: Barr Associates Inc.
Diameter: 1 inch
Center wavelength: 354.67nm
Bandwidth FWHM: 0.97nm
Transmission: 58% @355nm
Out-of-band transmission: OD>4

Manufacturer: Barr Associates Inc.
Diameter: 1 inch
Center wavelength: 354.63nm
Bandwidth FWHM: 1.14nm
Transmission: 56% @355nm
Out-of-band transmission: OD>4

Bandpass filter (F2)

Manufacturer: Barr Associates Inc.
Diameter: 1 inch
Center wavelength: 386.4nm
Bandwidth FWHM: 3.0nm
Transmission: 78.5% @387nm
Out-of-band transmission: OD>5

Manufacturer: Barr Associates Inc.
Diameter: 1 inch
Center wavelength: 386.65nm
Bandwidth FWHM: 0.50nm
Transmission: 66% @387nm
Out-of-band transmission: OD>5

Bandpass filter (F3)

Manufacturer: Barr Associates Inc.
Diameter: 1 inch
Center wavelength: 408.55nm
Bandwidth FWHM: 3.80nm
Transmission: 66% @408nm
Out-of-band transmission: OD>5

Manufacturer: Barr Associates Inc.
Diameter: 1 inch
Center wavelength: 407.49nm
Bandwidth FWHM: 0.5nm
Transmission: 53% @408nm
Out-of-band transmission: OD>5

Bandpass filter (F4)

Manufacturer: L.O.T.-Oriel GmbH
Diameter: 1 inch
Center wavelength: 532.16nm
Bandwidth FWHM: 0.93nm
Transmission: 73% @532nm
Out-of-band transmission: OD>4

Manufacturer: Andover Corporation
Diameter: 1 inch
Center wavelength: 532.05nm
Bandwidth FWHM: 1.2nm
Transmission: 41% @532nm
Out-of-band transmission: OD>4

Bandpass filter (F5)

Manufacturer: Barr Associates Inc.
Diameter: 1 inch
Center wavelength: 607.28nm
Bandwidth FWHM: 0.9nm
Transmission: 69% @607nm
Out-of-band transmission: OD>5

Manufacturer: Barr Associates Inc.
Diameter: 1 inch
Center wavelength: 607.3nm
Bandwidth FWHM: 0.9nm
Transmission: 61% @607nm
Out-of-band transmission: OD>4

Bandpass filter (F6)

Manufacturer: Barr Associates Inc.
Diameter: 1 inch
Center wavelength: 1063.89nm
Bandwidth FWHM: 1.1nm
Transmission: 81% @1064nm
Out-of-band transmission: OD>4

Manufacturer: Barr Associates Inc.
Diameter: 1 inch
Center wavelength: 1064.07nm
Bandwidth FWHM: 1.0nm
Transmission: 72% @1064nm
Out-of-band transmission: OD>4

Wollaston prism (WP)

| | |
|---------------------|--|
| Manufacturer: | Casix PWT5010 |
| Material: | Calcite with Single layer MgF2 AR Coating @633nm |
| Extinction ratio: | $<5 \times 10^{-5}$ |
| Angular separation: | $15^{\circ} - 20^{\circ}$ |
| Diameter: | 10mm |

Photomultiplier (PMT1)

| | |
|----------------------------|---|
| Manufacturer and reference | Hamamatsu photosensor module, H6780-06 series |
| Type: | End-on photomultiplier with built-in high voltage power supply |
| Effective area: | 8mm |
| Spectral response range: | 185-650nm |
| Time response: | 0.78ns @0.8V on control voltage |
| Gain: | 6.0×10^5 |
| Radiant sensitivity: | 43 μ A/nW @0.8V on control voltage |
| Dark current: | Typ. 0.2nA @0.8V on control voltage Max. 10nA @0.8V on control voltage |

Photomultiplier (PMT2)

| | |
|----------------------------|--------------------------|
| Manufacturer and reference | Thorn EMI, QA9829 series |
| Type: | End-on photomultiplier |
| Effective area: | 45mm |
| Spectral response range: | 320-650nm |
| Time response: | 3ns |
| Anode sensitivity: | 500A/lm |
| Gain: | 6.7×10^6 |
| Dark current: | 0.4nA |

Photomultiplier (PMT3)

| | |
|----------------------------|-------------------------|
| Manufacturer and reference | Thorn EMI, B9202 series |
| Type: | End-on photomultiplier |
| Effective area: | 45mm |
| Spectral response range: | 320-850nm |
| Time response: | 5ns |
| Anode sensitivity: | 200A/lm |
| Gain: | 0.8×10^6 |
| Dark current: | 1.0nA |

Si-Avalanche Photodiode (APD)

| | |
|----------------------------|---|
| Manufacturer and reference | EG&G, C30954/5e |
| Type: | Integrated TE cooler and temperature controller |
| Effective area: | 1.5mm |
| QE @650nm: | >80% |
| Responsivity @1060nm: | 34A/W typ., QE=38% |
| Dark current @22°C: | 100nA |
| Spectral noise current: | 0.5 pA/sqrt(Hz) max. |
| Preamplifier: | |
| bandwidth: | DC-200MHz |
| gain: | 11mV/μA into 50Ω |
| output polarity: | negative |
| output signal: | 0...-1V max. |
| Geiger mode operation: | |
| single photon rise time: | <5ns |

Transient recorder

| | |
|------------------------------|--|
| Manufacturer and model: | Licel |
| General description: | Built in analog and photon counting acquisition device |
| Analog acquisition: | |
| Signal input range: | 0-20, 0-100, 0-500 mV @ 50 Ω load |
| A/D resolution: | 12 bit |
| Sampling rate: | 20 MHz, giving a lidar spatial resolution of 7.5 m |
| Summation memory: | 4094 acquisitions for the two channels together |
| SNR single shot: | 66 dB @ 100 mV |
| Memory depth: | 8192 or 16384 bins (i.e. 61440 m or 122880 m) |
| Max repetition rate: | 150 Hz @ 400 μs signals, 75 Hz @ 800 μs signals |
| Trigger delay and jitter: | 50 ± 12.5 ns |
| Photon counting acquisition: | |
| Signal input range: | 0-20, 0-100 mV @ 50 Ω load |
| Discriminator: | 64 levels software controlled |
| Bandwidth: | 10 - 250 MHz |
| Summation memory: | 4094 acquisitions for the two channels together |
| Memory depth: | 8192 or 16384 bins (i.e. 61440 m or 122880 m) |
| Trigger: | |
| Generalities: | Two trigger inputs to acquire signals in two separate memories |
| | Threshold and slope 2.5 V, positive, 50 Ω load |
| Delay and jitter: | 50 ± 12.5 ns |

10.3. Overlap function

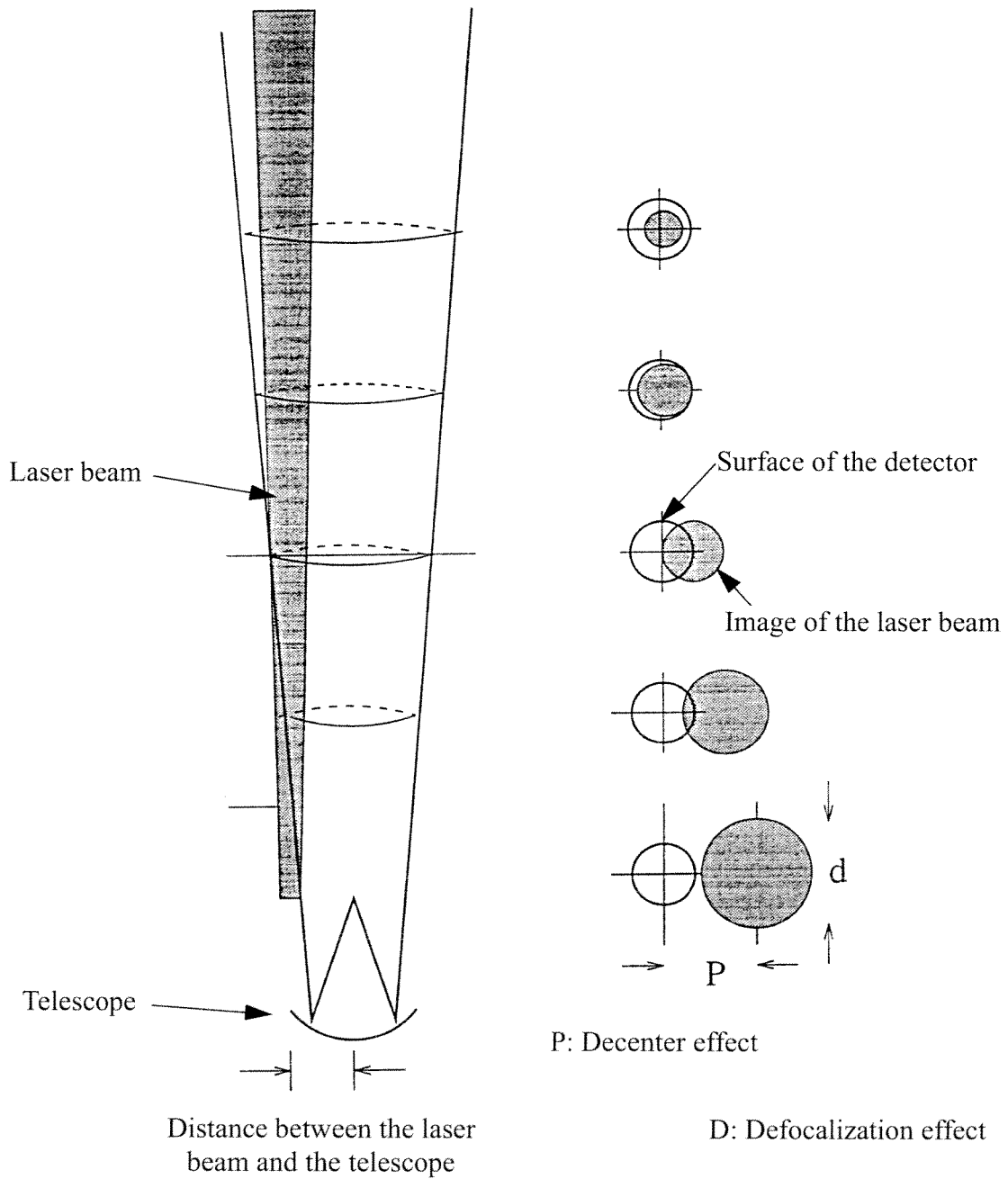


FIGURE 10-3. Schematic representation of the decenter and the defocalization effects versus the altitude.

10.4. Laser beam radius depending on the altitude above the Station

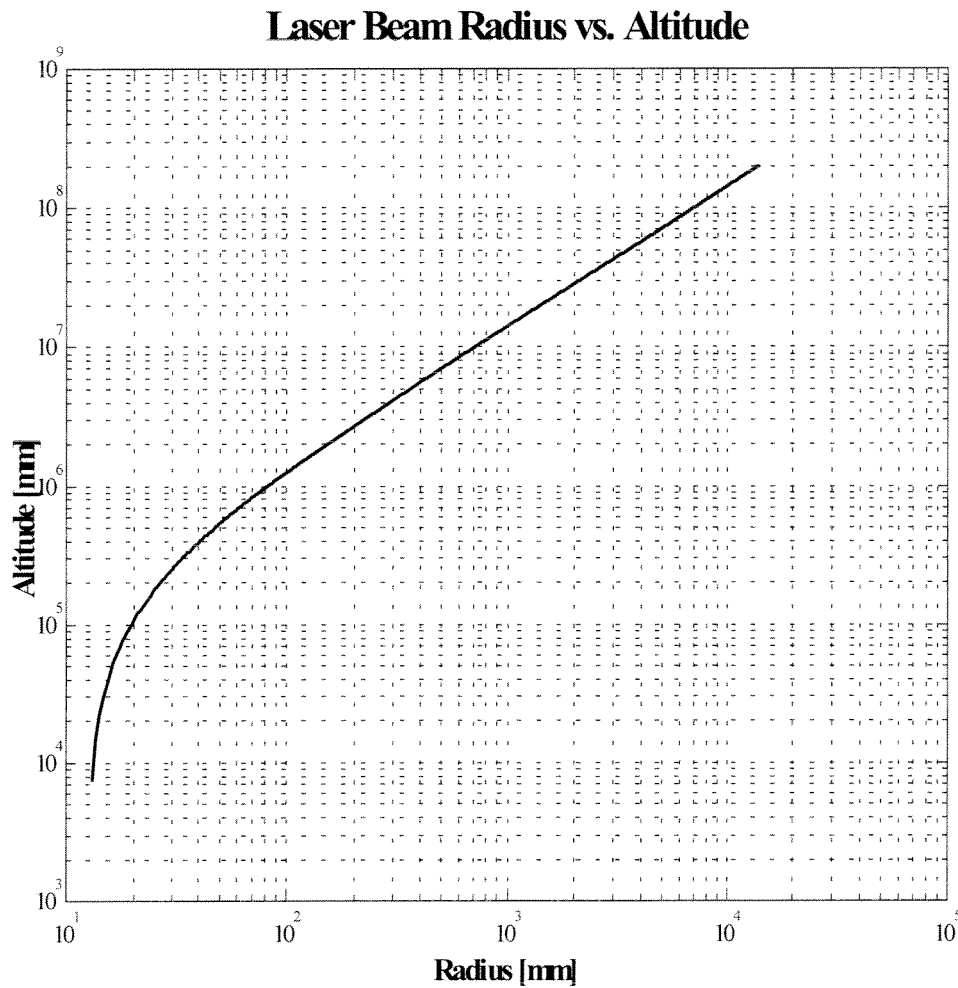


FIGURE 10-4. Laser beam radius depending on the altitude above the station. The divergence of the laser is 0.14mrad.

10.5. Error on the backscatter coefficient determined by Raman lidar

The total error on the backscatter coefficient determined by Raman lidar is given using the error propagation on the scattering ratio

$$\beta_p(\lambda_0) = \{\Re(\lambda_0) - 1\} \beta_m(\lambda_0) \quad (\text{EQ 10.1})$$

where R is given by (EQ 4.20) and thus rewriting (EQ 10.1) gives

$$\beta_p(\lambda_0) = \left\{ \left[\frac{P^\#(\lambda_L)}{P^\#(\lambda_R)} \times \frac{T_R}{T_L} \right] - 1 \right\} \beta_m(\lambda_0) \quad (\text{EQ 10.2})$$

where T_X is the atmospheric transmissivity at wavelength X. The variables are the two normalized signals at the reference altitude R_f , the four extinctions coefficients and the molecular backscatter coefficient whose partial derivatives are given by

$$\frac{\partial \beta_p(\lambda_0)}{\partial P^\#(\lambda_L)} = \left\{ \left[\frac{1}{P^\#(\lambda_R)} \times \frac{T_R}{T_L} \right] \beta_m(\lambda_0) \right\} \quad (\text{EQ 10.3})$$

$$\frac{\partial \beta_p(\lambda_0)}{\partial P^\#(\lambda_L)} = \left\{ \left[-\frac{P^\#(\lambda_L)}{(P^\#(\lambda_R))^2} \times \frac{T_R}{T_L} \right] \beta_m(\lambda_0) \right\} \quad (\text{EQ 10.4})$$

$$\frac{\partial \beta_p(\lambda_L)}{\partial \alpha_p(\lambda_L)} = \frac{\partial \beta_p(\lambda_L)}{\partial \alpha_m(\lambda_L)} = \left\{ \left[\frac{P^\#(\lambda_L)}{P^\#(\lambda_R)} \times \frac{T_R}{T_L} \right] \beta_m(\lambda_0) \right\} (R - R_f) \quad (\text{EQ 10.5})$$

$$\frac{\partial \beta_p(\lambda_L)}{\partial \alpha_p(\lambda_R)} = \frac{\partial \beta_p(\lambda_L)}{\partial \alpha_m(\lambda_R)} = \left\{ \left[\frac{P^\#(\lambda_L)}{P^\#(\lambda_R)} \times \frac{T_R}{T_L} \right] \beta_m(\lambda_0) \right\} (R_f - R) \quad (\text{EQ 10.6})$$

$$\frac{\partial \beta_p(\lambda_0)}{\partial \beta_m(\lambda_0)} = \left\{ \left[\frac{P^\#(\lambda_L)}{P^\#(\lambda_R)} \times \frac{T_R}{T_L} \right] - 1 \right\}$$

(EQ 10.7)

The uncertainties on the variable are discussed in “Error analysis”, p 90, but those on the normalized signals are the sum of the error on the signal plus the error on the signal at the reference altitude

$$\delta P^\# = \left\{ (\partial P^*)^2 + (\partial P^*|_{R_f})^2 \right\}^{1/2}$$

(EQ 10.8)

The total error on the backscatter coefficient obtained by Raman lidar is thus given by

$$\delta \beta_p(\lambda_L) = \left\{ \begin{aligned} & \left(\frac{\partial \beta_p(\lambda_L)}{\partial P^\#(\lambda_R)} \delta P^\#(\lambda_R) \right)^2 + \left(\frac{\partial \beta_p(\lambda_L)}{\partial P^\#(\lambda_L)} \delta P^\#(\lambda_L) \right)^2 \\ & + \left(\frac{\partial \beta_p(\lambda_L)}{\partial \beta_m(\lambda_L)} \delta \beta_m(\lambda_L) \right)^2 \\ & + \left(\frac{\partial \beta_p(\lambda_L)}{\partial \alpha_p(\lambda_L)} \delta \alpha_p(\lambda_L) \right)^2 + \left(\frac{\partial \beta_p(\lambda_L)}{\partial \alpha_p(\lambda_R)} \delta \alpha_p(\lambda_R) \right)^2 \\ & + \left(\frac{\partial \beta_p(\lambda_L)}{\partial \alpha_m(\lambda_L)} \delta \alpha_m(\lambda_L) \right)^2 + \left(\frac{\partial \beta_p(\lambda_L)}{\partial \alpha_m(\lambda_R)} \delta \alpha_m(\lambda_R) \right)^2 \end{aligned} \right\}^{1/2}$$

(EQ 10.9)

10.6. Elastic intercomparisons

10.6.1. Case 1

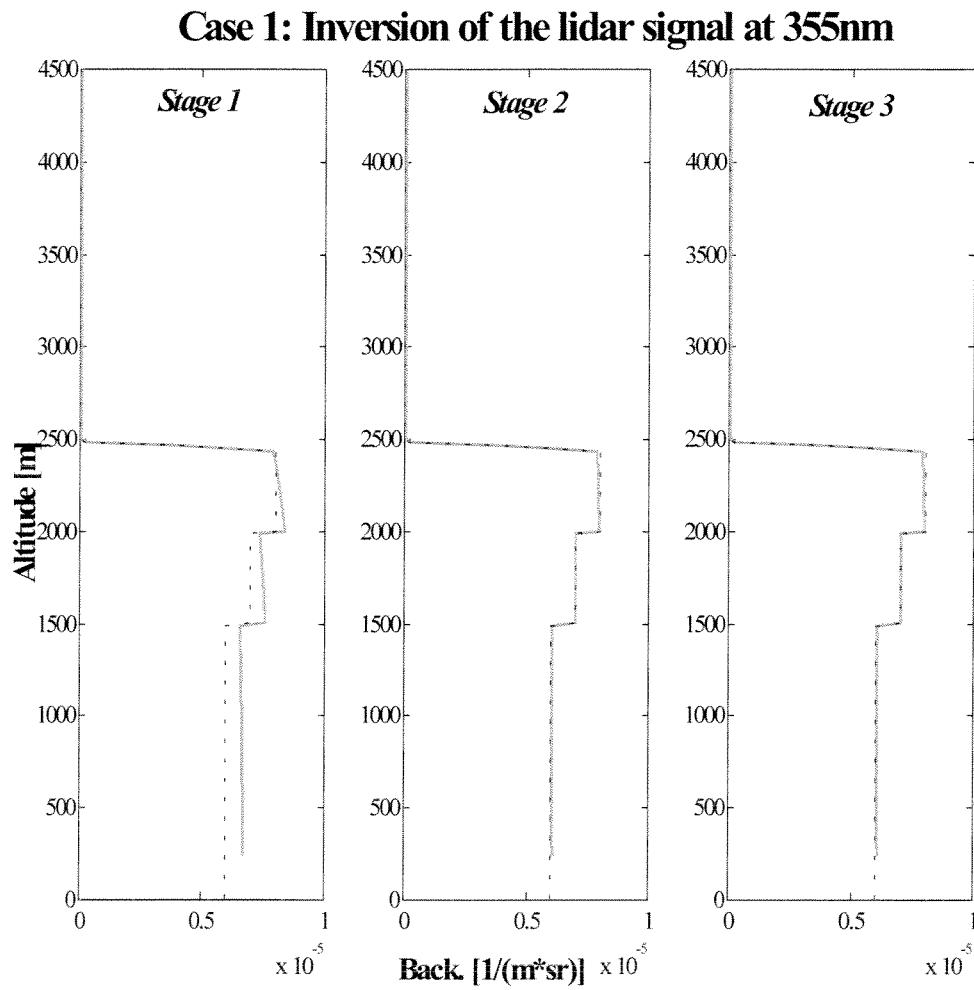


FIGURE 10-5. Retrieved aerosol backscatter coefficient at 355nm (gray line) in comparison to the simulation input profile (black dot-line) for the case1. The left, middle and right panels give the stage 1, stage 2 and stage 3, respectively

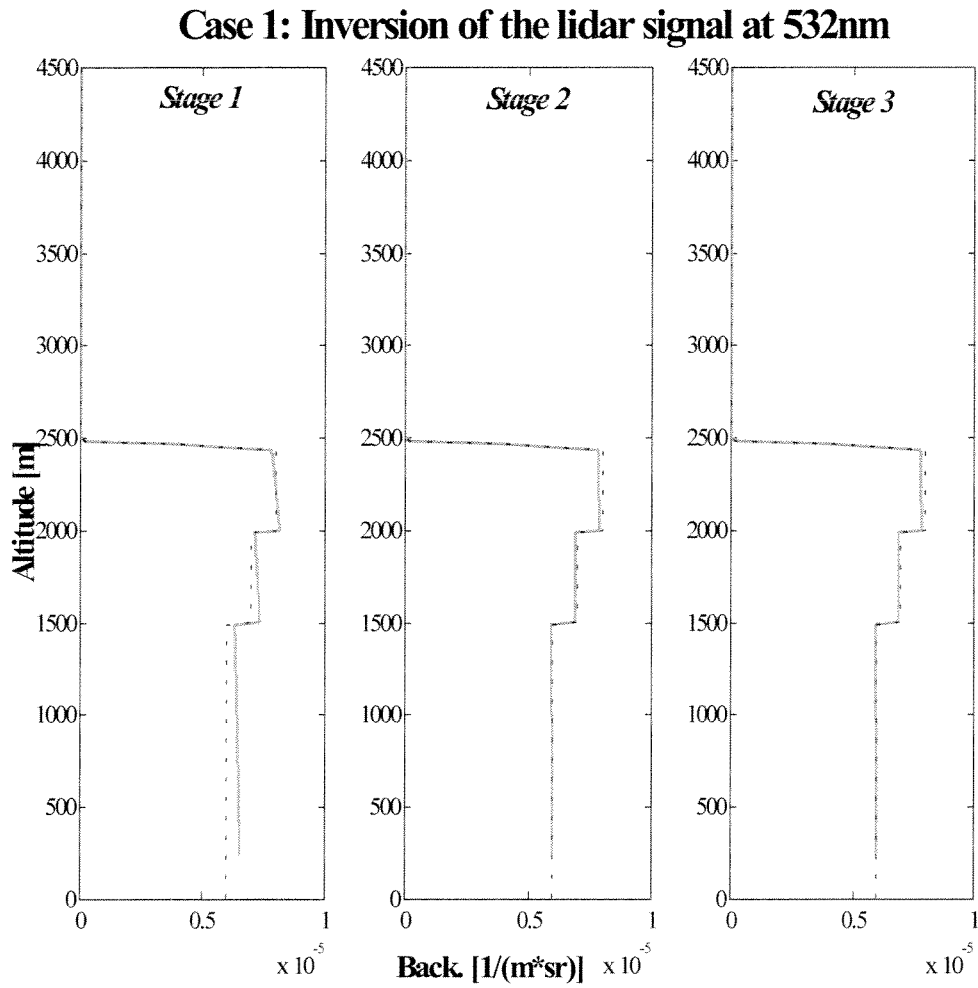


FIGURE 10-6. Retrieved aerosol backscatter coefficient at 532nm (gray line) in comparison to the simulation input profile (black dot-line) for the case1. The left, middle and right panels give the stage 1, stage 2 and stage 3, respectively

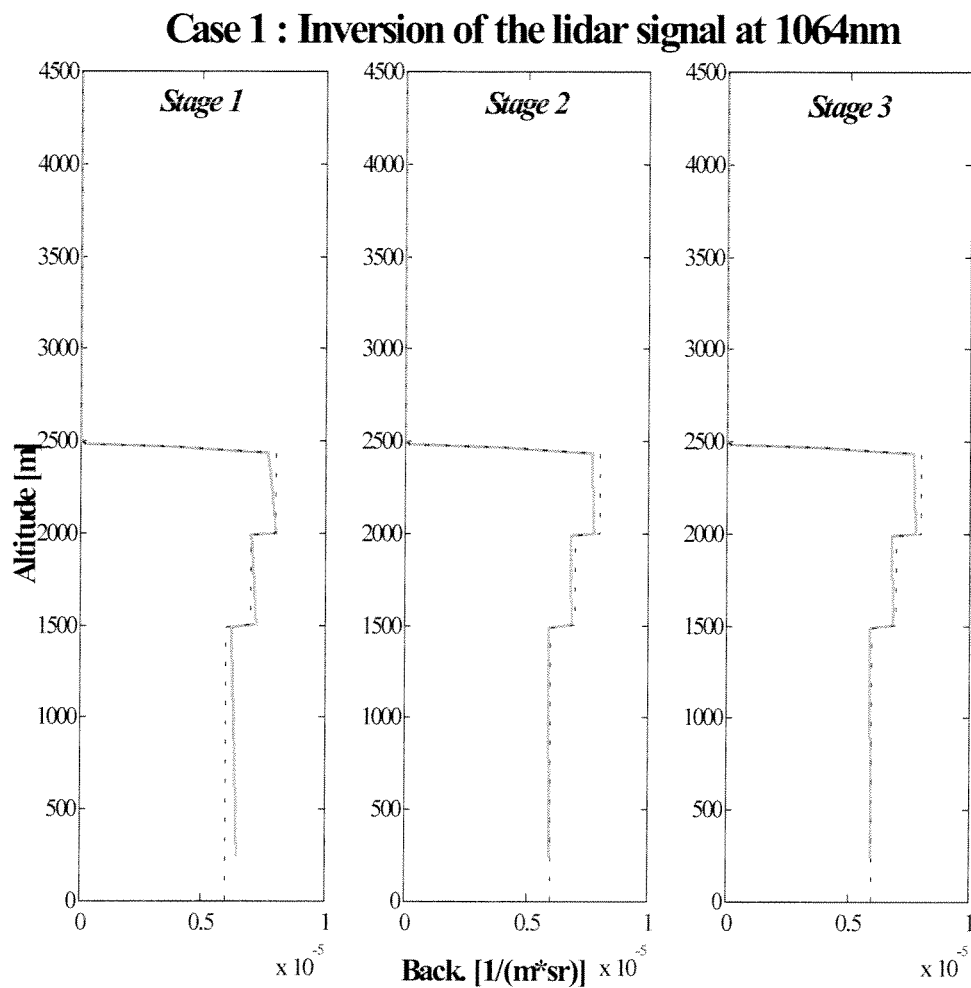


FIGURE 10-7. Retrieved aerosol backscatter coefficient at 1064nm (gray line) in comparison to the simulation input profile (black dot-line) for the case1. The left, middle and right panels give the stage 1, stage 2 and stage 3, respectively

10.6.2. Case 2

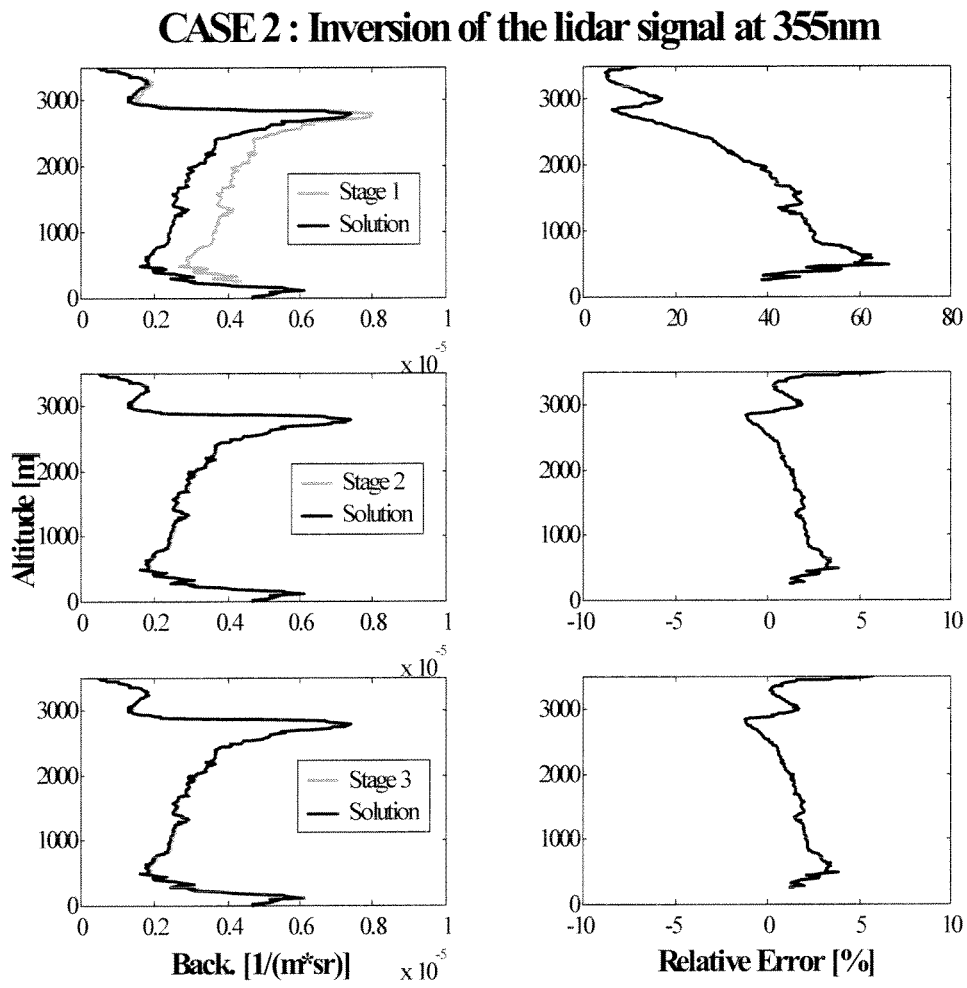


FIGURE 10-8. Retrieved aerosol backscatter coefficient at 355nm in comparison to the simulation input profile for the case 2

CASE 2 : Inversion of the lidar signal at 532nm

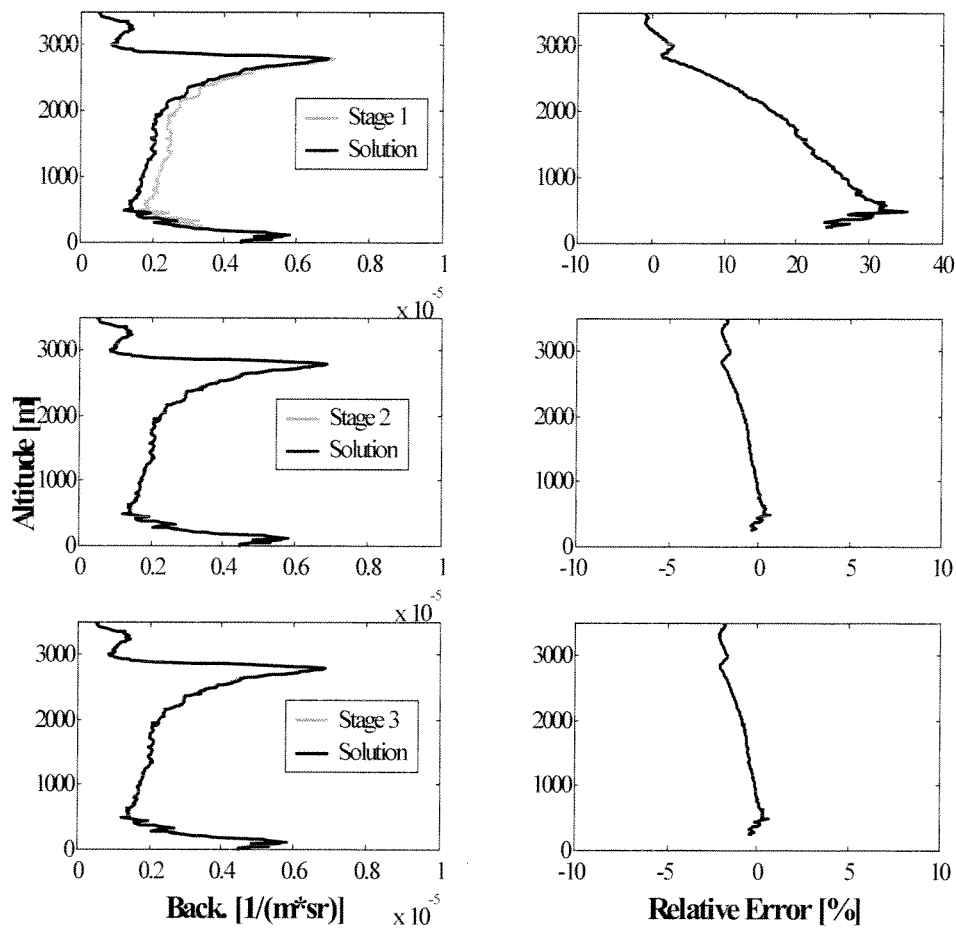


FIGURE 10-9. Retrieved aerosol backscatter coefficient at 532nm in comparison to the simulation input profile for the case 2

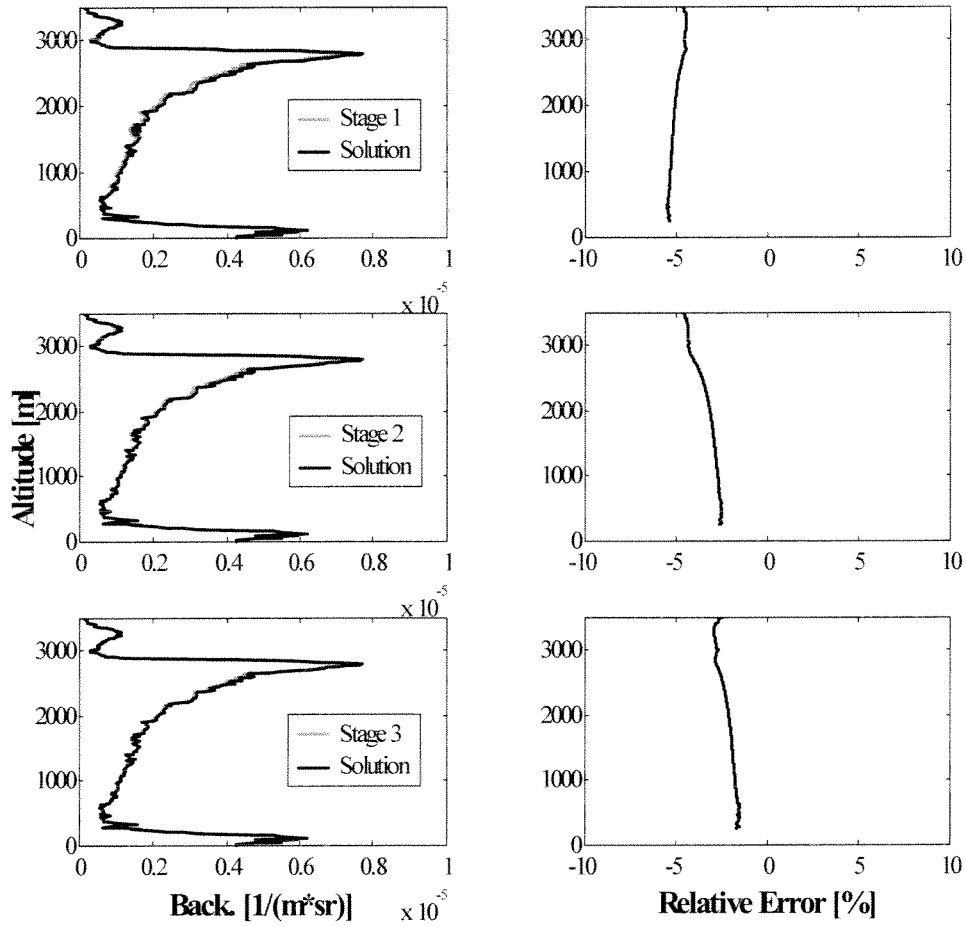
CASE 2 : Inversion of the lidar signal at 1064nm

FIGURE 10-10. Retrieved aerosol backscatter coefficient at 1064nm in comparison to the simulation input profile for the case 2

10.6.3. Case 3

CASE 3 : Inversion of the lidar signal at 355nm

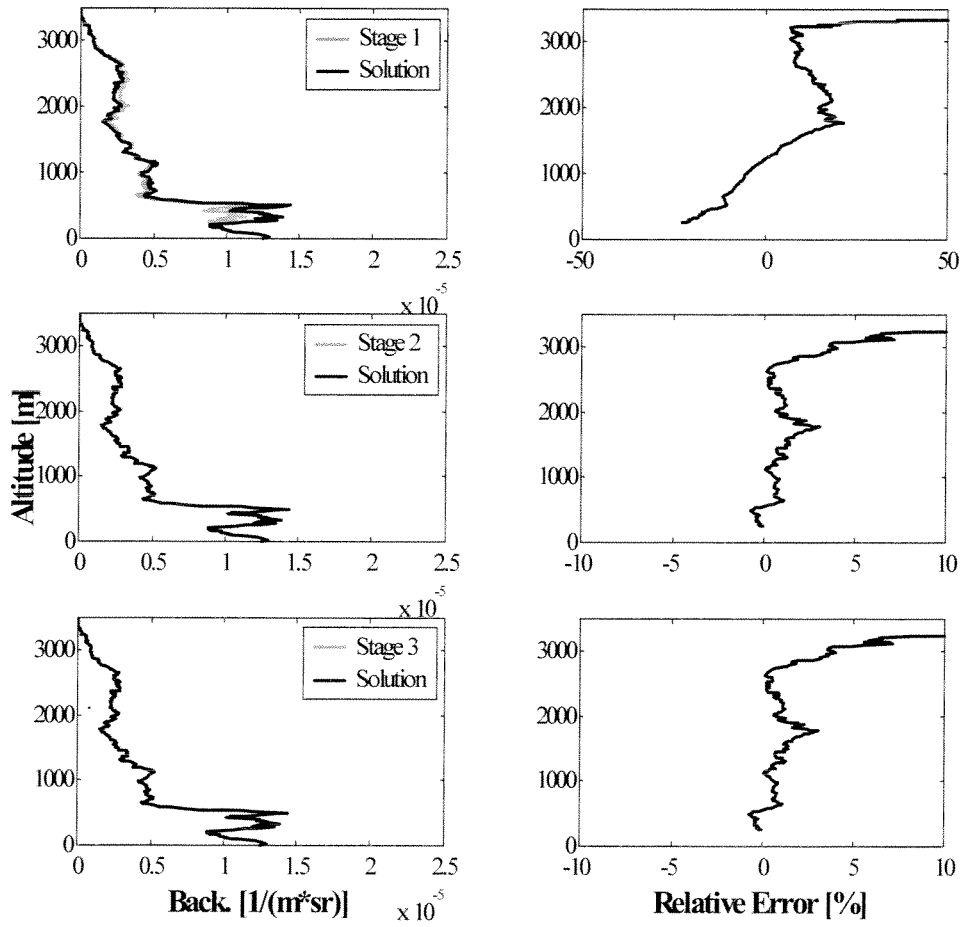


FIGURE 10-11. Retrieved aerosol backscatter coefficient at 355nm in comparison to the simulation input profile for the case 3

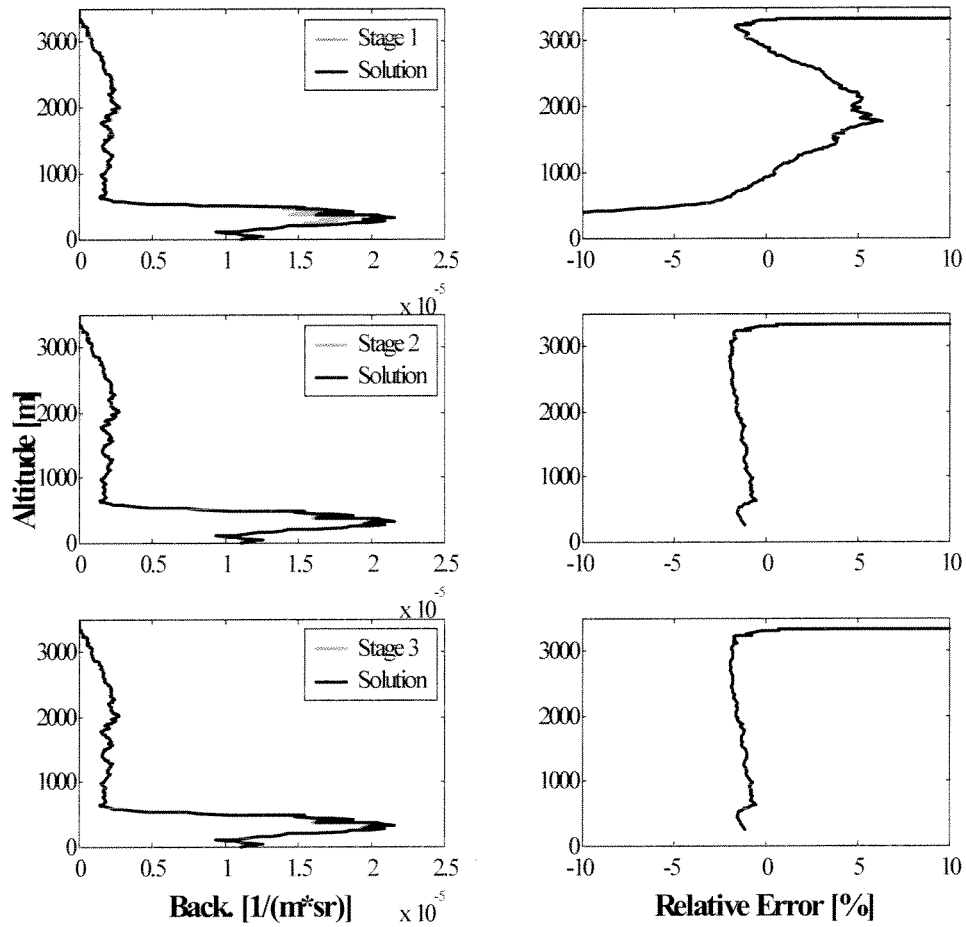
CASE 3 : Inversion of the lidar signal at 532nm

FIGURE 10-12. Retrieved aerosol backscatter coefficient at 532nm in comparison to the simulation input profile for the case 2

CASE 3 : Inversion of the lidar signal at 1064nm

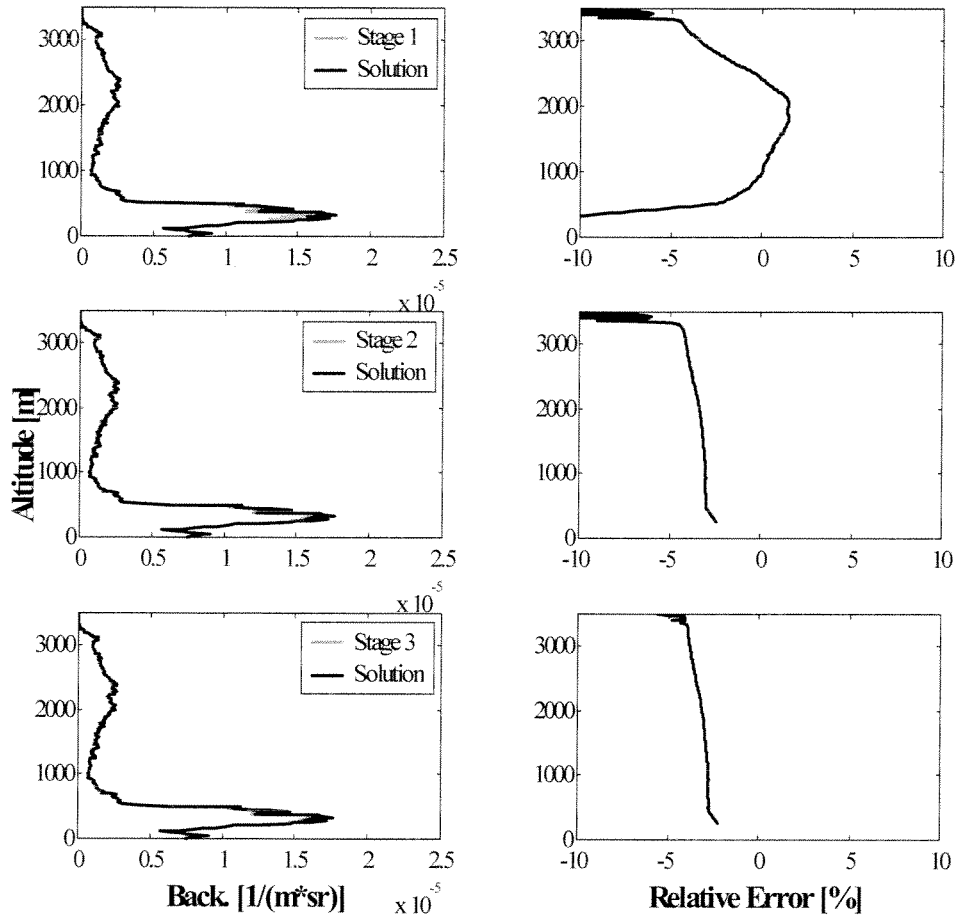


FIGURE 10-13. Retrieved aerosol backscatter coefficient at 1064nm in comparison to the simulation input profile for the case 3

Curriculum Vitae & Personal publications

Larchevêque Gilles
Av. du 1^{er} Mai 12
1020 Renens
SWITZERLAND

Born in July 26th 1968
Swiss citizenship.
Single.

Graduate in Rural Engineering EPFL

CURSUS

- 2002-1997: Ph.D. thesis work, atmospheric remote sensing by laser. Institute of environmental engineering, Air pollution laboratory, Swiss Federal Institute of Technology (EPFL, Switzerland). Thesis title: Development of the Jungfrauoch multi-wavelength lidar system for continuous observations of the aerosol optical properties in the free troposphere.
- 1992-1997: **Graduate in Rural Engineering**, EPFL.

LANGUAGES

French: Mother language.
English: Read, written, spoken.
German: Basic notions.

INFORMATIC KNOWLEDGE

Language: Pascal, C/C#, HTML and CGI.
Software: Labview, Matlab, MS Office2000, Adobe FrameMaker
OS: W9x, NT4 server, Linux, Unix, Macintosh.

PUBLICATION

- Balin, I., Larchevêque, G., Quaglia, P., Simeonov, V., van den Bergh, H., and Calpini, B. (2001). Water vapor profile by Raman lidar in the free troposphere from the Jungfraujoch Alpine Station. Advances in global change research, Kluwer Academic Publisher. **9**.
- Calpini, B., Clappier, A., Jimenez, R., Larchevêque, G., Lazzarotto, B., Martilli, A., Pasi, F., Quaglia, P., Simeonov, V., Van den Bergh, H. (1999). Photo-Oxydant Formation in the Milan Metropolitan Area. Eurotrac Symposium 98.
- Calpini, B., Larchevêque, G., and Simeonov, V. (2001). "Study of vertical fluxes of aerosols in the lower atmosphere by LIDAR measurements: characterization of the PBL development during the WINTEX experiment." Theoretical and applied Climatology **70**(1-4): Electronic Supplementary Material: Documented datasets.
- Couach, O., Balin, J., Jimenez, R., Quaglia, P., Simeonov, V., Larchevêque, G., Lazzarotto, B., Kuebler, J., Sathya, V., Martilli, A., Junier, M., Roulet, Y.-A, Kirchner, F., Clappier, A., Calpini, B., Van den Bergh, H. (2000). Campagne de mesure intensives 1999 sur la région grenobloise. Ensemble des résultats et Analyse des Périodes d'Observations Intensives (POI), EPFL-ASCOPARG.
- Jimenez, R., Dubois, C., Jeanneret, F., Larchevêque, G., Lazzarotto, B., Simeonov, V., Calpini, B. (1997). Assessment of Air Quality in the Canton of Obwald. Field Measurement Campaign 1997, preliminary experimental report. Lausanne.
- Larchevêque, G., Balin, I., Nessler, R., Quaglia, P., Simeonov, V., van den Bergh, H., and Calpini, B. (2001). "Development of a multiwavelength aerosol and water vapor lidar at the Jungfraujoch Alpine Station (3580m ASL) in Switzerland." submitted in Applied Optics.
- Larchevêque, G., Simeonov, V., van den Bergh, H., and Calpini, B. (1998). "Determination of the PBL height by LIDAR in boreal condition." Proceedings of the 23th EGS.
- Larchevêque, G., Simeonov, V., van den Bergh, H., and Calpini, B. (1998). Is the PBL well determined by aerosol lidar in very clean boreal conditions? Extended Abstract of the 19th ILRC.
- Lazzarotto, B., Brönnimann, S., Cattin, R., Couach, O., Eugster, W., Hasler, N., Larchevêque, G., Liston, G. E., Simeonov, V., Van den Bergh, H., Calpini, B. (2001). "Vertical profiles of O₃ and H₂O by Raman lidar, compared with tethered balloon and numerical simulation." To be submitted.
- Lazzarotto, B., Frioud, M., Larchevêque, G., Mitev, V. M., Quaglia, P., Simeonov, V., Thompson, A., Van den Bergh, H., Calpini, B. (2000). "Ozone and Water Vapor Measurements by Raman Lidar in the Boundary Layer : Error Sources and Field Measurements." accepted in Applied Optics.
- Lazzarotto, B., Larchevêque, G., Quaglia, P., Simeonov, V., Van den Bergh, H., Calpini, B. (1999). "Raman DIAL Measurement of Ozone and Water Vapor in the Lower Troposphere." SPIE Europto series "Environmental Sensing and Applications" **3821**: 54-61.

- Lazzarotto, B., Simeonov, V., Quaglia, P., Larchevêque, G., Van den Bergh, H., Calpini, B. (1998). Retrieval of Ozone and Water Vapor in the Lower Troposphere by Raman DIAL. Extended Abstract of the 19th ILRC.
- Lazzarotto, B., Simeonov, V., Quaglia, P., Larchevêque, G., Van den Bergh, H., Calpini, B. (1999). "A Raman Differential Absorption Lidar for Ozone and Water Vapor Measurement in the Lower Troposphere." International Journal of Environmental Analytical Chemistry **74**: 255-261.
- Lazzarotto, B., Simeonov, V., Quaglia, P., Larchevêque, G., Van den Bergh, H., Calpini, B. (2000). Ozone and Water Vapor by Raman Lidar in the PBL. Extended Abstract of the 20th ILRC.
- Papayannis, A., Amoiridis, V., Baldasano, J., Balin, J., Balis, D., Boselli, A., Chaikovsky, A., Chatenet, B., Chourdakis, G., Freudenthaler, V., Frioux, M., Herman, J., Larlori, M., Kreipl, S., Larchevêque, G., Matthey, R., Mattis, I., Müller, D., Pandolfi, M., Pappalardo, G., Pelon, J., Perrone, M.R., Rizi, V., Rodriguez, A., Sauvage, L., Sobolewski, P., Spinelli, N., de Tomasi, F., Trickl, T., and Wiegner, M. (2001). "Continental-scale vertical profile measurements of free tropospheric Saharan dust particles performed by a coordinated ground-based European Aerosol Research Lidar Network (EARLINET project)." submitted to JGR.
- Quaglia, P., Larchevêque, G., Jimenez, R., Lazzarotto, B., Simeonov, V., Ancellet, G., Van den Bergh, H., Calpini, B. (1999). "Planetary Boundary Layer Ozone Fluxes from Combined Airborne, Ground Based Lidars and Wind Profilers Measurements." Analisis **27**(4): 304-310.
- Simeonov, V., Larchevêque, G., Quaglia, P., van den Bergh, H., and Calpini, B. (1999). "Influence of the photomultiplier tube spatial uniformity on lidar signals." Applied Optics **38**(24): 5186-5190.
- Simeonov, V., Lazzarotto, B., Larchevêque, G., Quaglia, P., Calpini, B. (1999). "UV Ozone DIAL based on a Raman Cell Filled with Two Raman Actives Gases." SPIE Europto series "Environmental Sensing and Applications" **3821**: 54-61.

